
INVESTIGATIONS OF LOW MASS X-RAY BINARIES

by Andrzej Gibiec

A thesis submitted for the degree of Doctor of Philosophy
to the Jagiellonian University in Cracow.

Astronomical Observatory

Jagiellonian University

June 2012

Abstract

Spectral and timing studies of Low Mass X-ray Binaries (LMXB) are presented including the super-Eddington Z-track sources and the Atoll sources. Firstly, the Cygnus X-2 like Z-track sources, Cygnus X-2 and GX 340+0 were investigated using a spectral approach based on the now substantial evidence that the accretion disk corona (ADC) is extended requiring a form for the Comptonized emission embodying seed photons from the disk below the ADC. The mass accretion rate \dot{M} increases between soft and hard apex contrary to the standard model and the neutron star temperature increases substantially. The large resultant increase of radiation pressure disrupts the inner disk launching the relativistic jets observed in radio on this part of the Z-track. Again, contrary to the standard view, \dot{M} increase does not cause the Flaring Branch which is shown to have constant \dot{M} , but there is compelling evidence that this is unstable nuclear burning on the neutron star as the onset agrees well with the theoretical condition for unstable burning. These results show that the above physical model proposed by Church et al. (2006) applies to all the Cyg-like sub-group. The variation in frequency of the kHz Quasi Periodic Oscillations (QPO) on the Horizontal Branch suggests that the higher frequency QPO is an oscillation at the inner disk edge. The observed variation is consistent with radial movement of the edge due to varying radiation pressure of the neutron star. This extends the results of Jackson et al. (2009) so comprising a model for the higher frequency kHz QPO. The investigation was extended to the Sco-like sub-group of Z-track sources. As in the Cyg-like sources, \dot{M} increases on the Normal Branch and the increasing neutron star temperature kT leads to strong radiation pressure. However, in Sco X-1 and GX 349+2, kT is always more than 2 keV and it is proposed that the consequent strong radiation pressure can launch jets on all parts of the Z-track as observed. Flaring is found to consist of unstable nuclear burning combined with \dot{M} increase. These two physical differences are responsible for the observational differences in X-rays between the Cyg and Sco-like sources. Examination of the 14-year lightcurves from the *RXTE* All-Sky Monitor shows the continual nature of flaring in the Sco-like sources and suggests a model in which this flaring heats the neutron star. This is supported by an observation of Sco X-1 with reduced flaring, having somewhat lower kT . GX 17+2 appears transitional between the two sub-groups of Z-track sources.

Finally, a survey of eight Atoll sources explains the nature of the Banana and Island states. In the Banana State, there is thermal equilibrium between the neutron star and the ADC. But, below a critical luminosity, this breaks down and heating of the ADC by an unknown process causes the high energy Comptonization cut-off energy to increase from a few keV towards 100 keV producing the previously unexplained hardness of the Island State. Increase of radiation pressure may lead to the launching of weak jets. The size of the emission region on the neutron star in LMXB agrees well with the theory of accretion flow spreading on the neutron star (Inogamov & Sunyaev 1999). The present work constitutes a unified physical model of the Z-track and Atoll LMXB, in which the importance of radiation pressure and unstable nuclear burning in addition to accretion theory is demonstrated.

Statement of originality

The work presented in this thesis is, unless stated otherwise, the original work of the author and has been prepared under the supervision of Dr hab. Monika Bałucińska-Church.

Acknowledgements

I am immensely grateful to my Ph D supervisor Dr hab. Monika Bałucińska-Church and also to Prof Michael J. Church for all their support, guidance and effort over the years of my studies and visits to Birmingham. I would also like to thank Prof Michał Ostrowski for his advice and help on many occasions.

My work was supported by the Polish grants 3946/B/H03/2008/34 and 5843/B/H03/2011/40, and by the *Young Scientist Programme* stipend funded by the Polish Ministry of Science and Higher Education and the British Council. Financial aid was also kindly provided by “Fundacja Astronomii Polskiej im. Mikołaja Kopernika” and within the “Małopolskie Stypendium Doktoranckie” project funded by the European Social Fund.

This research has made use of data and software provided by the High Energy Astrophysics Science Archive Research Center (HEASARC), which is a service of the Astrophysics Science Division at NASA/GSFC and the High Energy Astrophysics Division of the Smithsonian Astrophysical Observatory.

Contents

1	Introduction	1
1.1	The X-ray sky and the power of accretion	1
1.1.1	Accretion from a wind	4
1.1.2	Accretion via Roche-lobe overflow	5
1.2	X-ray Binaries	9
1.2.1	High Mass X-ray Binaries	9
1.2.2	Low Mass X-ray Binaries	12
1.3	The two groups of LMXB	14
1.3.1	Z-track sources	15
1.3.2	Atoll sources	19
1.3.3	What makes Z-track and Atoll sources different?	20
1.4	Phenomena observed in LMXB	22
1.4.1	X-ray bursts	22
1.4.2	Jets	26
1.4.3	Dipping	28
1.4.4	Quasi-periodic oscillations	31
1.5	Rossi X-ray Timing Explorer	35
1.5.1	The Proportional Counter Array	36
1.5.2	The High-Energy X-ray Timing Experiment	37
1.5.3	The All-Sky Monitor	39
2	Spectral models for LMXB	41
2.1	The complex spectra of LMXB	41
2.2	The Extended ADC model	43

2.2.1	The evidence for an extended nature of the ADC	44
2.2.2	Blackbody from the surface of the neutron star	47
3	Review of previous work	51
3.1	A model for the Z-track in the Cyg X-2 like LMXB	51
3.1.1	The analysis method	51
3.1.2	At the soft apex	52
3.1.3	The changes of mass accretion rate along the Z-track	53
3.1.4	The nature of flaring	54
3.1.5	The importance of radiation pressure	56
3.1.6	The ADC and line emission	60
3.1.7	A summary of the model	61
3.2	The Cyg X-2 like Z-track sources	63
3.2.1	GX 340+0 (4U 1642-45)	63
3.2.2	Cyg X-2 (4U 2142+38)	65
3.3	Sco X-1 like Z-track sources	68
3.3.1	Sco X-1 (H 1617-155)	68
3.3.2	GX 17+2 (4U 1813-14)	70
3.4	Atoll sources	72
3.4.1	2S 0918-549 (4U 0919-54)	72
3.4.2	4U 1636-536 (Norma X-1)	73
3.4.3	4U 1705-44	75
3.4.4	4U 1728-34 (GX 354-0)	77
3.4.5	4U 1735-44	78
3.4.6	SLX 1735-269	79
3.4.7	4U 1820-30 (Sgr X-4)	80
3.4.8	4U 1916-053	82
4	Spectral & timing studies of the Cyg-like Z-track sources	86
4.1	Cygnus X-2	87
4.1.1	Observations	87
4.1.2	Data analysis	87
4.1.3	Spectral fitting results	92

4.1.4	Timing results	98
4.2	GX 340+0	101
4.2.1	Observations	101
4.2.2	Data analysis	101
4.2.3	Spectral fitting results	104
4.2.4	Timing results	110
4.3	Discussion	113
4.3.1	A comparison with previous work	113
4.3.2	The neutron star blackbody and strong radiation pressure	114
4.3.3	The ADC luminosity and changes of mass accretion rate	118
4.3.4	The Flaring Branch	119
4.3.5	The temperature of the neutron star and the ADC	121
4.3.6	The behaviour of the kHz QPO	122
5	Spectral investigations of the Sco-like Z-track sources	127
5.1	GX 17+2	127
5.1.1	Observations	127
5.1.2	Analysis	127
5.1.3	Results	130
5.1.4	Discussion	135
5.2	Scorpius X-1	140
5.2.1	Observations	140
5.2.2	Analysis	141
5.2.3	Spectral fitting results	143
5.2.4	Discussion and comparison with previous work	148
5.3	Explaining the Sco-like sources	154
5.3.1	The high neutron star temperature	154
5.3.2	The Z-track sources seen by the <i>RXTE</i> /All-Sky Monitor	155
5.3.3	On the possible heating of the neutron star by flaring	158
5.3.4	How do the Sco-like sources differ from the Cyg-like sources ?	160
6	A survey of Atoll sources	163
6.1	Observations	163

6.2	Analysis	165
6.2.1	Lightcurves	166
6.2.2	Colour-colour & hardness-intensity variations	171
6.2.3	Results of spectral fitting	174
6.3	Discussion	182
6.3.1	Changes of mass accretion rate	182
6.3.2	Emission from the neutron star	183
6.3.3	The transition from the Banana to the Island state	189
7	Conclusions and future work	193
7.1	Conclusions of the present work	193
7.2	The directions of future studies	197
	References	200
	Appendices	215
A	A guide to <i>RXTE</i> data analysis	215
A.1	Data retrieving and organization	215
A.2	The analysis procedure	216
A.3	Data selections and spectra	220
A.4	Corrections	222
A.4.1	Deadtime	222
A.4.2	Pulse pile-up	222
A.4.3	Pointing offset	223
A.5	Power spectra and timing analysis	223
A.5.1	Signal decomposition	223
A.5.2	Preparation of PCA data	224
A.5.3	Producing power spectra	224
A.5.4	Conversion into an <i>Xspec</i> -usable format	225

- B.1 *A model for the Z-track phenomenon, jet formation and the kilohertz QPO based on Rossi-XTE observations of the Z-track sources*
- B.2 *On the nature of the Cygnus X-2 like Z-track sources*
- B.3 *The nature of the Cygnus X-2 like Low Mass X-ray Binaries*
- B.4 *On the nature of the Z-track in GX 17+2*
- B.5 *Dipping in Cygnus X-2 in a multi-wavelength campaign due to absorption of extended ADC emission*
- B.6 *Resolving the nature of the dipping/flaring branch in Cygnus X-2*
- B.7 *On the nature of the Sco X-1 like super-Eddington sources*
- B.8 *Dipping versus Flaring in Z-track sources: resolving the controversy*
- B.9 *Spectral investigations of the nature of the Sco X-1 like sources*

Chapter 1

Introduction

1.1 The X-ray sky and the power of accretion

The majority of the 339 X-ray sources listed in the famous 4th catalogue from the *Uhuru* satellite (Forman et al. 1978) are X-ray binaries (XRB). This includes the first known extrasolar X-ray source, Scorpius X-1, the discovery of which (Giacconi et al. 1962) was of fundamental importance for the development of young X-ray astronomy at that time. The sky distribution of XRB is not random (Fig. 1.1) showing that they reside mostly in the plane and the central bulge of the Milky Way. XRB have since then been found to be common in other galaxies (e.g. Fabbiano 1989) and, thanks to the high imaging capabilities of modern X-ray observatories, could be resolved as individual sources and studied. We know of about 300 X-ray binaries in the Milky Way (Liu et al. 2006, 2007) and others in nearby galaxies, such as the Magellanic Clouds (Liu et al. 2005). They shine at luminosities covering several orders of magnitude from about 10^{30} erg s $^{-1}$ to $\sim 10^{38}$ erg s $^{-1}$.

It was soon recognized (e.g. Shklovsky 1967) that the high luminosities and variability of XRB could be explained by accretion onto a neutron star. The existence of neutron stars was proposed already in the 1930s by Baade & Zwicky (1934) who investigated the possible origin of cosmic rays in supernovae. The discovery of a rotating neutron star in a radio pulsar was finally made by radio astronomers Bell and Hewish in 1967 (Hewish et al. 1968). Almost all of XRB are known today to harbour neutron stars which has been found based on several observables, such as the presence of nuclear explosions on their surfaces (Sect. 1.4.1) or simply similarities to other neutron star systems. Thus, in the present work, XRB will be taken to mean neutron star binaries. However,

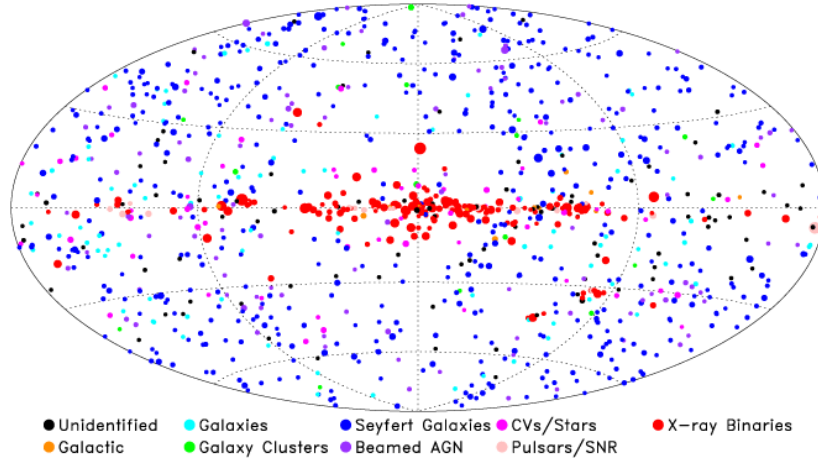


Figure 1.1: An X-ray sky map from the Swift/BAT 58-month survey in the 14 - 195 keV energy range (Baumgartner et al. 2010). Sizes of circles are proportional to fluxes and their colours represent different types of objects. The majority of sources are uniformly scattered active galactic nuclei (blue). Galactic objects are dominated by X-ray binaries (red).

it is worth noticing that (as of 2003) 18 (McClintock 2006) of X-ray binaries are known to contain black holes, forming a sub-class called Black Hole Binaries. An example of such a system is the well-known source Cygnus X-1, which, based on e.g. the lower mass limit given by the mass function and the spectral type of the mass donor HDE 226868, most certainly hosts a $> 7M_{\odot}$ black hole (Gies & Bolton 1986). A similar conclusion was drawn already by Paczynski (1974) who, assuming that the donor does not fill its Roche lobe and having taken into account lack of X-ray eclipses, obtained a lower mass limit of Cyg X-1 as a function of the distance only. This, for the assumed distance of 2.5 kpc, gave the mass of the compact object of at least $9.5 M_{\odot}$, much above the upper mass limit of about $3 M_{\odot}$ for a neutron star (e.g. Rhoades & Ruffini 1974; Shapiro & Teukolsky 1983).

In a process of radial accretion onto a star of mass M_* and radius R_* (e.g. Frank et al. 1992), a portion of matter gains free-fall kinetic energy in expense of its gravitational potential energy. At the surface of the star, the energy can be dissipated as is given by

$$L_{acc} = \frac{1}{2} \dot{M} v^2 = \frac{GM_* \dot{M}}{R_*}, \quad (1.1)$$

where v is the free-fall velocity at the surface, $G \approx 6.674 \times 10^{-8} \text{ cm}^3 \text{ g}^{-1} \text{ s}^{-2}$ is the gravitational constant and \dot{M} is mass accretion rate.

The efficiency η of the process can be estimated by comparing Eqn. 1.1 with $\eta \dot{M} c^2$, where c is the speed of light, which gives

$$\eta = \frac{1}{2} \left(\frac{v}{c} \right)^2 = \frac{G M_*}{c^2 R_*}. \quad (1.2)$$

This shows that the accretion efficiency is proportional to the compactness M_*/R_* of the central body. By substituting canonical neutron star parameters, $M_* = 1.4 M_\odot$ and $R_* = 10$ km, one finds that $\eta \sim 0.2$ which makes accretion a very efficient process when compared with thermonuclear fusion of hydrogen into helium in stars, for which $\eta \sim 0.007$.

In the case of a black hole, free-fall accretion is inefficient due to the fact that there is no solid surface at which energy could be dissipated and the kinetic energy is lost below the event horizon. However, if matter spirals-in onto a black hole via disk accretion and dissipates energy on the way (Sect. 1.1.2), the efficiency of the process can be much higher. The maximal energy release depends then on the binding energy of the innermost stable orbit leading to the efficiency of up to ~ 0.423 for a black hole maximally co-rotating with the disk (Shapiro & Teukolsky 1983).

Accretion luminosities are often quoted as fractions of the Eddington luminosity L_{Edd} , being the value at which radiation pressure is strong enough to balance the gravitational force on accreted matter. Its value can be easily derived for the case of spherical accretion of ionized hydrogen onto a neutron star. In such a case radiation exerts a force on electron-proton pairs by Thomson scattering, the cross section of which is $\sigma_T \approx 6.65 \times 10^{-25}$ cm². A balance between this force and gravitational attraction at a given distance r from the centre is given by

$$\frac{G M (m_p + m_e)}{r^2} = \frac{L_{Edd} \sigma_T}{4 \pi r^2 c}, \quad (1.3)$$

where m_p and m_e are the masses of a proton and an electron, respectively. Taking into account that $m_e \ll m_p$ and reorganizing Eqn. 1.3 gives the Eddington luminosity

$$L_{Edd} = \frac{4 \pi G M m_p c}{\sigma_T} \approx 1.3 \times 10^{38} \left(\frac{M}{M_\odot} \right) \text{ erg s}^{-1}. \quad (1.4)$$

If one assumes an equilibrium in which a neutron star radiates away all of its accretion energy as a blackbody, then the source effective temperature $T_{\text{eff}} = \sqrt[4]{L_{\text{acc}}/4 \pi R_*^2 \sigma}$, where $\sigma \approx 5.67 \times 10^{-5}$ erg cm⁻² s⁻¹ K⁻⁴ is the Stefan-Boltzmann constant, is only very weakly sensitive to L_{acc} . Thus, for a luminosity of e.g. 10^{38} erg s⁻¹ the characteristic temperature is $\sim 10^7$ K corresponding to peak energy at about 1 keV, well within the energy range (0.1 - 100 keV) typical to X-rays. This rough estimate shows why accretion-powered neutron stars are natural X-ray emitters.

Based on how much angular momentum is carried by gravitationally captured matter, two main types of accretion take place in binary systems and these are strictly related to the spectral type and mass of the companion. Thus, XRB are naturally divided (Bradt & McClintock 1983) into two main fundamental classes: High Mass X-ray Binaries (HMXB) and Low Mass X-ray Binaries (LMXB). Young ($10^6 - 10^7$ years) and massive ($M > 10M_\odot$) stars provide strong winds which carry little angular momentum and are accreted approximately radially in a HMXB. On the other hand, low mass ($M < 1.5M_\odot$) stars, which do not give strong winds, may give rise to disk accretion at their later evolutionary stages through a Roche-lobe overflow (RLO) forming a LMXB. These two accretion scenarios are discussed next, followed by discussion of HMXB and LMXB.

1.1.1 Accretion from a wind

In a binary system with a massive supergiant companion, the compact object moves through and accretes from the companion's wind as schematically pictured in Fig. 1.2. The geometry of the flow of the captured matter depends on its angular momentum J which defines the circularization radius

$$R_{circ} = \frac{J^2}{GM_*}, \quad (1.5)$$

corresponding to the Keplerian orbit of minimal energy for the carried angular momentum. If the angular momentum of accreted matter is too low, the circularization radius will be smaller than

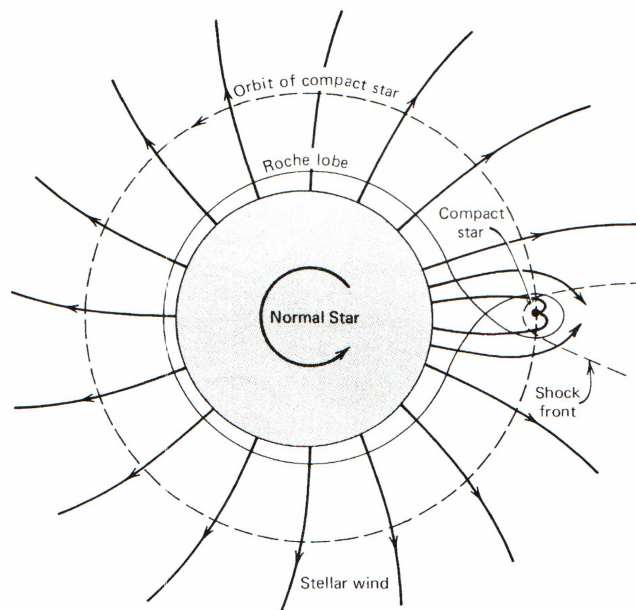


Figure 1.2: A schematic depiction of a wind-fed X-ray Binary (Shapiro & Teukolsky 1983).

the size of the accretor and matter will fall onto the compact object which is thought to be the case in the majority of wind-fed binaries (King 1995).

Basic theory applicative to such a scenario was developed by Hoyle & Lyttleton (1939); Bondi & Hoyle (1944); Bondi (1952) and a recent review comes from Edgar (2004). Following this theory, the compact object with an orbital velocity v_{orb} can capture the wind (moving with the velocity v_{wind}) within the radius

$$r_{acc} = \frac{2GM_*}{v_{rel}^2}, \quad (1.6)$$

where $v_{rel}^2 = v_{orb}^2 + v_{wind}^2$ and v_{rel} is the relative speed of the compact object with respect to the wind. In the case of a supergiant type O or B companion, the wind leaves the star in all directions with a high velocity of typically $v_{wind} \sim 10^3 \text{ km s}^{-1}$ (Morton 1967a,b). This gives $r_{acc} \sim 10^{10} \text{ cm}$ which is relatively small when compared to a typical binary separation of 10^{12} cm (Bradt & McClintock 1983). Thus, the process is inefficient and only a small ($\leq 10^{-3}$) fraction of wind can be accreted, but with a typical mass loss of $\lesssim 10^{-4} M_{\odot} \text{ year}^{-1}$ from the companion, this can still lead to sub-Eddington accretion luminosities (King 1995).

1.1.2 Accretion via Roche-lobe overflow

A very different type of accretion takes place when a compact object is accompanied by a star which fills its Roche volume. Mass transfer onto the compact star starts via the first Lagrangian point (L1) separating the Roche lobes of the two stars. Matter flows towards the compact object and has high enough angular momentum to meet the condition given by Eqn. 1.5 and form a ring. Minimum energy corresponds to circular orbits and can be further reduced by two mechanisms: a mass transfer inwards and an angular momentum transfer outwards (Lynden-Bell & Pringle 1974) which happen due to viscous torques in the ring. The result of this is that matter spirals in towards the compact object stretching the ring and forming an accretion disk as depicted in Fig. 1.3.

In the so-called standard disk theory (e.g. Pringle 1981; Frank et al. 1992), the disk is assumed to be steady (matter lost at the inner edge is balanced by that added at the outer edge), geometrically thin ($H \ll r$) and optically thick. Potential energy is converted into kinetic energy of the orbital motion and into heat through viscosity which acts between adjacent, differentially rotating disk rings. Viscous heat is radiated away through faces of the disk at a rate per unit area

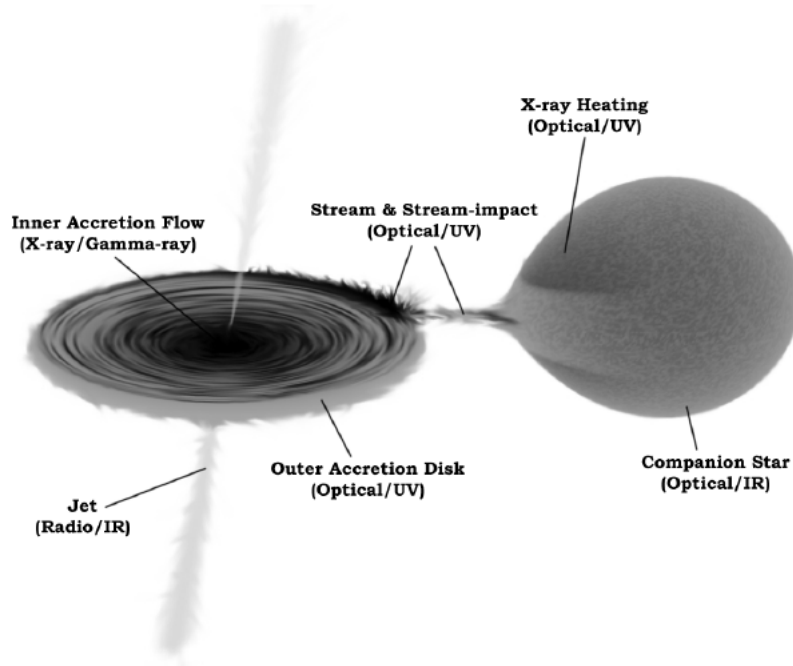


Figure 1.3: A schematic view of an XRB in which disk accretion takes place through a Roche-lobe overflow (the brightness scale is inverted) (Hynes 2010).

$$D(r) = \frac{3 G M_* \dot{M}}{4 \pi r^3} \left[1 - \sqrt{\frac{R_*}{r}} \right], \quad (1.7)$$

where R_* is the radius of the neutron star (lower limit for the disk inner radius); and it can be seen that $D(r)$ is independent of viscosity. The total disk luminosity can be calculated by integrating the radiation flux given by Eqn. 1.7 over all disk radii which gives

$$L_{disk} = \frac{G M_* \dot{M}}{2 R_*}, \quad (1.8)$$

a simple result, which is half of the initial potential energy given by Eqn. 1.1. The second half of energy is not radiated away, but kept in the disk as the kinetic energy of the orbital motion and may be transferred to the neutron star.

An optically thick disk radiates locally as a blackbody whose flux is

$$S(r) = \sigma T^4, \quad (1.9)$$

where σ is the Stefan-Boltzmann constant. Assuming $S(r) = D(r)$, replacing $D(r)$ by the right-hand side of Eqn. 1.7 and reorganizing gives a radius-dependent temperature profile

$$T(r) = \sqrt[4]{\frac{3 G M_* \dot{M}}{8 \pi R_*^3 \sigma} \left[1 - \sqrt{\frac{R_*}{r}} \right]}, \quad (1.10)$$

which for $r \gg R_*$ leads to a characteristic temperature - radius relation

$$T(r) \propto (r/R_*)^{-3/4}. \quad (1.11)$$

For an observer at a distance d , a ring between r and $r + dr$ subtends a solid angle $2 \pi r dr \cos i / d^2$, where i stands for system inclination. The total emission spectrum F_ν of the disk is an integral of many local blackbody spectra over all rings between the inner R_* and the outer R_{out} disk edge

$$F_\nu = \frac{2 \pi \cos i}{d^2} \int_{R_*}^{R_{out}} B_\nu r dr, \quad (1.12)$$

where B_ν is blackbody intensity at frequency ν

$$B_\nu[T(r)] = \frac{2 h \nu^3}{c^2} \frac{1}{\exp[h\nu/kT(r)] - 1} \text{erg}^{-1} \text{cm}^{-2} \text{Hz}^{-1} \text{sr}^{-1}, \quad (1.13)$$

in which $h \approx 6.626 \times 10^{-27}$ erg s is Planck's constant. This yields a characteristic shape of the multicolour disk spectrum of the form

$$F_\nu \propto \nu^{1/3}. \quad (1.14)$$

The disk spectrum decreases at low energies, showing the Rayleigh-Jeans tail of the coolest disk elements, and has an exponential cut-off at higher energies corresponding to the innermost hot region of the disk. The disk spectrum given by Eqn. 1.12 and 1.14 may in practice be modified by several effects, such as irradiation by X-rays from the central body or Comptonization in a hot electron corona (e.g. Frank et al. 1992).

Shakura & Sunyaev (1973) assumed that effective viscosity should be proportional to the size and rotation velocity of the largest eddies in a turbulent disk which can be written

$$\nu = \alpha c_s H, \quad (1.15)$$

where c_s is the sound speed, H is the vertical height of the disk, and α parametrizes the unknown physics of the process and is most likely of order 0.1 (Smak 1982, 1984). Nowadays, the most appealing view of the nature of viscosity is based on the magneto-rotational instability proposed

by Balbus & Hawley (1991). Their mechanism requires existence of a magnetic field and a radius-dependent orbital velocity and is thus relevant to LMXB.

At high (sub-Eddington) accretion rates, the vertical structure of the disk close to the compact object may be modified by the radiation pressure (scaling as T^4) of the disk itself which becomes comparable to or even dominates over gas pressure thickening the disk. In such a case, the thin disk approximation breaks down and the radiatively-supported half-height profile of the inner disk is given by (Frank et al. 1992)

$$H = \frac{3 \sigma_T \dot{M}}{8 \pi m_p c} \left[1 - \left(\frac{R_*}{r} \right)^{1/2} \right] = H_{eq} \left[1 - \left(\frac{R_*}{r} \right)^{1/2} \right], \quad (1.16)$$

where H_{eq} is the equilibrium height achieved asymptotically and the radial function is fast (also Sect. 2.2.2). Although it was suggested that such a disk should be unstable (Lightman & Eardley 1974; Shakura & Sunyaev 1976), the observational evidence for instabilities is very limited (Done et al. 2007; Janiuk & Misra 2012). Apart from this, it has been suggested that the disk becomes stable if e.g. the viscous stress is proportional to gas pressure alone (Meyer & Meyer-Hofmeister 1982; Stella & Rosner 1984).

The angular velocity of the motion in the disk is radius-dependent and Keplerian

$$\Omega(r) = \sqrt{\frac{GM_*}{r^3}}. \quad (1.17)$$

Thus, the closer to the central object, the higher the velocity in the disk. For a non-magnetized neutron star the disk extends down to the surface of the star and in the standard view, there is a boundary layer between the inner disk and the neutron star surface, where the angular velocity drops from the Keplerian value down to that of the star Ω_* (Pringle 1981). Alternatively (Inogamov & Sunyaev 1999), the boundary layer where the adjustment takes place is not in the inner disk, but on the stellar surface. In this scenario, matter reaches the star at the equator and then spreads vertically forming an X-ray emitting belt due to viscous interaction of the accreted matter with the underlying material. Regardless of the exact scenario, in the boundary layer the remaining energy is finally released. In the case of an accreting black hole, however, matter will fall below the event horizon and there is no boundary layer between the disk and the black hole.

1.2 X-ray Binaries

The two main classes of XRB - Low Mass and High Mass systems, corresponding to the two types of accretion types presented above, are now discussed in more detail. Their properties are summarized and compared in Table 1.1.

Table 1.1: The characteristics of the two main classes of X-ray Binaries: Low Mass and High Mass systems.

Property	Low Mass XRB	High Mass XRB
Donor star	low mass ($M < 1.5M_{\odot}$), population II or I	massive ($M \gtrsim 10M_{\odot}$), population I
Distribution in galaxies	bulge and globular clusters	galactic plane
Accretion process	Roche-lobe overflow (RLO)	Stellar wind (and/or RLO)
L_X/L_V	$> 20 - 100$	< 1
Main source of optical emission	X-ray heated disk and companion	companion
Orbital period	11 minutes - 10 days	1 - 100 days
Magnetic field (neutron star)	$10^8 - 10^{10}$ G	$> 10^{11}$ G
Phenomena involved	dips, eclipses, bursts, flares, QPO, jets, pulsations	pulsations, eclipses, jets

1.2.1 High Mass X-ray Binaries

The primary (mass donor) in a HMXB is either a dwarf, giant or a supergiant of a spectral type O, B (or Be) (Rappaport & van den Heuvel 1982). The donor dominates in the visual light and the X-ray to optical luminosity ratio in these systems is comparable to or less than unity (e.g. Bradt & McClintock 1983). It is usually a strong wind from the atmosphere of the primary (although Roche-lobe overflow may also take place) which fuels the accretion process onto the compact object which is most commonly a neutron star. Indeed, as of 2006, only three HMXB (Cyg X-1 in the Milky Way and also LMC X-1 and LMC X-3 in the Large Magellanic Cloud) are known to harbour black holes (Liu et al. 2006). With a total number of 114 known systems in the Milky Way (Liu et al. 2006), HMXB comprise 38% of all X-ray binaries. They are distributed in the Galactic plane and, as they are linked to young stars, situated close to their birthplaces. In fact, Grimm et al. (2003) proposed that the number of HMXB (or their collective luminosity) can be used as a measure of the star formation rate of a galaxy.

Formation scenarios leading to a HMXB (Rappaport & van den Heuvel 1982; Verbunt 1995; Tauris 2006) start with a binary system of a $\sim 8M_{\odot}$ and $\gtrsim 15M_{\odot}$ stars in a ~ 100 day orbit. In such scenarios, the more massive star evolves faster and after $\sim 10^7$ years fills its Roche lobe transferring

mass onto the second star. Rappaport & van den Heuvel (1982) argued that this stage takes place before a type II supernova explosion of the donor leading to the formation of a neutron star. During the supernova explosion, only less than half of the mass of the system can be lost so that the binary could survive (Blaauw 1961). The neutron star in a newly formed HMXB captures stellar wind from its companion or, as the companion evolves and fills its Roche lobe, accretes via an accretion disk (King 1995). Young neutron stars in HMXB possess strong magnetic fields of $\sim 10^{12}$ G (e.g. Trümper et al. 1978) and accretion takes place along magnetic field lines onto the neutron star polar caps giving rise to X-ray pulsations and revealing the spin of the neutron stars (Davidson & Ostriker 1973). Finally, when the second star also explodes as a supernova, the binary system will be left with two compact objects.

HMXB are divided (Maraschi et al. 1976; Rappaport & van den Heuvel 1982) into two main groups - HMXB with a Be companion star, Be HMXB, and HMXB with a supergiant companion, supergiant HMXB. In a **Be HMXB**, the companion has slow ($v \sim 150 - 300 \text{ km s}^{-1}$) equatorial wind (Waters et al. 1988) forming a circumstellar disk which can be observed in the infrared and $\text{H}\alpha$ emission line, hence the letter “e” added to the B spectral type of the donor (e.g. Coe 2000). The neutron star on an eccentric orbit crosses through the circumstellar disk of its companion at the periastron which leads to major accretion events called type I outbursts (Maraschi et al. 1976; Rappaport & van den Heuvel 1982). Lack of eclipses or ellipsoidal optical variations and long ($\lesssim 100$ days) orbital periods show that the companion star does not fill its Roche-lobe (e.g. Waters et al. 1988).

In a **supergiant HMXB**, in contrast to a Be HMXB, the mass of the companion star is typically in excess of $20M_{\odot}$ (Rappaport & van den Heuvel 1982) and its lifetime at the HMXB stage is expected to be limited to less than 10^5 years (Savonije 1979). Such a companion, of a spectral type O or B, loses mass in the form of a $\sim 1000 \text{ km s}^{-1}$ radially escaping wind (Morton 1967a,b). The wind is accreted by the neutron star in orbit (Davidson & Ostriker 1973) giving luminosities of $10^{35} - 10^{36} \text{ erg s}^{-1}$. X-rays emitted in the process reach out through the wind resulting in observed increased intrinsic absorption (e.g. Walter et al. 2006). When the companion star in a HMXB is more evolved, Roche-lobe overflow leads to the formation of an accretion disk giving higher mass transfers and luminosities of $> 10^{37} \text{ erg s}^{-1}$ (e.g. Bonnet-Bidaud & van der Klis 1979). In such cases the optical lightcurve of a HMXB often reveals the distorted shape of the Roche lobe-filling companion (e.g. Tjemkes et al. 1986).

Corbet (1984) discovered a relation between the orbital period P_{orb} and the spin period P_{spin} of HMXB which is known as the Corbet diagram (Fig. 1.4). In the diagram, a natural division of HMXB into groups described above is clearly visible. Be HMXB, with accretion from the companion's dense equatorial wind show a positive correlation between P_{spin} and P_{orb} , wind-fed supergiant HMXB show no clear correlation, whereas disk-fed supergiant HMXB show the two periods to be anti-correlated (Corbet 1986). Corbet (1984, 1986) attributed the relations observed to the different efficiencies of angular momentum transport in particular accretion types characteristic to the three groups, but a detailed quantitative understanding has not yet been achieved (Waters & van Kerkwijk 1989).

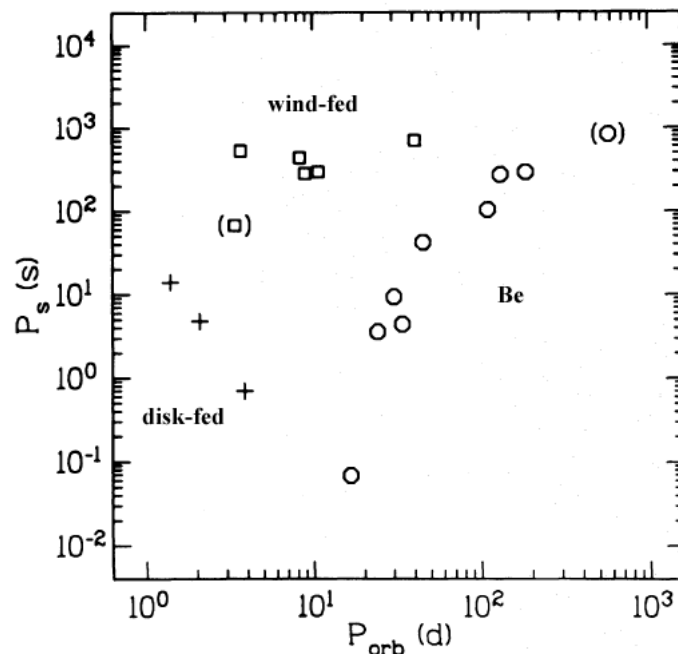


Figure 1.4: The Corbet diagram (Corbet 1984) showing the spin period versus the orbital period of HMXB. Squares: wind-fed supergiant HMXB, plus signs - disk-fed supergiant HMXB, circles - Be HMXB, brackets indicate uncertain position (Waters & van Kerkwijk 1989).

The majority of Galactic HMXB are Be systems with 52 (as of 2006) examples known (identifications of 13 of them are still to be confirmed), all harbouring neutron stars (Liu et al. 2006). There are also (Liu et al. 2006) 29 Galactic supergiant HMXB (including 11 uncertain identifications), of which all, but one (Cyg X-1), contain accreting neutron stars. It is also noticeable that 128 HMXB have been identified in the Magellanic Clouds, with 92 and 36 systems (including candidates) in the Small and the Large Magellanic Cloud, respectively (Liu et al. 2005). It is believed (e.g. Yokogawa et al. 2003) that a recent history of interactions between the Milky Way and the

Magellanic Clouds led to formation of intergalactic bridges and an increased rate of star birth and HMXB formation.

1.2.2 Low Mass X-ray Binaries

In a low mass X-ray binary a neutron star accretes matter from its low mass ($M \leq 1.5M_{\odot}$) companion star. Mass transfer occurs via Roche-lobe overflow giving rise to disk accretion as discussed in Sect. 1.1.2. The catalogue of Liu et al. (2007) lists 187 LMXB in the Galaxy, 92% of which are neutron star systems. According to McClintock & Remillard (2003), only 15 LMXB in the Milky Way (thus 8% of the population) are confirmed black hole systems which are all transient such as the progenitor of this group, A 0620-00 (McClintock & Remillard 1986), discovered during an outburst by Elvis et al. (1975).

The magnetic field of a neutron star is expected to decay on a timescale of 10^7 years which is deduced from studies of radio pulsars (Lyne et al. 1985; Kulkarni & Narayan 1988). Thus, given the age of a typical LMXB of $\sim 10^9$ years, the magnetic field of a neutron star will be weak ($\sim 10^8$ G) and the majority of LMXB do not show any pulsar-like behaviour and their accretion disks may reach close to the compact object. However, a few known pulsars, such as Her X-1 and GX 1+4 are classified as LMXB (e.g. Mereghetti & Stella 1995; Bildsten et al. 1997). Also, there is a number of relatively recently discovered accreting millisecond LMXB pulsars, such as SAX J 1808.4-3658 (Wijnands & van der Klis 1998a; di Salvo et al. 2008), which are thought to be an evolutionary link between LMXB and millisecond radio pulsars.

Formation and evolution

A possible formation process of a LMXB (Tauris 2006) begins with a binary system consisting of a massive ($M \sim 15M_{\odot}$) star and a solar-mass companion having an orbital period of about 10^3 days. The model predicts that after millions of years of evolution, the massive star begins its supergiant phase and the low mass companion is forced to move through the envelope of the massive star. The resultant frictional drag causes two effects (Paczynski 1976). First, the low-mass companion spirals in and the orbit of the system shrinks. Second, the envelope of the massive star is expelled exposing its helium core. Thus, at this stage the binary system contains a helium star and a low-mass companion in a tight orbit having a period of about 1 day. In the scenario of Tauris (2006), a helium star, still having about 5 solar masses, explodes as a supernova forming a neutron star. After several billion years, due to loss of angular momentum via gravitational

waves or because of the evolutionary expansion of the donor, the low-mass companion fills its Roche lobe which leads to a mass transfer onto the compact object giving a LMXB. It is worth noticing here that the scenario of Tauris (2006) predicts that even later the companion will end up as a white dwarf, accretion will stop and an old neutron star will become a millisecond radio pulsar recycled by a long history of accretion-driven gain of angular momentum (Backer et al. 1982; Radhakrishnan & Srinivasan 1982).

Globular clusters have been found to favour LMXB formation (Katz 1975). Indeed, globular clusters contain only about 10^{-4} of the mass of the Galaxy (Arp 1965), and yet the number of known LMXB in globular clusters is 13 (Liu et al. 2007), thus $\sim 7\%$ of all LMXB. According to the model of Clark (1975), LMXB in dense clusters can be formed by gravitational capture of a single star by a neutron star. Another possibility (Verbunt & Hut 1987) is that an existing binary system of two cluster stars may encounter a neutron star which expels the least massive star and forms a new system with the remaining star.

Variability over the orbital period

The unified model explaining that different types of variability of LMXB over the orbital period can all be explained as related to the same type of object viewed at different inclination angles was proposed by Frank et al. (1987) and is shown graphically in Fig. 1.5. In this model the sources which do not show strong orbital-phase modulation are observed at inclinations smaller than about 60° . On the other hand, sources with higher inclinations do show orbital-related phenomena.

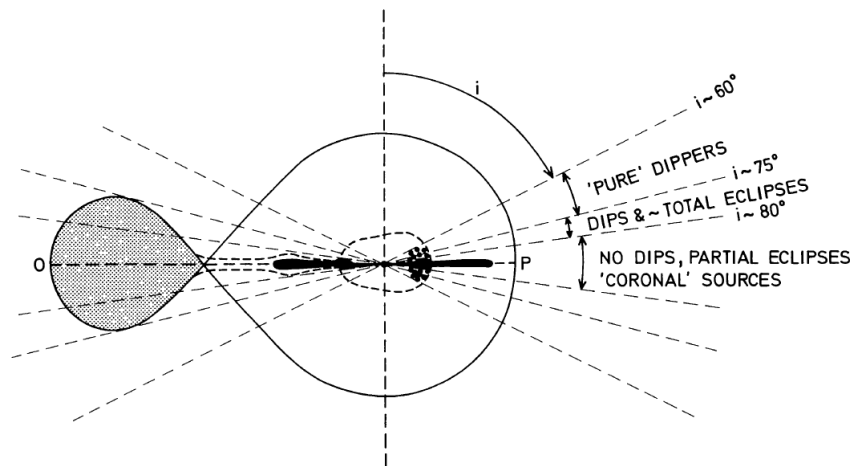


Figure 1.5: The model to explain different types of orbital-related modulation in lightcurves of LMXB in terms of their inclinations (Frank et al. 1987).

For an inclination range of $60 - 75^\circ$ we observe dipping - recurrent intensity reductions interpreted as obscuration of X-rays by a thickened structure in the disk crossing our line of sight. A more detailed treatment of this phenomenon is given in Sect. 1.4.3. Sources with even higher inclination ($75 - 80^\circ$) show not only dipping but also total eclipses - regular reductions of intensity to nearly zero caused by the companion. There are also sources (e.g 4U 1822-37, 2S 0921-63) known as the Accretion Disk Corona (ADC) sources. In the model of Frank et al. (1987) these are observed nearly edge-on and thus we no longer see the neutron star, but only partial eclipses and a smooth modulation of a small fraction of their flux due to X-rays scattered from the accretion disk corona, this explaining also their lower than usually $L_X/L_V \sim 20$.

1.3 The two groups of LMXB

Progress in understanding LMXB came with increased usage of hardness-intensity (HID) and colour-colour (CCD) diagrams which clearly displayed strong physical changes in the sources. To produce these, the total count rate of a source is subject to energy filtering in which typically count rates in three energy bands, such as low, medium and high, are extracted. In a colour-colour diagram (showing hard colour versus soft colour), hard colour is defined as the ratio of high and medium count rates, whereas soft colour is the ratio of medium to low count rates. In a hardness-intensity diagram, hardness is hard colour and intensity stands for the total count rate. It should be noted that although both types of diagrams are commonly used, hardness-intensity diagrams have an advantage over colour-colour diagrams as they show directly intensity increases or reductions which may be ambiguous when seen in colour-colour only.

Hasinger & van der Klis (1989) carried out a survey of a sample of LMXB and recognized two characteristic patterns traced by the sources in such diagrams. Thus, they classified LMXB in two groups: Z-track sources and Atoll sources. The names reflect the shapes of the patterns that are traced in time by sources belonging to a given group as shown in Fig. 1.6.

Only about 6 of the known LMXB fall into the category of Z-track sources, whereas the vast majority (~ 150) are Atoll sources or “probable Atoll sources”. A fundamental difference between the two main groups of LMXB lies in their average luminosities. Z-track sources emit persistently at close to the Eddington luminosity and vary in brightness by a factor of about 2. In contrast to this, Atoll sources are much weaker, emitting at only 0.01 - 0.5 of the Eddington luminosity, but may be variable by a larger factor of 3 - 5.

The classification of LMXB into Z-track sources and Atoll sources of Hasinger & van der Klis

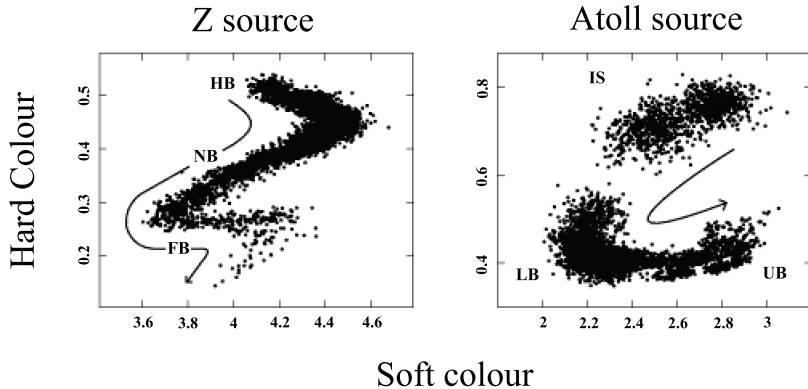


Figure 1.6: Colour-colour variations typical to Z-track (left) and Atoll (right) LMXB. Particular spectral states are visible: the Horizontal (HB), the Normal (NB) and the Flaring Branch (FB) in Z-track sources, and also the Island (IS), the Lower Banana (LB) and the Upper Banana (UB) Branches in Atoll sources. Arrows indicate the often assumed direction in which \dot{M} increases (Wijnands & van der Klis 1999).

(1989) also takes into account the time variability of these two groups. Lightcurves of LMXB can be analysed and used to produce power spectra that reveal any typical timescales or periodicities and a detailed discussion of such methods is given in Appendix A.5. Early timing studies of van der Klis et al. (1985) using data from *EXOSAT* revealed that the power spectra of LMXB show two characteristic types of variability features. Among them, quasi-periodic oscillations (QPO) were found as peaks of power with Lorentzian-like shapes, whereas other features corresponded to noise components with power law-like shapes (e.g. van der Klis 2004). The timing features showed that some as yet unknown physical processes modulated the X-ray flux and thus studies of QPO/noise phenomena could be used to constrain physical models of LMXB. It is out of place here to discuss details regarding physical models proposed to explain spectra of LMXB or the nature of quasi-periodic oscillations in general and hence these discussions are postponed until Sect. 2.1 and 1.4.4, respectively. Here, only the observed behaviour in HID/CCD and associated time variability of Z-track and Atoll sources, as the basis of the classification of Hasinger & van der Klis (1989), is presented.

1.3.1 Z-track sources

Behaviour in hardness-intensity and colour-colour diagrams

Z-track sources show three main, clearly distinguishable spectral states that form a pattern resembling the letter Z in colour-colour or hardness-intensity (Fig. 1.6, left). Particular parts of the Z are called the Horizontal Branch (HB), the Normal Branch (NB) and the Flaring Branch

(FB). The transition points between the Flaring Branch and the Normal Branch, and between the Normal and the Horizontal Branch are called the soft apex and the hard apex, respectively.

A scenario in which a single parameter, such as \dot{M} , was responsible for a movement along the Z was proposed by Friedhorsky et al. (1986). This was additionally motivated by the fact that no jumps between branches have been observed. Relevant to the problem was a multiwavelength campaign on one of the Z-track sources, Cygnus X-2, carried out in radio (Hjellming et al. 1990a), optical (van Paradijs et al. 1990a), UV (Vrtilek et al. 1990) and X-rays (Hasinger et al. 1990). Vrtilek et al. (1990) argued that UV emission resulting from X-ray heating of the disk is a better tracer of \dot{M} than X-rays (that in their opinion come from a small central region and may be affected by geometric effects) or optical emission (contributed also by the companion). In their results obtained with the *International Ultraviolet Explorer*, the strength of the UV continuum and emission lines were increasing in the direction from the Horizontal Branch towards the Flaring Branch, which they interpreted as being due to \dot{M} increasing in this direction. This led to the standard view in which \dot{M} increases monotonically along the Z in the direction HB→NB→FB, as indicated by an arrow in Fig. 1.6, despite the apparent decrease of X-ray intensity along the Normal Branch. The standard view has not, however, been commonly accepted and Church et al. (2006) found evidence (Sect. 3.1.3) that mass accretion rate actually increases on the Normal Branch in the direction opposite to that in the standard view, and the problem will be addressed later in the present work.

The sub-groups of Z-track sources

Z-track sources have been found (Kuulkers et al. 1994) to form two distinct sub-groups. As shown in Fig. 1.7 (left panel), the sources Cygnus X-2, GX 5-1 and GX 340+0 show a regularly-shaped Z, in which the Horizontal Branch is almost horizontal and long, and the Flaring Branch is not prominent. Sources showing such patterns have been called Cyg-like Z-track sources (i.e. the Z-track sources similar to the archetype of the sub-group - Cygnus X-2). On the other hand, the sources Scorpius X-1, GX 349+2 and GX 17+2 have a short (or even absent) Horizontal Branch, whereas the Flaring Branch is impressively long and almost parallel to the Normal Branch (Fig. 1.7, right). This sub-group was named the Sco-like sources (i.e. sources similar to Scorpius X-1).

Differences between the two sub-groups of the Z-track sources were attributed to several parameters, such as the strength of the magnetic field (Psaltis et al. 1995) or inclination (Kuulkers et al. 1994, 1995). The model of Psaltis et al. (1995) assumed an interaction of the inner accretion flow

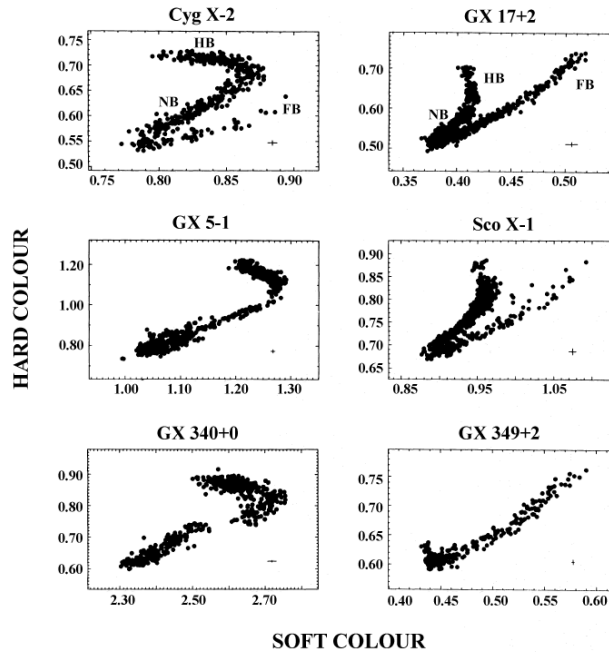


Figure 1.7: Colour-colour patterns characteristic to the two sub-groups of Z-track sources: Cygnus X-2 like (left) and Scorpius X-1 like (right) (Hasinger & van der Klis 1989).

with the magnetosphere of the neutron star. Their spectral fitting results could reproduce the Sco-like behaviour if the magnetic field of these sources was taken to be weaker than in Cyg-like sources.

Kuulkers et al. (1994, 1995) discussed different shapes of the Flaring Branch in Cyg-like and Sco-like sources and argued that this depends on the inclination of a source. Their scenario assumed that mass accretion rate increases along the Z-track according to the standard view (Vrtilek et al. 1990) being maximal ($L_X \gtrsim L_{Edd}$) on the Flaring Branch. Kuulkers et al. (1994) noticed that at such high luminosities, the inner radiatively-supported disk should be puffed up and come into the line of sight if the inclination of a source was high enough. Thus, occasional intensity reductions seen at the end of the FB in the Cyg-like sources (Hasinger et al. 1990; Penninx et al. 1991; Asai et al. 1994) suggested higher inclinations of these systems, in contrast to Sco-like sources whose flaring branches always correspond to increases in X-ray intensity indicating lower inclinations (Kuulkers et al. 1994). The known inclinations of 62° of Cyg X-2 (Cowley et al. 1979) and $15 - 40^\circ$ of Sco X-1 (Crampton et al. 1976) provided partial support to the idea.

The above possibilities, however, have been found very unlikely (Homan et al. 2010), given the recent observation of the transient source XTE J1701-462 (Remillard et al. 2006). The source apparently exhibited a change from the Cyg-like behaviour (at $L_X > L_{Edd}$) into the Sco-like

behaviour (at $L_X \sim L_{Edd}$) as its luminosity was decaying during an outburst. Based on this observation, Homan et al. (2007a); Lin et al. (2009); Homan et al. (2010) argued that the difference between the two sub-groups of Z-track sources, based on the case of XTE J1701-462, can be attributed to changes in mass accretion rate only. Whether the source indeed changed from being Cyg-like into Sco-like will be questioned later in this work (Sect. 5.3.4). The problem is more general being also relevant to differences between Z-track and Atoll sources, and will be discussed in Sect. 1.3.3.

Timing properties

Timing properties are similar to both sub-groups of Z-track sources and are often discussed with relation to the spectral branches. The left panel of Fig. 1.8 shows power spectra typical to each of the Z-track branches with a vertical shift introduced to allow their comparison (Hasinger & van der Klis 1989).

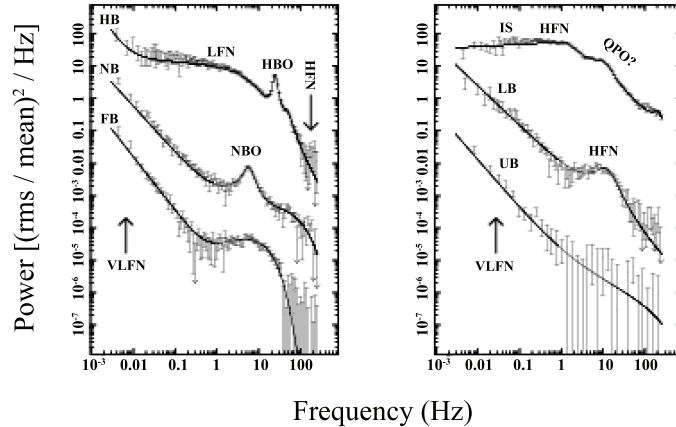


Figure 1.8: Power spectra corresponding to spectral states of Z-track sources (left) and Atoll sources (right) revealing their characteristic features: QPO and noise components. In this plot, normalizations of power spectra from different spectral branches were shifted vertically for visual purposes. (Wijnands & van der Klis 1999)

On the Horizontal Branch, a QPO with a frequency between about 15 and 60 Hz is observed and denoted as Horizontal Branch Oscillation (HBO in Fig. 1.8). It was first discovered by van der Klis et al. (1985) in GX 5-1 with the frequency correlated with X-ray intensity increasing along the branch from its left end towards the hard apex. It was also found (van der Klis et al. 1985) that the Horizontal Branch Oscillation was accompanied by Low Frequency Noise (LFN) in the range 0.1 - 30 Hz shaped as a power law with a cut-off at 5 - 10 Hz. With the advent of *RXTE*, twin quasi-periodic oscillations (kHz QPO) were discovered (van der Klis et al. 1996; Wijnands et al.

1997; Jonker et al. 1998). These have frequencies in the range 200 - 1100 Hz increasing with X-ray intensity along the Horizontal Branch. HB QPO, LFN and kHz QPO get weaker and disappear as the source approaches the hard apex and enters the upper Normal Branch (van der Klis 1989; Wijnands & van der Klis 1998b). A clear exception is Sco X-1 in which the kHz QPO have been observed all along the Normal Branch and even on the Flaring Branch (van der Klis et al. 1996). Another QPO, called a Normal Branch Oscillation (NBO in Fig. 1.8), appears in the middle of the Normal Branch with a frequency of about 6 Hz and was first detected by Middleditch & Priedhorsky (1985) in Sco X-1. It has been occasionally seen to exist simultaneously with the HB QPO (e.g. Hasinger et al. 1990; Lewin et al. 1992) when the source was on the upper Normal Branch meaning that the two QPO are different phenomena.

In Sco X-1, at the soft apex between the Normal Branch and the Flaring Branch, the ~ 6 Hz NB QPO was found to change into Flaring Branch Oscillation (FB QPO) whose frequency then rose from 10 to 20 Hz along the left part of this branch (Priedhorsky et al. 1986; van der Klis et al. 1996). The NB QPO and the FB QPO are thus thought to be the same phenomenon, especially as no other components (such as low frequency noise) are associated with either of them (van der Klis 1989).

Some timing properties are common to all spectral branches of Z-track sources and are described here after Hasinger & van der Klis (1989). Power spectra below ~ 0.1 Hz are dominated by the noise component called Very Low Frequency Noise (VLFN) having a power law spectrum with a steep index of 1.5 - 2.0. VLFN gets stronger and steepens as a Z-track source moves from the HB towards the FB. Also observed is High Frequency Noise (HFN), typically > 10 Hz, whose name comes from it being clearly separated from the LFN on the Horizontal Branch. Similar to LFN, it usually has a flat power law shape, but with a higher frequency cut-off above ~ 30 Hz (Hasinger & van der Klis 1989; van der Klis 1995).

The spectral and timing characteristics of particular Z branches differ significantly from those observed in Atoll sources which are now described in the following section.

1.3.2 Atoll sources

Behaviour in hardness-intensity and colour-colour diagrams

Atoll sources show two distinct spectral states (branches), as shown in the right panel of Fig. 1.6, corresponding to different X-ray luminosities. At higher luminosities, Atoll sources trace the

Banana Branch, whose two parts - the Upper Banana (UB) and the Lower Banana (LB) are often distinguished. As the luminosity drops, they make a transition into a harder state called the Island Branch (IS). Hasinger & van der Klis (1989) concluded that such a dependence on the X-ray luminosity clearly suggests that mass accretion rate increases in the direction Island \rightarrow Banana in Atoll sources, as marked with an arrow in the right panel of Fig. 1.6. The whole colour-colour variation of an Atoll source takes place on a timescale of typically weeks or months. It is thus clear, that strong physical changes take place in Atoll sources and that they are different from Z-track sources, having longer timescales and occurring at lower luminosities. In Sect. 1.3.3 the attempts that have been made to understand these differences will be discussed.

Timing properties

The power spectra of Atoll sources are less diversified than those of Z-track sources as can be seen in the right panel of Fig. 1.8. Their main characteristics were given by Hasinger & van der Klis (1989) as relevant to the identification of this group of LMXB. Low frequency QPO, similar to those observed in Z-track sources, are generally not seen in Atoll sources. KiloHertz QPO are observed on the Island Branch and the Lower Banana Branch in a similar frequency range as in Z-track sources and their frequencies increase as a source moves up along the Banana (van der Klis 2004). Their amplitudes are usually 5 - 10 times larger than in higher luminosity Z-track sources (Jonker et al. 2001). Hasinger & van der Klis (1989) distinguished two power components: Very Low Frequency Noise and High Frequency Noise. They noticed that VLFN has a power law shape with an index of about 1.0, thus flatter than in the case of Z-track sources. In the Island State, above 0.1 Hz there is a clear power excess called High Frequency Noise which in fact resembles LFN on the Z-track/HB. As the source moves from the Island State towards the Upper Banana Branch, VLFN becomes stronger and HFN, still visible above ~ 1 Hz, gets weaker (van der Klis 1989).

1.3.3 What makes Z-track and Atoll sources different?

The apparent division of neutron star LMXB into Z-track sources and Atoll sources, based on both the spectral changes observed in HID/CCD and timing properties (Hasinger & van der Klis 1989), leads to obvious questions regarding the physical causes of this.

Hasinger & van der Klis (1989) speculated that in contrast to Atoll sources, except of higher luminosities, Z-track sources may harbour neutron stars with stronger magnetic fields. A possi-

bility in line with this was already put forward by van der Klis et al. (1985) and Lewin & van Paradijs (1986) who suggested that high mass transfer from an evolved companion could lead to an accretion-induced collapse of a white dwarf producing a young neutron star with a relatively strong magnetic field. Moreover, evolved companions would explain (Webbink et al. 1983) higher mass transfers (and luminosities) in Z-track sources and would imply (Hasinger & van der Klis 1989) larger orbits with longer orbital periods which is so far supported by observations (Barziv et al. 1997). Indeed, the only known orbital periods of Z-track sources are 19^{hr} (Sco X-1; Gottlieb et al. 1975), 22^{hr} (GX 349+2; Wachter & Margon 1996) and 9.8^d (Cyg X-2; Cowley et al. 1979) and are systematically longer than orbital periods of Atoll sources ($< 5^{hr}$) (Hasinger & van der Klis 1989; White 1995). Hasinger & van der Klis (1989) also argued that weaker magnetic fields of neutron stars in Atoll sources could explain their, in general, lack of low frequency QPO assuming these were generated by interaction of the magnetosphere with the accretion flow (Alpar & Shaham 1985).

Gierliński & Done (2002), having studied three LMXB (4U 1608-52, Aql X-1 and 4U 1705-44) noticed that their colour-colour patterns observed over a long time resembled Z-shaped tracks. In such cases, their Island State became elongated and resembled the Horizontal Branch in Z-track sources. They also found that the sources moved along their atoll patterns in the same way as Z-track sources do - from the left end of the elongated Island State towards the right end of the Upper Banana State as the inferred mass accretion rate was increasing. Gierliński & Done (2002) suggested that Atoll sources and Z-track sources are in fact the same type of sources with similar colour-colour patterns, but with the former tracing them more slowly than the latter. However, the proposed similarity of the observed colour-colour patterns to those of the Z-track sources has been questionable.

A similar study on a larger sample of sources was independently performed by Munro et al. (2002). They also reported that Z and Atoll patterns were similar, but pointed out problems of such a simple unification scenario. They argued that the timing features of Atoll sources are different due to generally lack of low frequency QPO that are strong in Z-track sources and also that the Island State spectra of Atoll sources are harder than spectra of Z-track sources on the Horizontal Branch. Most importantly, Munro et al. (2002) argued that Atoll patterns are traced on timescales that are 1 or 2 orders of magnitude longer than in Z-track sources and that they correspond to lower luminosities involving several times larger changes in luminosity, again unlike in Z-track sources. Furthermore, van Straaten et al. (2003) studied timing properties along the colour-colour pattern

of 4U 1608-52 which had been suggested by Gierliński & Done (2002) to trace a Z-track. Their results were inconsistent with such a scenario showing no gradual changes of timing features as would be expected from a Z-track source.

Most recently, the transient source XTE J 1701-462 was observed by Remillard et al. (2006) during its 20-month-long outburst in 2006 and 2007. During the outburst, they saw for the first time that the colour-colour behaviour of a single source was changing from resembling a Cyg-like Z-track, then a Sco-like Z-track and finally an Atoll pattern, as the luminosity of XTE J 1701-462 was decreasing from being super-Eddington to quiescence. They argued that their observation provided strong evidence for the luminosity (mass accretion rate) only being responsible for the difference between Z-track (including Cyg-like and Sco-like sub-division) and Atoll types of behaviour. However, this interpretation introduces a problem of what, if not mass accretion rate, drives the source round the Z-track.

1.4 Phenomena observed in LMXB

Low Mass X-ray Binaries, although interesting in themselves, exhibit a number of most intriguing phenomena. These include thermonuclear flashes on the surfaces of the accreting neutron stars, X-ray dipping in highly inclined systems, quasi-periodic oscillations over a broad range of frequencies and relativistic jet-like outflows. Below, an overview of these phenomena is given.

1.4.1 X-ray bursts

X-ray bursts were discovered by Grindlay et al. (1976) in the globular cluster source 4U 1820-30 and independently by Belian et al. (1976). The events were seen as jumps in intensity by a factor of 20 - 30 with a very fast ~ 1 s rise time and then an exponential decay on a timescale of ~ 10 s (Fig. 1.9). The total energy released in a burst is of the order of 10^{39} - 10^{40} ergs (Lewin et al. 1993). It was soon realized, via the α ratio (below) (Woosley & Taam 1976; Maraschi & Cavaliere 1977), that these bursts could be associated with the so-called ‘thin shell instability’ predicted by Schwarzschild & Härm (1965), when considering stellar evolution, and developed later by Hansen & van Horn (1975) for the case of accreting neutron stars. In this scenario (Joss & Rappaport 1984), accreted hydrogen and/or helium forms several meter-thick shells on a neutron star. Matter, compressed under gravity of the neutron star and pressure of newly accreted matter, gets heated within hours or days reaching conditions for thermonuclear ignition (Bildsten 2000). Burning shells

are subject to a thermal instability which, having occurred, results in runaway nuclear burning and X-ray flashes observed (Joss & Rappaport 1984). (Hoffman et al. 1978) classified this kind of bursts as type I to distinguish them from type II bursts observed in MXB 1730-335 (known as the Rapid Burster). During outbursts of the Rapid Burster (active periods of the source), even 1000 short-lasting (seconds - minutes) type II bursts with peak luminosities of an order of 10^{38} erg s^{-1} can be observed per day (e.g. Mahasena et al. 2003). Lewin et al. (1976) found that energy of a given type II burst was linearly proportional to the time interval to the next burst which could be explained by a model in which clumps of matter, before reaching a critical mass and being suddenly accreted, are stored for some time close to the compact object. Thus, type II bursts are related to accretion instabilities and not thermonuclear runaways (Hoffman et al. 1978).

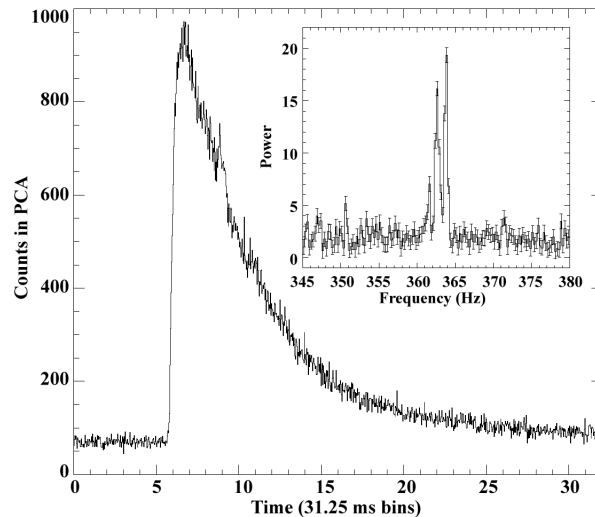


Figure 1.9: A type I X-ray burst observed in 4U 1728-34 with *RXTE*/PCA with an inset showing a power spectrum during this event (Strohmayer et al. 1996).

The primary evidence that type I X-ray bursts are of thermonuclear nature comes from an examination of burst energetics. The amount of energy per nucleon released in fusion of hydrogen into helium, and helium into heavier elements is about 7 MeV and 2 MeV, respectively. On the other hand, the energy release per nucleon in accretion, $G M_* m_p / R_*$, is about 200 MeV. One would then expect that the ratio of time-averaged persistent energy (accretion) to time-averaged burst energy (thermonuclear), designated α , should be 30 - 100, depending on the fuel composition, which is consistent with many observations (Galloway et al. 2008).

A detailed theoretical discussion of physics behind unstable nuclear burning was given by Bildsten (1998) and more recently summarized by Strohmayer (2006). In this approach, when considering

the neutron star atmosphere as plane-parallel, burning ignition and thermal stability depend on the mass accretion rate per unit area

$$\dot{m} = \frac{\dot{M}}{A}, \quad (1.18)$$

where A is area on the neutron star. Bildsten (1998) showed that depending on \dot{m} several burning régimes are identified as summarized in Table 1.2. The dependence on \dot{m} makes comparison of observations and theory very practical as \dot{m} can be related to \dot{M} and hence calculated from the X-ray luminosity of a source using e.g. Eqn. 1.1.

Table 1.2: Burning régimes for H/He mixture on the surface of a neutron star defined by the mass accretion rate per unit area (after Bildsten 1998).

Régime	\dot{m} range (g cm ⁻² s ⁻¹)
H unstable in mixed H/He shell	$\dot{m} < 1 \times 10^3$
He unstable in H-poor shell	$1 \times 10^3 < \dot{m} < 5 \times 10^3$
He unstable in mixed H/He shell	$5 \times 10^3 < \dot{m} < 1.3 \times 10^5$
H & He stable burning	$1.3 \times 10^5 < \dot{m}$

Intervals between bursts last about a few hours or days. As \dot{M} increases, more and more matter is accumulated in the same time and bursts should occur more often, as e.g. was observed in 4U 1323-619 and GS 1826-24 (Church et al. 2005; Bałucińska-Church et al. 2008). However, there are sources in which just the opposite was observed, such as 4U 1705-44 (Langmeier et al. 1987) so a full understanding is yet to be achieved. A more detailed model should take into account different composition, metallicity, the amount of fuel burnt or left-over in a previous burst, the core temperature of neutron stars and the accretion rates in binaries (e.g. the review of Galloway et al. 2008).

The spectral fitting of bursts met with the difficulty that different approaches were possible (e.g. Sztajno et al. 1986). The most common method is to subtract persistent emission from burst emission and analyse only net burst emission. It is then found that blackbody is the best spectral description of a burst (Swank et al. 1977) giving a temperature kT of 1.0 - 2.5 keV and a ~ 10 km blackbody radius consistent with the surface of a neutron star. However, it is possible that the non-burst blackbody emission could develop into burst blackbody emission. During the burst rise, the burst spectra become harder and then in decay they soften showing the initial heating and the subsequent cooling of the emitter. Based on the spectral analysis of a bright Z-track source GX 17+2, Kuulkers et al. (2002) found that the persistent emission was not affected during

bursts. They thus concluded that the ‘net burst emission’ approach is correct. When a blackbody component is present in the persistent emission it appears to have a different origin, i.e. the boundary layer.

It is generally assumed that the Eddington limit is reached at the peaks of some bright bursts which can be used as a technique to determine source distance (Basinska et al. 1984; Kuulkers et al. 2002). At the Eddington luminosity, the star’s atmosphere is lifted up by radiation pressure, the effect known as photospheric radius expansion (PRE), which can be recognized spectrally by an increasing blackbody radius and a decreasing blackbody temperature at constant luminosity (Kuulkers et al. 2002). Kuulkers et al. (2003) studied a number of bright bursts in globular cluster sources for which distances are well known. They derived an average peak PRE burst luminosity of $(3.79 \pm 0.15) \times 10^{38}$ erg s⁻¹, consistent with the Eddington limit for hydrogen-poor matter, that could be used with an accuracy of 15 % as a standard candle to determine distance provided that PRE is seen.

About one half of known LMXB exhibit type I X-ray bursts, in particular Atoll sources in their Island States. Bursts are typically found at luminosities below 1.5×10^{37} erg s⁻¹ defining the so-called ‘burst box’ (Fig. 1 in Barret et al. 1996). At higher luminosities bursts are rare and among the Z-track sources only GX 17+2 (Tawara et al. 1984; Kuulkers et al. 2002) and Cyg X-2 (Kahn & Grindlay 1984; Smale 1998) show occasional type I X-ray bursts, but they are not correlated with spectral states. In these cases, the α values reported were about 10^3 , suggesting that not all of the accumulated fuel is subject to unstable burning. Observations show that many Atoll sources show a lot of type I X-ray bursts but weak Very Low Frequency Noise, whereas, in contrast, Z-track sources show stronger VLFN but hardly any bursts (van der Klis et al. 1987; Hasinger & van der Klis 1989; Bildsten 1995). Moreover, in sources with large \dot{M} variations (e.g. 4U 1705-44, 4U 1636-536) presence and regularity of bursts is anti-correlated with the strength of VLFN (van der Klis et al. 1990). The theoretical work of Bildsten (1993, 1995) predicted that as mass accretion rate increases, unstable nuclear burning would preferentially take the form of slow burning fires propagating over the surface of the neutron star on a timescale of 10^3 s, thus different from fast ~ 10 s type I bursts at low \dot{M} . They proposed that the observed anti-correlation between VLFN and type I bursts is a result of the two types of nuclear burning competing for the same accreted fuel with slow burning seen as VLFN corresponding to 5 - 10 % of intensity variations.

It has been expected that inhomogeneous burning on the surface of a neutron star could lead to

a modulation of X-ray flux with neutron star's spin frequency (Bildsten 1995; Jongert & van der Klis 1996). Such burst oscillations were actually discovered with *RXTE* in the source 4U 1728-34 by Strohmayer et al. (1996) and in many sources subsequently. In 4U 1728-34 the burst oscillation had a frequency of 363 Hz (as shown in the inset of Fig. 1.9) revealing the spin frequency of the neutron star. The long-term studies of Strohmayer et al. (1998a) showed that burst frequencies (in 4U 1728-34 and 4U 1636-53) are very stable in time, confirming their rotational nature.

1.4.2 Jets

About 20 neutron star LMXB have been discovered to have radio counterparts (Hjellming & Han 1995). As early as 1969, radio emission was detected in Sco X-1 by Ables (1969) based on the position given by Andrew & Purton (1968). Their observations at 6 cm showed flux variations on a timescale of hours. Later came radio detections of the other Z-track sources: GX 17+2 (Hjellming & Wade 1971), GX 5-1 (Braes et al. 1972), Cyg X-2 (Hjellming & Blankenship 1973; Hjellming et al. 1990a), GX 349+2 (Cooke & Ponman 1991) and GX 340+0 (Penninx et al. 1993). Radio emission of a Z-track source has been found (Penninx 1989) to depend strongly on position along the Z pattern. It is strongest and most variable when the source is on the Horizontal Branch / the upper Normal Branch and becomes weaker on the lower NB and often not detected on the Flaring Branch (e.g. Penninx 1989; Hjellming & Han 1995; Fender & Hendry 2000). Radio spectra are of a power law shape ($F_R \sim \nu^\alpha$) and found to be rather flat ($\alpha \sim 0$), suggesting an optically thick environment, except periods of radio flaring when they are steeper ($\alpha \leq 0$) and thought to come from a synchrotron-emitting, optically thin region (e.g. Penninx et al. 1993; Migliari et al. 2007). One of the best studies of Sco X-1 is that of Fomalont et al. (2001b) with the *VLBI*. They found a pair of ejecta moving away from the centre with an average speed of $\sim 0.45 c$. These blobs of radio emitting plasma persisted for about 2 days and were then replaced by new ones of similar patterns of variability emerging from the source. Also, Fomalont et al. (2001a) showed that there was a correlation between core emission and lobe emission suggesting via the delay involved an energy transfer between these regions with a speed of $\sim 0.95 c$.

Only a few Atoll sources have been detected in radio so far and it has become apparent that their radio fluxes are 5 - 30 times weaker than those of Z-track sources (e.g. Migliari et al. 2003). Possible detections were made for 4U 1820-30 (Migliari et al. 2004), 4U 1728-34 (Marti et al. 1998) and GX 13+1 (Homan et al. 2004) (which actually shares some characteristics of the Z-track sources) and the transient source Aql X-1 (Tudose et al. 2009; Miller-Jones et al. 2010). In 4U 1728-34, radio

emission was detected in the Island State of the source where it showed a correlation with X-ray flux (Migliari et al. 2003). The strongest and most variable behaviour was related to a transition between the Island State and the Lower Banana State. According to Fender & Hendry (2000), the most probable reason for which Atoll sources are weaker than Z-track sources is their lower mass accretion rate and in fact stronger radio fluxes from Atoll sources were reported during periods of their higher X-ray luminosities. However, Fender & Hendry (2000) noticed that Atoll sources are also many times weaker in radio than black hole systems although their mass accretion rates seem comparable in many cases. Thus, they suggested an alternative possibility that jet activity is related mostly to state transitions and these occur more often in Z-track sources than in Atoll sources in which X-ray spectral changes take place on a time-scale of days and weeks/months, respectively (Hasinger & van der Klis 1989).

Interestingly, radio detections of jets have not been reported from any X-ray pulsar in HMXB systems and therefore it is believed that high magnetic fields disrupting inner disks do not allow for the formation of jets (Fender et al. 1997; Fender & Hendry 2000). The problem of a possible role and importance of the inner disk in the formation of jets has since been considered (Migliari et al. 2003) and will also be addressed in the present work.

Observations show that radio emission is stronger in black hole binaries than in neutron star systems (e.g. Migliari & Fender 2006), but some similarities have been pointed out. When a black hole source is in its low/hard state (luminosity $\lesssim 0.03 L_{Edd}$), the radio spectrum is flat or mildly inverted suggesting the presence of a self-absorbed, compact jet (Fender et al. 2004). A jet have been spatially resolved for example in Cyg X-1 (Stirling et al. 2001) using the *VLBA* in the 8.4 - 15.4 GHz range. The steady jet is no longer visible when a black hole system goes into its soft/high state (Fender et al. 2004). Additionally, bright radio events that have been occasionally resolved spatially as relativistic motions from the core (Mirabel & Rodríguez 1994), as in Fig. 1.10, have been reported during state transitions in black hole systems. In such cases, steeper radio spectra consistent with synchrotron emission from an optically thin environment (Hjellming & Han 1995; Fender 1999) are observed. These similarities to neutron star systems would suggest that jet launching may be independent of the nature of the compact object, i.e. presence or absence of a surface (Migliari & Fender 2006). However, in neutron star systems (in the Island State of Atoll sources and on the Horizontal Branch of Z-track sources), the dependence of radio on X-ray luminosity has a different form ($L_R \sim L_X^{1.4}$, Migliari & Fender 2006) than in black hole systems in their hard states ($L_R \sim L_X^{0.7}$, Corbel et al. 2003). Also, in the soft state in black hole systems

jet emission is more strongly suppressed than in neutron star systems when their spectra are also soft (Migliari & Fender 2006).

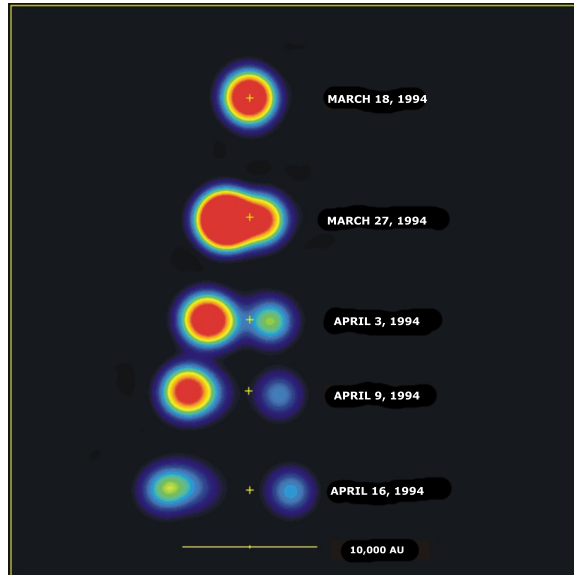


Figure 1.10: Ejection of two condensations spotted on several occasions in the black hole binary GRS 1915+105 with the *VLA* at 8.4 GHz. Ejecta were moving at sub-light speed away from the central core (marked with a yellow cross). Image courtesy of the National Radio Astronomy Observatory/Associated Universities, Inc./the National Science Foundation.

X-ray binaries are very good laboratories to study radio jets on sensible time-scales when compared with active galactic nuclei. Simultaneous radio and X-ray observations allow to track jet presence in relation to a spectral state of the source and should reveal conditions needed for the launching of jets. A model for this was proposed by Church et al. (2006) in the case of the Z-track source GX 340+0. In their model jets are launched under strong radiation pressure exerted on the inner disk by radiation from the neutron star surface (Sect. 3.1.5). This thus suggests that the stellar surface is important and that neutron star systems are in this respect different from black hole systems.

1.4.3 Dipping

A group of about 10 LMXB show reductions in intensity, called dipping, related to the orbital period. Basic understanding of dipping was provided by White & Swank (1982) and Walter et al. (1982) who studied the LMXB 4U 1915-053 and noticed that intensity dips were occurring stably every ~ 50 minutes which they attributed to be the orbital motion of the system (confirmed later by Grindlay et al. 1987). The effect was thought (White & Swank 1982; Walter et al. 1982)

to be caused by the azimuthally elongated, absorbing bulge crossing the line of sight, formed where the stream of matter from the companion hits the outer accretion disk, the interpretation now widely accepted. The formation of the obscuring structure has been addressed theoretically and e.g. in the model of Frank et al. (1987) dipping was caused by matter that overshoots the stream-disk impact point and forms a thickening at the circularization radius somewhere between the outer edge and the centre of the disk. The simulations of Armitage & Livio (1996, 1998) and Armitage (1998) showed that some overshooting may indeed take place, with the absorbing material eventually distributed between the outer disk rim and the circularization radius, but this would not be efficient in all systems. Hellier & Mason (1989) argued that the modelling of the lightcurves of the dipping source 4U 1822-37 strongly favours the formation of the bulge at the outer rim of the disk. Similarly, more recent simulations of Bisikalo et al. (2005) suggest that an absorbing, vertically extended structure can form at the outer edge of the disk and cause dipping.

White & Swank (1982) tried to explain dipping as simple photoelectric absorption of a single emission component by cold material but without complete success as this would require under-abundance in metals by at least a factor of 17. Moreover, in 4U 1755-33 (White et al. 1984) dips seemed to be energy-independent whereas photoelectric absorption in the X-ray band is strongest at low energies (e.g. Wilms et al. 2000). Thus, to avoid energy dependence it was necessary to postulate a large under-abundance of metals by a factor of 600 (White et al. 1984).

In several sources it was found that during dipping, part of the non-dip emission was absorbed and part was not absorbed. This was modelled by an approach in which dipping spectra could be fitted by splitting the non-dip emission into two components representing the absorbed and the unabsorbed parts (Parmar et al. 1986; Smale & Mukai 1988). The model was applied to several dipping sources: EXO 0748-676 (Parmar et al. 1986; Smale et al. 1992), XB 1254-690 (Courvoisier et al. 1986), XB 1624-490 (Jones & Watson 1989), 4U 1915-053 (Smale & Mukai 1988; Smale et al. 1992; Yoshida et al. 1995). Although it was possible to fit dip spectra in this way, the problems were twofold. First, it was not clear why only a part of emission was absorbed. Second, the unabsorbed part of emission was reduced in dipping in an energy-independent way which was thought to simulate effects of electron scattering (Parmar et al. 1986; Smale & Mukai 1988). However, this would mean scattering in a region much closer to the neutron star than the bulge in the outer accretion disk which appeared unlikely (e.g. Church et al. 1998a).

A self-consistent explanation was finally proposed by Church & Balucinska-Church (1993) who used a model consisting of two components: a blackbody and a power law. Dipping in 4U 1755-33 was well explained by an increased column density of a cosmic abundance absorber at the outer disk rim, absorption being mostly of the neutron star blackbody by an absorber of limited angular extent. Moreover, given the combination of model components, the net dipping spectrum looked energy-independent, which was difficult to explain before (White et al. 1984). The same model gave also a good description of dipping in XB 1624-49 (Church & Balucinska-Church 1995).

4U 1916-053 exhibited very deep dipping with intensity reductions by 90 - 100 % (Fig. 1.11). Church et al. (1997) found that during dipping the power law component, representing the Comptonized emission from the source, was gradually removed in the spectrum which meant that it must have originated from an extended region which they associated with the accretion disk corona. They introduced a partial covering factor to the model and showed that it was increasing from zero (non-dip spectra) to almost one (deep dipping) demonstrating progressive coverage of an extended emission region. The same approach worked for EXO 0748-676, where dipping was often by 100 % (Church et al. 1998a), showing again that photoelectric absorption was enough to explain dipping in an energy range of 1 - 10 keV in which it should naturally dominate.

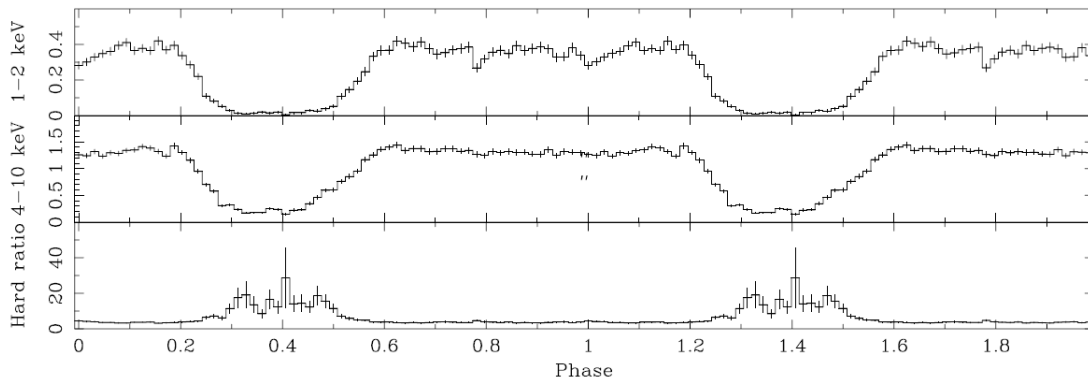


Figure 1.11: A folded lightcurve (on the period of ~ 3000 s) of 4U 1916-053 as observed with *BeppoSAX/MECS* in 1 - 2 keV (upper panel) and 4 - 10 keV (middle panel) energy ranges. Dipping is seen as a gradual flux removal down to a complete obscuration. Spectral hardening typical to dipping is seen in the lower panel (Church et al. 1998b).

Further studies with *BeppoSAX* (Church et al. 1998b; Bałucińska-Church et al. 2000), *XMM-Newton* (Church et al. 2005) and *Suzaku* (Bałucińska-Church et al. 2009) confirmed the ability of the two-component model of Church & Balucinska-Church (1993) to fit non-dip and dip spectra of all dipping LMXB.

Most recently, another proposition for explaining dipping sources has been exploited (e.g. Boirin et al. 2005). The model was proposed based on absorption features (such as of iron) observed in high-resolution *XMM-Newton* spectra and their evolution in dipping (Boirin et al. 2004). It was suggested (Boirin et al. 2005) that dipping could be related to an ionized absorber whose high ionization, as derived from spectral fitting, required that the absorber was localized relatively close to the central X-ray source. In this approach, as dipping progresses, the ionization decreases and the column density increases, but it was not suggested how this was related to the orbital phase, i.e. what azimuthal structure caused dipping.

The model has been applied to several highly inclined sources (e.g. EXO 0748-676, XB 1254-690, XB 1624-490, XB 1659-298, 4U 1916-053) observed with *XMM-Newton* (Díaz Trigo et al. 2006). However, the model is doubted (Bałucińska-Church et al. 2009) as it ignores the extensive evidence that the emission region in LMXB is extended. Moreover, as argued by Bałucińska-Church et al. (2009), it does not explain why the bulge would not cause dipping in contrast to what is widely accepted.

1.4.4 Quasi-periodic oscillations

Since the discovery (van der Klis et al. 1985) of time variability features in early observations with *EXOSAT*, timing analysis has become a powerful tool in studies of LMXB. As already introduced in Sect. 1.3, low-frequency ($\nu < 100$ Hz) power spectra of neutron star LMXB are dominated by 15 - 60 Hz Horizontal Branch QPO, 5 - 20 Hz Normal Branch / Flaring Branch QPO in Z-track sources and also noise components present in both Z-track sources and Atoll sources in all their spectral branches (van der Klis 1989). More recently, very high time resolution and the large effective area of *RXTE* led to the major discovery (van der Klis et al. 1996) of the twin kHz QPO (Fig. 1.12). These are observed typically on the Horizontal Branch in Z-track sources and in the Island/Lower Banana Branch in Atoll sources (Sect. 1.3).

QPO are usually modelled using Lorentzian peaks characterized by an amplitude, width and centroid frequency. The coherence and strength of a QPO is often described in terms of the quality factor

$$Q = \frac{\nu}{\Delta\nu}, \quad (1.19)$$

where ν is the frequency of a QPO and $\Delta\nu$ is its width (FWHM). Conventionally, QPO are distinguished from noise and defined as signals having $Q > 2$ (van der Klis 2004) and in LMXB the

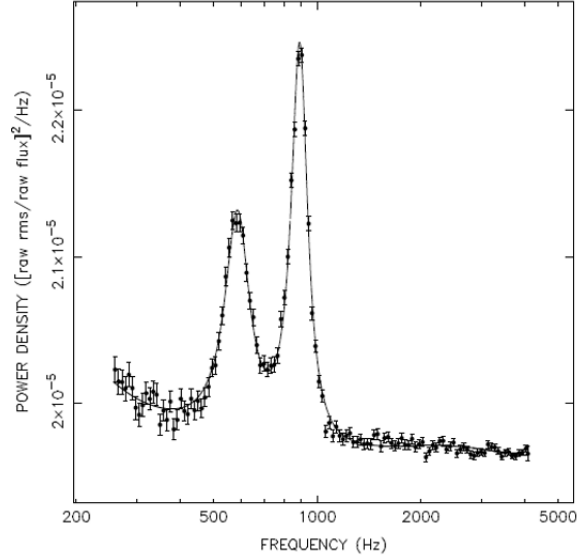


Figure 1.12: Left: Twin kilohertz QPO observed in Sco X-1 by van der Klis et al. (1997) and modelled with a pair of Lorentzian peaks.

quality factors observed are high (10 - 200, e.g. Belloni 2010) which means that effects responsible for these oscillations have relatively long (when compared to a Keplerian orbital period of $\sim 10^{-3}$ s in the inner disk) lifetimes of the order of $\lesssim 0.1$ s (e.g. Barret et al. 2005a; van Straaten et al. 2005). A drop in the quality factor of the kHz QPO observed in a few LMXB at a certain QPO frequency was interpreted as related to the disk reaching the innermost stable circular orbit (ISCO) (e.g. Barret et al. 2005b, 2006, 2007), with the maximum frequency of the upper kHz QPO suggesting the radius of the ISCO. Indeed, that the kHz QPO, and typically the upper one, corresponds to e.g. the Keplerian motion in the inner accretion disk has been often treated as an attractive possibility (e.g. van der Klis 2005).

Low-frequency QPO and twin kHz QPO in LMXB have been widely studied over recent years as they offer the possibility of testing the physics of accretion under strong gravity conditions. Below, the most common theoretical models that have been proposed to explain the QPO phenomena are described and discussed in terms of observed properties of QPO.

Models for QPO vs observations

The beat-frequency models The most recent incarnation of this group of models is the sonic-point beat-frequency model proposed by Miller et al. (1998) to explain kHz QPO. It assumes that there are clumps of matter in the accretion disk orbiting the central star. At the sonic radius the radial drift velocity increases rapidly to become supersonic and an orbiting clump releases matter

which spirals down onto the star surface forming a hot spot. The spot moves around the star with the Keplerian frequency of the clump in-orbit giving rise to the upper kHz QPO. Simultaneously, the weak magnetic field channels some of disk's matter onto the poles of the neutron star giving a pulsar-like beam rotating at the spin frequency of the star. The lower kHz QPO frequency is then due to the beat between the orbital frequency at the sonic radius and the spin frequency of the star. The model is based on the magnetospheric beat-frequency model of Lamb et al. (1985); Alpar & Shaham (1985) for the low frequency 5 - 60 Hz QPO which was explained as the beat between the magnetospheric radius frequency and the star spin frequency.

An advantage of the beat-frequency models is that they involve natural frequencies in LMXB: the Keplerian orbital frequency in the disk and the spin frequency of the neutron star. However, as the models demand the presence of the surface of a star, they cannot be applied to black hole binaries. Moreover, in the original form of the sonic point model, the separation between the two kHz QPO $\Delta\nu$ peaks was expected to be equal to the neutron star spin frequency ν_{spin} and therefore constant. This was, however, later ruled out because it had been found that the kHz QPO separation is *not* constant in all sources, as in e.g. the Z-track source Sco X-1 (van der Klis et al. 1997) and the Atoll source 4U 1608-52 (Mendez et al. 1998). Another problem is that in some cases the kHz QPO separation is equal not to the neutron star spin frequency, but to about half of it (e.g. Wijnands & van der Klis 1997; Strohmayer et al. 1998b; Wijnands et al. 2003). All these issues introduced further problems for the beat-frequency models making them unlikely to be correct.

The relativistic precession model The model was proposed by Stella & Vietri (1998, 1999) to explain QPO in terms of relativistic effects under strong gravity conditions. The spin of the central object implies the Lense-Thirring effect, also known as frame-dragging, according to which a slightly tilted accretion disk should precess around the angular momentum axis of the spinning compact object. This nodal precession is expected to give the low frequency QPO in the 5 - 60 Hz range. The lower kHz QPO is supposed to be the periastron precession frequency of slightly eccentric disk orbits and the upper kHz QPO is interpreted as the Keplerian frequency at the radius in the disk where clumps of matter are assumed to orbit giving rise to flux oscillations.

In the relativistic precession model all fundamental QPO can be explained in terms of relativistic effects and thus applied to both neutron star and black hole systems. The model predicts a quadratic relation between the low frequency QPO and the upper kHz QPO which is consistent with some observations, such as of van Straaten et al. (2003) (Atoll sources) and Jonker et al.

(1998); Homan et al. (2002) (Z-track sources). Nevertheless, the relation is the same for binaries with neutron stars having different spin frequencies, which is not expected (van Straaten et al. 2003, 2005). The quadratic relation would also require an unrealistically large ratio of the neutron star moment of inertia to its mass (e.g. Jonker et al. 1998; Psaltis et al. 1999) and is not accurately met over all frequencies (Psaltis et al. 1999). A disadvantage of the model is also the fact that a clump of matter in the disk, assumed by the model, is not expected to exist long whereas QPO are very coherent suggesting otherwise (Kluźniak 2008).

The disk resonance model This model was proposed by Kluzniak & Abramowicz (2001) and suggested by the apparent concentration of kHz QPO frequency ratios at around 3 : 2. The model of Kluzniak & Abramowicz (2001) assumes that deviations from Keplerian disk movement in the vertical and the radial direction under strong gravity conditions result in disk oscillations seen as kHz QPO. The upper and the lower kHz QPO could then be due to the vertical and the radial oscillation, respectively (Kluzniak & Abramowicz 2002; Abramowicz et al. 2003). The oscillations are in a non-linear resonance and may be excited by instabilities in the disk or, in the case of a neutron star, by its spin (Wijnands et al. 2003; Abramowicz et al. 2003). The strongest resonance occurs when oscillation frequencies are in the ratio of 3 : 2 (Kluzniak & Abramowicz 2002) as was found to be the case in the Black Hole Binaries GRO J1655-40 (Strohmayer 2001a,b) and XTE J1550-564 (Miller et al. 2001; Remillard et al. 2002). A similar frequency ratio was postulated to hold in Sco X-1 (Abramowicz et al. 2003). However, the kHz QPO frequencies in neutron star LMXB vary and are not in the exact ratio of 3 : 2 showing only a clustering around this value (Belloni et al. 2005). Moreover, as shown by Boutelier et al. (2010), the observed clustering around the above frequency ratio can be reproduced even from a uniform distribution of QPO frequencies given that observations may be biased by sensitivity limits and that QPO significance depends on frequency. An advantage of the model is that it can be applied to all disk accreting systems (Kluźniak 2008), including white dwarf systems whose QPO could be due to the resonance excited by the spin of the central star and would not require strong gravity (Kluźniak et al. 2005). The weakness of the model is the difficulty to explain the QPO relation to spectral states in LMXB and to explain the actual X-ray modulation mechanisms (Abramowicz et al. 2007; Rebusco 2008).

An observational approach towards the understanding of kHz QPO was taken by Church et al. (2006) and Jackson et al. (2009). They assumed, as is widely expected, that at least one of the kHz

QPO is related to the motion of matter in the inner accretion disk. By comparing their results of spectral fitting with the behaviour of the kHz QPO in the Z-track source GX 5-1, Jackson et al. (2009) proposed that the formation of the kHz QPO can be related to effects of strong radiation pressure in the vicinity of the neutron star. This model will be presented in more detail in Sect. 3.1.5 and exploited further in the present work.

1.5 Rossi X-ray Timing Explorer

The *Rossi X-ray Timing Explorer*, or *RXTE*, is one of the most significant NASA missions and X-ray observatories (Bradt et al. 1990, 1993; Swank 2006). Its name honours Bruno Rossi - one of the pioneers in X-ray astronomy. When compared with other high-energy missions, it has been so far the longest-lasting after the *Hubble Space Telescope*. *RXTE*, whose schematic view is shown in Fig. 1.13, was launched on 30th of December 1995 by a Delta II rocket from the Kennedy Space Flight Center and reached a 90 minute orbit at an altitude of 580 km and an inclination of 23° . The satellite was operated from the Goddard Space Flight Center (GSFC) in Greenbelt, Maryland (USA). After 16 years of service, the *RXTE* mission was decommissioned on the 5th of January, 2012.

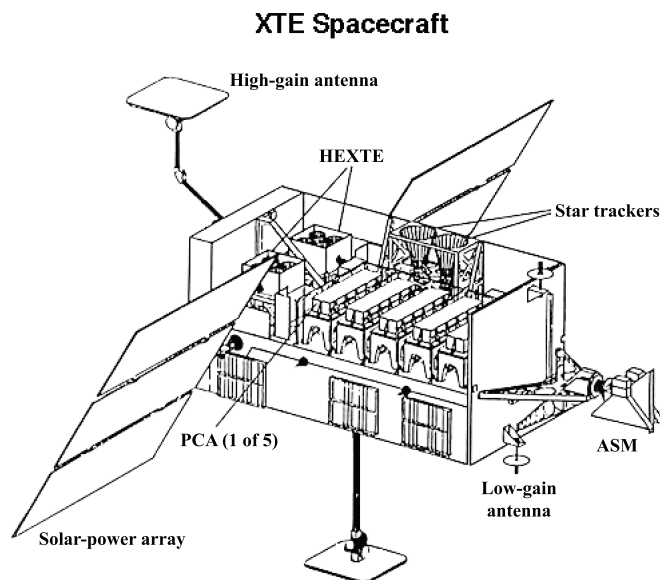


Figure 1.13: A schematic view of *Rossi-XTE* and its basic components, including scientific instruments: 5 PCU units, 2 HEXTE clusters and All-Sky Monitor (Swank 2006).

The mission was designed to study the timing properties of X-ray sources, such as rapid aperiodic variability (flickering) in Cyg X-1 (Meekins et al. 1984), low frequency (< 100 Hz) QPO, and

was meant to search for millisecond QPO in X-ray Binaries, hence a very large collecting area of 6500 cm^2 to allow an unprecedented time resolution of microseconds. The broad energy coverage of 3 - 200 keV of *RXTE* is provided by two main pointing instruments on-board: the Proportional Counter Array (PCA) and the High Energy X-ray Timing Experiment (HEXTE), which are based on the *HEAO-1* detectors (they are larger and improved versions of those). Additionally, the All-Sky Monitor (ASM) instrument, by continuously monitoring most of the sky, detects interesting events (e.g. outbursts) which can then be studied in detail by the other instruments and other observatories. The satellite's attitude during observations is controlled by the Attitude Control System which secures pointing accuracy using optical star trackers, gyroscopes and Sun sensors that can operate under varying conditions. Observations are restricted mostly by the Sun avoidance angle which must be always greater than 30° , however 93% of the sky is available at any time.

Among the most important successes of *RXTE* are the discovery of kHz QPO in X-ray binaries, the discovery of rotation periods of neutron stars and studies of gamma-ray burst afterglows. The number of refereed publications based on *RXTE* data is over 2100 (as of 2011). The very long lifetime of the mission makes it also one of best-calibrated, hence the PCA is often used as a reference instrument during multi-mission spectral analyses.

1.5.1 The Proportional Counter Array

The PCA instrument was provided by the Goddard Space Flight Center and consists of five Proportional Counter Units (PCU) (Jahoda et al. 1996). Each PCU consists of a collimator, the main detection chamber and electronics (Fig. 1.14). The hexagonal collimator in front of the detector gives a field of view of 1° . The front propane-filled anti-coincidence layer, used to discriminate between source photons and background particle events, is situated between two mylar windows. The bottom window leads to three xenon-methane main detecting layers of the proportional counter. The three main xenon-methane layers are divided into two halves and connected to left and right amplifier chains. In this way six separate signal detection regions are defined and designated as 1L & 1R, 2L & 2R, and 3L & 3R. Additional anti-coincidence layers are located at the sides and the rear of a PCU improving the background rejection capabilities. Most of the photons are detected in the first xenon-methane layer (LR1) which is hence most often used for data analysis given its best signal to noise ratio. Incoming photons ionize xenon gas atoms releasing photoelectrons which move towards the nearest anode in the chamber. The

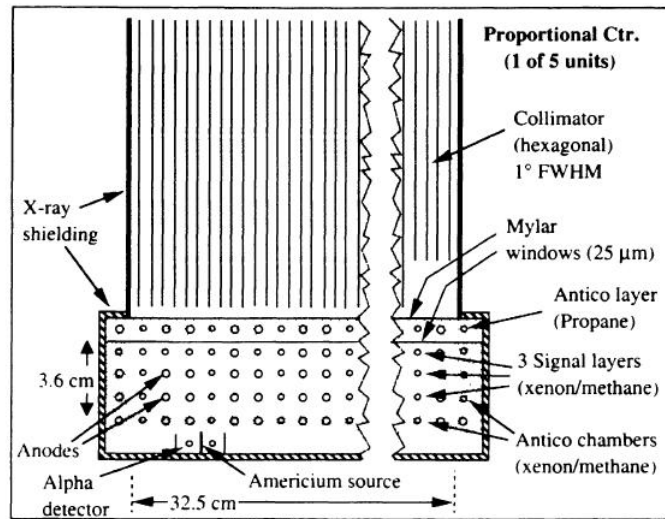


Figure 1.14: A cross-section view of a PCU detector (Bradt et al. 1990).

high kinetic energy of the electrons allow for subsequent ionizations and amplification of the signal which reaches the anode giving a measurable pulse detected by the on-board electronics. However, some xenon atoms may be excited rather than ionized, and then they deexcite producing visual or UV photons that could affect the detection process. Thus, methane is added as a quench gas to absorb (without ionization) such unwanted photons and make sure that the electron avalanche will be stopped. In the PCU proportional-counter, the applied voltage (~ 2000 V) is such, that the energy of the electron avalanche reaching an anode is proportional to the energy of the original photon allowing energy reconstruction based on the height of pulse amplitudes. The PCU detectors are sensitive nominally in the 2 - 100 keV energy range with an energy resolution $\Delta E/E$ of 18% at 6 keV. Each of the PCU has a large collecting area of 1600 cm^2 . On-board calibration and gain control is provided by an Am^{241} radioactive isotope whose decays provide X-ray photons for calibration. Every recorded signal goes to the Experimental Data System (EDS) which applies a time tag to each event, performs event selection and data compression in several modes (most commonly Standard1 and Standard2). The instrument background is modelled and provided for the purpose of data analysis by mission specialists. Its credibility is based on many tests and many-year experience, and is thus high.

1.5.2 The High-Energy X-ray Timing Experiment

The High Energy X-ray Timing Experiment, or HEXTE, is the second main pointing instrument on-board *RXTE*. Its nominal energy range between 15 and 250 keV makes it complementary to

the PCA with some overlap in the 15 - 100 keV range. HEXTE consists of two clusters, A and B (Fig. 1.15, left), each having four identical detectors giving a combined, net effective area of 890 cm^2 in each cluster. The instrument was built at the University of California, San Diego at the Center for Astrophysics & Space Sciences and consists of a collimator, the main detection chamber, the photomultiplier (PMT) and electronics. A field of view is defined by a collimator at the front which is co-aligned with the PCA. A beryllium window beneath this leads to the main “phoswich” detecting chamber (Fig. 1.15, right) in which there is the primary NaI(Tl) crystal and the secondary CsI(Na) crystal. An incoming X-ray interacts with iodine atoms in the primary crystal which, having been excited, produces a scintillation (a pulse of light in the visual range), the intensity of which is proportional to the energy of the original photon. The scintillation light expels from the anode of the PMT a photoelectron which is next boosted via a series of interactions with dynodes carrying out amplification of the signal detected at the cathode as an electric pulse.

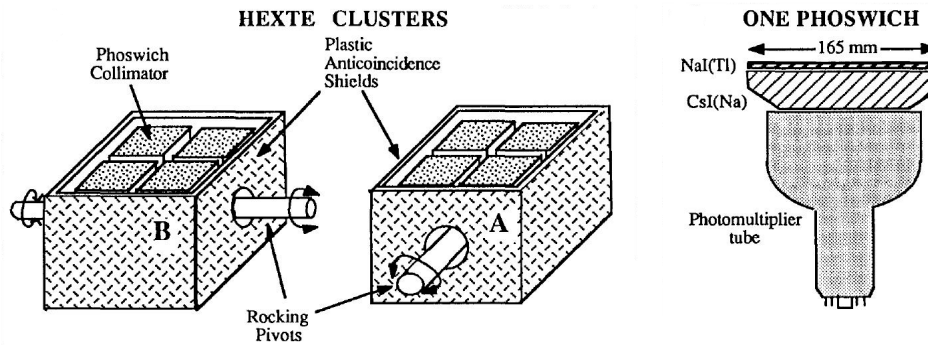


Figure 1.15: Left: A perspective view of the two HEXTE clusters. Right: A cross-sectioned view of a phoswich detector (Bradt et al. 1990).

Photons from a source are detected in the first crystal, whereas spurious signals (cosmic rays or instrumental noise) excite also the second crystal and can be discriminated from the real source photons by pulse shape analysis. Additional active (crystals) and passive (magnetic field) shielding is attached on the sides and the rear of each cluster. Am^{241} radionuclei are present for on-board calibration.

Background is measured by rocking of the HEXTE instrument in which the two clusters change their pointings between on-source and background sky regions. The off-source positions are typically 1.5 - 3.0 degrees away from the on-source positions. In this way, the two clusters together can gather background information from background regions on each side of the source. Their movements are synchronized in such a way that at every moment one of the clusters observes the

source (to give full coverage in time). This mechanism allows for a very good real-time and accurate background estimation. A single on-source observation lasts for 16 - 128 seconds and then a cluster moves off source to a background pointing. The movement itself takes only 2 seconds and this is subtracted from the background off-source time and taken into account during background subtraction. The energy resolution (15% at 60 keV) is very stable although it changed during the 16 year mission by a few percent. Gain changes are compensated for by proper adjustments to voltages in the PMT. All these effects and others, such as detection efficiency, are incorporated into response files that are standard and generated using appropriate software. Data from HEXTE are pre-analysed on-board *RXTE* by the Flight Data System and then telemetered to Earth.

1.5.3 The All-Sky Monitor

The All-Sky Monitor consists of three Scanning Shadow Camera (SSC) detectors, mounted on a movable assembly, with two cameras observing perpendicular to the rotation axis of the assembly, and the third camera observing along the axis (Fig. 1.16, left). This design ensures that the instrument can cover up to 80% of the sky every 90 minute orbit with a total effective area of 90 cm². In front of each camera (Fig. 1.16, right) is an elongated collimator giving a field of view of 6° × 90°. At the entrance to the collimator there is a coded mask - a set of transparent (50%) and opaque (aluminium) areas forming a unique, pre-defined pattern (Dicke 1968). The mask casts shadows of X-ray sources upon the xenon position-sensitive proportional counter (PSPC). This proportional counter, whose basic detection concept is the same as in the PCA, can additionally measure the spatial distribution of shadow patterns cast on a set of anodes. For every X-ray source, the observed shadow pattern is a real source image convolved with the known mask pattern so

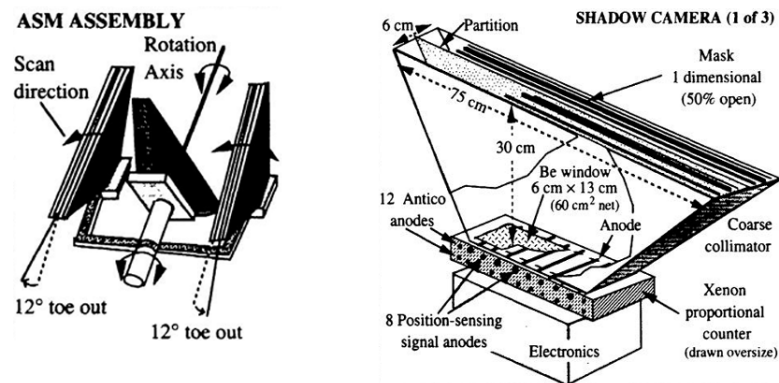


Figure 1.16: Left: A schematic view of the ASM assembly. Right: A descriptive schematic of a Scanning Shadow Camera (Bradt et al. 1993).

that the shift of the shadow pattern with respect to the central position of the detector encodes the position of the source in the sky, whereas the strength of the signal corresponds to the source intensity. During every observation, the camera records shadow patterns from many X-ray sources at the same time, and the sky image can be deconvolved with the mask pattern using dedicated algorithms since the process is additive.

The ASM operates in the 2 - 10 keV energy range with a spatial resolution of about $3' \times 15'$. Particle events are rejected by side and rear anti-coincidence chambers. An in-flight calibration is provided by an Fe^{55} isotope. A single observation lasts about 90 seconds and then data are transferred to the EDS system which applies time stamps to events. The main scientific goal of the ASM is to alert observers to any potential new sources or outbursts of known sources. The process of detecting new objects or outbursts is iterative. First, the deconvolved sky image is compared with the catalogue of known sources. Any significant residuals from the comparison give information about potentially new objects whose parameters (e.g. position, intensity) are added to the catalogue, and the process repeats. Initial quick-look products are available shortly after the observation itself and can be used for alerts and targets of opportunity. Definitive products (corrected for a number of filtering criteria such as goodness of the source-detection solution, the number of sources in the field of view, the angle from the Earth and the exposure time etc.) become publicly available later.

Chapter 2

Spectral models for LMXB

2.1 The complex spectra of LMXB

In the vast majority of cases it has been found that the 1 - 20 keV spectrum of a LMXB cannot be fitted with one-component models (e.g. Vacca et al. 1987). Many two-component models do the job very well which is consistent with theoretical expectations (Sect. 1.1.2) that emission from a LMXB should come mainly from two regions: the boundary layer and the accretion disk. Furthermore, both regions may be possibly covered (surrounded) by a hot corona which Comptonizes seed radiation from underneath and this leaves us with several possibilities (e.g. Mukherjee & Bhattacharyya 2011). The boundary layer and the disk can simply shine as a blackbody and a multicolour blackbody, respectively. Also, if one or both regions are surrounded by a corona, they will give a power law-like Comptonized emission.

It should be noted, that in many early studies in the 1970s and the early 1980s, good fits to LMXB spectra were obtained using a model involving thermal bremsstrahlung component representing thermal emission of optically thin plasma (e.g. Parsignault & Grindlay 1978; Pravdo 1983; Ercan & Cruise 1984). This description was however soon recognized to be unphysical in the case of neutron star LMXB (e.g. White et al. 1985, 1986). This is because values of the emission measure, $EM \sim n_e^2 R^3$, where n_e is the electron density of plasma and R is the plasma cloud radius, obtained from spectral fitting were typically $\sim 10^{60} \text{ cm}^{-3}$ (Soong & Rothschild 1983; White et al. 1986; Vrtilik et al. 1986; Christian & Swank 1997). Such high values of EM , assuming low optical depth of the plasma $\tau = \sigma_T n_e R$, implied a size of the emission region of $R \sim 10^{10} \text{ cm}$, thus very large, and even comparable to the size of the binary system itself. On the other hand, if one assumed

that the size of the plasma cloud was reasonably small, such as 10^7 cm, then the optical depth would have to be high, making the usage of the model inappropriate (Christian & Swank 1997).

Observations favour a scenario in which one part of the emission is Comptonized and hence two classical approaches were proposed in the 1980s. The **Eastern model** of Mitsuda et al. (1984), assumed originally that the softer blackbody component was from the accretion disk (and had the form of a multicolour blackbody) and the second harder component was a simple ~ 2 keV blackbody originating from the surface of the neutron star (or the boundary layer). This idea was later modified (Mitsuda & Dotani 1989) to explain low luminosity sources by including Comptonization of the neutron star emission in a small optically thin corona around it.

Another approach, called the **Western model** (White et al. 1985, 1986), assumed that Comptonized, harder emission originated from the accretion disk corona and the softer blackbody component was emitted from the boundary layer or the neutron star surface. The blackbody component was actually often not required in spectral fitting of low luminosity sources which could be described in terms of Comptonization alone given the relatively low count rates obtained with instruments (such as on *EXOSAT*) available at that time.

The two models differ significantly in size, geometry and type of emission. Hasinger et al. (1990) and Asai et al. (1994) tested the Eastern and the Western models using *Ginga* data on Cyg X-2 and GX 5-1, respectively. They found that both models give acceptable fits to the data and thus could not be distinguished on the basis of the reduced χ^2 . Moreover, in the observation of Hasinger et al. (1990), both models gave continuous variations of spectral parameters along the colour-colour Z-track of Cyg X-2. Despite numerous spectral analyses of the Z-track sources with the Eastern model (e.g. Done et al. 2002; Di Salvo et al. 2002; Agrawal & Sreekumar 2003; D'Aí et al. 2007), no commonly accepted understanding of the physical changes in the sources has emerged from use of that model. However, in some cases, although the same emission geometry as in the Eastern model was assumed, the best fitting model required the usage of a simple blackbody instead of the disk blackbody (e.g. Di Salvo et al. 2000, 2001). This was also the case in some observations of Atoll sources (Bloser et al. 2000; Barret & Olive 2002; Piraino et al. 2003, 2007) and in fact, especially at their lowest luminosities, the best spectral description (in terms of the goodness of fits) has been achieved with a model composed of a simple blackbody and a power law or cut-off power law (e.g. White et al. 1986; Langmeier et al. 1987; Haberl et al. 1987; van Paradijs et al. 1988a; Bloser et al. 2000; Juett & Chakrabarty 2003; in't Zand et al. 2005) although physical interpretations were often limited.

This ambiguous situation started to change in the 1990s mostly due to studies of a small group of about 10 sources, called the dipping LMXB, which are LMXB seen at high inclination. It is widely accepted that in these sources, the bulge formed at the impact point, where matter from the companion hits the outer accretion disk, periodically crosses the line of sight and leads to drops in intensity called dipping (Sect. 1.4.3). The phenomenon has been widely studied and investigation of spectral evolution in dipping showed directly that the region of Comptonized emission must be spatially extended, i.e. it has a radial extension of order $10^9 - 10^{10}$ cm, as it was removed only gradually and thus could not be a point-like source. This fact put serious constraints on the geometry of a LMXB and was incorporated into a new model, called at the beginning the complex continuum model or the Birmingham model (Church & Balucinska-Church 1995) and more recently the Extended Accretion Disk Corona (ADC) model. The model is now described in detail below.

2.2 The Extended ADC model

The Extended ADC model assumes the presence of two continuum emission regions in LMXB: the surface of the neutron star and the extended corona of the accretion disk. Schematically, its form can be written

$$\text{absorption} \times (\text{blackbody} + \text{cut-off power law}),$$

where absorption stands for the Galactic absorption and possibly also absorption intrinsic to the source. Details regarding model components and their parameters are listed in Table 2.1.

Table 2.1: A detailed description of the Extended ADC model components.

Component (XSPEC name)	Meaning	Mathematical form	Parameters
bbody	point-like blackbody emission from the surface of the neutron star	$\frac{dN}{dE} = \frac{KE^2}{kT_{bb}^4} \frac{1}{\exp(E/kT_{bb}) - 1}$	kT_{bb} - blackbody temperature, K - normalization
cutoffpl	Comptonized emission from the extended accretion disk corona	$\frac{dN}{dE} = \frac{KE^{-\Gamma}}{1\text{keV}} \exp\left(-\frac{E}{E_{co}}\right)$	E_{co} - cut-off energy, Γ - photon index, K - normalization

As was already demonstrated in Sect. 1.4.3, the Extended ADC model has successfully explained the dipping LMXB and their spectra at different stages of dipping. During dipping, the blackbody

component was absorbed quickly, whereas the extended accretion disk corona was being progressively covered by the bulge (Fig. 2.1, left). This also explained different levels of hardening or softening observed in dipping by blackbody components having different temperatures in particular sources. With use of better instruments it was shown, that in contrast to the Western model, the blackbody component is always present in a spectrum of a LMXB. Moreover, different depths of dipping were well explained by different covering fractions of the extended corona. A discussion of this early work was already given in section 1.4.3. The model has since been applied to many LMXB (e.g. Church 2001; Church et al. 2006, this work) to find if it can give a self-consistent description and physical understanding of all groups of LMXB.

2.2.1 The evidence for an extended nature of the ADC

In cases when dipping is $\sim 100\%$ deep, the angular size of the absorber must be larger than any emission region in a source. Based on this condition, the size of the largest region (which can only be the accretion disk corona), R_{ADC} , can be measured from the ingress/egress time and deriving the velocity of the absorbing bulge in the outer disk (from the orbital period and the disk radius) (Fig. 2.1) using the relation:

$$\frac{2\pi R_{AD}}{P} = \frac{2R_{ADC}}{\Delta t} \implies R_{ADC} = \frac{\pi R_{AD} \Delta t}{P}, \quad (2.1)$$

where: R_{AD} is the radius of the accretion disk (at the outer edge of which is the absorbing bulge), P is the orbital period, and Δt is the dip ingress or egress time found to be of the order of 100 - 10000 s and thus easily measured. Church (2001) calculated R_{ADC} for a number of sources

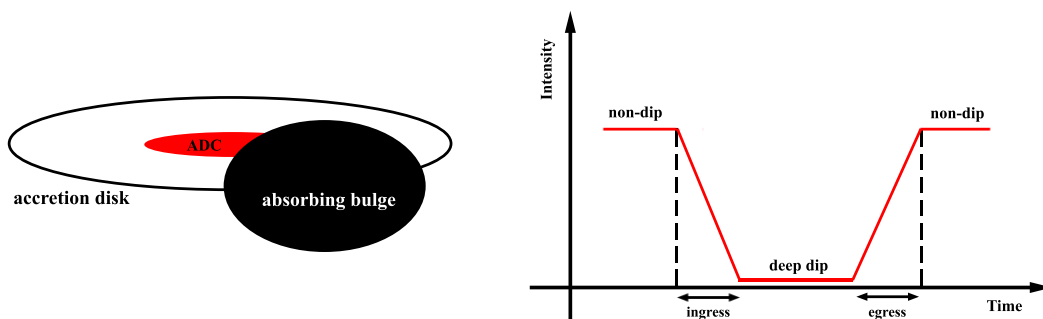


Figure 2.1: Left: Geometry of the accretion disk corona progressively covered in dipping. Right: the dip ingress/egress time which depends on the size of the ADC (as in Church & Bałucińska-Church 2004).

and found that it was in the range of $8.5 \times 10^8 - 5.3 \times 10^{10}$ cm. These values correspond to a corona covering 2.5 - 50 % of the disk radius depending on the source luminosity. This was further confirmed by Church & Bałucińska-Church (2004) who also showed that the relation between the size of the ADC and the total luminosity (Fig. 2.2) was $R_{ADC} = L_{tot}^{0.88 \pm 0.16}$, hence probably a direct proportionality of the two quantities.

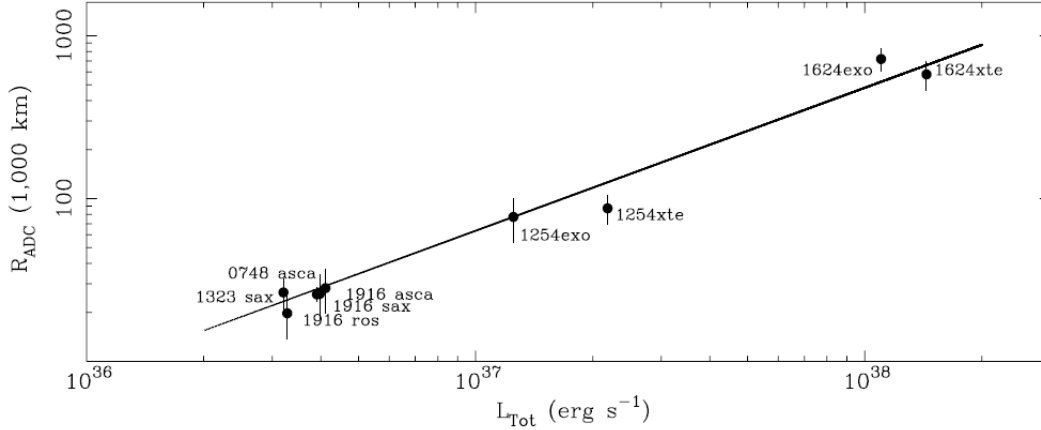


Figure 2.2: The radius of the Accretion Disk Corona as a function of the total 1 - 30 keV luminosity as measured in a sample of dipping LMXB (Church & Bałucińska-Church 2004).

The cut-off energy E_{co} of the power law component, which represents emission from the ADC, can be used to derive the electron temperature of the Comptonizing corona. The electron temperature kT_e should be between $kT_e \geq E_{co}/3$ (for high optical depth) and $kT_e \leq E_{co}$ (for low optical depth) (e.g. Haardt et al. 1993; Petrucci et al. 2001). From spectral fitting Church & Bałucińska-Church (2004) found that the electron temperature was in the range of 4 - 80 keV, lower in more luminous sources. Based on this, for each source they could calculate the Compton radius $r_C \approx GMm_p/kT_e$ which gives a maximum radial distance up to which the hydrostatic equilibrium can hold at a given temperature kT_e and should in fact be the upper limit for the size of the ADC (above this radius a wind from the disk is to be expected). Values obtained in this way ($r_C > 2.4 \times 10^9$ cm; Church & Bałucińska-Church 2004) were in a good agreement with sizes of coronae calculated from dip ingress/egress timing. Church & Bałucińska-Church (2004) concluded that the properties of such an extended ADC could be determined by an external mechanism, such as illumination of the disk by the central X-ray source, which had been proposed (White et al. 1981; White & Swank 1982) as a likely mechanism for the formation of the corona and was studied theoretically later (e.g. Fabian et al. 1982; Begelman et al. 1983; Begelman & McKee 1983; Rozanska & Czerny 1996; Jimenez-Garate et al. 2002).

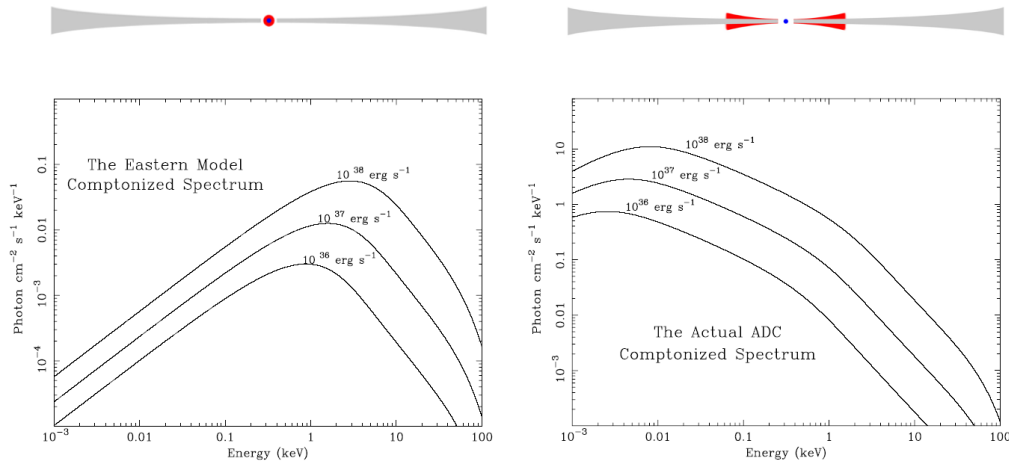


Figure 2.3: A schematic edge-on view of an accreting neutron star according to the Eastern (top left) and the Extended ADC (top right) model showing the accretion disk (grey), the neutron star (blue), and the corona (red). The corresponding Comptonization spectra are shown below (Church & Bałucińska-Church 2004).

Church & Bałucińska-Church (2004) compared seed photon spectra and the resultant Comptonization spectra for the cases of the Eastern model and the Extended ADC model (Fig. 2.3). In the Eastern model the seed photon spectrum is often assumed to be a ~ 1 keV blackbody which is then Comptonized in a centrally localized electron cloud. In this case, the seed photon spectrum decreases below 1 keV and so does the Comptonized spectrum (Done et al. 2002). In contrast to this, with an extended corona, seed photons must predominantly come from the accretion disk below the corona giving seed spectra extending down to ~ 0.01 keV and hence the Comptonized emission keeps increasing below 1 keV. It has been argued (Done et al. 2002) that spectral fitting with the Extended ADC model, based in practice on the composition of a simple blackbody plus a cut-off power law to represent Comptonization, cannot be valid as these forms are too simplified. In their opinion, unlike in the Eastern model, the cut-off power law does not take into account the turn-over at low energies (Fig. 2.3, left) which leads to overestimation of the Comptonization component and underestimation of the blackbody component. Done et al. (2002) suggested that this was the reason for which Church & Bałucińska-Church (2001), who tested a model composed of a disk blackbody and cut-off power law, obtained unphysically small radii of the inner disk advocating against the Eastern model. However, Church & Bałucińska-Church (2004) pointed out that, given the extended nature of the corona, it is the description of the Comptonization spectrum in the Eastern model which is incorrect, and thus there is no turn-over at ~ 1 keV (Fig. 2.3, right) justifying the usage of the cut-off power law plus a simple blackbody.

In a recent Chandra study of Cygnus X-2, Schulz et al. (2009) observed a number of emission lines of high ionization states implying their origin in the ADC. They found that lines from H-like and He-like elements of Ne, Mg, Si, S and Fe were broad implying Doppler velocities of 1100 - 2700 km s⁻¹. These, translated into radial distances gave values of 18000 - 110000 km clearly showing that the corona is indeed extended. This is in a very good agreement with previous numerical values obtained based on the study of dipping sources where the coronal size was found to be in a range of 20000 - 700000 km depending on the luminosity of the source. Schulz et al. (2009) estimated that the corona had a density of 1×10^{15} cm⁻³ and a temperature in excess of 10⁶ K. A similar result was delivered by Xiang et al. (2009) in a *Chandra* study of the dipping source 4U 1624-490. Their results suggested the presence of a highly ionized, hot ($\sim 3 \times 10^6$ K) and extended (up to 3×10^{10} cm) accretion disk corona.

One of the arguments against the Extended ADC model is that it is theoretically unappealing. This is because the standard accretion theory, although containing only very basic assumptions, predicts that half of energy should be released from the disk and another half from the boundary layer (Sect. 1.1). In fact, having taken into account relativistic corrections, the ratio of boundary layer to disk emission should be even larger than 1 (most of the energy is expected to be released from a deep potential well close to the compact object). Although it is completely reasonable to expect this, observations show a rather different picture. First, it was recognized quite early that spectra of LMXB are dominated by the Comptonized emission. Then, the Comptonizing cloud would have to be around the compact object (as proposed in the Eastern model) to satisfy theoretical demands. However, this is in contradiction with many observations (such as those involving ingress and egress timing studies) showing that the Comptonized component is extended. Thus, the only alternative consistent with observations is the extended accretion disk corona.

2.2.2 Blackbody from the surface of the neutron star

The blackbody component of the Extended ADC model is interpreted as originating from the surface of the neutron star. To check if another option is possible (i.e. if blackbody can be emitted from the inner disk), Church & Balucińska-Church (2001) made a test and replaced the blackbody component with disk blackbody in their *ASCA* survey of LMXB (including dipping sources, Atoll sources and Z-track sources). They found that in the majority of cases, the inner disk radius R_{in} obtained directly from fitting was unphysically small with values down to ~ 0.5 km - clearly smaller than the radius of the neutron star. Church & Balucińska-Church (2001) noticed that any

reasonable correction factors of 2 - 4, that could be applied to R_{in} , would still mean that the inner disk was reaching to inside of the neutron star. In several cases, the inner radii were larger in the range 10 - 24 km, but the photon index of the power law component was then often negative. Thus, Church & Balucińska-Church (2001) concluded that the origin of blackbody in the inner disk was unlikely. As mentioned earlier (Sect. 2.2.1), Done et al. (2002) argued that unphysically small radii of the inner disk obtained by Church & Balucińska-Church (2001) are artefacts of using the wrong representation of the Comptonized emission in the form of a cut-off power law, this however was shown not to be true given the extended corona (Church & Balucińska-Church 2004). Furthermore, Church & Balucińska-Church (2001) plotted the blackbody luminosity against the total luminosity for the sample of sources under study. What they found was that there was a tendency for brighter sources to have a larger blackbody contribution to the total luminosity, i.e. in these sources the blackbody contribution was closer to 50 % (as expected in the standard theory in the Newtonian approximation). Church & Balucińska-Church (2001) noticed that these changes were related mostly to changes in the blackbody radius which was getting systematically larger for brighter LMXB. In many cases the blackbody radius was smaller than the theoretical ~ 10 km radius of the neutron star meaning that emission was not coming from the whole neutron star surface, but from an equatorial belt on the star. The blackbody radius was then converted into the half-height of the belt using

$$2\pi R_* 2h = 4\pi R_{bb}^2 \implies h = \frac{R_{bb}^2}{R_*}, \quad (2.2)$$

where R_{bb} is the blackbody radius obtained from spectral fitting and R_* is the radius of the neutron star (assumed to be 10 km). The formula 2.2 has been derived by intersecting a sphere (representing a neutron star) by two parallel planes with the area between the planes representing the equatorial belt on the star. Next, Church & Balucińska-Church (2001) compared the results to the half-height of the inner radiatively-supported disk H , taking $H = H_{eq}$ as the first approximation of the disk vertical extent (Eqn. 1.16, Sect. 1.1). The comparison showed that there was a relation $h \approx H$ over a broad range (10^{36} - 10^{38} erg s $^{-1}$) of luminosities (see Fig. 2.4).

This result implied two possible scenarios. First, the inner accretion flow may be radially advected onto the star across the narrow gap between the inner disk and the neutron star surface and thus h is directly determined by H . Another possibility relates to the work of Inogamov & Sunyaev (1999) who showed that matter accreted onto a neutron star in the equatorial plane spreads vertically to form a bright belt; this having considered the effects of centrifugal force and radiation pressure.

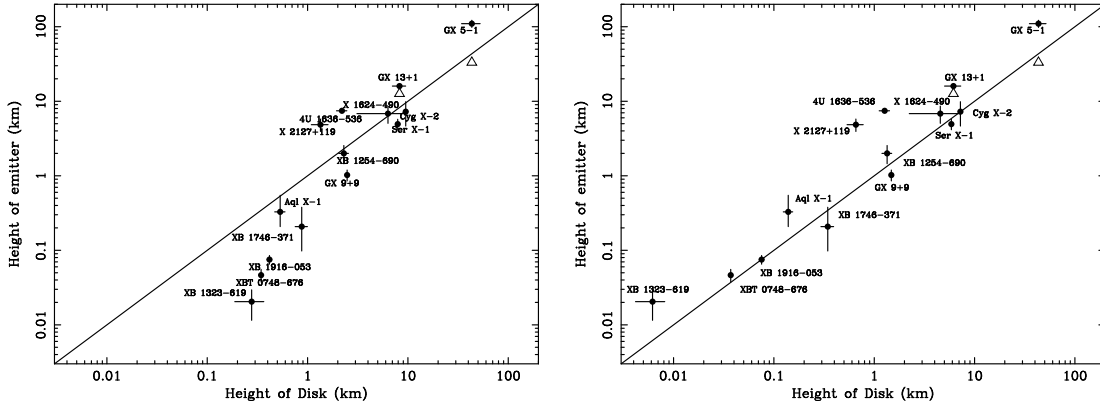


Figure 2.4: Left: The half-height of blackbody emission region h (equatorial belt on the neutron star) is close to the equilibrium half-height of the inner radiatively-supported disk H_{eq} . In lower luminosity sources H_{eq} is not achieved. Right: relation $h \approx H$ is restored at lower luminosities when the real disk half-height is more accurately calculated at the radius where radiation pressure is 10 times larger than gas pressure (Church & Balucińska-Church 2001).

In this case the height of the belt depends on luminosity (as does H) and the relation $h \approx H$ would also be fulfilled. Regardless of the exact scenario, relation $h \approx H$ found for a large sample of sources supports the view in which blackbody originates at the surface of the neutron star. A detailed examination of these possibilities by Church et al. (2002) led to the result that both radial advective inflow and the mechanism of Inogamov & Sunyaev (1999) could account for $h \approx H$.

Although it has been tested and shown that the thermal component in spectra of LMXB is not a disk blackbody (Church & Balucińska-Church 2001), it could be questioned if modelling with a pure, point-like blackbody is valid without any modification. A possible effect of electron scattering in the atmosphere of the neutron star has been addressed theoretically (e.g. Czerny & Sztajno 1983; London et al. 1984; Lapidus et al. 1986; Ebisuzaki 1987; Pavlov et al. 1991; Madej 1991). In this case, Comptonization of blackbody emission in the neutron star atmosphere may lead to hardening of the spectrum and, when fitting with the Planck function, temperature overestimation and apparent super-Eddington luminosities. Some evidence for this was found in a few cases in type I X-ray bursts in which the measured high blackbody temperature kT_{bb} was ~ 3.0 keV, i.e. inconsistent with the Eddington limit (e.g. Marshall 1982). Furthermore, Inoue et al. (1984) and Sztajno et al. (1985) showed that blackbody fits during some X-ray bursts yield an observed anti-correlation between kT_{bb} and R_{bb} that could be understood in terms of the modified Planck spectrum. Recently, Majczyna et al. (2005) and Suleimanov et al. (2011) studied model neutron star atmospheres in terms of chemical composition, luminosity and surface gravity of the neutron star and argued that the spectral hardening factor (colour correction) $f_c = T_c/T_{eff}$,

expressing the ratio of the observed colour temperature to the effective blackbody temperature, is typically ~ 1.5 . However, as noted by Balucińska-Church et al. (2001), whether substantial scattering in the atmosphere takes place depends on the electron density which is poorly known. Czerny & Sztajno (1983) argued that the effect is small except for the burst peak and London et al. (1984) confirmed that the effect increases with the temperature. In line with this, bursts with lower temperatures were shown to be well fitted with a simple blackbody (e.g. Swank et al. 1977). Moreover, spectral fitting of non-burst emission (e.g. Church & Balucińska-Church 2001) did not reveal any deviation from a simple blackbody and showed that the blackbody radius in bright sources was close to 10 km, consistent with the theoretical neutron star radius. Thus, observations indicate that modelling with a pure blackbody, in particular in the case of non-burst emission in LMXB, is rather valid and does not necessarily lead to erroneous results.

Emission from the neutron star is also subject to the gravitational redshift, which is particularly important when analysing type I X-ray bursts (e.g. Lewin et al. 1993) from which distances and neutron star parameters are often derived, and for a neutron star having $M = 1.4 M_{\odot}$ and $R_* = 10$ km the redshift factor $(1 + z) = (1 - 2GM/R_*c^2)^{-1/2} \approx 1.3$. An example of the possible combined effect of spectral hardening in the neutron star atmosphere and the relativistic correction has been explicitly shown by Suleimanov et al. (2011) who derive $T_{bb} = f_c/(1 + z) T_{\text{eff}}$ and $R_{bb} = (1 + z)/f_c^2 R_{bb,*}$, relating the observed T_{bb} and R_{bb} with the effective temperature T_{eff} and radius $R_{bb,*}$ of the blackbody emitted from the surface of the neutron star. By substituting the typical values of the corrections given above one finds that $T_{bb} \approx 1.15 T_{\text{eff}}$ and $R_{bb} \approx 0.6 R_{bb,*}$, and that the observed blackbody luminosity $L_{bb} \propto T_{bb}^4 R_{bb}^2$ may be underestimated by about 30%. A possible effect of shielding of the neutron star emission region by e.g. the inner disk and the ADC cannot be excluded. Nevertheless, in the Atoll sources the inner disk, as will be shown later, is relatively thin, with the half-height of the order 0.1 - 1 km, and becomes thicker only in more luminous sources. Moreover, the inclinations of the Z-track and most of the Atoll sources are low or moderate (Table 3.1) and this probably diminishes any shielding effect.

The above discussion shows that a few systematic effects, some of which may in general be difficult to evaluate, may affect the emission from the neutron star. However, it is noted here that the exact combined effect of all the corrections is a matter of debate and the results obtained in this work are presented as they were obtained from spectral fitting in order to allow most direct comparison with the previous work of the *X-ray Binaries Group* and others. When particularly relevant, possible effects of the corrections mentioned above will be discussed.

Chapter 3

Review of previous work

The first section of this chapter (Sect. 3.1) is devoted to a detailed overview of the physical model for the Z-track in Cyg-like sources of Church et al. (2006) based on the results of spectral fitting with the Extended ADC model to *RXTE* spectra of the source GX 340+0. Similar analyses were next carried out for GX 5-1 (Jackson et al. 2009) and Cyg X-2 (Bałucińska-Church et al. 2010). The latter results supported the model of Church et al. (2006) showing that the Extended ADC model can provide a unified explanation of the Z-track in all three Cyg-like sources, as summarized by Bałucińska-Church et al. (2010).

Next, a review is given of previous work on twelve individual sources studied in this work. These sources are: Cyg X-2 and GX 340+0 (Cyg-like Z-track sources - Sect. 3.2), GX 17+2 and Sco X-1 (Sco-like Z-track sources - Sect. 3.3) and 2S 0918-549, 4U 1636-536, 4U 1705-44, 4U 1728-34, 4U 1735-44, SLX 1735-269, 4U 1820-30 and 4U 1916-053 (Atoll sources - Sect. 3.4). General information on the sources has been assembled in Table 3.1 at the end of the Chapter.

3.1 A model for the Z-track in the Cyg X-2 like LMXB

3.1.1 The analysis method

In the case of each of the three Cyg-like sources, the analyses of Church et al. (2006); Jackson et al. (2009); Bałucińska-Church et al. (2010) involved producing a number of hardness-intensity data selections along the Z-track. An example of this is given in Fig. 3.1 which shows data selections (boxes) made along the Z-track of GX 340+0 in the original work of Church et al. (2006). In this way, spectral changes that take place along the Z were studied by fitting the Extended ADC model

to the selected spectra and obtaining best-fit parameter values. The understanding of the Z-track in Cyg-like sources in terms of those results is presented below.

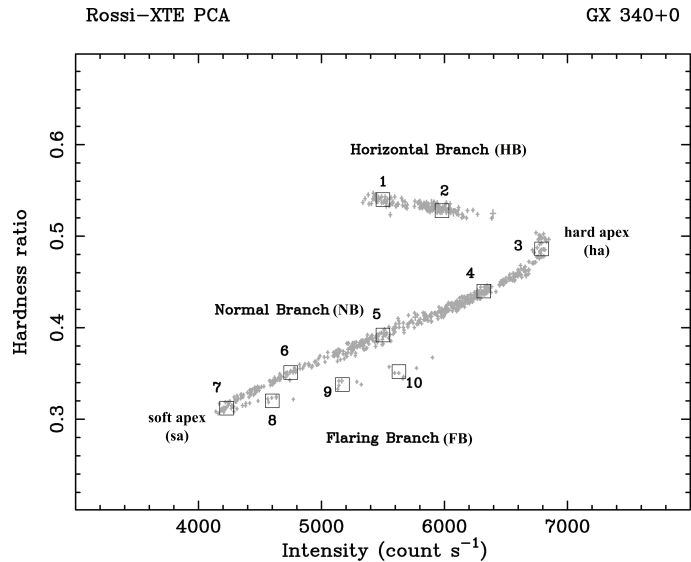


Figure 3.1: The Z-track of GX 340+0 with boxes showing data selections for the spectral analysis of Church et al. (2006).

3.1.2 At the soft apex

In the Extended ADC model, the blackbody component is interpreted as emission from the surface of the neutron star. Fig. 3.2 (left) shows changes of the blackbody parameters: the temperature kT_{bb} and radius R_{bb} along the Z-track as a function of the total 1 - 30 keV luminosity. It can be seen that in all three sources the blackbody temperature (top panel) is lowest when a source is at the soft apex of the Z-track, with measured values in the range 1.19 - 1.31 keV (depending on the source). At the same time, the blackbody radius (bottom panel) at the soft apex in the three sources, with the mean of 11.4 ± 0.6 km (Bałucińska-Church et al. 2010) clearly suggests that the whole neutron star is emitting.

The above results were interpreted (Church et al. 2006) by saying that, when a source is at the soft apex of the Z-track, there is a low mass accretion rate and so a low luminosity in all three sources. The soft apex can thus be considered as a type of a quiescent state (Church et al. 2006), from which the source can move in hardness-intensity along either the Flaring Branch or the Normal Branch.

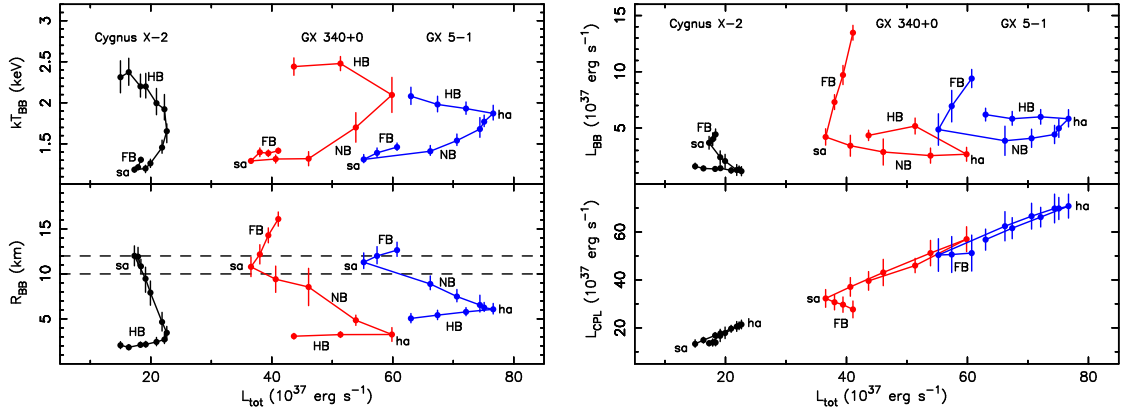


Figure 3.2: The combined spectral fitting results of the three Cyg-like sources: Cyg X-2, GX 340+0 and GX 5-1 shown versus the total (1 - 30 keV) luminosity. Left: blackbody temperature (upper panel) and radius (lower panel). Right: luminosity of the blackbody component (upper panel) and the cut-off power law model component (lower panel) (Bałucińska-Church et al. 2010).

3.1.3 The changes of mass accretion rate along the Z-track

As the source moves from the soft apex along the Normal Branch, the luminosity of the cut-off power law component L_{cpl} (Fig. 3.2, right) increases by a factor of 1.3 - 2.7 (depending on the source) and becomes maximal at the hard apex - the point on the Z where X-ray intensity is maximal. Church et al. (2006) argued that such a substantial change, bearing in mind that the power law component contributes $\sim 80\%$ to L_{tot} at all times, is very unlikely to happen if \dot{M} decreases, as is assumed in the standard view that \dot{M} increases in the direction HB \rightarrow NB \rightarrow FB (Sect. 1.3.1). On the contrary, Church et al. (2006) suggested that the observed change of L_{cpl} implies that mass accretion rate increases in the direction soft apex \rightarrow hard apex, which does not support the standard view. Furthermore, they noticed that increased \dot{M} should result in increased temperature of the neutron star which was indeed observed. Fig. 3.2 (upper left panel) shows that in all Cyg-like sources the blackbody temperature increases along the Normal Branch by a factor of ~ 2 indicating heating of the neutron star (Church et al. 2006).

Between the hard apex and the left end of the Horizontal Branch, L_{cpl} decreases back to low values. The most natural interpretation is that mass accretion rate decreases and becomes low again at the left end of the HB (at a value close to that from the soft apex). This is consistent with X-ray intensity which decreases in this direction in all sources. Other model parameters (Church et al. 2006; Jackson et al. 2009; Bałucińska-Church et al. 2010), such as the column density and the energy of the emission line followed this trend supporting a view in which \dot{M} decreases in the direction: hard apex \rightarrow left HB.

However, the blackbody temperature continues to increase on this branch. In fact, it changes monotonically from the soft apex to the left end of the HB with increasing temperature and decreasing radius (Fig. 3.2, left panel). Church et al. (2006) discussed a possibility that \dot{M} does decrease as the source moves along the HB, but the effect is delayed in reaching the neutron star while already affecting the dominant Comptonization emission as the reduction in \dot{M} moves through the disk. They suggested that the delay could be related to the viscous timescale t_{visc} , which is of an order of hours, on which a disk annulus can drift radially inwards (Frank et al. 2002), such that any change in \dot{M} in the disk would reach the neutron star later. The estimated time spent by the source on the HB was comparable to t_{visc} (Church et al. 2006) making this scenario plausible. However, given the important role of the strong radiation pressure on the HB (below in Sect. 3.1.5), Church et al. (2006) noticed that the total luminosity may not well reflect the real changes in the mass accretion rate as part of the accretion flow may be diverted away from the system, such as in the form of jets.

During flaring, the luminosity of the Comptonized component is \sim constant (see Fig. 3.2, bottom right). Thus, following the same argument as above, it is most likely that the mass accretion rate is constant on the Flaring Branch, and hence the intensity flares observed are not accretion-powered, but correspond to unstable nuclear burning (Church et al. 2006) as discussed below.

3.1.4 The nature of flaring

Church et al. (2006) asked the question what the energy source responsible for flaring is in Cyg-like sources. From their fitting results with the Extended ADC model, they noticed that it is actually the blackbody component whose luminosity increases along the branch (Fig. 3.2, top right). During flaring, the blackbody temperature also increases, but not very strongly. In the same time, the blackbody radius changes slightly and is consistent with the whole neutron star emitting (Fig. 3.2, bottom left). In GX 340+0 there is evidence that emission radius expands beyond the surface of the neutron star and Church et al. (2006) found it to increase significantly from 10.8 ± 1.1 km to 16.1 ± 0.8 km along the branch. They noticed a similarity of this effect to the photospheric radius expansion occasionally observed during type I X-ray bursts (Sect. 1.4.1). Having noticed that flaring was native to the neutron star blackbody emission, the onset of flaring was compared with the theory of nuclear burning of Bildsten (1998) by calculating \dot{m} , the mass accretion rate per unit emitting area on the neutron star - the critical parameter in determining

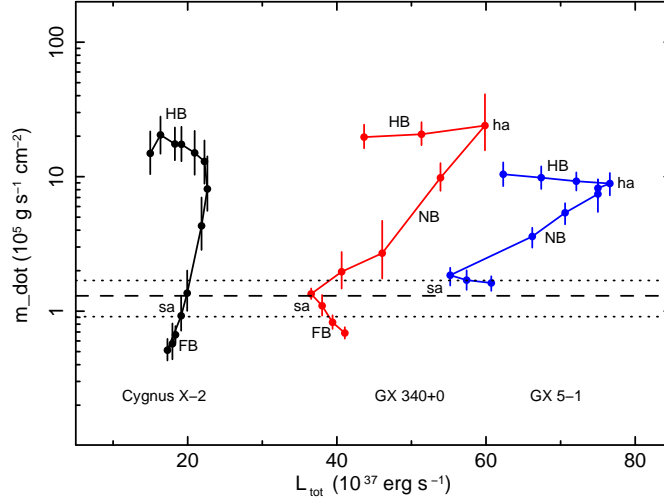


Figure 3.3: Mass accretion rate per unit emitting area (\dot{m}) versus the total (1 - 30 keV) luminosity. The horizontal dashed line marks the critical value of \dot{m}_{ST} for unstable nuclear burning, whereas the dotted lines its estimated 30% errors (Bałucińska-Church et al. 2010).

the stability of nuclear burning in the neutron star atmosphere. The values of \dot{m} were obtained via the total mass accretion rate \dot{M} derived from the total luminosity of the source using Eqn. 1.1 (Sect. 1.1) and divided by the emitting area $4\pi R_{bb}^2$ on the neutron star obtained from the spectral fitting. In this way changes of mass accretion rate per unit area, \dot{m} , along the Z-track were studied. The result for the three Cyg-like sources is shown in Fig. 3.3. On the upper Normal Branch and the Horizontal Branch, \dot{m} is high, well within the stable burning régime (Table 1.2 in Sect. 1.4.1). However, as the source descends the Normal Branch, \dot{m} reaches the critical level of $\dot{m}_{ST} = 1.3 \times 10^5 \text{ g cm}^{-2} \text{ s}^{-1}$ for unstable nuclear burning of helium in H/He rich environment. Based on this agreement with the theory, Church et al. (2006) proposed that flaring could be explained as nuclear burning on the surface of the neutron star. Moreover, the relation $\dot{m} \leq \dot{m}_{ST}$ met exclusively on the Flaring Branch explained why flaring occurred at this part of the Z-track only. It is noted here that the above definition of \dot{m} neglects possible systematic effects affecting the blackbody radius, and if the actual R_{bb} was underestimated as in the example discussed in Sect. 2.2.2, then $\dot{m} \propto R_{bb}^{-2}$ would be somewhat overestimated. Nonetheless, it should be stressed that the exact value of a possible modification is uncertain and also other effects, such as radiation pressure close to the neutron star, may play a role in determining the actual \dot{m} . However, it can be seen from Fig. 3.3 that any correction by a factor of a few would not undermine the above result, the Flaring Branch remaining well within the unstable burning régime and the upper parts of the Z-track above the critical threshold.

3.1.5 The importance of radiation pressure

The increase of the blackbody temperature along the Normal Branch by a factor of ~ 2 (from typically 1.2 keV at the soft apex to about 2.4 keV at the hard apex in the three sources) must lead to strong radiation pressure scaling as $\sim T^4$. Church et al. (2006) expressed the radiation pressure using the ratio of the observed blackbody flux per unit area ($f_{bb} = L_{bb}/4\pi R_{bb}^2$, based on spectral fitting results) to the Eddington flux ($f_{Edd} = L_{Edd}/4\pi R_*^2$, where R_* is the radius of the neutron star assumed to be 10 km and L_{Edd} is given by Eqn. 1.4). They argued that such a flux ratio better reveals local conditions at the neutron star, in contrast to the more typically used luminosity ratio (L_{bb}/L_{Edd}) which averages over the whole sphere as if observed by a distant observer. Also in this case, it is noted that the flux ratio defined above may not be literally correct due to possible modifications to the blackbody parameters (Sect. 2.2.2) and because the Eddington limit at the surface of the neutron star is actually larger than that from Eqn. 1.4 by the gravitational redshift factor. Nevertheless, the definition of Church et al. (2006) is definitely useful to approximately estimate the strength of the radiation pressure and as such will be used also later in this work without modification to allow a direct comparison with the previous results.

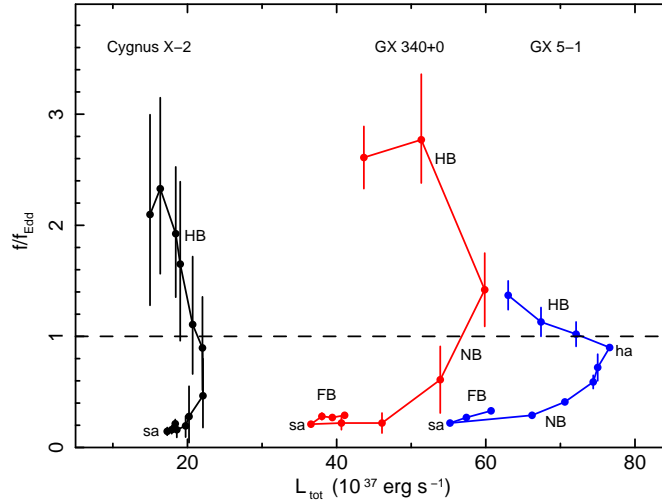


Figure 3.4: The ratio of the blackbody flux f_{bb} to the Eddington flux f_{Edd} at the surface of a neutron star with the 10 km radius versus the total 1 - 30 keV luminosity (Bałucińska-Church et al. 2010).

The left panel of Fig. 3.4 shows f_{bb}/f_{Edd} against the total (1 - 30 keV) luminosity as calculated from spectral fitting results obtained for the three Cyg-like sources by Church et al. (2006); Jackson et al. (2009) and Bałucińska-Church et al. (2010). The flux ratio is low ($f_{bb} < f_{Edd}$) when the source is close to the soft apex, but then increases quickly as the source moves towards the hard

apex where it becomes super-Eddington ($f_{bb} > f_{Edd}$) and increases further along the Horizontal Branch. Church et al. (2006) argued that strong radiation pressure very probably affects the inner accretion disk region and the proposed consequences of this are discussed below.

The reduction of the emission region size on the neutron star

As the source moves away from the soft apex along the Normal Branch, the blackbody radius becomes smaller than ~ 11 km as can be seen in Fig. 3.2, bottom left. At the hard apex, the measured blackbody radii were 2 - 7 km (depending on the source) and then stayed small on the Horizontal Branch (Church et al. 2006; Jackson et al. 2009; Bałucińska-Church et al. 2010). Church et al. (2006) interpreted this behaviour as a change of emission geometry from spherical (the whole neutron star emitting at the soft apex) into a narrow equatorial belt on the neutron star. They calculated the half-height h of the equatorial belt on the neutron star from Eqn. 2.2 using values of R_{bb} quoted above. It was found that at the hard apex, h was within 0.5 - 1.1 km in Cyg X-2 and GX 340+0, and ~ 3.7 km in GX 5-1.

Church et al. (2006) proposed a possible explanation of the equatorial belt formation based on the results of the survey of LMXB of Church & Bałucińska-Church (2001) whose work was discussed in Sect. 2.2.2. It was shown that for the sample of LMXB studied, the half-height h of the belt on the neutron star was equal to the half-height H of the inner accretion disk, the relation $h \approx H$ spanning three decades of source luminosity. This relation could be explained (Church et al. 2006) by one of the two models presented in Sect. 2.2.2. In the first model, there is an advective (radial) flow of matter from the full vertical extent of the inner accretion disk edge onto the neutron star leading directly to $h \approx H$. The second scenario, following from the theory of Inogamov & Sunyaev (1999), assumes that matter from the inner disk reaches the star at the equator and the boundary layer forms on the surface of the neutron star as an equatorial belt, whose h depends on \dot{M} . Then, as the half-height of the disk H also depends on the mass accretion rate, the relation $h \approx H$ is also met. Now, at high luminosities $L \sim L_{Edd}$ in the Cyg-like sources, close to the neutron star the height of the inner radiatively-supported disk H (Eqn. 1.16) is typically ~ 50 km. Church et al. (2006) suggested that plasma towering around the neutron star in the disk can hence be disrupted by the strong radiation pressure on the upper Normal Branch and the Horizontal Branch. Assuming the first of the scenarios mentioned above, the strong radiation pressure reduces H of the inner disk substantially and, based on the results of Church & Bałucińska-Church (2001), the emission region on the neutron star responds to this change forming the equatorial belt whose h becomes close

to the reduced H . Alternatively, in terms of the second scenario, the strong radiation pressure reduces the mass accretion rate that reaches the neutron star so that h , depending on \dot{M} , would also be reduced.

The launching of jets

As already mentioned in Sect. 1.4.2, Z-track sources are active in radio but predominantly in one of their spectral states only, i.e. on the Horizontal Branch. This is known to be related to ejection of plasma in jets (e.g. Hjellming et al. 1990a), yet their presence on one branch of the Z only has not been explained. Church et al. (2006), based on spectral fitting results with the Extended ADC model applied to GX 340+0, proposed that at the hard apex and on the Horizontal Branch plasma in the inner disk, disrupted by the strong radiation pressure, would be diverted into the vertical direction leading to the launching of jets, this agreeing with the Z-track position where jets are detected in the radio. They noted that additional evidence for the plasma release is given by changes of the column density which increases between the soft apex and the hard apex (Church et al. 2006). The same effect was observed in GX 5-1 (Jackson et al. 2009) and Cyg X-2 (Bałucińska-Church et al. 2010). Thus, it was proposed that strong radiation pressure in the vicinity of the neutron star is the mechanism for launching of jets (Church et al. 2006). Furthermore, as it was shown above, when the source ascends the Normal Branch and moves along the Horizontal Branch, the emission area on the neutron star is reduced to a narrow equatorial belt. Church et al. (2006) argued that with such a geometry there is a strong vertical component of the radiation pressure acting on the inner disk towering around the star, again favouring jet formation. The model of Church et al. (2006) explains also why jets are observed predominantly when the source is on the Horizontal Branch in the Cyg-like sources, as at other Z-track positions radiation pressure is low, and hence the inferred inner disk disruption, would be small.

The behaviour of the kHz QPO

On the Horizontal Branch of every Z-track source, two kHz QPO are observed with frequencies increasing along the branch towards the hard apex, but the explanation of this is unknown. Some theoretical models (Sect. 1.4.4) ascribe the upper kHz QPO as being related to the motion of matter close to the neutron star at a preferred radius, such as the Keplerian radius in the disk corresponding to a given QPO frequency.

Jackson et al. (2009) studied the behaviour of the two kHz QPO in GX 5-1. They used the same data selections for timing and spectral analyses to study any potential correlations between these. In particular, they were interested, if the kHz QPO (assuming their origin at the inner accretion disk) would show any effects related to the high radiation pressure on the Horizontal Branch, as the possible relation between the QPO and radiation pressure had been suggested by Church et al. (2006). To check this, Jackson et al. (2009) expressed the measured frequencies of the two kHz QPO in terms of their corresponding Keplerian radii of the orbital motion in the disk following

$$\nu = \frac{1}{2\pi} \sqrt{\frac{GM_*}{r^3}} \implies r = (GM_*)^{1/3} (2\pi\nu)^{-2/3}, \quad (3.1)$$

where: ν is a QPO frequency, G is the gravitational constant, M_* is the mass of the central star, and r is a radius in the disk. Next, the calculated radii were plotted against f_{bb}/f_{Edd} measuring the strength of radiation pressure as shown in Fig. 3.5.

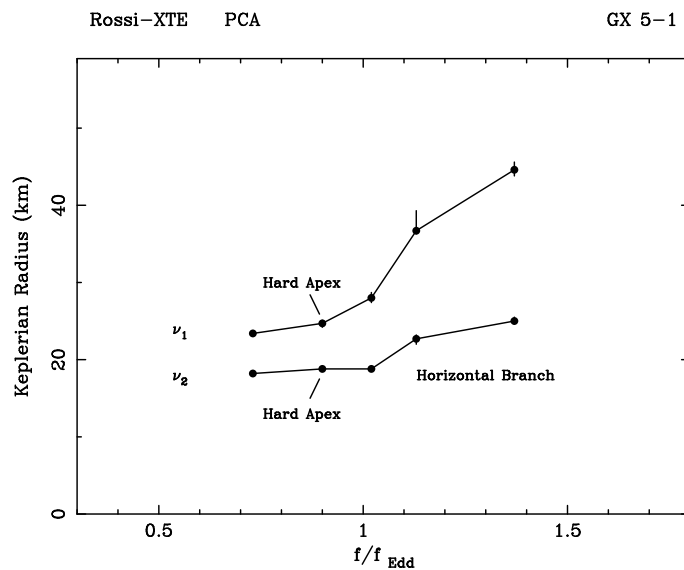


Figure 3.5: The Keplerian radii calculated from the frequencies of the two kHz QPO versus the ratio of the blackbody to the Eddington flux in GX 5-1 (Jackson et al. 2009).

Jackson et al. (2009) noticed that in GX 5-1 the radius corresponding to the upper kHz QPO, labelled ν_2 , is basically constant at about 18 km on the upper Normal Branch and then shows a sudden change when radiation pressure becomes super-Eddington ($f_{bb}/f_{Edd} \sim 1$) close to the hard apex. This was followed by a further increase of the Keplerian radius up to 25 km along the Horizontal Branch. It was proposed that the strong radiation pressure pushes the inner disk

away from the neutron star and leads to the oscillation frequency decreasing due to the increasing radius of the inner disk edge. This provides a very simple explanation of the upper kHz QPO. The lower kHz QPO followed the same pattern responding to changes in the upper QPO, but at larger radii in the range of 23 - 45 km. The nature of the lower kHz QPO is however less clear and the possible mechanism for its behaviour was not identified (Jackson et al. 2009). Jackson et al. (2009) argued that their results do not require the disk to be truncated in general, but that the truncation may occur on the upper Normal Branch and the Horizontal Branch due to the strong radiation pressure, but not elsewhere on the Z-track where $f_{bb}/f_{Edd} < 1$ and the disk is in contact with the neutron star. Their proposition would require no relation to e.g. the sonic radius as assumed by the beat-frequency models (Sect. 1.4.4).

The results of Jackson et al. (2009) suggested that the behaviour of the kHz QPO in GX 5-1 could be explained in terms of the model of Church et al. (2006). However, a similar study has not been done for the two remaining Cyg-like sources, for which only spectral investigations were carried out. Thus, part of this work presented in Chapter 4 is aimed at carrying out a combined spectral and timing study of Cyg X-2 and GX 340+0 following the method of Jackson et al. (2009).

3.1.6 The ADC and line emission

Church et al. (2006) noticed that, at least on the Normal Branch and the Horizontal Branch, the cut-off energy of the power law component E_{co} was correlated with the temperature of the neutron star blackbody kT_{bb} . This indicated a possible relation between the temperature of the neutron star and that of the ADC. Following e.g. Petrucci et al. (2001), for optically thick plasma, the electron temperature of the ADC is related to the cut-off energy by $3kT_e = E_{co}$. Church et al. (2006) argued that the observed shape of the knee at the cut-off energy of the Comptonized component suggested a single temperature in the ADC, and that any deviation from this, as one would expect if the electron temperature had a substantial gradient, has not been observed. They thus concluded that the ADC was isothermal and that E_{co} reflected a single electron temperature of the ADC.

In the case of GX 340+0, Church et al. (2006) calculated that the average ratio E_{co}/kT_{bb} was 2.49 ± 0.46 . This ratio was thus consistent with 3 which they interpreted as evidence that $kT_e \approx kT_{bb}$, i.e. that there is thermal equilibrium between the neutron star and the corona. A similar study of Jackson et al. (2009) in the case of GX 5-1 showed that in this source $E_{co}/kT_{bb} = 2.7 \pm 0.5$, again indicating an optically thick corona in thermal equilibrium with the neutron star.

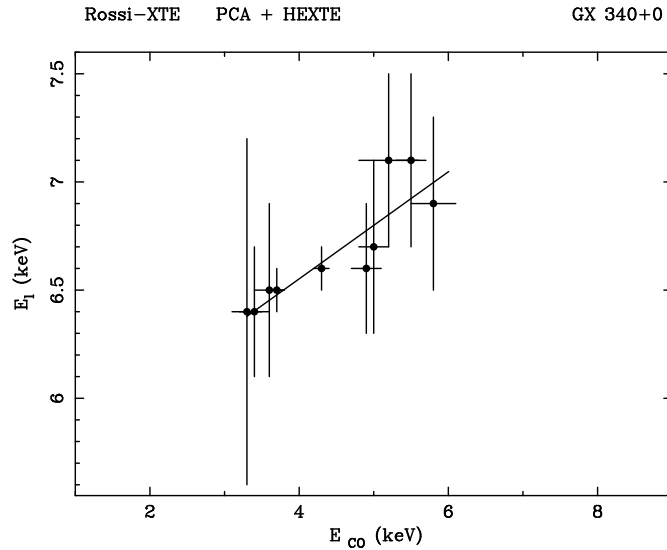


Figure 3.6: A correlation between the cut-off energy E_{co} and the centroid line energy E_l in GX 340+0. The linear fit has a slope of 0.25 ± 0.04 and the correlation coefficient is 0.985 (Church et al. 2006).

Moreover, Church et al. (2006) addressed the issue of the origin of the emission line of iron clearly visible in the spectrum of GX 340+0 between 6 and 7 keV. In their spectral results, Church et al. (2006) observed a correlation between E_{co} , being the measure of the electron temperature in the ADC, and the centroid line energy as depicted in Fig. 3.6. According to Church et al. (2006), the correlation observed provides evidence that the line is formed in the corona. The line energy was lowest at the soft apex and increased towards the hard apex, this interpreted as due to increase of the ionization parameter $\xi = \frac{L}{n r^2}$, where L is the luminosity of the illuminating central body, n is the plasma density and r is the distance from the central X-ray source (Tarter et al. 1969). The increase of the ionization parameter was thought to be caused by the changing geometry of the neutron star blackbody, from spherical emission at the soft apex into the equatorial belt on the upper NB and the HB concentrating irradiation towards the disk and the corona.

3.1.7 A summary of the model

The main points of the model of Church et al. (2006) for the Z-track in Cyg-like sources, can be summarized as shown in Fig. 3.7:

- The soft apex is a type of a quiescent state of a source at which the mass accretion rate is low. The neutron star accretes matter with its whole surface and its temperature is minimal. From this point the source moves along either the Flaring Branch or the Normal Branch.

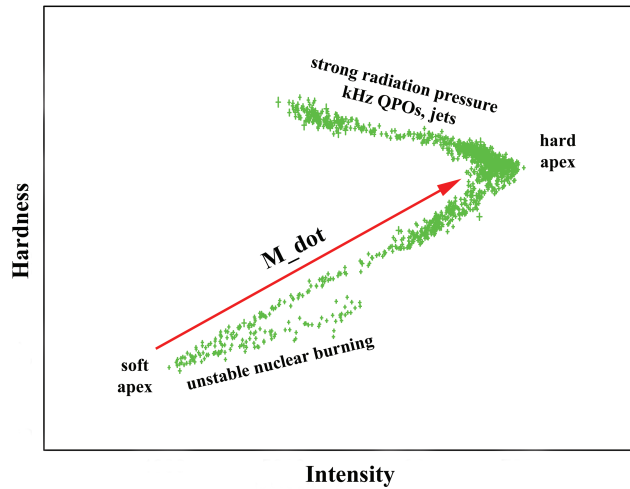


Figure 3.7: A schematic presentation of main physical properties of spectral branches in Cyg-like sources as obtained from spectral fitting with the Extended ADC model. The inferred direction in which mass accretion rate \dot{M} increases is marked with an arrow.

- A movement of the source along the Normal Branch is due to increasing mass accretion rate from the soft apex to the hard apex followed by an increase of the temperature of the neutron star.
- A movement along the Flaring Branch is not caused by changes in mass accretion rate which is constant. Flaring observed is powered by unstable nuclear burning of helium on the surface of the neutron star which begins when the source descends the Normal Branch and \dot{m} becomes less than \dot{m}_{ST} .
- Close to the hard apex, radiation pressure close to the neutron star becomes strong so that
 - the height of the inner disk becomes reduced or part of the mass accretion rate to the neutron star is diverted away, and in response to that, following respectively from the scenario of vertical spreading of matter on the neutron star of Inogamov & Sunyaev (1999) or the scenario involving an advective flow between the inner disk and the neutron star, the emission region on the neutron star contracts to an equatorial belt.
 - the strong radiation pressure acts on the inner disk diverting plasma into the vertical direction, this corresponds to increased absorption observed and is the necessary condition for the launching of jets observed in radio particularly on this part of the Z.
 - the inner disk truncation leads to the formation of the kHz QPO, whose frequencies then decrease along the HB with increasing radiation pressure pushing the inner disk edge away from the neutron star.

3.2 The Cyg X-2 like Z-track sources

3.2.1 GX 340+0 (4U 1642-45)

GX 340+0 was discovered by Friedman et al. (1967) using Geiger counters on-board *Aerobee* rockets. A rough fit to the spectrum of the source with a blackbody by Margon et al. (1971) revealed an emitter radius of 8 km providing evidence that the compact object was probably a neutron star. A distance to the source of 11.0 ± 3.3 kpc was estimated by Fender & Hendry (2000) from radio measurements. Their result was consistent with the upper limit obtained by Christian & Swank (1997) in their LMXB survey with *Einstein* who assumed all Z-track sources radiate at the Eddington limit, although this clearly disregards luminosity changes that may be factor of two.

GX 340+0 was classified as a Z-track source by Hasinger & van der Klis (1989). Evidence for secular intensity shifts in GX 340+0, similar to those observed in Cyg X-2, was reported by Kuulkers & van der Klis (1996) who also found different slopes of the Horizontal Branch in HID/CCD in separate observations of the source.

The radio counterpart was found by Penninx et al. (1993) using *VLA* at 1.4 and 4.8 GHz. They interpreted its spectrum as synchrotron emission with a power law index of 1.0. Radio properties of the source were studied by Oosterbroek et al. (1994) using the *VLA* simultaneously with an X-ray observation with *Ginga*. They found that radio was strongest and most variable when the source was on the upper Normal Branch and the Horizontal Branch. The accurate radio position (Penninx et al. 1993) allowed for a detection of the infrared counterpart by Miller et al. (1993) revealing a ~ 17.3 magnitude star in the K band.

A broadband *BeppoSAX* study of GX 340+0 was performed by Iaria et al. (2006). They examined the behaviour of the source around the Z-track by selecting only three regions (HB, upper and lower NB) from the colour-colour diagram. They used the Eastern model consisting of an absorbed blackbody and a Comptonization component CompTT (Titarchuk 1994). The blackbody was interpreted as emission from the inner accretion disk, that was approaching the neutron star as the source was descending the Normal Branch (Iaria et al. 2006). At the same time, the electron temperature of the Comptonizing cloud, which Iaria et al. (2006) interpreted as a spherical corona around the neutron star, was typically ~ 3 keV. The spectral modelling of Lavagetto et al. (2004) and Iaria et al. (2006) required an additional power law (“hard tail”) with the photon index of 2.5 on the Horizontal Branch which they interpreted as possible emission from a synchrotron jet.

However, the feature seems to be seen when the Eastern model is used and may not be real.

Church et al. (2006) proposed a model for the Z-track in GX 340+0 using data from *RXTE*. Their results and the model were discussed in detail in Sect. 3.1. They found that the blackbody temperature was minimal (~ 1.25 keV) at the soft apex where the blackbody radius was ~ 11 km suggesting emission from the whole surface of the neutron star. The temperature then increased to over 2.4 keV on the HB causing strong radiation pressure ($\sim T_{bb}^4$) likely to disrupt plasma at the inner disk and lead to the launching of jets. This would explain why radio was strongest on this part of the Z as found by Oosterbroek et al. (1994). The blackbody radius decreased along the NB and remained small on the HB at about 3 km which was interpreted as emission from an equatorial belt on the neutron star. The change of the power law component by a factor of ~ 2 between the soft apex and the hard apex was interpreted as an increase of mass accretion rate along the Normal Branch. Flaring was found related to the blackbody only and proposed to be unstable nuclear burning on the neutron star, an equivalent of X-ray bursts seen in less luminous sources.

The presence of an emission line which had a centroid energy of 6.7 keV in the spectrum of GX 340+0 was reported by van Paradijs et al. (1988a). The energy of the line increased between the soft apex and the hard apex (Iaria et al. 2006; Church et al. 2006) which was consistent with the suggestion of Church et al. (2006) that mass accretion rate increases in this direction. In an *XMM-Newton* observation of GX 340+0, D’Ai et al. (2009) observed the iron line to have asymmetric shape which they interpreted as deformation by the Keplerian movement and relativistic effects in the inner disk.

Studies of timing features around the Z-track of GX 340+0 were performed by van Paradijs et al. (1988a); Hasinger & van der Klis (1989); Penninx et al. (1991) and Kuulkers & van der Klis (1996) with *EXOSAT*. A 5.6 Hz NB QPO and noise components (LFN, VLFN) were discovered by van Paradijs et al. (1988a). A (32 - 50 Hz) HB QPO was discovered by Hasinger & van der Klis (1989) on the Horizontal Branch and further studied by Penninx et al. (1991).

High frequency kHz QPO were discovered by Jonker et al. (1998) with *RXTE*. They found the frequency of the lower QPO to change from 247 Hz to 625 Hz along the Horizontal Branch. At the same time, the frequency of the upper kHz QPO was increasing in the range of 567 Hz - 820 Hz. The separation between the two kHz QPO was measured to be 339 ± 8 Hz and constant (Jonker et al. 1998). Jonker et al. (1998) noticed that the lower QPO was narrower than the upper

QPO, opposite to the prediction of the beat-frequency models. Moreover, the test of the expected quadratic relation between frequencies of the HB QPO and the upper kHz QPO predicted by the relativistic precession model (Sect. 1.4.4), implied an unphysical ratio of the moment of inertia to the mass of the neutron star (Jonker et al. 1998).

3.2.2 Cyg X-2 (4U 2142+38)

Cygnus X-2 is one of the best studied Low Mass X-ray Binaries. Like GX 340+0, it was discovered with *Aerobee* rockets carrying Geiger counters (Bowyer et al. 1965). Giacconi et al. (1967) identified its optical counterpart with a variable 15th magnitude star V 1341 Cygni. Studies of luminosity-sensitive lines in the optical spectrum suggested that the companion was an F-type giant (Cowley et al. 1979). Optical line variability and lightcurve modulation revealed an orbital period of $9^d.8445$ and a distorted shape of the Roche-lobe filling $\leq 0.7 M_{\odot}$ donor (Cowley et al. 1979; Casares et al. 2010). Orosz & Kuulkers (1999) found that the system inclination and a neutron star mass were $62.5 \pm 4^{\circ}$ and $1.78 \pm 0.23 M_{\odot}$, respectively. Distance measurements are quite spread in the range 6.1 - 13 kpc (Cowley et al. 1979; Smale 1998; Orosz & Kuulkers 1999; Galloway et al. 2008).

Cyg X-2 was classified as a Z-track source by Hasinger & van der Klis (1989). A multiwavelength campaign on the source was conducted in 1989/1990 in the X-ray (Hasinger et al. 1990), UV (Vrtilek et al. 1990), radio (Hjellming et al. 1990a) and optical (van Paradijs et al. 1990a) bands. The UV continuum and optical/UV emission line strength (Vrtilek et al. 1990; van Paradijs et al. 1990a) increased in the direction HB \rightarrow NB \rightarrow FB, which was supposed to follow increasing \dot{M} despite apparent decrease of X-ray flux on the Normal Branch (Hasinger et al. 1990). Radio-quiet states were found to correspond to the lower NB and the FB, while radio-loud ones to the upper NB and the HB (Hjellming et al. 1990a). The high brightness temperature and the variability of radio emission indicated the presence of compact, synchrotron radiating jets in the source (Hjellming et al. 1990a).

The source shows substantial intensity variations, which cause its Z-track to shift and change shape in hardness-intensity. Kuulkers & van der Klis (1996) defined low, medium and high overall intensity states but did not find any clear periodicity of such secular changes. Wijnands et al. (1997) noticed that the source moved smoothly between the states, without intensity jumps. Possible scenarios to explain secular motion were proposed (e.g. long-term changes in mass accretion rate, disk precession), but the problem has not yet been resolved.

Cyg X-2 is one of the two Z-track sources (with GX 17+2) to exhibit type I X-ray bursts. Kahn &

Grindlay (1984), from the best blackbody fit to the burst spectrum, derived temperatures in the range 1.2 - 2.5 keV and a peak burst luminosity of 1.4×10^{38} erg s⁻¹, thus close to the Eddington limit for a $1.4M_{\odot}$ neutron star. In a study of a sample of bursts in *EXOSAT* data, Kuulkers et al. (1995) measured blackbody radii of ~ 10 km confirming the origin of bursts on the surface of the neutron star. It was suggested (Kuulkers et al. 1995) that the occasional bursting was due to unstable burning of helium, which is consistent with the short ~ 2 s burst duration (Galloway et al. 2008).

The X-ray continuum of Cygnus X-2 observed with *EXOSAT* was studied by Hasinger et al. (1985) using the CompST model of Sunyaev & Titarchuk (1980) and a blackbody. The blackbody was interpreted as emission from the boundary layer, whereas the harder component corresponded to $kT_e \sim 3$ keV Comptonizing plasma.

Hasinger et al. (1990) observed Cyg X-2 with *Ginga* during their multiwavelength campaign testing the Western model and the Eastern model along the Z-track. In the case of the Western model, the blackbody originating from the neutron star/boundary layer had a temperature between ~ 1.06 keV at the soft apex and ~ 1.4 keV on the Horizontal Branch and the Flaring Branch. The cut-off energy of the power law component, associated with emission from an inner disk corona, stayed in the range 4 - 6 keV with a minimum at the soft apex (Hasinger et al. 1990). In the Eastern model, emission from the disk was represented by a disk blackbody, whereas a simple blackbody corresponded to emission from the neutron star. In the scenario of Hasinger et al. (1990), as the source moves from the HB towards the FB, the mass accretion rate increases and the thin disk changes into a thick torus engulfing the neutron star and its magnetosphere explaining the intensity drops observed in flaring and also reduction in QPO/noise variability observed.

Many spectral studies were performed on a basis of the Eastern model (e.g. Done et al. 2002). A broad-band (0.1 - 200 keV) analysis with *BeppoSAX* was performed by Di Salvo et al. (2002) using a model composed of a disk blackbody and CompTT. On the Horizontal Branch, they needed to add a power law component with a photon index of ~ 2 to fit a hard excess at energies > 25 keV. The same feature was observed in GX 17+2 (Di Salvo et al. 2000) and interpreted as emission from a radio jet. However, the presence of such a tail was not confirmed by Lavagetto et al. (2006) using *INTEGRAL* in the 3 - 100 keV energy range.

Recently, Bałucińska-Church et al. (2010) applied the Extended ADC model to a set of *RXTE* spectra along the Z-track of Cygnus X-2 and found their results consistent with the physical explanation of the Z-track of Church et al. (2006) (Sect. 3.1). Their results implied that at

the soft apex the neutron star had a low temperature (~ 1.19 keV) and accreted with its whole surface. Then, along the Normal Branch and the Horizontal Branch, the emission region on the neutron star was reduced to an equatorial belt, while its temperature increased to almost 2.4 keV. In consequence, radiation pressure scaling as T_{bb}^4 was strong on the HB (Bałucińska-Church et al. 2010). Based on the observed increase of the luminosity of the dominant power law model component on the NB, they concluded that \dot{M} increases between the soft apex and the hard apex, thus in the opposite direction to that proposed by Vrtilik et al. (1990). Moreover, based on the comparison of calculated \dot{m} with the theory of Bildsten (1998), Bałucińska-Church et al. (2010) proposed that flaring was most likely related to unstable nuclear burning.

Bałucińska-Church et al. (2011) observed Cygnus X-2 with *XMM-Newton* as part of their multi-wavelength campaign in X-ray, optical and radio. In that observation, the source remained at the soft apex and exhibited $\sim 25\%$ intensity reductions that would have been commonly attributed to flaring. However, the spectral analysis with the Extended ADC model revealed that what was observed was not flaring but dipping (Bałucińska-Church et al. 2011). Fitting at several stages of dipping showed a progressive coverage of the ADC by a neutral absorber of increasing column density. It was argued that dipping in Cyg X-2 was often (e.g. Hasinger et al. 1990) misinterpreted as flaring. The confusion is a result of using colour-colour diagrams only, in which dipping and flaring look very similar, but can be distinguished when using hardness-intensity diagrams (Gibiec et al. 2011).

The spectrum of Cygnus X-2 often shows a clear emission line between 6 and 7 keV. Hirano et al. (1986) measured a line energy of 6.7 keV with an equivalent width of ~ 30 eV consistent with emission of Fe XXV originating from plasma above an irradiated accretion disk. A more recent study of Schulz et al. (2009) with *Chandra* revealed a number of emission lines, mostly H-like and He-like species of Fe, Al, S, Si, Mg and Ne. High ionization and Doppler broadening of these lines suggested their origin in the extended (up to 10^{10} cm), dense and hot ($> 10^6$ K) accretion disk corona whose size was in agreement with that obtained by Church & Bałucińska-Church (2004) by dip ingress timing in LMXB.

The Horizontal Branch QPO and the Low Frequency Noise (below 15 Hz) in Cygnus X-2 were discovered by Hasinger et al. (1986). The frequency of the HB QPO was increasing in the range 18 - 45 Hz with increasing intensity (Hasinger 1987). Another QPO at ~ 5 Hz was discovered by Norris & Wood (1987) when the source was on the Normal Branch. The NB QPO was found to coexist with the HB QPO when the source was on the upper Normal Branch, proving that the

two phenomena have different origins (Hasinger et al. 1990). There was also limited evidence that it survived a transition onto the Flaring Branch forming a 10 Hz FB QPO (Hasinger et al. 1990). Wijnands et al. (1998), using *RXTE* data, discovered the two simultaneous kHz QPO in the range 530 - 1007 Hz when the source was on the Horizontal Branch.

3.3 Sco X-1 like Z-track sources

3.3.1 Sco X-1 (H 1617-155)

Giacconi et al. (1962) discovered Scorpius X-1 as the first and the brightest extrasolar X-ray source in the sky. The optical counterpart of the source was discovered by Sandage et al. (1966) as a blue $V \sim 13$ magnitude star V 818 Scorpi. Many subsequent, often multiwavelength studies have been conducted since then (e.g. Mook et al. 1975; Willis et al. 1980; Petro et al. 1981). The source was most optically/X-ray variable during optically bright states (Mook et al. 1975; Petro et al. 1981). Optical photometry of Gottlieb et al. (1975) and spectroscopy of Cowley & Crampton (1975) revealed an orbital period of $18^h.9$. The optical spectrum of the object is dominated by broad H/He lines, thought to originate from the accretion disk, and narrow C III/N III lines, probably from the X-ray heated face of the companion (Crampton et al. 1976; LaSala & Thorstensen 1985; Schachter et al. 1989; Steeghs & Casares 2002). The distance of the source of 2.8 ± 0.3 kpc comes from the trigonometric parallax measurement with the *VLBA* by Bradshaw et al. (1999). The binary system, whose inclination is $\sim 38^\circ$ consists of a neutron star and a $\sim 0.4M_\odot$ companion which is probably an evolved sub-giant (Fomalont et al. 2001b; Steeghs & Casares 2002). Based on the accurate results of Bradshaw et al. (1999) and Steeghs & Casares (2002), the Galactic orbit was calculated (Mirabel & Rodrigues 2003) indicating a probable origin of this LMXB in the Galactic halo/globular cluster.

The source has long been known (e.g. Bradt et al. 1975; Canizares & Neighbours 1975) to exhibit two spectral states, quiescent and active (flaring). Priedhorsky et al. (1986) suggested that the transition between the quiescent and the active state corresponds to the change between optically faint and bright states (also Augusteijn et al. 1992). The two states were identified as the Normal and the Flaring Branches of the Z-track, respectively (Hasinger 1987). The third, Horizontal Branch was found by Hasinger & van der Klis (1989) but is seldom traced by the source.

The radio counterpart was detected by Ables (1969) and studied on several occasions later (Hjellming & Wade 1971; Hjellming et al. 1990b). The radio-quiet and radio-loud states were identified

with the Flaring Branch and the Normal/Horizontal Branch, respectively (Hjellming et al. 1990b), thus radio is generally anti-correlated with optical emission. Fomalont et al. (2001b) discovered radio jets in Sco X-1 with the *VLBI* at 1.7 and 5 GHz. Plasma ejecta moving symmetrically away from the radio core with an average speed of $0.45c$ were observed, the situation repeating every 1 - 2 days (Fomalont et al. 2001b). By correlating variability patterns in the ejecta and the radio core after a delay, a velocity of $\geq 0.95c$ was obtained for the energy transfer into the jet (Fomalont et al. 2001a).

The *EXOSAT* spectrum of Sco X-1 was studied by White et al. (1985) using a model composed of blackbody and Comptonization terms. A ~ 6.7 keV emission line was reported by Suzuki et al. (1984) and White et al. (1985) who identified it with Fe XXV originating from the X-ray heated corona. The Eastern model was successfully fitted to *Tenma* data by Mitsuda et al. (1984) who also recognized the variability of the blackbody component in flaring. However, the model could not be fitted to *EXOSAT* data (White et al. 1985). A hard (30 - 200 keV) power law component in the spectrum of Sco X-1 was reported by Strickman & Barret (2000), D'Amico et al. (2001), Di Salvo et al. (2006) and D'Aí et al. (2007). The component was correlated with X-ray states, being weakest on the FB, and interpreted as of probably non-thermal origin as no high-energy cut-off could be measured (Di Salvo et al. 2006; D'Aí et al. 2007). Barnard et al. (2003) analysed the source in terms of the Extended ADC model. They noticed that both blackbody and power law luminosity decreases as the source descends the Normal Branch which suggests that mass accretion rate does not increase in this direction, in contrast to many other claims (e.g. Vrtilik et al. 1991; Hertz et al. 1992). In flaring, the blackbody radius increased to almost 10 km supporting the origin of the blackbody component on the neutron star. Moreover, the cut-off energy of the power law component increased on the Flaring Branch interpreted as possible additional heating of the ADC by flares.

The source has been broadly studied in terms of its time variability. The ~ 6 Hz NB QPO was discovered on the lower Normal Branch (Middleditch & Priedhorsky 1985; Priedhorsky et al. 1986; Dieters & van der Klis 2000). On the Flaring Branch, the 10 - 20 Hz FB QPO was detected (Priedhorsky et al. 1986), but visible on the lower part of the branch only (Hertz et al. 1992). The kHz QPO were discovered by van der Klis et al. (1996) between 800 and 1130 Hz and, unlike in other Z-track sources, along the whole Normal Branch. A 45 Hz QPO with its second harmonic were seen on the NB and interpreted as equivalent to the known HB QPO in other Z-track sources. As found by van der Klis et al. (1997), the kHz QPO separation was not constant, but

varied between 310 and 230 Hz as frequencies of the QPO were increasing. They concluded that the beat-frequency models are unlikely to explain the kHz QPO in Sco X-1.

3.3.2 GX 17+2 (4U 1813-14)

GX 17+2 was discovered by rocket missions as a bright X-ray source in the highly absorbed Galactic bulge region (Friedman et al. 1967). Accurate coordinates are quoted by Ebisawa et al. (2003) and Liu et al. (2007). The distance to the source is estimated at ~ 7.5 kpc (5.6 - 10.4 kpc) (Tananbaum et al. 1971; Penninx et al. 1988; Kuulkers et al. 2002; Galloway et al. 2008).

The radio counterpart of GX 17+2 was discovered by Hjellming & Wade (1971) who detected it as a variable radio source resembling Sco X-1. A clear correlation between radio and X-ray spectral states was found by Penninx et al. (1988) who observed the radio flux to increase by an order of magnitude as the source was moving from the Flaring Branch to the Horizontal Branch. Simultaneous radio and X-ray observations were also performed by Migliari et al. (2007) who showed that periods of strongest radio emission on the HB were accompanied by the presence of a hard tail required in their modelling of the X-ray spectrum above ~ 30 keV suggesting (if the presence of the hard tail is confirmed) a common production mechanism for the jet and hard X-ray emission.

Many attempts have been made to find the optical counterpart of GX 17+2 (Blanco et al. 1968; Kunkel et al. 1970; Tarengi & Reina 1972; Hoag & Weisberg 1976; Davidsen et al. 1976); their results, however, were ambiguous. The search was only successful in the infrared after the observations of Deutsch et al. (1999) and finally Callanan et al. (1999, 2002) showing a very probable 15 magnitude (K band) counterpart close to a normal star NP Ser. IR emission was interpreted as of synchrotron nature based on extrapolation of the radio spectrum giving a K band brightness consistent with that measured (Callanan et al. 2002). This was supported by the lack of correlation between IR and soft X-rays that would have been expected from X-ray reprocessing (Callanan et al. 2002). More recently, Bornak et al. (2009) reported bright IR episodes occurring every 3 days and lasting about 4 hours interpreted as due to jet precession.

First reports of X-ray bursts in GX 17+2 come from Oda et al. (1981). With a typical risetime of ~ 1 s and decays over ~ 10 s, they were regarded as type I X-ray bursts. However, several peculiar bursts with very long durations of several minutes were observed by Tawara et al. (1984) arguing that their classification was not obvious. Both types of bursts, short and long, were observed by Sztajno et al. (1986). They performed a detailed spectral study testing several fitting

techniques. Burst spectra were found to be well fitted with a simple blackbody which was also present in persistent emission from the neutron star (Sztajno et al. 1986). Long bursts, in contrast to more typical short ones, were found not to show radius expansion implying emission below the Eddington limit. A slow energy release or additional geometric effects were thought to be responsible for their unique properties (Sztajno et al. 1986). Kuulkers et al. (2002) analysed a sample of bursts observed with *RXTE* and found that their occurrences were not correlated with any particular X-ray spectral state on the Z-track and thus presumably not with mass accretion rate (assuming the standard view that \dot{M} increases in the direction HB \rightarrow NB \rightarrow FB).

In a spectral analysis using *EXOSAT*, the spectrum of GX 17+2 revealed the presence of an emission line at 6.7 keV of ionized iron, most likely Fe XXV, whose width ($\sigma \sim 0.7$ keV) suggested (Ercan 1988) broadening by Comptonization. Ercan (1988) argued that other possible broadening mechanisms (Doppler or relativistic smearing) would only work close to the neutron star where very high ionization would not allow for line emission. Langmeier et al. (1990) performed a spectral analysis along the Z-track of GX 17+2 using a model composed of a blackbody and a cut-off power law and found that the latter dominated on the Horizontal Branch, whereas the blackbody radius was close to 10 km suggesting an origin on the neutron star.

A broadband analysis was performed by Di Salvo et al. (2000) using *BeppoSAX* with the Eastern model revealing an emission line at 6.7 keV and an absorption edge at 8.5 keV corresponding to ionized species of iron XXIII - XXV. The blackbody radius was of about 45 km and thus interpreted as emission from the inner accretion disk (Di Salvo et al. 2000). The CompTT model assumed 1 keV seed photons from the neutron star Comptonized in a ~ 3 keV plasma around it. On the Horizontal Branch the spectral model of Di Salvo et al. (2000) required an additional power law component with a photon index of 2.7 to fit a hard tail above 30 keV (also Piraino et al. 2004; Farinelli et al. 2005, 2007). The tail faded as the source was moving down the NB (Di Salvo et al. 2000). Piraino et al. (2004) discussed possible origin of this hard component considering a hybrid thermal/non-thermal plasma, bulk motion Comptonization or scattering off a synchrotron jet as candidates. It should, however, be stressed that the feature may be model-dependent.

First detections of QPO came with *EXOSAT* observations of Stella et al. (1987a) who found a 7 Hz QPO on the Normal Branch and a 24 - 28 Hz HB QPO on the Horizontal Branch. KHz QPO were discovered with *RXTE* by Wijnands et al. (1997). The upper QPO frequency changed between ~ 645 Hz and ~ 1087 Hz along the HB, whereas the lower QPO frequency had a frequency in the range 480 - 781 Hz. Wijnands et al. (1997) noticed that the simultaneous detection of the HB

QPO and kHz QPO meant that at least one of these phenomena could not be explained by the magnetospheric beat-frequency model.

3.4 Atoll sources

3.4.1 2S 0918-549 (4U 0919-54)

2S 0918-549 has been observed by many missions since its first appearance in the *Uhuru* catalogue (Forman et al. 1978). The counterpart of the source was identified to be a $V = 21$ magnitude star by Chevalier & Ilovaisky (1987) who estimated the distance to the source in the range 2 - 15 kpc, but favoured the upper limit. The L_X/L_{opt} ratio of ~ 800 indicated that it was a Low Mass X-ray Binary. Zhong & Wang (2011) found a sinusoidal 0.014 magnitude modulation in the optical lightcurve of 2S 0918-549 which they interpreted as the orbital period of 17.4 minutes suggesting an ultracompact binary and attributed the optical maximum to the superior conjunction of the companion heated by the central X-ray source. They estimated the companion mass to be 0.024 - 0.035 M_\odot and the inclination to be 10° (almost face-on).

Juett & Chakrabarty (2003) studied 2S 0918-549 using *Chandra* and *XMM-Newton*. Having investigated the depths of absorption edges in the spectrum, they found that the Ne/O ratio of 0.52 was about 3 times higher than in the interstellar medium and favoured the interpretation that Ne-rich material was local to the system, probably from the mass donor. Juett et al. (2001) pointed out that 2S 0918-549 shares this feature with 4U 0614+091 and 4U 1543-624 that are ultracompact systems suggesting a common type of a donor star for this group. Nelemans et al. (2004) reported a lack of strong spectral lines of hydrogen and helium, and only weak and inconclusive lines of carbon and oxygen. They suggested that the companions of ultracompact systems were carbon-oxygen white dwarfs. However, observations of type I X-ray bursts in 2S 0918-549, lasting 10 - 100 seconds, implied a mixed H and He accreted matter (Juett & Chakrabarty 2003).

X-ray bursts in 2S 0918-549 were discovered by Jonker et al. (2001) in *RXTE* data and by Cornelisse et al. (2002) using *BeppoSAX* leading to distance estimates of 4.2 - 4.9 kpc. These values are consistent with later estimates of in't Zand et al. (2005) and Galloway et al. (2008) of 4.0 - 5.4 for H-rich and H-poor burst fuel, respectively, so close to the lower limit of the range given by Chevalier & Ilovaisky (1987). A very long burst, lasting almost half an hour, was observed by in't Zand et al. (2005) with *BeppoSAX* when the source was in a very low state. They concluded that the burst must have been due to a long period of helium accumulation and favoured a helium

white dwarf companion.

Markert et al. (1979) found that the continuum spectrum of 2S 0918-549 was hard and not very absorbed. Cornelisse et al. (2002) could fit the spectrum of the source with a single cut-off power law model. In more recent observations with *Chandra* and *XMM-Newton* (Juett & Chakrabarty 2003) and *BeppoSAX* (in't Zand et al. 2005) the spectrum of the source was best described by a combination of a blackbody and a power law. A high temperature of 34_{-17}^{+110} keV of the Comptonizing plasma was obtained by in't Zand et al. (2005) with a model composed of a blackbody and CompTT.

The observation of Jonker et al. (2001) led to the discovery of a single kHz QPO at 1156 Hz when the source was in the Lower Banana Branch. The lack of another (lower) kHz QPO was consistent with the general finding of van der Klis (2000) that this is not observed when the frequency of the upper kHz QPO is above ~ 900 Hz. Jonker et al. (2001) also showed that the low frequency power spectrum was typical of an Atoll source and dominated by noise components (VLFN and HFN).

3.4.2 4U 1636-536 (Norma X-1)

The source 4U 1636-536 was first observed by Giacconi et al. (1974) with *Uhuru* and Willmore et al. (1974) with *Copernicus*. The optical counterpart of the source, V 801 Arae, was identified by McClintock et al. (1977) as a faint ~ 18 magnitude blue object. An orbital period of $3^h.8$ was found by Pedersen et al. (1981) and confirmed by Smale & Mukai (1988) and van Paradijs et al. (1990b). Such a period suggested a $\sim 0.36 M_{\odot}$ companion star whose face was thought to be responsible for X-ray reprocessing which could explain the optical modulation observed (Smale & Mukai 1988; Casares et al. 2006).

4U 1636-536 was classified as an Atoll source by Hasinger & van der Klis (1989) and the colour-colour and hardness-intensity pattern of the source was found to exhibit secular shifts (Di Salvo et al. 2003). The state transitions in the source were found to occur on a timescale of about a month (Shih et al. 2005; Belloni et al. 2007; Shih et al. 2011) overlaid on a long-term decline of X-ray intensity of the source that started in 2000 (Shih et al. 2005). Intensity variations in soft (1.5 - 12 keV) X-rays were found anti-correlated with variations in hard (> 14.5 keV) X-rays (Shih et al. 2005; Farrell et al. 2009) and interpreted as recurrent variations in the contribution from, respectively, the accretion disk and the inner corona (Shih et al. 2011) or jet formation (Farrell

et al. 2009). Shih et al. (2011) also noticed that the optical flux follows the soft X-ray count rate, which fits into the disk-reprocessing scenario (e.g. van Paradijs & McClintock 1994) for optical emission in LMXB.

The source is foremost a well-studied X-ray burster (Swank et al. 1976; Hoffman et al. 1977). The bursts (~ 5 per day) are characterized by a fast 1 s risetime and a 10 - 20 s decay phase consistent with thermonuclear flashes of helium (Turner & Breedon 1984). Burst profiles and peak fluxes vary significantly between bursts, but the blackbody radii during decay phases all give typically ≤ 10 km, consistently with the theoretical neutron star radius (Ohashi et al. 1982). Simultaneous visual/X-ray observations revealed that optical bursts are delayed with respect to X-ray bursts by < 3 s and have smeared profiles interpreted as reprocessing in the accretion disk (Pedersen et al. 1982; Lawrence et al. 1983; Matsuoka et al. 1984; Truemper et al. 1985; Turner et al. 1985). Burst durations and temperatures correlated well with the X-ray spectral state of the source and its timing properties, all these quantities being related to the mass accretion rate (van der Klis et al. 1990). Some of the bursts were found to be quite unusual, with either multiple-peak profiles (Sztajno et al. 1985; van Paradijs et al. 1986; Zhang et al. 2009) or several hour-long durations (Wijnands 2001). Based on *RXTE* observations of many type I X-ray bursts, some of which showed photospheric radius expansion at the Eddington limit, (Galloway et al. 2006, 2008) determined the distance to 4U 1636-536 of 6.0 ± 0.5 kpc.

The *EXOSAT* spectrum of 4U 1636-536 could be well fitted with a cut-off power law (Breedon et al. 1986; Vacca et al. 1987) but could not be fitted with the Eastern Model (Vacca et al. 1987). A broadband study of 4U 1636-536 was performed by Fiocchi et al. (2006) with *BeppoSAX* and *INTEGRAL*. They could fit the spectra with a model composed of one or two blackbodies plus Comptonization showing that the state transition from the soft to the hard branch was related mainly to an increase (from about 3.4 keV up to 23 keV) of the electron temperature of the Comptonization component. Pandel et al. (2008) used *RXTE* and *XMM-Newton* and interpreted the emission line of iron between between 3 and 9 keV as asymmetric due to relativistic broadening in the inner accretion disk.

The low frequency power spectrum of 4U 1636-536 is typical to an Atoll source (Hasinger & van der Klis 1989; Prins & van der Klis 1997). The kHz QPO were discovered by Zhang et al. (1997) (the lower kHz QPO) and Wijnands et al. (1997) (both kHz QPO). When the two kHz QPO were detected simultaneously, they had frequencies of 890 - 920 Hz (lower QPO) and 1150 - 1193 Hz

(upper QPO), with a separation of $\Delta\nu \sim 276$ Hz (Wijnands et al. 1997) or $\Delta\nu \sim 323$ Hz when mass accretion rate in the source was low (Jonker et al. 2002). The spin frequency ($\nu_s = 582$ Hz) of the neutron star in 4U 1636-536 was discovered as burst oscillations by Zhang et al. (1997) and observed later by Strohmayer et al. (1998a) and Strohmayer & Brown (2002). As $\Delta\nu$ is neither close to ν_s , nor to $\nu_s/2$, this was found inconsistent (Mendez et al. 1998; Strohmayer & Brown 2002) with the beat-frequency interpretation of QPO.

3.4.3 4U 1705-44

4U 1705-44 is a Galactic bulge LMXB discovered in the *Uhuru* survey by Giacconi et al. (1974). The distance of the source was estimated to be 7.4 ± 0.5 kpc by Haberl & Titarchuk (1995) who compared theoretical spectra of their neutron star model atmospheres with observations of X-ray bursts. The result of Galloway et al. (2008) for H-poor fuel is consistent with this, whereas for H-rich material 5.8 ± 0.2 kpc was obtained.

4U 1705-44 was classified as an Atoll source by Hasinger & van der Klis (1989). Barret & Olive (2002) analysed the observation in which 4U 1705-44 showed a vaguely Z-like pattern in colour-colour. This was in line with the earlier proposition of Gierliński & Done (2002) and Muno et al. (2002) that Atoll sources look like Z-track sources if their colour-colour variations are well sampled by observations, not however generally accepted.

Homan et al. (2009) identified the IR counterpart and found that its flux was correlated with X-ray count rate (higher IR on the Upper Banana). The shape of the infrared spectrum and lack of a few day time lags between IR and X-rays were consistent with emission due to X-ray heating of the outer disk and the face of the companion.

Langmeier et al. (1987) studied *EXOSAT* observations of 4U 1705-44 and discovered its numerous type I X-ray bursts occurring every ~ 2 hours and their decay time was decreasing from ~ 100 s to ~ 25 s as the source intensity was increasing. They also noticed the dependence of burst occurrence on long-term intensity changes in the source. The cycle observed was related to the period of $222^d.8$ proposed earlier by Priedhorsky et al. (1986) and was therefore interpreted as real changes in mass accretion rate (Langmeier et al. 1987).

The *EXOSAT* spectrum of the source could be fitted with a blackbody and a cut-off power law (White et al. 1986; Langmeier et al. 1987). Barret & Olive (2002) studied a long *RXTE* observation during which 4U 1705-44 traced a Z-like pattern in colour-colour exhibiting a factor of 5 changes in

intensity. Fitting the Eastern model, the temperature of the Comptonizing plasma, changing from about 4 keV in the Lower Banana Branch up to 11 - 15 keV in the Island branch, was found to be responsible for the state transition in the source. Spectral changes in the elongated Island Branch were mostly due to changes in the blackbody temperature increasing from 0.8 keV to 1.5 keV from left to right on this branch. In the resultant scenario of Barret & Olive (2002), the Banana Branch spectrum is dominated by emission from the disk which extends down to ~ 20 km from the neutron star, whereas the inner corona is optically thick hindering direct emission from the boundary layer. As the disk starts to recede away from the neutron star with decreasing \dot{M} , the inner disk is being gradually replaced by the boundary layer emission which now plays the role of the soft component as seen in the Island Branch (Barret & Olive 2002).

Piraino et al. (2003, 2007) fitted the broadband *BeppoSAX* (0.1 - 200 keV) continuum of 4U 1705-44 with the Eastern model which required an additional component to fit an excess above 25 keV contributing 11% to the total luminosity. Following Barret & Olive (2002) they argued that soft emission comes from the disk and yet they could only obtain good fits with a simple blackbody and not disk blackbody, which makes their interpretation and the presence of the hard tail uncertain.

Several authors focused on the modelling of the broad iron line at ~ 6.6 keV considering its origin (disk reflection or recombination in the ADC) and broadening mechanisms (Doppler and relativistic or Comptonization). Disk reflection scenarios were favoured by di Salvo et al. (2009), Reis et al. (2009) and Lin et al. (2010) who argued that the line profile was asymmetric although it should be noted that such effects can be model-dependent. D'Ai et al. (2010), analysing *XMM-Newton* data, found that although the line was clearly asymmetric in the Banana Branch, it became much more symmetric in the Island Branch. They found this consistent with the truncated disk scenario (Barret & Olive 2002) that would explain smaller relativistic effects on the line profile as the disk recedes away from the central star with decreasing mass accretion rate. However, di Salvo et al. (2004, 2005) observed with *Chandra* when the source was in the Banana Branch and could fit the line with a simple Gaussian form.

Langmeier et al. (1989) performed the first timing study of 4U 1705-44 with *EXOSAT*. Ford et al. (1998a) discovered kHz QPO using *RXTE* data, but did not detect the two QPO in the Island State.

3.4.4 4U 1728-34 (GX 354-0)

The LMXB 4U 1728-34 was discovered in the region of the Galactic centre by Kellogg et al. (1971) and designated at that time as GX 354+0. Its accurate position was established with the discovery of its radio counterpart by Marti et al. (1998). This allowed for the identification of the infrared $K=15$ magnitude counterpart whose most likely nature was a main sequence star. However, the recent *Chandra* detection (Galloway et al. 2010) of $10^{m.77}$ X-ray flux modulation in the source points towards an ultracompact nature of the binary system with probably a white dwarf donor. The optical counterpart has not yet been found as the source lies in a very obscured sky region.

X-ray bursts from 4U 1728-34 were discovered with the *SAS-3* mission (Lewin et al. 1976; Hoffman et al. 1976). Many of the bursts show photospheric radius expansion and, assuming that the Eddington limit has been reached, allow for distance estimations (van Paradijs 1978; Basinska et al. 1984; Kaminker et al. 1989; Di Salvo et al. 2000; Galloway et al. 2003). The most recent (Galloway et al. 2008) values are 4.0 - 5.2 kpc for the H-rich and H-poor matter, respectively. Galloway et al. (2003) showed that burst peak flux varies on a timescale of ~ 40 days (also Kong et al. 1998) interpreted as changing geometry caused by a precessing disk which modulates X-ray flux by variable disk irradiation. The burst properties in 4U 1728-34, such as the short duration of typically ~ 6 s, suggest He-rich fuel and resemble bursts in e.g. the ultracompact binary 4U 1820-30 (Galloway et al. 2003, 2008) and the possible orbital period detected by Galloway et al. (2010) is in line with this.

Two separate spectral states in 4U 1728-34 were first recognized by Schulz et al. (1989) and Hasinger & van der Klis (1989) classified it as an Atoll source. The *EXOSAT* and *ASCA* spectrum of the source could be fitted with an Unsaturated Comptonization (CompST) model alone with the cut-off energy at $\sim 7 - 8$ keV plus a Gaussian line at ~ 6.6 keV interpreted as of ionized iron in the accretion disk corona (White et al. 1986; Narita et al. 2001). Various two-component models gave good fits to *BeppoSAX* broadband data (Di Salvo et al. 2000). The 0.5 keV blackbody or the 0.8 keV disk blackbody component was interpreted as emission from the inner accretion disk, whereas the Comptonized emission was associated with a $kT_e \sim 10$ keV corona. Similar results were obtained by Piraino et al. (2000) with *RXTE/BeppoSAX* and Falanga et al. (2006) with *INTEGRAL*.

Timing properties of the source have been widely studied with *RXTE* by Strohmayer et al. (1996), Ford et al. (1998a) and Di Salvo et al. (2001) with a complex power spectrum showing a broken-

power law noise up to about 10 Hz and QPO-like peaks at 20 - 40 Hz and ~ 100 Hz. KHz QPO were discovered by Strohmayer et al. (1996) in the frequency range 400 - 1150 Hz. The frequencies of the observed features, except the ~ 100 Hz bump, were increasing as the source moved from the Island Branch towards the Upper Banana with increasing inferred mass accretion rate (Di Salvo et al. 2001). The separation of kHz QPO is variable (Méndez & van der Klis 1999; van Straaten et al. 2002) and Migliari et al. (2003) observed it to be as low as 274 ± 11 Hz, thus lower than the 363 Hz spin frequency of the neutron star (Strohmayer et al. 1996) and, again, inconsistent with the beat-frequency model (Méndez & van der Klis 1999).

3.4.5 4U 1735-44

4U 1735-44 was discovered with the *Uhuru* mission (Forman et al. 1978) and is one of the well known bursting sources (Lewin et al. 1977). The optical counterpart, the 17.6 magnitude blue star V 926 Sco, was found by McClintock et al. (1977). The orbital period of $4^h.654$, corresponding to brightness variations with an amplitude of ~ 0.15 magnitude in the B band, was determined by Corbet (1986) and confirmed later on several occasions (van Amerongen et al. 1987; van Paradijs et al. 1988b). The period, assuming a Roche-lobe filling main sequence donor star, implied a late K type companion having mass of about $0.45 - 0.60M_{\odot}$ and low or moderate ($i \sim 10 - 60^{\circ}$) system inclination (Corbet 1986; Smale & Corbet 1991; Casares et al. 2006). Smale & Corbet (1991), Augusteijn et al. (1998) and Casares et al. (2006) found that the optical and infrared line emission most likely originates from the bulge where the stream of matter from the donor star impacts the outer disk.

Penninx (1989) suspected the source to trace the Normal/Horizontal Branches, as in the Z-track sources, but in the power spectrum found no QPO or noise components that would support this. Indeed, 4U 1735-44 was finally classified as an Atoll source by Hasinger & van der Klis (1989) showing both the Island and the Banana Branches in colour-colour and a rather featureless power spectrum < 100 Hz typical of Atoll sources.

Type I X-ray bursts in the source are known to be very irregular with intervals of 0.5 - 50 hours (Lewin et al. 1980; van Paradijs et al. 1988a) and a typical recurrence time of $1^h.5$ (Galloway et al. 2008). No relation between the burst size and the interval since the previous burst (van Paradijs et al. 1988b) or between the burst frequency and hardness or intensity (Lewin et al. 1980) have been reported. The bursts are typically very short ≤ 4 s with a fast rise time ≤ 2 s consistent with very H-poor fuel (Galloway et al. 2008). This contrasts with the fact that, given the relatively

long orbital period and high X-ray luminosity of $0.16 - 0.55 L_{Edd}$, the donor is probably a main-sequence H-rich star which implies a mixed H/He fuel and thus also a smaller burst frequency and a larger burst length than those observed (Galloway et al. 2008). Photospheric radius expansion bursts give a distance estimate of 6.5 - 8.5 kpc (Galloway et al. 2008). A possible 86 minute-long superburst was reported by Cornelisse et al. (2000). X-ray bursts were also simultaneously observed in the visual range (Grindlay et al. 1978) revealing a ≤ 3 s delay with respect to X-rays and longer durations consistent with being due to X-ray reprocessing in the disk. No burst oscillations that would reveal the spin frequency of the neutron star in this system have been found so far (e.g. Ford et al. 1998b).

The *EXOSAT* spectrum could be fitted with a power law with the photon index of 1.8 and the cut-off energy of 7 keV (Smale et al. 1986) or with a model composed of a 2 keV blackbody and cut-off power law (van Paradijs et al. 1988a). The presence of an emission line at 6.8 keV was reported by Smale et al. (1986) who interpreted it as recombination of Fe XXV in the accretion disk corona. The line was later studied by Ng et al. (2010) with *XMM-Newton* who showed that its profile could be well fitted by a simple Gaussian line and supported the scenario of its origin in the corona.

The lower kHz QPO was found by Wijnands et al. (1996); Wijnands & van der Klis (1998b) and the two simultaneous kHz QPO were detected by Ford et al. (1998b). The QPO peak separation was not constant and varied significantly between 296 and 341 Hz (Ford et al. 1998b). The low frequency power spectrum observed with *RXTE* showed a 67 Hz QPO (Wijnands & van der Klis 1998b).

3.4.6 SLX 1735-269

SLX 1735-269 is one of the sources discovered by Skinner et al. (1987) using the coded mask instrument on-board *Spacelab-2* in a survey of the Galactic central region up to 30 keV. Further observations (e.g. in't Zand 1992; Pavlinsky et al. 1994) revealed X-ray flux variations in the source by a factor of about 2. The initial position of SLX 1735-269 given by Skinner et al. (1987) was improved by Goldwurm et al. (1996) and David et al. (1997), and was finally narrowed down to 0.6 arcsecond accuracy by Wilson et al. (2003) using *Chandra*.

That the compact object was a neutron star was revealed by the *BeppoSAX* observation of a ~ 30 second type I X-ray burst by Bazzano et al. (1997). A study of several type I bursts from

SLX 1735-269 was performed by Molkov et al. (2005) using *INTEGRAL* data. They reported on 6 ordinary bursts with a decay time of less than 10 seconds and a very long one having more than a 1000 s duration. The short bursts were consistent with typical helium fuelled bursts as was the one discovered by Bazzano et al. (1997). The long burst, which occurred soon after the transition from the Island to the Banana Branch in the source, was found to be most likely due to unstable burning of a large amount of mixed hydrogen and helium fuel (Molkov et al. 2005). This suggested that the source may switch between two nuclear burning régimes (pure He and mixed H/He burning). The long burst exhibited a photospheric radius expansion giving a distance between 6 kpc (pure helium burst) and 13 kpc (pure hydrogen fuel) in agreement with previous estimates of 8.5 kpc (Goldwurm et al. 1996) and 7.3 kpc from Galloway et al. (2008).

The spectrum of SLX 1735-269 has most often been described by a single power law component with the photon index of typically ≥ 2.0 (Goldwurm et al. 1996; David et al. 1997; Wijnands & van der Klis 1999; Wilson et al. 2003; Molkov et al. 2005). The lack of a strong blackbody component in the spectrum of the source suggested that SLX 1735-269 was not a Z-track source (David et al. 1997). Indeed, Wijnands & van der Klis (1999) argued that in their *RXTE* observation the source was in the Atoll/Island Branch based on its timing and spectral properties. Molkov et al. (2005) observed dramatic spectral changes in the source using *RXTE* and *INTEGRAL*. With their best-fit cut-off power law model they obtained the cut-off energy of ~ 11 keV and ~ 150 keV when the source luminosity was $\sim 5 \times 10^{36}$ erg s $^{-1}$ and $\sim 4 \times 10^{36}$ erg s $^{-1}$, respectively.

A timing analysis was performed by Wijnands & van der Klis (1999) with the power spectrum dominated by a broad band noise. At higher count rates there was a QPO-like bump at ~ 0.9 Hz superimposed on the noise which is often seen in Atoll sources.

3.4.7 4U 1820-30 (Sgr X-4)

4U 1820-30, situated in the globular cluster NGC 6624, is the brightest of 13 such sources known in the Milky Way (Liu et al. 2007) and is a well known Atoll source (Hasinger & van der Klis 1989). Canizares & Neighbours (1975) deduced that variability and a high luminosity of up to 1×10^{38} erg s $^{-1}$ suggested a binary system of a neutron star and a low mass companion (also Grindlay et al. 1984). Stella et al. (1987a) discovered the $11^m.4$ (685 s) orbital period of the system in *EXOSAT* data - the shortest LMXB orbital period known so far suggesting that the companion was a $\sim 0.055M_{\odot}$ helium white dwarf. The UV counterpart was found only $0''.66$ from the cluster centre by King et al. (1993) using the *Hubble Space Telescope*. Anderson et al. (1997)

confirmed this period in UV interpreted as X-ray heating and reprocessing in the disk and/or the face of the companion. Some early, but uncertain, radio detections at 1.4 GHz at the position of 4U 1820-30 were made by Geldzahler (1983) and Grindlay & Seaquist (1986). Finally, Migliari et al. (2004) claimed to have resolved spectrally the binary system from emission of a nearby pulsar.

Extensive work has been done on type I X-ray bursts in this source. They had been discovered by Grindlay et al. (1976) before their real nature as thermonuclear flashes became known (Joss 1977). Clark et al. (1976, 1977) observed bursts in 4U 1820-30 to have typically 1 s rise time and about 10 s decays, which agreed well with the H-poor companion scenario, the bursts occurring only when the source intensity was low and then stopped as the source was becoming brighter (also Šimon 2003). Priedhorsky & Terrell (1984) found a sinusoidal variation between low and high states with a period of $176^d.4$. The presence of type I X-ray bursts only close to minima of this period (Chou & Grindlay 2001) suggested that the cycle must be due to real changes in \dot{M} . This was supposed to be due to a third body exerting tidal forces on the binary and shifting position of the first Lagrangian point resulting in changes of \dot{M} . However, attempts to detect such a third body period have not been successful (Chou & Grindlay 2001). Zdziarski et al. (2007) discovered that the amplitude of the orbital modulation depends on the phase of the long-term \dot{M} modulation being larger when the source was in the Banana State and energy-independent. They interpreted this as scattering in hot gas surrounding the bulge at the outer accretion disk whose size and location depend on mass accretion rate. Detailed spectral analyses of bursts were performed by Haberl et al. (1987) and Galloway et al. (2008) giving a distance of 6.4 kpc, somewhat smaller than the 7.6 kpc distance to the host globular cluster of Kuulkers et al. (2003) based on the optical observations of Heasley et al. (2000).

The low frequency power spectrum of 4U 1820-30 was studied by Stella et al. (1987b). They reported on a 15 - 30 Hz QPO-like bump whose frequency did not depend on intensity or hardness. Dotani et al. (1989) obtained a power spectrum showing red noise and a broad bump decomposed into a QPO at 7 Hz and a knee-like feature at about 25 Hz. Kilohertz QPO with a constant 275 Hz separation and strength increasing substantially with energy were discovered by Smale et al. (1997) using *RXTE*. Their frequencies were increasing with X-ray flux until a saturation (at 1060 Hz for the upper QPO) above a certain count rate interpreted as the signature of the accretion disk reaching the last stable orbit (Zhang et al. 1998; Kaaret et al. 1999).

The spectrum of 4U 1820-30 was analysed on a number of occasions using typically a model composed of a blackbody and a version of Comptonization (Haberl et al. 1987; Stella et al. 1987b; Kaaret et al. 1999; Bloser et al. 2000; White et al. 1988; Kaaret et al. 1999; Bloser et al. 2000). The *EXOSAT* spectrum analysed with a blackbody and a cut-off power law revealed a change in the cut-off energy from more than 30 keV down to ~ 12 keV as the source was moving from the Island to the Banana State, whereas the blackbody temperature remained close to ~ 2 keV (Stella et al. 1987a).

A very comprehensive spectral study of 4U 1820-30 was performed by Bloser et al. (2000) using *RXTE*. Bloser et al. (2000) tested three models: blackbody plus cut-off power law, blackbody plus CompTT and disk blackbody plus cut-off power law, and observed changes in their parameters as the source was tracing its Atoll pattern in colour-colour. The blackbody temperature and radius did not show much change being typically ≤ 2.5 keV and $\sim 1 - 2$ km, respectively. The major change during the state transition from the Island to the Banana Branch corresponded to the change in the Comptonization model component (Bloser et al. 2000). With a cut-off power law, Bloser et al. (2000) found that the cut-off energy was decreasing substantially from about 23 keV in the Island State down to ~ 4 keV in the Banana Branch. In this case, the blackbody component was interpreted as emission from the boundary layer and the Comptonization was attributed to the accretion disk corona. The model with the disk blackbody component gave unphysical parameter values, such as an inclination of 78° (inconsistent with the absence of dipping in the source) and a quite small inner disk radius (7 - 16 km) (Bloser et al. 2000). Bloser et al. (2000) argued that this model assumed an inner compact corona, which would be inconsistent with the results of Church et al. (1998a) that the corona was not restricted to the inner disk region, but extended.

Bloser et al. (2000) found an emission line at ~ 6.8 keV identified with emission of Fe XXV/XXVI whose large width ($\sigma \approx 0.8$) suggested reflection from inner disk regions.

3.4.8 4U 1916-053

4U 1916-053 is a very well known LMXB discovered with *Uhuru* (Forman et al. 1978) and its X-ray position was recently accurately measured by Iaria et al. (2006). It was discovered as an X-ray burster by Becker et al. (1977) with *OSO-8* and Lewin et al. (1977) with *SAS-3* who found that bursts occurred typically every 4 - 5 hours. The bursts were usually short (~ 5 s) consistent with H-poor fuel. The distance to the source, based on PRE type I bursts, was estimated to be ~ 9 kpc (Smale & Mukai 1988; Galloway et al. 2008). The 50 minute (~ 3000 s) orbital period

was discovered by Walter et al. (1982) based on observations of recurrent X-ray dipping. This was in fact the first direct evidence that bursting X-ray sources are binary systems. White & Swank (1982) interpreted dipping as due to obscuration of the line-of-sight X-ray emission by the bulge at the outer accretion disk where accreted matter from the companion impacts on the disk. The very short period suggested a low mass $\sim 0.1M_{\odot}$ white dwarf companion (White & Swank 1982). The lack of eclipses suggested an inclination lower than $\sim 79^{\circ}$ (Frank et al. 1987; Smale & Mukai 1988).

The optical counterpart of 4U 1916-053, the blue $V = 21$ magnitude star V 1405 Aql was discovered by Grindlay et al. (1987). Grindlay et al. (1988) found that the optical period is longer by $\sim 1\%$ (a so-called superhump, quasi-periodicity shifted a little with respect to the orbital period) than the X-ray period leading to a long-term controversy on the cause of this discrepancy. Grindlay et al. (1988) proposed a triple star model in which a third body in the system on a 2.5 day retrograde orbit modulates the mass accretion rate in the LMXB which causes the X-ray period to be longer than the real orbital period seen in the optical modulation. Alternatively, as in the model to explain superhumps in SU UMa-like cataclysmic variables (Whitehurst 1988), the extreme mass ratio of the LMXB stars leads to an asymmetry of the disk through tidal interactions and the optical period modulation is due to the disk precession (Schmidtke 1988; Smale et al. 1992; Homer et al. 2001). Finally, the issue was resolved by Retter et al. (2002) who found a third period of 2979 s in the optical range. They argued that the X-ray period was the real orbital period, whereas the shorter and the longer optical periods corresponded to the nodal and the apsidal precession of the accretion disk giving the observed negative and positive superhumps.

4U 1916-053 exhibits different spectral states consistent with the Atoll pattern in HID/CCD and its X-ray spectrum has been studied by many authors. The *OSO-8* and *EXOSAT* spectrum could be fitted by a power law model with the photon index of 1.6 - 1.8 (White & Swank 1982; Smale & Mukai 1988). Extensive spectral studies were performed by Church et al. (1997) and Morley et al. (1999) with a model composed of a blackbody, thought to originate from the neutron star surface or the boundary layer, and a power law representing Comptonized emission. In particular, it was found (Church et al. 1997) that during dipping some of the non-dip emission remained unabsorbed which they attributed to an uncovered part of the ADC. Dipping was successfully explained in terms of the point-like blackbody, being fully absorbed and the Comptonized emission being progressively covered by the bulge at the outer disk (Morley et al. 1999) which suggested an extended nature of the ADC. Church et al. (1998b) made the first hard detection of the source up

to ~ 100 keV using *BeppoSAX* data. The non-dip spectrum of 4U 1916-053 was well fitted by the 1.6 keV blackbody and the power law with a photon index of 1.6 and the cut-off energy of 80 keV. The dip spectrum was dominated by photoelectric absorption below ~ 20 keV and could again be described by the progressive coverage model. At higher energies, where the Thomson cross-section becomes greater than the cross section for photoelectric absorption, there was evidence for energy-independent electron scattering probably in the partially ionized bulge at the outer disk (Church et al. 1998b). The same model was used later on several occasions (Bloser et al. 2000; Narita et al. 2003; Balman 2009). In the observation of Blaser et al. (2000), as the source was moving along the Banana with increasing intensity, the cut-off energy of the power law component changed from about > 100 keV down to ~ 9 keV. In several cases (Smale et al. 1992; Blaser et al. 2000; Asai et al. 2000) an emission line consistent with ~ 6.4 keV neutral iron was detected.

The study of timing features in 4U 1916-053 was carried out by Boirin et al. (2000). They found a QPO at 5 - 80 Hz and the two kHz QPO in the range 200 - 1300 Hz. As the source was moving from the Lower to the Upper Banana State, the QPO frequencies correlated with the inferred mass accretion rate. The separation of ~ 350 Hz between the two kHz QPO was not close to the frequency of burst oscillation (270 Hz) found by Galloway et al. (2001) which again posed problems to the beat-frequency models for QPO, which are now generally regarded as disproven.

Table 3.1: A choice of basic parameters of LMXB under study in this work.

Source	α & δ (J2000.0)	N_H (10^{22} atom cm^{-2}) ^a	Distance (kpc)	Orbital period	Inclination ($^\circ$)	Mass donor
Cyg X-2 like Z-track sources						
GX 340+0	$16^h 45^m 47^s.7$, $-45^\circ 36' 39''.5$ ^[7]	1.93	11.0 ± 3.3 ^[8]	unknown	< 60 ^c	unknown
Cyg X-2	$21^h 44^m 41^s.15$, $+38^\circ 19' 17''.1$ ^[1]	0.187	$9.0_{-2.9}^{+4.0}$ $[2, 3, 4, 5]$	$9^d.8445$ ^[2, 6]	62.5 ^[4]	$0.7 M_\odot$ giant ^[2]
Sco X-1 like Z-track sources						
Sco X-1	$16^h 19^m 55^s.085$, $-15^\circ 38' 24''.9$ ^[12]	0.148	2.8 ± 0.3 ^[12]	$18^h.9$ ^[13, 14, 15]	38 ^[16, 17]	$0.4 M_\odot$ sub-giant ^[16, 17]
GX 17+2	$18^h 16^m 01^s.4$, $-14^\circ 02' 10''.6$ ^[9, 10]	0.825	$7.5_{-1.9}^{+2.9}$ ^[5, 11]	unknown	< 60 ^c	unknown
Atoll sources						
2S 0918-549	$09^h 20^m 26^s.47$, $-55^\circ 12' 24''.5$ ^[18]	0.616	$5.3_{-3.3}^{+9.7}$ ^[5, 19, 20, 21, 47]	$17^m.4$ ^[22]	10 ^[22]	$0.03 M_\odot$ white dwarf ^[21, 22]
4U 1636-536	$16^h 40^m 55^s.50$, $-53^\circ 45' 05''.00$ ^[1]	0.276	6.0 ± 0.5 ^[5]	$3^h.8$ ^[23, 24, 25]	< 60 ^c	$0.36 M_\odot$ dwarf ^[24]
4U 1705-44	$17^h 08^m 54^s.47$, $-44^\circ 06' 07''.35$ ^[26]	0.674	$5.8_{-0.2}^{+2.1}$ ^[5, 27]	unknown	< 60 ^c	unknown
4U 1738-34	$17^h 31^m 57^s.7$, $-33^\circ 50' 02''.5$ ^[28]	0.124	5.2 ± 0.5 ^[5]	$10^m.77$ ^b ^[29]	< 60 ^c	unknown
4U 1735-44	$17^h 38^m 58^s.3$, $-44^\circ 27' 00''.0$ ^[1]	0.261	7.5 ± 2.5 ^[5, 48]	$4^h.654$ ^[33, 34, 35]	10 - 60 ^[33, 36, 37]	$0.45 - 0.60 M_\odot$ dwarf ^[33, 36, 37]
SLX 1735-269	$17^h 38^m 17^s.12$, $-26^\circ 59' 38''.6$ ^[30]	0.397	$8.5_{-2.9}^{+4.5}$ ^[5, 31, 32]	unknown	< 60 ^c	unknown
4U 1820-30	$18^h 23^m 40^s.45$, $-30^\circ 21' 40''.08$ ^[38]	0.129	$6.4_{-0.2}^{+1.6}$ ^[5, 39, 40]	$11^m.4$ ^[41, 42]	40 - 55 ^[42]	$0.055 M_\odot$ white dwarf ^[41]
4U 1916-053	$19^h 18^m 47^s.87$, $-05^\circ 14' 17''.09$ ^[43]	0.231	9.0 ± 1.3 ^[5, 44]	50^m ^[45]	60 - 75 ^c	$0.1 M_\odot$ white dwarf ^[46]

References: [1] Ebisawa et al. (2003), [2] Cowley et al. (1979), [3] Smale (1998), [4] Orsz & Kuulkers (1999), [5] Galloway et al. (2008), [6] Casares et al. (2010), [7] Penninx et al. (1993), [8] Fender & Hendry (2000), [9] Liu et al. (2007), [10] Grindlay & Sasaki (1986), [11] Kuulkers et al. (2002), [12] Bradshaw et al. (1999), [13] Cottlieb et al. (1975), [14] Cowley & Chantton (1975), [15] LaSala & Thorstensen (1985), [16] Fomalont et al. (2015), [17] Steuchs & Casares (2002), [18] Juet & Chakrabarty (2003), [19] Jonker et al. (2001), [20] Cornelisse et al. (2002), [21] in 't Zand et al. (2005), [22] Zhong & Wang (2011), [23] Peterson et al. (1981), [24] Smale et al. (1988), [25] van Paradijs et al. (1990a), [26] di Salvo et al. (2005), [27] Habel & Trinchik (1995), [28] Marti et al. (1998), [29] Galloway et al. (2010), [30] Wilson et al. (2003), [31] Melkov et al. (2005), [32] Golovtsov et al. (1996), [33] Corbet (1986), [34] van Paradijs et al. (1987), [35] van Paradijs et al. (1988b), [36] Smale & Corbet (1991), [37] Casares et al. (2006), [38] Migliari et al. (2004), [39] Kuulkers et al. (2003), [40] Havelley et al. (2000), [41] Stehle et al. (1987a), [42] Anderson et al. (1987), [43] Iaria et al. (1997), [44] Smale & Mukai (1988), [45] Walter et al. (1982), [46] White & Swank (1982), [47] Chavaler & Ilievsky (1987), [48] Christian & Swank (1997).
Right ascension and declination as in Liu et al. (2007); Distances given are as used in this work, errors reflect spread of distance estimates in the literature. Errors are not quoted for estimates of system parameters (orbital period, inclination and companion mass)

^a from Leiden/Argentine/Bonn (LAB) Survey of Galactic HI (Kalberla et al. 2005).

^b period suggested by Galloway et al. (2010) and consistent with a probable ultracompact nature of the system, the period requires confirmation.

^c lack of eclipses implies $i < 75^\circ$, lack of dipping implies $i < 60^\circ$ (Frank et al. 1987).

Chapter 4

Spectral & timing studies of the Cyg-like Z-track sources

The first spectral analysis of a Cyg-like Z-track source, i.e. GX 340+0, using the Extended ADC model was carried out by Church et al. (2006). Based on their results, they proposed a model discussed in Sect. 3.1, to explain the physical changes that take place on the branches of the Z-track. The Extended ADC model was later applied to GX 5-1 (Jackson et al. 2009) and Cyg X-2 (Bałucińska-Church et al. 2010) and in both cases the results supported the model for the Z-track of Church et al. (2006).

Jackson et al. (2009) performed also a timing analysis of GX 5-1 using the same data selections as those from their spectral analysis to allow a direct comparison of the spectral and timing properties of the source. They obtained evidence that the two kHz QPO observed on the Horizontal Branch responded to changes of the radiation pressure and this allowed a deeper understanding of the physical changes at the inner accretion disk (Sect. 3.1.5). However, a similar combined spectral and timing study has not yet been done for the other two Cyg-like sources. Thus, the aim of the work presented in this Chapter is to carry out a simultaneous spectral and timing study of Cyg X-2 and GX 340+0, compare the results with those of Jackson et al. (2009) and discuss them in terms of the model of Church et al. (2006).

The analyses of Cyg X-2 and GX 340+0 are presented in Sect. 4.1 and Sect. 4.2, respectively, whereas the discussion of these follows in Sect. 4.3.

4.1 Cygnus X-2

4.1.1 Observations

The *RXTE* observation of Cyg X-2 chosen for this work has the observation ID P20053 and was made between June 30th and July 3rd, 1997. It consists of eleven sub-observations spanning together more than 200 ks. Detailed information regarding the data is presented in Table 4.1.

Table 4.1: A list of *RXTE* sub-observations of Cygnus X-2 made in June/July 1997.

Sub-observation	Start Date & Time (UT)	Duration (s)
20053-04-01-00	June 30, 1997, 19:57:46	26000
20053-04-01-010	July 1, 1997, 06:00:36	28800
20053-04-01-01	July 1, 1997, 14:00:36	12384
20053-04-01-020	July 1, 1997, 18:12:36	24320
20053-04-01-02	July 2, 1997, 00:58:07	7312
20053-04-01-06	July 2, 1997, 04:20:30	7536
20053-04-01-030	July 2, 1997, 07:01:36	28800
20053-04-01-03	July 2, 1997, 15:01:36	14432
20053-04-01-04	July 2, 1997, 20:21:14	23936
20053-04-01-07	July 3, 1997, 04:19:15	13424
20053-04-01-05	July 3, 1997, 08:38:35	14848

The same observation was already spectrally analysed in terms of the Extended ADC model by Bałucińska-Church et al. (2010), however, a timing study has not been done.

4.1.2 Data analysis

Data analysis was performed with the *HEASOFT* v.6.3.1 software used together with the up-to-date calibration database *CALDB*. For this is the first source analysed in this work, the analysis procedure, for which a full description is given in Appendix A, is presented below in a detailed way. In subsequent sections, to avoid repetition, only an overview of the procedure will be given highlighting the most important information.

The first step involved an examination of the housekeeping data of the observation, based on which screening criteria could be applied to raw data. Deviations from the required pointing direction (keyword *OFFSET*) were restricted to no more than 0.02° and the elevation above the Earth's limb (*ELV*) was required to be greater than 10° . The parameter *NUM_PCU_ON* showed that PCU detectors 0, 1 and 2 were constantly on during the observation time and hence these units

were used. All these conditions were translated into Good Time Intervals (GTI) using MAKETIME providing ~ 95 ks of usable data.

Next, using Standard2 data from the top (left and right) layers of PCU 0, 1 and 2, lightcurves were produced using SAEXTRACT in several energy bands: low (1.9 - 4.1 keV, channels 5 - 10), medium (4.1 - 7.3 keV, channels 11 - 18) and high (7.3 - 20.3 keV, channels 19 - 55). The choice of the energy ranges was made for consistency with the previous analysis of Bałucińska-Church et al. (2010) and was achieved approximately by specifying the detector channels based on the energy-to-channel conversion table corresponding to *RXTE* calibration epoch 3 of the observation. Also, the total 16 s-binned lightcurve covering an energy range of 1.9 - 20.3 keV was extracted and rebinned to 64 seconds (reducing scatter in hardness-intensity variation of the source).

The corresponding background lightcurves were produced using PCABACKEST from data generated from the bright PCA background model (pca.bkgd_cmbrigtvle_Mv20051128.mdl) which is recommended in the case of sources with intensities higher than $40 \text{ count s}^{-1} \text{ PCU}^{-1}$. This is surely the case here, as the source intensity (see Fig. 4.1) is at all times higher than $\sim 730 \text{ count s}^{-1} \text{ PCU}^{-1}$. On-source lightcurves were next background-subtracted using LCMATH and deadtime-corrected with PCADEAD which in the case of Cyg X-2 raised the original intensity by $\sim 4\%$. The background-subtracted and deadtime-corrected, 64 s-binned lightcurve of Cygnus X-2 is presented in Fig. 4.1.

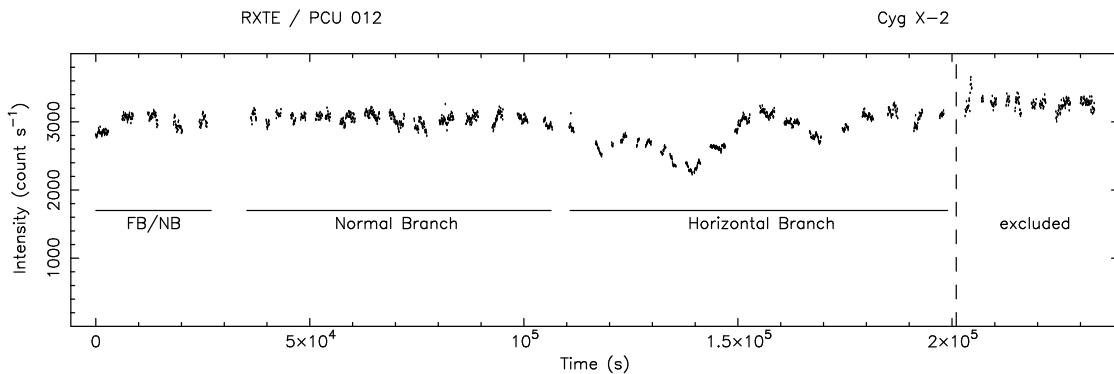


Figure 4.1: The 1.9 - 20.3 keV background-subtracted and deadtime-corrected lightcurve of Cyg X-2. One point corresponds to 64 seconds of observation. Sections of data (marked with horizontal bars) corresponding to Z-track branches are labelled as FB - Flaring Branch, NB - Normal Branch, and HB - Horizontal Branch. The last two sub-observations (beyond the vertical dashed line) were excluded from the analysis (see text).

The lightcurves produced in low, medium and high energy bands were used in LCURVE to produce a hardness-intensity diagram (HID) with hardness defined as the ratio of the hard (7.3 - 20.3 keV) and the medium (4.1 - 7.3 keV) count rates. A quick examination of the lightcurve and the HID

revealed that the last two sub-observations (20053-04-01-05 and 20053-04-01-07), made on July 3rd, 1997, correspond to a slightly increased overall intensity of the source and so were excluded from this analysis. They are also not shown in the hardness-intensity diagram presented in Fig. 4.2.

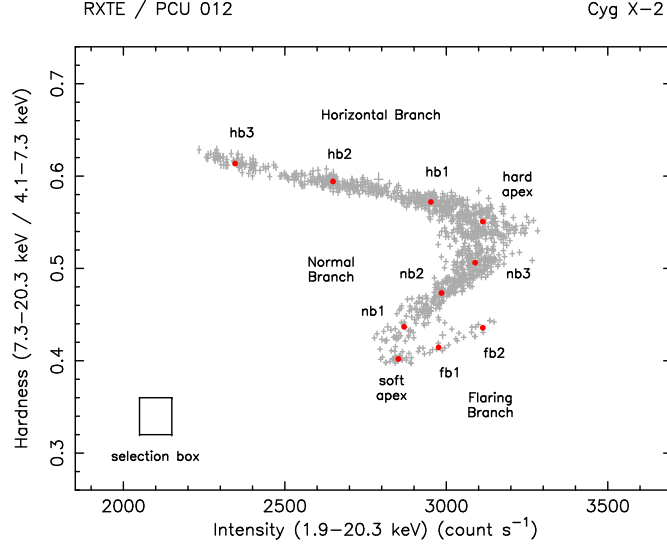


Figure 4.2: The background-subtracted and deadtime-corrected hardness-intensity variation of Cygnus X-2 with a binning of 64 seconds. Filled, red circles mark the positions of the data selections.

Next, small sections of the lightcurve were selected and the corresponding hardness-intensity variations obtained to be compared with Fig. 4.2. This allowed identification of the Z-track position of each section and follow the behaviour of the source in time. Thus, from Fig. 4.1 it can be seen that at the beginning of the observation, the source was close to the soft apex exhibiting weak flaring which forms the Flaring Branch in hardness-intensity. It then moved to the Normal Branch and the Horizontal Branch, and a complete Z-track was traced within ~ 2 days.

Ten data selections were made along the Z-track for the purpose of spectral and timing analysis. This was done prior to the deadtime correction and then the selections were moved to proper positions to match the deadtime-corrected Z-track displayed in Fig. 4.2. There are three selections along the HB (hb3 - hb1), one selection at the hard apex (ha), three selections along the NB (nb3 - nb1), one selection at the soft apex (sa), and two selections on the FB (fb1 - fb2). The size of every selection was $100 \text{ count s}^{-1} \times 0.04$ in intensity and hardness, respectively, as shown by a rectangular box in the lower left corner of the diagram. Such a size was established by trial and error to allow for detection of weak kHz quasi-periodic oscillations (Sect. 4.1.4). Large selections may cause unwanted spectral averaging, especially on the Normal Branch where hardness, and

hence the spectral properties of the source, changes substantially. However, an independent spectral analysis of this dataset was performed using smaller selection boxes by Bałucińska-Church et al. (2010). The results from the two approaches are, as will be demonstrated, in a very good agreement revealing the same picture of the spectral evolution of Cyg X-2 along the Z-track.

The selected conditions on intensity and hardness were next translated into Good Time Intervals. PCU spectra were extracted using SAEXTRCT from the top (left and right) layers of detectors 0, 1 and 2 using these GTI. The number of counts per spectral channel was typically $10^4 - 10^5$, thus very large. The spectra were then deadtime-corrected following the mission-specific procedure incorporated into a dedicated script. The correction takes into account the known deadtime ($\sim 10 - 150 \mu\text{s}$) of the detector and corrects the recorded count rate by a few percent to its real rate, and in the case of spectra this is corrected by reducing the nominal value of the exposure time. Systematic errors of 1% (as recommended by mission specialists) were applied in GRPPHA to spectral channels in order to take into account calibration uncertainties of the PCU detectors as the calibration is improved during the mission. Background spectra were extracted in SAEXTRCT from Standard2 background data as in the case of lightcurves. An appropriate response file was generated in PCARSP taking into account both the housekeeping data of the observation and the newest calibration data for the instrument. The response file (RSP) in the case of the PCA comprises a combination of the redistribution matrix file (RMF) and the auxiliary response file (ARF) which provide information about the channel-to-energy relation and the effective area of the instrument.

HEXTE (Cluster A) spectra were extracted using the multitask script HXTLCURV which produces both on-source and off-source (background) spectra for selection GTI. Data belonging to a given selection in hardness-intensity may come from several sub-observations. In that case, HXTLCURV produces individual spectra for each of the sub-observations involved and then these are added together in SUMPHA to obtain a single on-source and off-source spectrum for each selection. Additionally, the tool performs a deadtime correction based on the standard deadtime coefficients file `hxtdead_200002_pwa.fits`. The standard HEXTE RMF file, `hexte_97mar20c_pwa.rmf` and the ARF file, `hexte_00may26_pwa.arf`, which together make up the response of the instrument, were used. HEXTE spectral channels were additionally grouped in GRPPHA to improve their signal to noise ratio at higher energies where the number of counts per bin was lowest. Typically, 10^3 counts per new channel were available for spectral fitting.

The same data selections were used for timing analysis. For this purpose, PCA data obtained in

the Single Bit mode SB_125us_14_249_1s were used. These, unlike Standard2 data, cover an energy range of 5 - 100 keV and have a high time resolution of 125 μ s which allows one to obtain power spectra up to 4096 Hz. This follows from the Nyquist theorem that any signal can only be detected up to a frequency which is half of the sampling frequency, and here: $1/125 \mu\text{s} = 8192$ Hz. This range is sufficient to study high frequency kHz QPO which are investigated. It should be noted that other data modes usable for timing analysis were available in this *RXTE* observation, i.e. Event mode data E_125us_64M_36_1s (13 - 100 keV, 125 μ s) and Single Bit data SB_125us_0_13_1s (2 - 5 keV, 125 μ s). However, tests performed in POWSPEC (below) involving different combinations of data modes revealed that the latter modes do not improve detection of QPO as their power spectra show noise only. This is most probably related to their energy ranges (either above 13 keV or below 5 keV). The same was reported by Wijnands et al. (1997) who could not detect kHz QPO when using combined data from several data modes.

Raw 13 - 100 keV Single Bit data files were identified within each of the sub-observations and the selection GTI were applied in GROSSTIMEFILT. The filtered data were then used in POWSPEC to produce power spectra. POWSPEC divides data into many intervals for which it performs a Fast Fourier Transform producing individual power spectra, and then these are averaged to get a single power spectrum for a given data selection. The division into intervals allows a choice of the frequency resolution of the power spectrum, the resolution being an inverse of the interval duration. In this case, intervals were 0.5 - 1.0 second in length, giving a resolution of 1 - 2 Hz which was found to work well for initial searches for QPO. The power spectrum was next normalized using the Leahy normalization (Leahy et al. 1983) so that the photon statistical noise (the baseline of a power spectrum) had a power value of 2. In practice, the baseline noise level is slightly different from 2 due to deadtime effects. A deadtime correction is sometimes taken into account by fitting an additional broad sinusoid to the power spectrum, especially when studying the properties of broad low-frequency ($\lesssim 100$ Hz) features, such as noise components, and the effect becomes smaller with frequency (Zhang et al. 1995). Here, the noise level in the obtained power spectra was well fitted with a power law alone without need for another broad-band component to improve fitting and detection of relatively narrow QPO signals.

The output power spectrum was converted into *Xspec*-friendly '.pha' format (Revnivtsev et al. 2000) using FDUMP and FLX2XSP so allowing the usage of *Xspec* with the advantage of its rich model database and fitting capabilities. A fake response function was also produced with FLX2XSP in the form of a unit diagonal matrix which provides an ideal channel-to-frequency relation and

causes no modification to data in any way, but is required by *Xspec*. The procedure described above was repeated in the case of every data selection to allow for a direct comparison of spectral and timing results along the Z-track of Cygnus X-2.

4.1.3 Spectral fitting results

PCA and HEXTE energy spectra were used simultaneously in *Xspec*. Spectral ranges were restricted to typically 3 - 29 keV and 18 - 50 keV in the case of the PCA and the HEXTE, respectively. The lower energy boundaries correspond to limits below which calibration of the two instruments is not well known and the effective area is small, whereas the upper boundaries were chosen so as to ignore background-dominated channels. An additional multiplicative constant was introduced to the model to take into account uncertainty in cross-calibration between the PCA and the HEXTE. This constant was frozen at 1.0 for the PCA spectrum, but left free for HEXTE and in free fitting its value was always about 0.7 - 0.8, which is typical. The spectra from the two instruments were fitted simultaneously with the other model parameters chained in *Xspec* to be equal.

Spectral fitting was first performed with the Extended ADC model (Sect. 2.2) in the form $\text{const} \times \text{wabs} \times (\text{bbody} + \text{cutoffpl})$, where the names correspond to *Xspec* models: ‘const’ - a constant factor, ‘wabs’ - absorption, ‘bbody’ - point-like blackbody, ‘cutoffpl’ - cut-off power law. The absorption model uses the cross-sections of Morrison & McCammon (1983) and the elemental abundances of Anders & Ebihara (1982). Initial fitting revealed an excess at around 6.7 keV suggesting the presence of an emission line of iron which has been reported in the source on many occasions. A Gaussian line was therefore added to the model and it was found that in free fitting the line width had a tendency to become very broad absorbing the continuum around it. To avoid this, a choice was made to fix it at $\sigma = 0.1$ keV based on the inspection of fitting residuals which worked well giving acceptable fits in every selection. Nevertheless, the effect of the line width on other model parameters was checked and it was found that when using e.g. $\sigma = 0.5$ keV the differences are very small (such as 0.04 keV in blackbody temperature, thus within errors).

The column density N_H , the parameter of the ‘wabs’ component, was left free and allowed to vary along the Z-track to reveal any changes intrinsic to the source. N_H was found smallest ($\sim 1.2 \times 10^{22}$ atom cm^{-2}) when the source was close to the soft apex, and this value worked also well on the Flaring Branch giving acceptable fitting results and a decision was made to freeze it on that branch. A similar approach was taken by Church et al. (2006) in the case of GX 340+0,

in which the column density was also found to vary little along the FB and could be frozen to stabilize the fitting.

In the case of bright Z-track LMXB, the cut-off energy in the spectrum is low ~ 5 keV and hence there is a limited energy range below the cut-off to determine the slope of the power law component (the photon index) from spectral fitting. Thus, following Church et al. (2006) and Bałucińska-Church et al. (2010), the photon index Γ was kept frozen at 1.7, a physically reasonable value for a Comptonizing region of low temperature and high optical depth (Shapiro et al. 1976), allowing for a direct comparison with their work. It was also checked here that even in free fitting the photon index was no different by more than 10% from 1.7. Moreover, fitting with different values of Γ , such as 1.6 or 1.8, did not affect the other parameters in any substantial way (e.g. only 2% difference in kT_{bb} and 5% in E_{co}) leaving the general picture of the behaviour of the source unaffected.

Spectral fitting was performed in all selections using the model described giving good fits with $\chi^2/\text{d.o.f.}$ between 39/58 and 61/59 with the exception of selection fb2 in which it was not so good ($\chi^2/\text{d.o.f.} = 89/60$). Fig. 4.3 shows typical folded and unfolded spectra from each of the Z-track branches with PCA and HEXTE data fitted simultaneously with the Extended ADC model, the residuals showing the quality of the fits. Spectral fitting results and values of additional physical quantities derived from them are presented in Table 4.2 and Table 4.3. The behaviour of the source in terms of these results is examined below.

Absorption At the soft apex, the column density is lowest (1.2×10^{22} atom cm^{-2}) and then systematically increases along the Normal Branch reaching a maximum value of $3.1 \pm 0.5 \times 10^{22}$ atom cm^{-2} on the upper NB close to the hard apex, and so the increase is significant. Then, on the Horizontal Branch, N_H decreases towards the left end of this branch. Such variations indicate changes intrinsic to the source as they correlate well with the Z-track position. The same behaviour was observed by Bałucińska-Church et al. (2010) and the values of N_H agree well within errors, small differences being due to data averaging in larger data selections in this work.

The blackbody Figure 4.4 shows variations of the blackbody parameters, kT_{bb} (upper panel) and R_{bb} (lower panel), revealing a clear pattern of changes along the Z-track, the small errors making the changes very well determined. First, the blackbody temperature increases monotonically between the soft apex ($kT_{bb} = 1.19 \pm 0.02$ keV) and the left end of the Horizontal Branch, where it reaches a maximum value of 2.49 ± 0.11 keV. Such a strong change of the blackbody

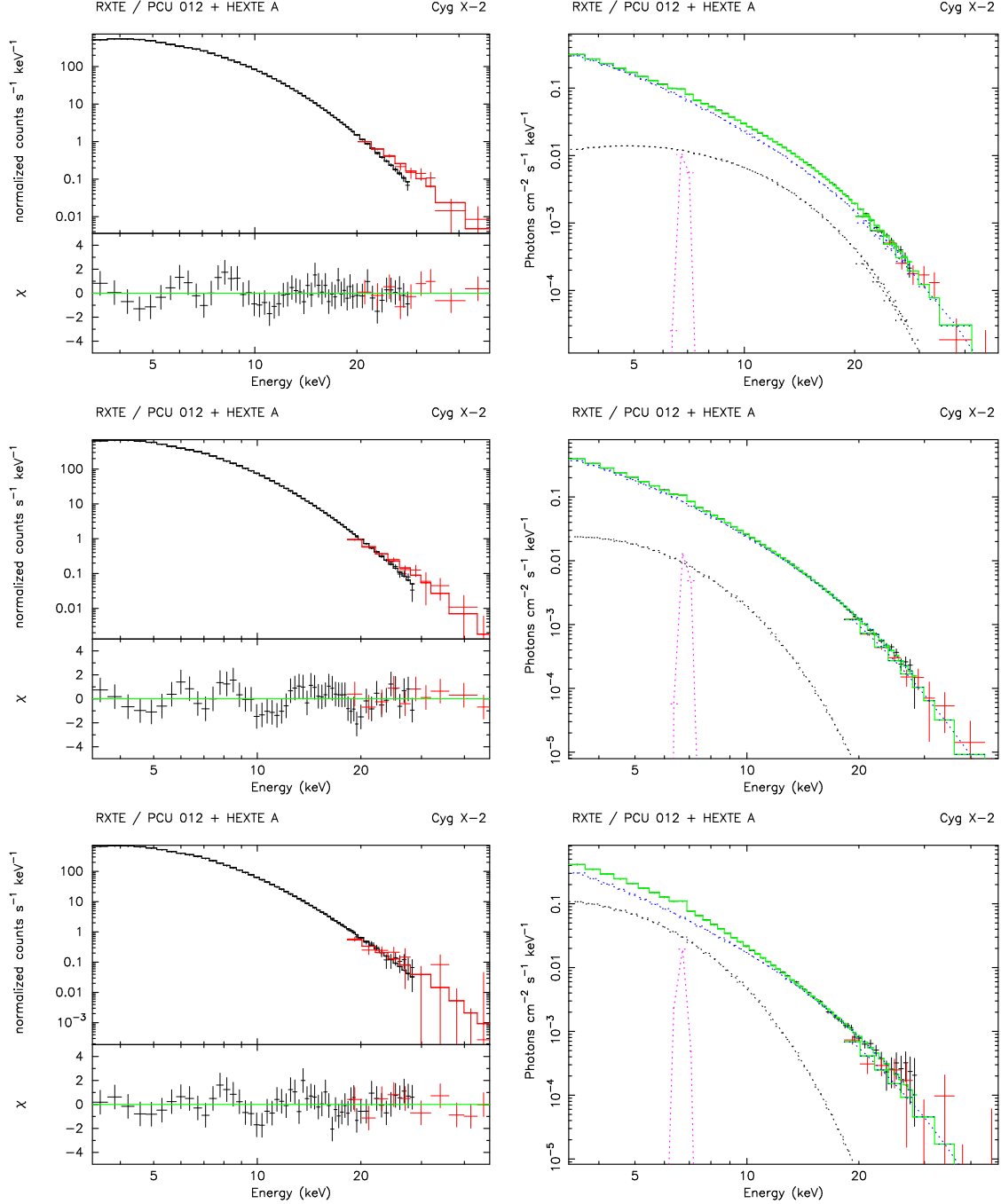


Figure 4.3: Representative folded spectra (left) and unfolded spectra (right). Top panel: Horizontal Branch (selection hb2); middle: Normal Branch (nb2) and bottom: Flaring Branch (fb1). Left: PCA (black) and HEXTE (red) data and the best-fit model are shown with residuals. Right: the model components are shown separately: blackbody (black), cut-off power law (blue), emission line (magenta), and the total spectrum (green).

Table 4.2: The results of fitting the Extended ADC model to spectra of Cygnus X-2. The parameters shown are: the column density, the blackbody temperature and its normalization, the line energy and its equivalent width, the power law cut-off energy and the normalization, and χ^2 over degrees of freedom. Errors are given at 90% (2σ) confidence level.

Sel.	N_H	Blackbody		Emission line		Cut-off power law		$\chi^2/\text{d.o.f.}$
		kT_{bb}	norm	E_l	EW	E_{co}	norm	
hb3	2.1 ± 0.4	2.49 ± 0.11	1.8 ± 0.2	6.79 ± 0.22	71	6.73 ± 0.34	4.6 ± 0.3	46/58
hb2	2.6 ± 0.4	2.40 ± 0.11	1.77 ± 0.16	6.85 ± 0.22	71	6.43 ± 0.25	5.6 ± 0.3	39/58
hb1	2.8 ± 0.4	2.18 ± 0.12	1.5 ± 0.2	6.91 ± 0.25	67	6.38 ± 0.16	6.6 ± 0.3	41/59
ha	2.9 ± 0.4	1.98 ± 0.13	1.3 ± 0.3	6.95 ± 0.25	68	6.22 ± 0.14	7.2 ± 0.4	45/58
nb3	3.1 ± 0.5	1.76 ± 0.19	0.8 ± 0.4	6.92 ± 0.23	72	5.68 ± 0.13	8.0 ± 0.5	53/58
nb2	2.7 ± 0.5	1.36 ± 0.08	1.3 ± 0.5	6.83 ± 0.20	71	5.52 ± 0.14	7.6 ± 0.6	49/59
nb1	1.9 ± 0.5	1.20 ± 0.05	2.5 ± 0.5	6.80 ± 0.19	74	5.42 ± 0.17	6.5 ± 0.6	59/59
sa	1.2^f	1.19 ± 0.02	3.9 ± 0.4	6.67 ± 0.13	94	5.17 ± 0.11	5.8 ± 0.3	61/59
fb1	1.2^f	1.23 ± 0.02	4.5 ± 0.5	6.68 ± 0.15	87	5.40 ± 0.15	5.5 ± 0.4	45/60
fb2	1.2^f	1.31 ± 0.03	4.5 ± 0.5	6.66 ± 0.14	93	5.45 ± 0.14	5.7 ± 0.4	89/60

The column density is expressed in 10^{22} atom cm^{-2} . The blackbody temperature, the cut-off energy and the line energy are given in keV. The blackbody normalization is given in 10^{37} erg s^{-1} assuming a distance of 10 kpc, and the normalization of the cut-off power law component is in photons $\text{keV}^{-1} \text{cm}^{-2} \text{s}^{-1}$ at 1 keV. The line equivalent width is given in eV.

^f - the parameter was frozen in fitting.

Table 4.3: The auxiliary physical quantities derived from spectral fitting results: the blackbody radius, the half-height of the emitting strip on the neutron star, the ratio of blackbody flux to the Eddington flux, the mass accretion rate per unit of emitting area, the luminosities of the main model components, the total luminosity and the half-height of the inner disk. Errors are quoted at 90% confidence level.

Selection	R_{bb}	h	f_{bb}/f_{Edd}	\dot{m}	L_{bb}	L_{cpl}	L_{tot}	H_{eq}
hb3	1.74 ± 0.18	0.30 ± 0.06	2.6 ± 0.3	23 ± 5	1.49 ± 0.15	14.8 ± 0.9	16.3	13.9 ± 0.9
hb2	1.83 ± 0.18	0.33 ± 0.07	2.3 ± 0.2	24 ± 5	1.43 ± 0.13	17.5 ± 0.9	19.0	16.2 ± 0.9
hb1	2.0 ± 0.3	0.41 ± 0.11	1.6 ± 0.2	22 ± 6	1.20 ± 0.17	20.3 ± 1.1	21.6	18.4 ± 1.0
ha	2.3 ± 0.4	0.53 ± 0.18	1.1 ± 0.2	19 ± 7	1.0 ± 0.2	21.8 ± 1.3	22.9	19.5 ± 1.1
nb3	2.3 ± 0.8	0.5 ± 0.4	0.7 ± 0.3	19 ± 13	0.7 ± 0.3	22.9 ± 1.5	23.6	20.1 ± 1.3
nb2	4.9 ± 1.2	2.4 ± 1.1	0.23 ± 0.09	4.0 ± 1.9	1.0 ± 0.4	21.0 ± 1.7	22.1	18.9 ± 1.5
nb1	8.8 ± 1.2	8 ± 2	0.14 ± 0.03	1.1 ± 0.3	2.0 ± 0.4	17.9 ± 1.7	19.9	17.0 ± 1.6
sa	11.0 ± 0.7	12.1 ± 1.5	0.139 ± 0.015	0.65 ± 0.08	3.1 ± 0.3	15.2 ± 0.9	18.4	15.7 ± 0.9
fb1	11.2 ± 0.7	12.6 ± 1.6	0.156 ± 0.017	0.64 ± 0.08	3.6 ± 0.4	15.0 ± 1.1	18.7	16.0 ± 1.1
fb2	9.8 ± 0.6	9.7 ± 1.2	0.20 ± 0.02	0.86 ± 0.11	3.6 ± 0.4	15.7 ± 1.0	19.5	16.6 ± 1.0

The blackbody radius and the half-height h of the corresponding equatorial belt on the neutron star are given in km, the blackbody luminosity is bolometric in 10^{37} erg s^{-1} , the blackbody flux is expressed as a fraction of the emissive Eddington flux (1.4×10^{25} $\text{erg cm}^{-2} \text{s}^{-1}$) for a 10 km neutron star, \dot{m} is in 10^5 $\text{g cm}^{-2} \text{s}^{-1}$, the cut-off power law and the total luminosities are given in the 1 - 30 keV range in 10^{37} erg s^{-1} . The equilibrium half-height H_{eq} of the inner radiatively-supported disk is in km. The distance to the source was assumed to be 9 kpc. Errors on the luminosities are calculated based on errors of the normalizations of these components. Conventionally, errors are not quoted for the total luminosity.

temperature, by a factor of 2.1 in this case, suggests underlying heating of the neutron star and must lead to increased radiation pressure, scaling as T^4 . Changes in kT_{bb} are anti-correlated with the changes of the blackbody radius. R_{bb} is 11.0 ± 0.7 km at the soft apex suggesting that at this point the neutron star radiates with its whole surface. However, this changes along the NB and the HB, where the blackbody radius decreases to ~ 2 km indicating a substantial change in the emission region on the star.

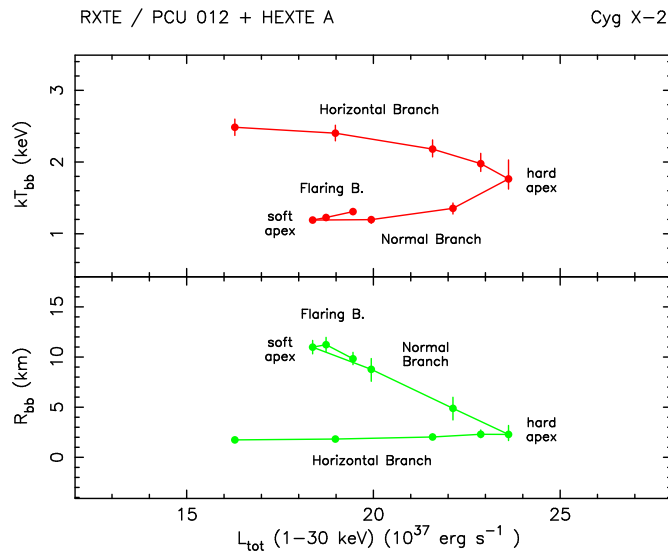


Figure 4.4: The temperature (upper panel) and the radius (lower panel) of the blackbody model component shown as a function of the total 1 - 30 keV luminosity of the source. Errors were obtained from fitting results and are given at the 90 % (2σ) confidence level.

On the Flaring Branch, there is a slight increase of the blackbody temperature and the blackbody radius remains in the narrow range of 9.8 - 11.2 km showing no clear trend. Given the errors of ± 0.7 km, R_{bb} can thus be considered constant on the FB. This suggests that the emission region remains similar to that at the soft apex and is consistent with the whole neutron star emitting.

The luminosities of the model components The variation of the luminosities of the two main model components, L_{bb} and L_{cpl} , are shown in Fig. 4.5. It is appropriate to discuss the Comptonization term L_{cpl} first, as it dominates, contributing more than 80% of L_{tot} at all times. It is apparent, that L_{cpl} increases by 150% on the Normal Branch and reaches the maximum as the source approaches the hard apex. It then decreases along the Horizontal Branch to a low value close to that at the soft apex. Substantial changes of the luminosity of the dominant model component are unlikely to take place without similar changes in \dot{M} (Church et al. 2006) on these branches, this having immediate consequences on the direction in which \dot{M} changes on the Z-track

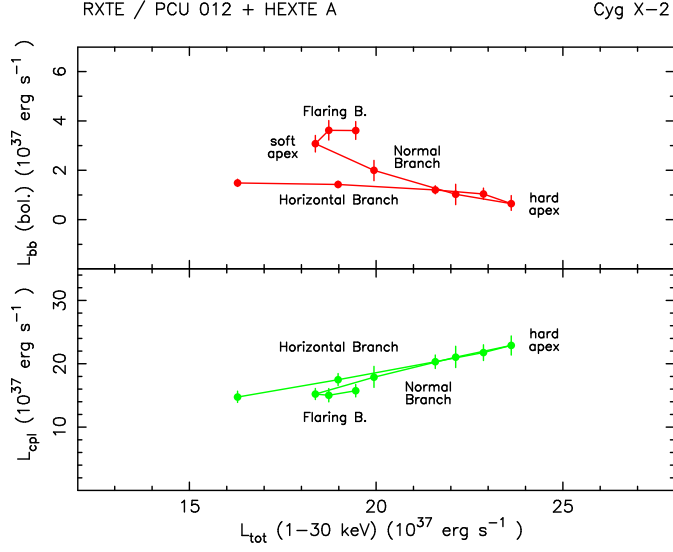


Figure 4.5: The blackbody bolometric luminosity (upper panel) and the 1 - 30 keV cut-off power law luminosity (lower panel) as a function of the total 1 - 30 keV luminosity.

as will be discussed later. On the Flaring Branch, there is not much change in L_{cpl} and hence one would expect that mass accretion rate remains constant. However, from Fig. 4.5 it can be seen that it is the blackbody luminosity that changes on this branch increasing by a factor of almost two with respect to its value from the lower NB, before the onset of flaring. The constancy of L_{cpl} suggests constant \dot{M} so that flaring is related to changes in the neutron star blackbody. On the other branches of the Z-track, L_{bb} responds to combined changes in kT_{bb} and R_{bb} decreasing along the Normal Branch and remaining small on the Horizontal Branch without substantial changes.

The cut-off power law The cut-off energy E_{co} and the normalization of the Comptonization model component are shown in Fig. 4.6, in the upper and the lower panel, respectively. E_{co} is 5.17 ± 0.11 keV and minimal at the soft apex. It then increases monotonically along the Normal and the Horizontal Branch reaching 6.7 ± 0.3 keV at the left end of the HB. This behaviour closely resembles the changes of kT_{bb} suggesting a possible relation between the two quantities, i.e. that the neutron star temperature affects the ADC temperature. The normalization of the power law component follows the changes of L_{cpl} described before.

The emission line The emission line has a centroid energy of 6.67 ± 0.13 keV at the soft apex and the Flaring Branch, and this is the lowest energy of this line on the Z-track. As the source moves from the soft apex towards the hard apex, the line energy increases to a maximal value of 6.95 ± 0.25 keV and then decreases to lower values as the source enters the Horizontal Branch and

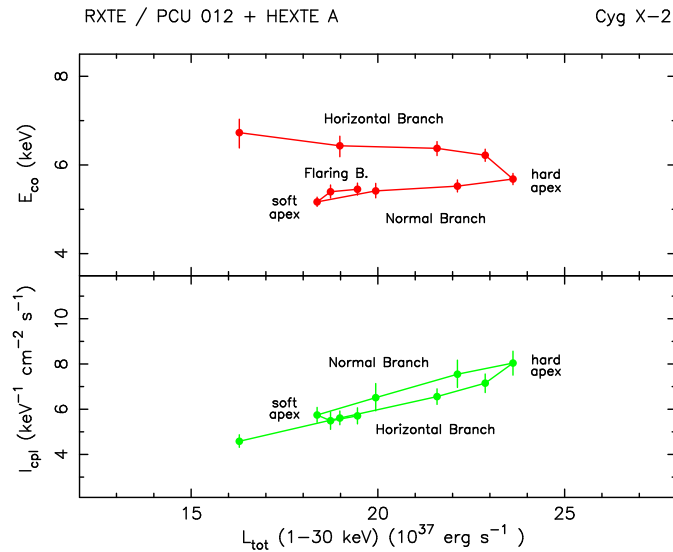


Figure 4.6: The cut-off energy (upper panel) and the normalization (lower panel) of the power law model component.

moves towards its left end. The energies indicate high ionization state and so formation in the ADC. This behaviour is well correlated with the changes of L_{cpl} suggesting that the line responds to the changes in the corona. The equivalent width of the line was ~ 70 eV.

4.1.4 Timing results

The presentation of timing results now follows, and these were obtained in the same data selections as the spectral results, to allow their direct comparison (Sect. 4.3). Power spectra obtained for every data selection were examined in *Xspec* in order to search for kHz QPO. An additional grouping of typically more than 40 - 80 count s⁻¹ per bin was applied to improve the signal to noise ratio and allow use of the χ^2 statistic in fitting. This choice, as found by trial and error, gave the best visibility of QPO signals. Having done this, QPO were found in selections on the Horizontal Branch but were not detected elsewhere. This is consistent with other observations of Cyg-like Z-track sources, and in particular of Cyg X-2 (Wijnands et al. 1997).

As the kHz QPO occur between roughly 200 and 1000 Hz, the frequency range was restricted to typically 100 - 4096 Hz. Frequencies below 100 Hz, where power spectra are complicated with broad-band noise components which would introduce additional difficulties in fitting, are not of interest. On the other hand, frequencies above 1000 Hz are very useful, as power spectra are practically flat there and allow for a better estimation of the noise level. A constant and a power law function were tested as models to fit the continuum. A power law was found to work better

as it takes into account subtle curvature of the noise at low frequencies. QPO were taken to be detected, when at least two data points were significantly above the noise determined by the power law fit. If this condition was met, an additional Lorentzian line was added to the model. Actually, in all cases, QPO were well visible and could be formally detected by eye in the power spectrum. All this helped to avoid confusion of real QPO signals with noise fluctuations and the identifications appear secure.

In selection hb3 (left end of the HB), only a single kHz QPO was detected and the power spectrum was fitted with a power law plus a Lorentzian line. The frequency of this QPO (693 ± 30 Hz) leaves no doubt that it must be the upper kHz QPO as the lower QPO would be expected below ~ 440 Hz, at which it appeared further along the HB. Similarly, a single kHz QPO at the left end of the HB was observed by Wijnands et al. (1997) who interpreted it as the upper kHz QPO, while the second peak appeared at higher count rates. In selections hb2, hb1 and ha (middle and right HB), both kHz QPO were visible and fitted with a pair of Lorentzian lines superimposed on the power law. Table 4.4 lists these fitting results and Fig. 4.7 shows representative power spectra from selections hb3 and hb2.

Table 4.4: The results on the kHz QPO detected in the data selections along the Horizontal Branch of Cygnus X-2. For each detection, the centroid frequency ν , the full width at half-maximum (FWHM) and the quality factor Q of the best-fit Lorentzian line are given. Errors are at the 90 % (2σ) confidence level.

Selection	Lower kHz QPO			Upper kHz QPO		
	ν (Hz)	FWHM (Hz)	Q	ν (Hz)	FWHM (Hz)	Q
hb3	-	-	-	693 ± 30	130 ± 50	5.3 ± 2.1
hb2	440 ± 40	100 ± 50	4.5 ± 2.3	820 ± 27	112 ± 81	7.3 ± 5.0
hb1	642 ± 65	140 ± 50	4.6 ± 1.7	928 ± 50	140 ± 50	6.6 ± 2.4
ha	652 ± 54	100 ± 50	6.5 ± 3.3	987 ± 44	130 ± 50	7.6 ± 2.9

The kHz QPO were detected on the Horizontal Branch with centroid frequencies increasing between ~ 440 Hz and ~ 987 Hz as presented as a function of the total 1 - 30 keV luminosity in Fig. 4.8. The width of the QPO was poorly determined in fitting due to the limited number of data points. Thus, a FWHM of a QPO was carefully estimated by measuring the frequencies of the left and the right sides of the Lorentzian line at its half-height. Errors on the FWHM were then taken to be twice the width of a typical frequency bin in the vicinity of a QPO. A QPO width obtained in this way was typically 100 - 140 Hz and this was in agreement with the value

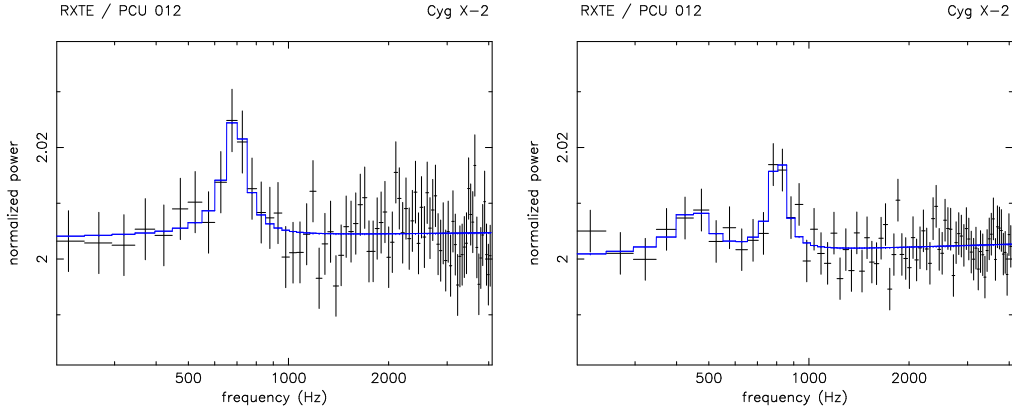


Figure 4.7: Example power spectra of Cyg X-2 when the source was on the Horizontal Branch with the best-fit model (blue). Left: selection hb3 (left end of the HB) in which a single QPO was visible only. Right: twin kHz QPO visible simultaneously in selection hb2.

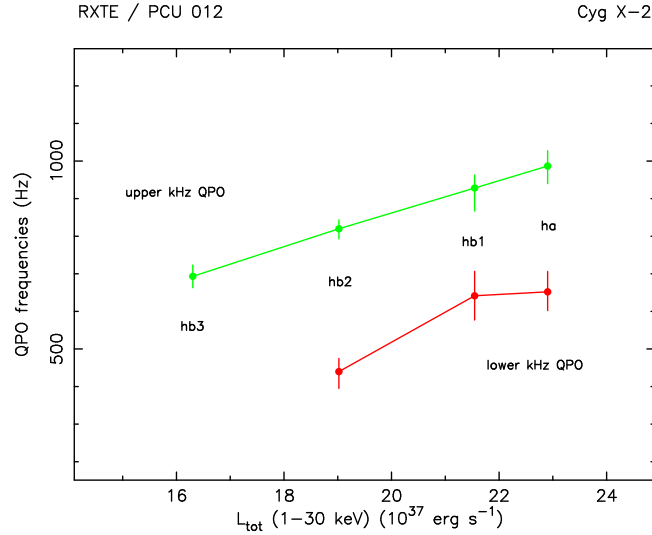


Figure 4.8: Frequencies of the lower and the upper kHz QPO as a function of the total 1 - 30 keV luminosity.

obtained directly from fitting in a single case (selection hb2, upper QPO), where the QPO width was 112 ± 81 Hz.

The quality factor ($Q = \nu/\Delta\nu$) was used to measure the QPO coherence (sharpness). In all cases, Q was higher than 2.0, thus meeting the often used formal condition for a QPO identification (e.g. Lewin et al. 1995). The QPO maintain approximately constant widths while their frequencies increase as the source moves towards the hard apex. In consequence, the quality factor tends to increase along the HB in the case of both kHz QPO, but errors are large.

The discussion of the results will be postponed until Sect. 4.3, where they will be discussed together with the results for GX 340+0, the analysis of which is now presented in the following section.

4.2 GX 340+0

A spectral analysis of GX 340+0 using the Extended ADC model, but not a timing analysis, was carried out by Church et al. (2006). It would be desirable to carry out a timing analysis using the same data (observation ID P20053 from September 21-25, 1997). However, during that observation data were not gathered in any of the useful high time resolution modes and cannot be used for this purpose. Thus, in this work, a different *RXTE* observation of GX 340+0, allowing both a spectral and timing study, is analysed.

4.2.1 Observations

The retrieved *RXTE* observation ID P20059 covers June 6th to 10th, 1997 (thus within the *RXTE* calibration epoch 3) having a total timespan of ~ 350 ks. Details of the constituent sub-observations are shown in Table 4.5.

Table 4.5: Details regarding the *RXTE* observation P20059 of GX 340+0 made in June 1997.

Sub-observation	Start Date & Time (UT)	Duration (s)
20059-01-01-000	June 06, 1997, 06:08:13	23024
20059-01-01-00	June 06, 1997, 12:32:06	10672
20059-01-01-01	June 06, 1997, 21:42:10	7136
20059-01-01-02	June 07, 1997, 11:18:09	21184
20059-01-01-03	June 07, 1997, 23:54:50	20528
20059-01-01-04	June 08, 1997, 07:54:07	21292
20059-01-01-05	June 09, 1997, 00:12:05	16864
20059-01-01-06	June 10, 1997, 01:30:31	21280

4.2.2 Data analysis

Data analysis was performed using *HEASOFT* v.6.5 as described in the previous section and in Appendix A. To avoid repetition, the procedure described below is limited to information specific to the observation analysed here.

Examination of the housekeeping data showed that all five PCU were operational during the observation and could be used for analysis. Standard screening criteria were applied: **OFFSET** $< 0.02^\circ$ and **ELV** $> 10^\circ$. The above conditions were translated into GTI giving a total of 86.4 ks of clean data.

Lightcurves were extracted from Standard2 data using the top layers (left and right) of all 5 PCU

with a time resolution of 64 seconds. The lightcurves were produced in four energy ranges, i.e.: low (1.9 - 4.1 keV, channels 5 - 10), medium (4.1 - 7.3 keV, channels 11 - 18), high (7.3 - 20.3 keV, channels 19 - 55) and total (1.9 - 20.3 keV). The channel-to-energy correspondence was based on the appropriate conversion table recommended for the 3rd *RXTE* calibration epoch of the observation to obtain the desired energy bands.

Given the source count rate of more than $4000 \text{ count s}^{-1}$ ($> 800 \text{ count s}^{-1} \text{ PCU}^{-1}$), relevant background lightcurves were produced using the most recent PCA bright background model. Background subtraction was next performed in all energy bands. Deadtime correction was carried out raising the original count rate by $\sim 3.5\%$. The total, background-subtracted and deadtime-corrected lightcurve is shown in Fig. 4.9. Hardness was defined as the ratio of count rates in high and medium energy bands and is shown against the total (1.9 - 20.3 keV) intensity of the source in Fig. 4.10.

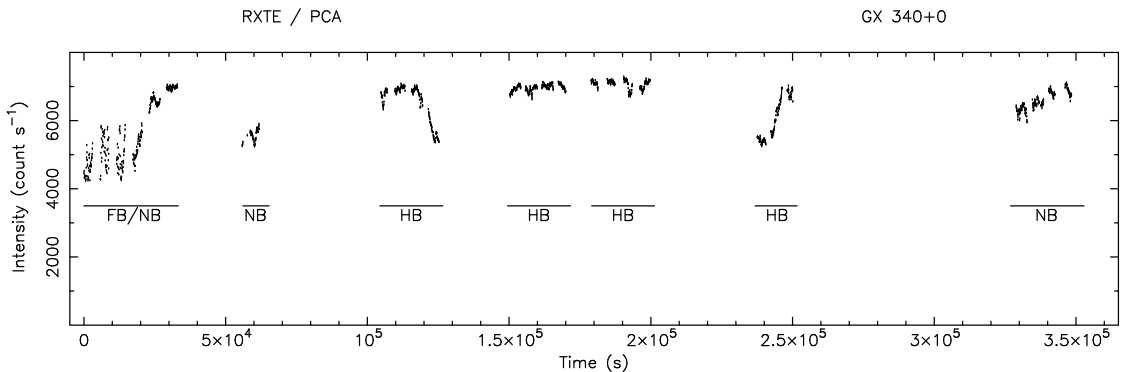


Figure 4.9: The background-subtracted and deadtime-corrected 1.9 - 20.3 keV lightcurve of GX 340+0 with 64 second binning. Particular sections were identified as: FB - Flaring Branch, NB - Normal Branch, and HB - Horizontal Branch.

Sections of the lightcurve were identified with corresponding sections in hardness-intensity and the behaviour of the source in time could be deciphered. As can be seen from Fig. 4.9, during the first 20 ks of the observation, the source was close to the soft apex and exhibited flaring forming a Flaring Branch in hardness-intensity. Then the source moved onto the Normal Branch and the Horizontal Branch, where it spent most of the remaining observation time. In particular, GX 340+0 made excursions along the HB (up and down in intensity) which are clearly visible at $\sim 1.2 \times 10^5 \text{ s}$ and at $\sim 2.5 \times 10^5 \text{ s}$. At the end of the observation, the source was again on the Normal Branch. Despite relatively large data gaps between sub-observations, a full Z-track was traced (Fig. 4.10) during the 4 days of the observation.

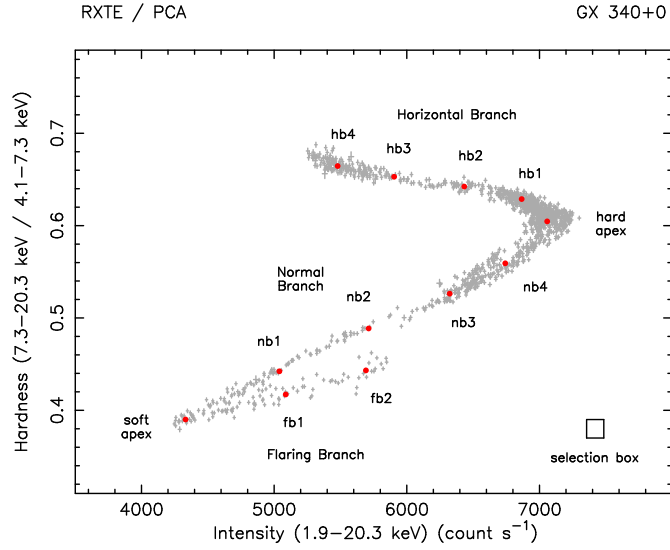


Figure 4.10: The hardness-intensity variation of GX 340+0 (background-subtracted and deadtime-corrected). Every point corresponds to 64 seconds of data. The data selections, marked with red filled circles had a size as the box shown in the bottom right corner.

A set of selections was next chosen along the Z-track. Four selections (hb4 - hb1) were placed along the Horizontal Branch, one selection at the hard apex (ha), four selections (nb4 - nb1) along the Normal Branch, one selection (sa) at the soft apex and two selections (fb1 - fb2) on the Flaring Branch. The selection size was 130 count s^{-1} (in intensity) $\times 0.02$ in hardness. The choice of the selection size was an issue here, as in the case of Cyg X-2. Selections had to be large enough to reveal QPO signals (Sect. 4.2.4) and also as small as possible in order not to average too much data for spectral analysis. This is especially important in those parts of the Z-track, where the hardness changes most rapidly (i.e. along the NB). Thus the size chosen was a compromise between these two opposed requirements.

From the selection criteria, Good Time Interval files were produced and used to extract PCA spectra (from the top layers of all 5 PCU) together with corresponding background spectra. Deadtime correction was done following the standard procedure. Systematic errors of 1% were applied to every energy channel to take into account any PCU calibration uncertainties. Higher energy channels (above $\sim 25 \text{ keV}$) were in several cases additionally grouped to improve their signal to noise ratio. A PCA response file was produced.

HEXTE spectra were produced by extracting Cluster B data (with 3 of 4 detectors operational, detector 2 having failed early in the mission) obtaining a single on-source and a single off-source (background) spectrum per data selection. The redistribution matrix file (RMF) and the auxiliary response files (ARF) were used in their standard versions. HEXTE spectra were additionally

improved when needed by grouping high energy channels into typically groups of two or four.

The number of counts per spectral channel was very high, typically $10^4 - 10^5$ (PCA) and $10^2 - 10^3$ (HEXTE), allowing high quality spectral fitting.

The only data useful for the timing analysis in this observation were PCA Event mode data designated E.8us.32B_14.1s and covering 5 - 100 keV energy range with $8 \mu\text{s}$ time resolution. The analysis procedure of this sort of data was not covered earlier and hence is given here. For each sub-observation, a set of raw Event mode data was identified. From these, the sections corresponding to the selection GTI were retrieved using GROSSTIMEFILT. The Event mode provides information about the energy of collected photons and thus allows energy filtering. This is very useful, as on many occasions it has been found (e.g. Jonker et al. 1998) that data below ~ 5 keV and above ~ 60 keV are dominated by noise and could thus be removed. To find the energy-to-channel relation needed to define the energy filter, a spectrum was produced from Event mode data, the extraction carried out using SEEXTRACT, whereas a proper response file could be produced as usual with PCARSP. These were next read into *Xspec* in which the energy-to-channel relation was found. The condition, to remove energies below 5 keV (which in this case is the lower limit anyway) and above 60 keV, was first translated into binary code, called a bitmask, using SEBITMASK. The bitmask could then be applied to Event mode data using FSELECT giving the final time-filtered and energy-filtered data ready for a timing analysis.

Cleaned Event mode data were then loaded into POWSPEC. The original time resolution of $8 \mu\text{s}$ in this case is much higher than needed for studies of QPO occurring in the $\sim 100 - 1000$ Hz range and was thus decreased 16 times to $125 \mu\text{s}$ allowing for production of power spectra extending to 4096 Hz. Data were divided into intervals chosen to be 0.5 - 1.0 s long which were used in POWSPEC to produce a power spectrum for which the Leahy normalization was made. An output power spectrum was then converted into *Xspec* format. The whole procedure was repeated for every data selection along the Z-track. Thus, spectral and timing results were obtained for the same data selections allowing their direct comparison.

4.2.3 Spectral fitting results

Xspec was used for simultaneous fitting of PCA and HEXTE spectra. An inter-instrumental constant was introduced to take into account cross-calibration uncertainty between the two *RXTE* instruments and frozen at 1.0 for the PCA, and left free for the HEXTE. It was found to be in

the acceptable range of 0.73 - 0.98. The PCA spectrum was restricted to the range from 3 keV to about 20 - 29 keV. In HEXTE the energy range was typically between 18 keV and 35 - 40 keV. The cut-off power law photon index was frozen at 1.7 as explained in Sect. 4.1.

The column density was left free except on the Flaring Branch where it was necessary to freeze it at a value from the soft apex to get stable fitting results. In fact, it was checked that the free fitting values of N_H in selections on the Flaring Branch were close to the value from the soft apex so freezing N_H on this branch did not lead to systematic errors.

Initial fitting with the Extended ADC model revealed the presence of an emission line at around 6.5 keV. The width of the line, based on the residuals was found to be about $\sigma \sim 0.5$ keV with no apparent changes along the Z-track and was therefore frozen at this value to prevent absorption of the continuum. The inclusion of the line improved the goodness of fit in all cases, giving a $\chi^2/\text{d.o.f.}$ of typically 18/54 - 51/54 although not that good on the Flaring branch (55/37 in the worst case).

Figure 4.11 shows typical spectra, one from each of the Z-track branches, in the folded form (with the residuals demonstrating the goodness of fit) and the unfolded form. Spectral fitting results and associated auxiliary physical quantities calculated from model parameters are listed in Table 4.6 and Table 4.7, respectively. The analysis results are now presented below.

Absorption Low values of N_H are not well constrained in fitting with the PCA given its sensitivity only above ~ 3 keV which may affect values of other model parameters. This however is not the case here as in this source the column density is relatively high, with a minimal value of $N_H = 6.9 \pm 0.9 \times 10^{22}$ atom cm^{-2} at the soft apex. As the source moves up the NB, the column density increases to a maximum value of $11.2 \pm 0.5 \times 10^{22}$ atom cm^{-2} at the hard apex and then decreases slightly on the HB. The changes are significant and well correlated with the position of the source on the Z-track which suggests they are intrinsic to the source.

Blackbody temperature and radius The systematic variations of the blackbody parameters, kT_{bb} and R_{bb} are presented in Fig. 4.12. The blackbody temperature (upper panel) is lowest at the soft apex with the value of 1.25 ± 0.02 keV. The temperature then increases monotonically to 2.31 ± 0.14 keV at the hard apex and 2.43 ± 0.09 keV at the end of the HB. The change by a factor of over 1.9 implies increased radiation pressure (scaling as T^4) by a factor of ~ 15 , which is likely to affect the inner disk, and the discussion of the effects of this will be given in Sect. 4.3.

Table 4.6: The results of spectral fitting to the data selections along the Z-track of GX 340+0.

Sel.	N_H	Blackbody		Emission line		Cut-off power law		$\chi^2/\text{d.o.f.}$
		kT_{bb}	$norm$	E_l	EW	E_{co}	$norm$	
hb4	9.4 ± 0.5	2.43 ± 0.09	3.4 ± 0.3	6.83 ± 0.30	86	5.72 ± 0.25	9.7 ± 0.7	18/53
hb3	9.9 ± 0.6	2.40 ± 0.11	3.9 ± 0.6	6.90 ± 0.32	85	5.31 ± 0.38	11.5 ± 1.0	30/54
hb2	10.5 ± 0.5	2.39 ± 0.10	3.6 ± 0.4	7.07 ± 0.30	88	5.31 ± 0.27	13.2 ± 1.0	38/56
hb1	10.9 ± 0.5	2.35 ± 0.09	3.4 ± 0.3	7.20 ± 0.33	81	5.17 ± 0.20	14.9 ± 0.9	37/57
ha	11.2 ± 0.5	2.31 ± 0.14	2.6 ± 0.4	7.26 ± 0.32	85	5.03 ± 0.20	16.6 ± 1.1	27/58
nb4	10.7 ± 0.6	1.80 ± 0.26	1.4 ± 0.8	7.11 ± 0.38	79	5.12 ± 0.14	15.9 ± 1.3	27/57
nb3	10.2 ± 0.7	1.47 ± 0.16	1.6 ± 1.1	6.84 ± 0.37	76	4.85 ± 0.14	15.3 ± 1.6	33/54
nb2	9.4 ± 0.8	1.31 ± 0.08	3.1 ± 1.5	6.65 ± 0.34	75	4.66 ± 0.20	12.8 ± 2.1	33/54
nb1	8.5 ± 0.8	1.27 ± 0.04	4.2 ± 1.2	6.50 ± 0.32	70	4.31 ± 0.18	11.2 ± 1.8	51/54
sa	6.9 ± 0.9	1.25 ± 0.02	6.9 ± 1.0	6.26 ± 0.26	68	3.82 ± 0.23	7.8 ± 1.9	51/54
fb1	6.9^f	1.36 ± 0.02	10.6 ± 0.5	6.4^f	36	3.46 ± 0.15	8.1 ± 0.8	58/47
fb2	6.9^f	1.44 ± 0.16	14.1 ± 0.7	6.4^f	22	2.62 ± 0.33	10.9 ± 2.0	55/37

N_H is in 10^{22} atom cm^{-2} , kT_{bb} , E_l and E_{co} are given in keV, the line equivalent width is in eV. The blackbody normalization is in 10^{37} erg s^{-1} for the distance of 10 kpc, the power law component normalization is in photons $\text{keV}^{-1} \text{cm}^{-2} \text{s}^{-1}$ at 1 keV.

^f - the parameter was frozen in fitting.

Table 4.7: The additional physical quantities derived from the spectral fitting results.

Selection	R_{bb}	h	f_{bb}/f_{Edd}	\dot{m}	L_{bb}	L_{cpl}	L_{tot}	H_{eq}
hb4	3.0 ± 0.3	0.91 ± 0.15	2.4 ± 0.2	22 ± 4	4.1 ± 0.3	42 ± 3	46	39 ± 3
hb3	3.3 ± 0.4	1.1 ± 0.2	2.3 ± 0.3	20 ± 4	4.7 ± 0.6	47 ± 4	52	44 ± 4
hb2	3.2 ± 0.3	1.0 ± 0.2	2.2 ± 0.3	24 ± 5	4.3 ± 0.5	53 ± 4	58	49 ± 4
hb1	3.2 ± 0.3	1.1 ± 0.2	2.1 ± 0.2	26 ± 5	4.1 ± 0.4	59 ± 4	63	54 ± 3
ha	2.9 ± 0.4	0.9 ± 0.2	2.0 ± 0.3	34 ± 9	3.1 ± 0.4	64 ± 4	68	58 ± 4
nb4	3.5 ± 1.4	1.6 ± 1.0	0.7 ± 0.4	22 ± 17	1.7 ± 0.9	63 ± 5	64	55 ± 4
nb3	5.7 ± 2.3	3 ± 3	0.3 ± 0.2	8 ± 7	1.9 ± 1.3	58 ± 6	60	51 ± 5
nb2	10.0 ± 2.5	10 ± 5	0.20 ± 0.09	2 ± 1	3.7 ± 1.7	47 ± 7	51	43 ± 7
nb1	12.4 ± 1.9	15 ± 5	0.18 ± 0.05	1.2 ± 0.4	5.0 ± 1.4	38 ± 6	43	37 ± 6
sa	16.2 ± 1.2	26 ± 4	0.17 ± 0.02	0.53 ± 0.08	8.2 ± 1.2	24 ± 6	32	28 ± 7
fb1	17.1 ± 0.7	29 ± 2	0.233 ± 0.012	0.52 ± 0.04	12.6 ± 0.6	23 ± 2	35	30 ± 3
fb2	17.6 ± 0.6	31 ± 2	0.293 ± 0.014	0.56 ± 0.04	16.8 ± 0.8	23 ± 4	40	34 ± 6

The units are: km (blackbody radius R_{bb} , half-height of the equatorial belt h , equilibrium half-height H_{eq} of the inner accretion disk), $10^5 \text{ g cm}^{-2} \text{ s}^{-1}$ (\dot{m}), $10^{37} \text{ erg s}^{-1}$ (the luminosities, in 1 - 30 keV range for the cut-off power law and the total luminosity, and bolometric for the blackbody). The distance to the source was assumed to be 11 kpc.

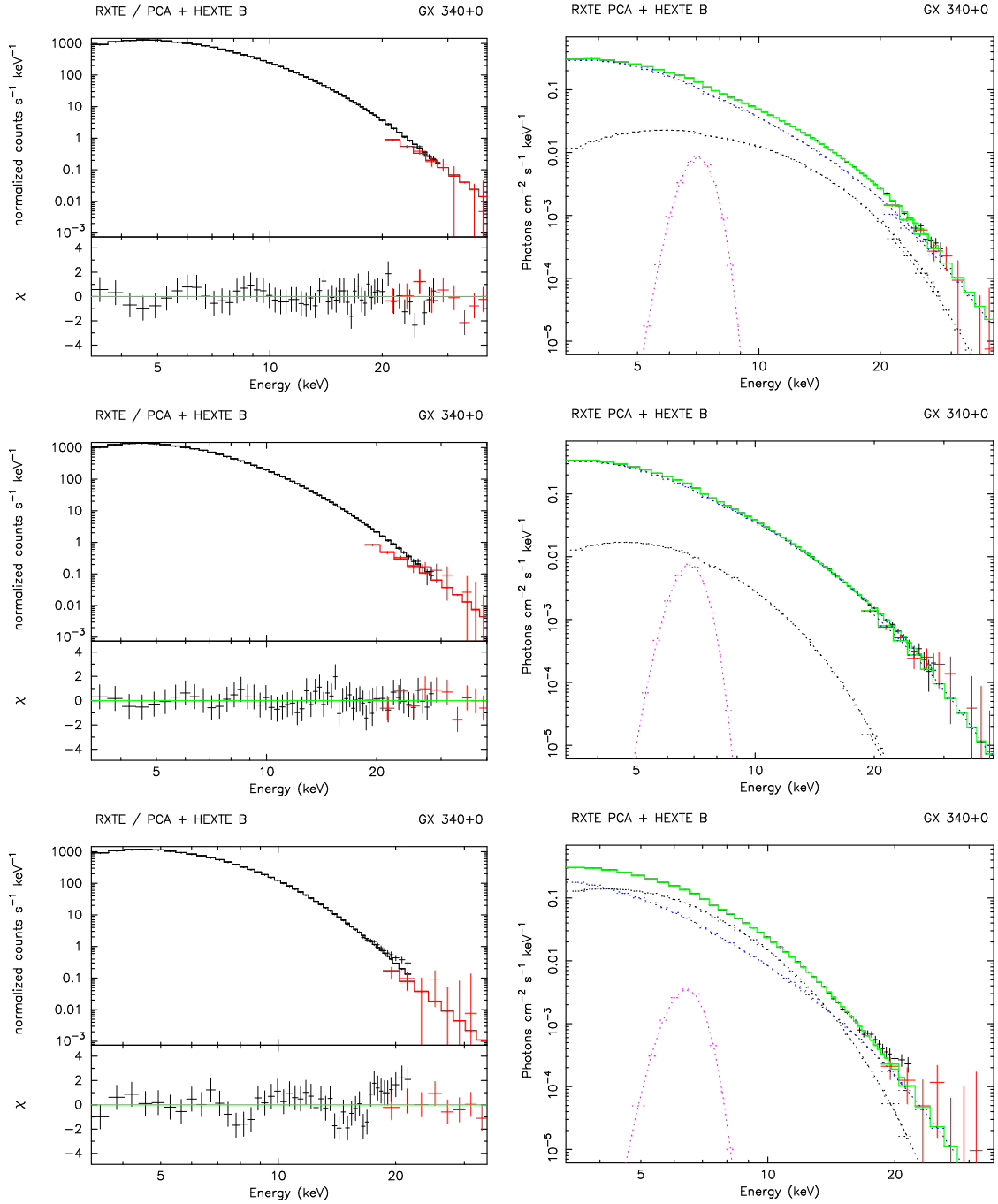


Figure 4.11: Example folded spectra (left) and unfolded spectra (right). Top: Horizontal Branch (selection hb3); middle: Normal Branch (nb3); bottom: Flaring Branch (fb1). Left: PCA and HEXTE data are shown in black and red, respectively. The best-fit model is shown in green. Right: the individual model components shown in the unfolded spectra: blackbody (black), cut-off power law (blue), emission line (magenta), and the total spectrum (green).

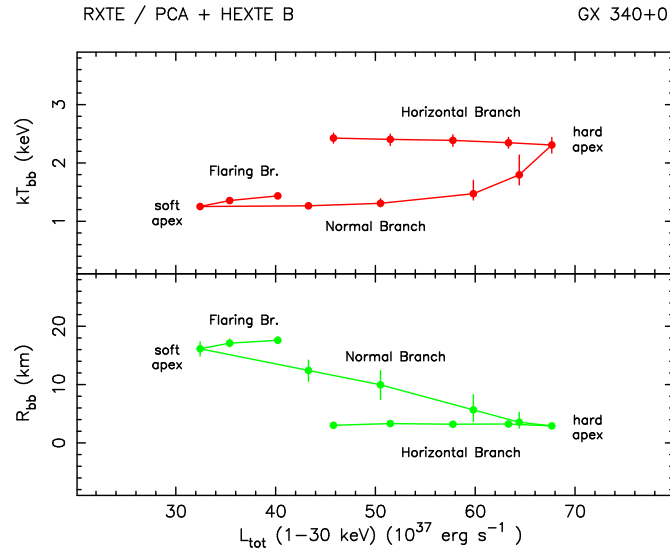


Figure 4.12: The blackbody parameters: temperature (top) and radius (bottom) shown versus the total 1 - 30 keV luminosity of the source. 90% confidence errors are given.

The changes of kT_{bb} are accompanied by a clear reduction of the blackbody radius, most pronounced on the Normal Branch. Its value decreases as soon as the source leaves the soft apex and is only 2.9 ± 0.4 km at the hard apex remaining then close to ~ 3 km on the HB. This indicates that on the NB and the HB the emission region most probably corresponds to a narrow structure, such as an equatorial belt, whose area corresponds to that of a sphere having the blackbody radius measured.

Close to the soft apex the blackbody radius is larger, and at the soft apex itself R_{bb} is 16.2 ± 1.2 km increasing slightly further on the Flaring Branch (lower panel of Fig. 4.12). This implies that the emission region may have expanded beyond the surface of the neutron star during flaring. This behaviour is consistent with that observed earlier by Church et al. (2006), although their value of $R_{bb} = 10.8 \pm 1.1$ km at the soft apex was significantly smaller than that obtained in the present work, and this difference will be addressed in the discussion. However, it is noted that on the lower Normal Branch the value of R_{bb} measured here is 12.4 ± 1.9 km and consistent with the whole star emitting, and thus the expansion of the emission region on the FB is clearly related to the onset of flaring. At the same time, the blackbody temperature increases slightly in flaring reaching ~ 1.44 keV suggesting some heating of the neutron star.

Luminosities of the model components Figure 4.13 shows changes of the luminosities of the blackbody (upper panel) and the power law (lower panel). The luminosity of the Comptonized emission is more than 75% to the total, except on the FB ($\sim 60\%$ of L_{tot}) where the blackbody

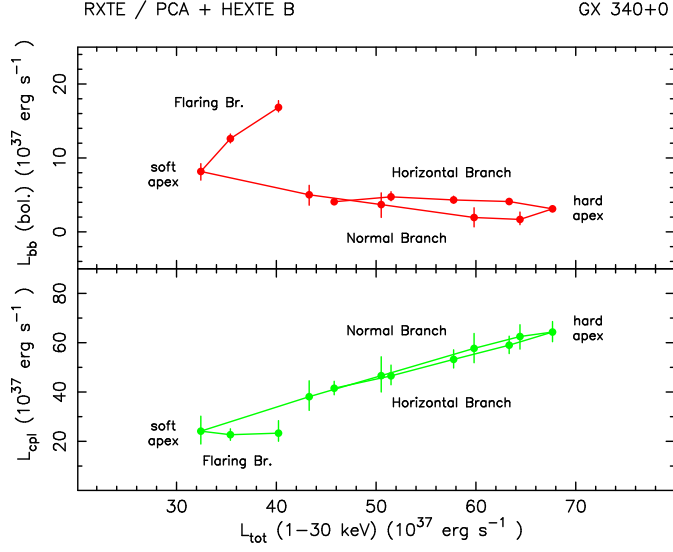


Figure 4.13: The luminosity of the blackbody component (bolometric, upper panel) and the 1 - 30 keV luminosity of the cut-off power law component as a function of the total (1 - 30 keV) luminosity.

strongly increases (below). L_{cpl} increases strongly in the direction from the soft apex towards the hard apex by a factor of ~ 2.7 . Then, from the maximum at the hard apex, L_{cpl} decreases on the Horizontal Branch by a factor of ~ 1.5 . As argued before (Sect. 3.1 and Sect. 4.1), these changes are unlikely to happen without changes in mass accretion rate. This contrasts with an apparent constancy of L_{cpl} on the Flaring Branch. However, there is a striking increase of the blackbody contribution to the total, from about 11% at the lower NB up to almost 42% of L_{tot} at the right end of the Flaring Branch. A simple examination of Fig. 4.10 reveals that intensity changes on the FB by $\sim 30\%$ are consistent with this change in the blackbody luminosity alone. This provides clear evidence that flaring is caused by changes on the neutron star and not a variation in mass accretion rate which, following L_{cpl} , is most probably constant on the FB.

The power law cut-off energy and normalization The variations of the power law component, E_{co} and normalization, are shown in Fig. 4.14. The cut-off energy shows a clear trend increasing all the way along the Z-track from a low value of 2.6 ± 0.4 keV at the right end of the FB to 5.7 ± 0.3 keV at the left end of the HB. Thus, except on the FB, E_{co} is correlated with the blackbody temperature. The normalization of the power law changes most strongly on the NB and the HB corresponding to the changes in L_{cpl} .

The normalization is rather constant on the FB and there is no significant change of L_{cpl} . In fact, the values of E_{co} and the power law normalization reported by Church et al. (2006), whose

quality of fits was better on the FB, do not show any significant variations on the Flaring Branch, supporting the above argument.

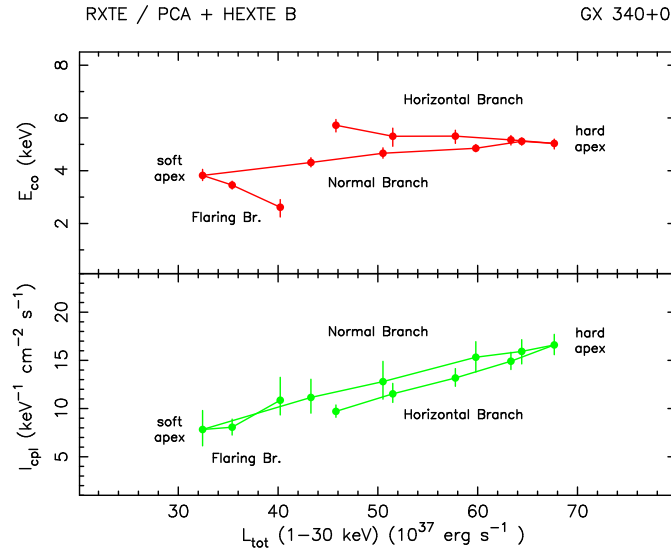


Figure 4.14: The cut-off power law parameters: cut-off energy (top panel) and normalization (bottom panel).

The Fe emission line The emission line has a minimal centroid energy (6.3 ± 0.3 keV) at the soft apex and is, within errors, consistent with the 6.4 keV $K\alpha$ line of low ionization state of iron. It was frozen at this value on the FB where the line energy was similarly small, but difficult to be constrained in free fitting. The line energy then significantly increases in the direction soft apex \rightarrow hard apex, where it reaches a maximum of 7.3 ± 0.3 keV, and then decreases along the HB to a slightly lower value. Thus the changes of the line energy clearly reveal varying ionization in the emission region along the Z-track and correlate well with the luminosity of the power law pointing towards the origin of the line in the accretion disk corona.

4.2.4 Timing results

A power spectrum from every data selection was read into *Xspec* and restricted to the 150 - 4096 Hz frequency range in which kHz QPO occur. Original power spectra from POWSPEC were noisy and an additional grouping was applied to have at least 70 - 90 counts per frequency bin. The noise level was then satisfactorily fitted with a power law and a search for QPO was made by looking for any power excesses above the noise. As in the case of CygX-2 (Sect. 4.1.4), the formal condition for a QPO detection was to have at least two points with their errors above the

fitted noise level. However, with the additional grouping applied, the QPO became easily visible and there was no problem with their detection. KiloHertz QPO were detected in selections along the Horizontal Branch only. In four selections (hb4, hb2, hb1 and ha) two simultaneous kHz QPO were visible and fitted with a pair of Lorentzian lines. In selection hb3, only a single QPO was found, the second peak not visible probably due to a lower number of counts in this selection (the Z-track is sparsely covered with data points at this position, Fig. 4.10).

Representative power spectra from the HB of GX 340+0 are shown in Fig. 4.15 with their best-fit models. Table 4.8 gathers fitting results from all selections along the Horizontal Branch and Fig. 4.16 shows QPO frequencies as a function of the total (1 - 30 keV) luminosity of the source.

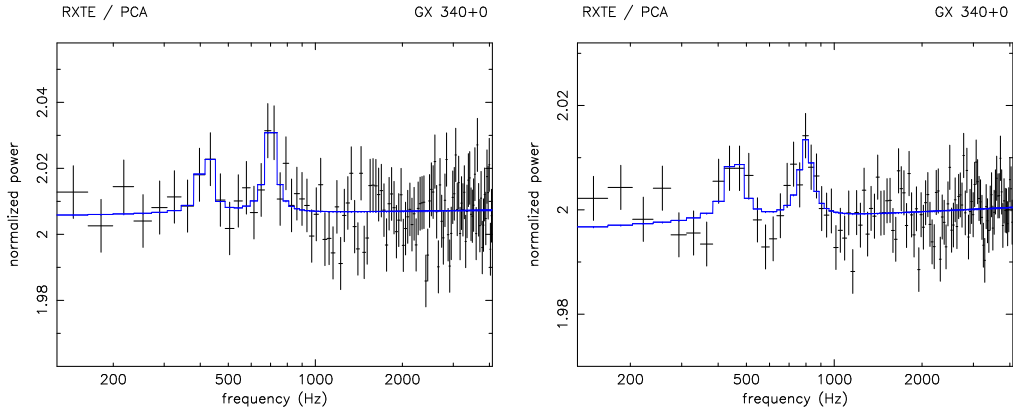


Figure 4.15: Representative power spectra of GX 340+0 when the source was on the Horizontal Branch. Left: in selection hb2; Right: in selection hb1. The best-fit model is shown in blue with the two kHz QPO fitted with a pair of Lorentzian lines and the noise level approximated by a power law function.

Table 4.8: The results on the kHz QPO found in data selections along the Horizontal Branch of GX 340+0. The parameters shown are: the centroid frequency ν , the full width at half-maximum (FWHM) and the quality factor Q . Errors are given at the 90% (2σ) confidence level.

Selection	Lower kHz QPO			Upper kHz QPO		
	ν (Hz)	FWHM (Hz)	Q	ν (Hz)	FWHM (Hz)	Q
hb4	263 ± 37	80 ± 40	3.3 ± 1.7	643 ± 36	177 ± 97	3.6 ± 2.0
hb3	-	-	-	640 ± 50	150 ± 70	4.3 ± 2.0
hb2	419 ± 60	75 ± 35	5.6 ± 2.8	702 ± 24	70 ± 35	10.0 ± 5.0
hb1	456 ± 33	68 ± 75	6.7 ± 6.7	800 ± 29	89 ± 69	9.0 ± 7.0
ha	494 ± 72	100 ± 45	4.9 ± 2.4	866 ± 45	70 ± 45	12.4 ± 8.0

Both the lower and the upper kHz QPO are visible already at the left end of the HB. Their

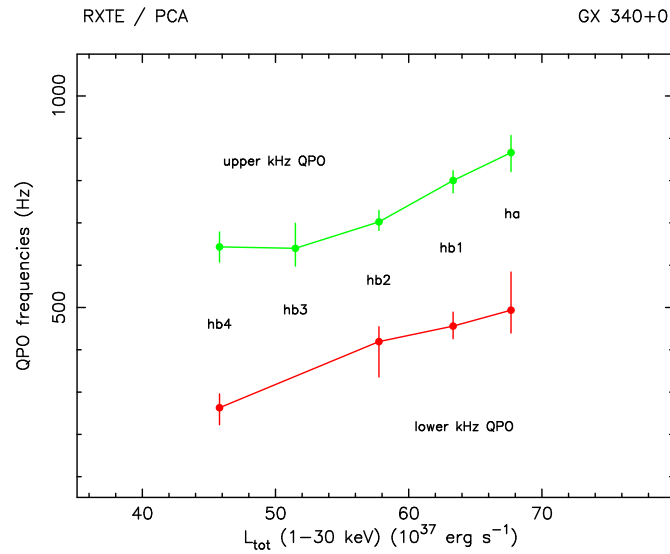


Figure 4.16: The lower and the upper kHz QPO frequency as a function of the total (1 - 30 keV) luminosity of GX 340+0. Five detections were made in data selections along the Horizontal Branch, in four of them the two QPO were detected simultaneously.

frequencies increase along the branch towards the hard apex to 494 ± 72 Hz and 866 ± 45 Hz, respectively. The single QPO visible in selection hb3 is clearly the upper kHz QPO, given its high frequency of ~ 640 Hz.

The QPO FWHM is in the range 70 - 100 Hz and 70 - 180 Hz for the lower and upper kHz QPO, respectively. In the case of the lower kHz QPO, the width shows no clear trend along the HB and within errors appears constant. The upper kHz QPO is broader than the lower QPO, but its width decreases along the branch towards the hard apex. The result of this is that its quality factor Q increases along the branch in that direction. The quality factor of the lower kHz QPO shows no clear trend along the branch.

4.3 Discussion

The results obtained here for Cyg X-2 and GX 340+0 share many similarities and thus it is convenient to discuss them together in this section. First, the spectral changes in the two sources will be compared with the previous work and discussed in terms of the model for the Z-track in the Cyg-like sources of Church et al. (2006) presented in Sect. 3.1. Then, following the approach of Jackson et al. (2009), the spectral results will be compared with the behaviour of the kHz QPO which is the main purpose of this chapter.

4.3.1 A comparison with previous work

Firstly, it is shown that the present spectral fitting results are in good agreement with those obtained before by Church et al. (2006) in the case of GX 340+0 and Bałucińska-Church et al. (2010) for Cyg X-2. Figure 4.17 shows an example of a comparison of the parameters of the blackbody model component in this and the previous work.

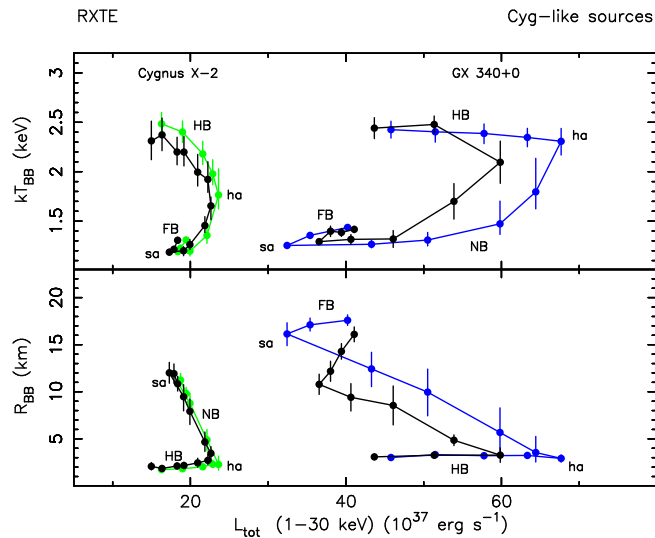


Figure 4.17: A comparison of the spectral fitting results obtained in this work for Cyg X-2 (green) and GX 340+0 (blue) with those obtained by Church et al. (2006) and Bałucińska-Church et al. (2010) for the two sources (black), respectively.

The agreement is particularly good in the case of Cyg X-2 and this is because in the present work the same dataset was re-analysed, but using larger data selections. The current results for GX 340+0 also closely resemble those of Church et al. (2006), although a different observation was analysed in the present work and also the selections were larger.

Most importantly, the patterns of the model parameters along the Z-track remain very similar showing that independent analyses give the same spectral behaviour of these sources.

4.3.2 The neutron star blackbody and strong radiation pressure

Let us begin with the discussion of the changes associated with the neutron star blackbody. It is convenient to start from the point where the blackbody temperature is minimal on the Z-track. i.e. the soft apex, and the values measured here (~ 1.2 keV) are in a good agreement with those previously reported (Church et al. 2006; Bałucińska-Church et al. 2010). At this point, the measured blackbody radius in Cyg X-2 is 11.0 ± 0.7 km, thus clearly indicating that emission originated from the whole surface of the neutron star. It is also in agreement with $R_{bb} = 12.0 \pm 1.1$ km reported by Bałucińska-Church et al. (2010). In the case of GX 340+0, the measured R_{bb} at the soft apex was 16.2 ± 1.2 km and thus larger than that measured by Church et al. (2006) (10.8 ± 1.1 km). This however, as noticed in Sect. 4.2.3, may be related to the radius expansion taking place in flaring and larger size of data selections used in this work, so that there is some mixing of soft apex data with flaring data leading to overestimation of the blackbody radius. In fact, the value of R_{bb} , measured on the lower NB where such mixing of data was not an issue, was smaller (12.4 ± 1.9 km).

It is thus apparent (Fig. 4.17, bottom panel) that away from the soft apex, the emission region on the neutron star is either reduced, as on the NB/HB, or extends beyond the neutron star surface (as on the FB in GX 340+0). All this supports the proposition of Church et al. (2006) that the soft apex is a type of a quiescent state of the source, beyond which substantial physical changes take place.

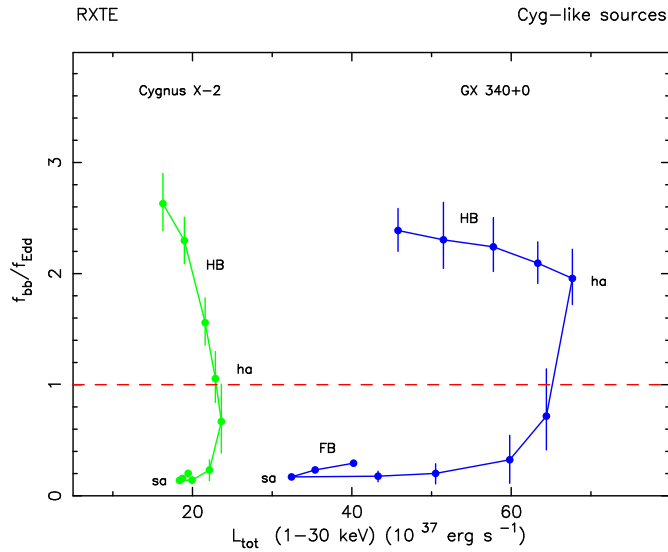


Figure 4.18: The ratio of the blackbody flux f_{bb} to the Eddington flux f_{Edd} .

As the source moves on the Normal Branch towards the hard apex, the blackbody temperature

increases by a factor of ~ 2 leading to increased radiation pressure from the neutron star. Following Church et al. (2006) it is possible to trace the changes in the radiation pressure using the ratio f_{bb}/f_{Edd} (Sect. 3.1.5) which is a better estimate of conditions local to the neutron star surface than the ratio L_{bb}/L_{Edd} which averages over the whole sphere as if it was observed by a distant observer. The emissive blackbody flux is taken as $f_{bb} = L_{bb}/4\pi R_{bb}^2$, whereas the Eddington flux given by $L_{Edd}/4\pi R_*^2 = 1.4 \times 10^{25}$ erg cm $^{-2}$ s $^{-1}$. The flux ratio as a function of the total 1 - 30 keV luminosity of the source is shown in Fig. 4.18 for the two sources analysed here. It is clear from the figure, that the flux ratio is low ($f_{bb} < f_{Edd}$) when the source is close to the soft apex, but then increases quickly as it moves towards the hard apex. Close to the hard apex the flux ratio becomes super-Eddington ($f_{bb} > f_{Edd}$) and increases further along the Horizontal Branch. This agrees with the results of Church et al. (2006) and Bałucińska-Church et al. (2010) confirming the importance of the strong radiation pressure on the upper NB and the HB.

As mentioned in Sect. 1.1.2, at high luminosities the inner accretion disk is dominated by radiation pressure and deviates from its standard thin form being puffed close to the neutron star. The half-height H of the inner disk, reaching an equilibrium half-height H_{eq} very close to the neutron star, is given by Eqn. 1.16 and depends on the mass accretion rate, which can be derived from the total luminosity via Eqn. 1.1. Given the luminosities of the two sources, the inner disk towers ~ 20 km (Table 4.3) and ~ 50 km (Table 4.7) above the disk plane in Cyg X-2 and GX 340+0, respectively. However, this may change with increased radiation pressure from the surface of the star which can disrupt the top layers of the disk and effectively reduce its height as schematically depicted in Fig. 4.19.

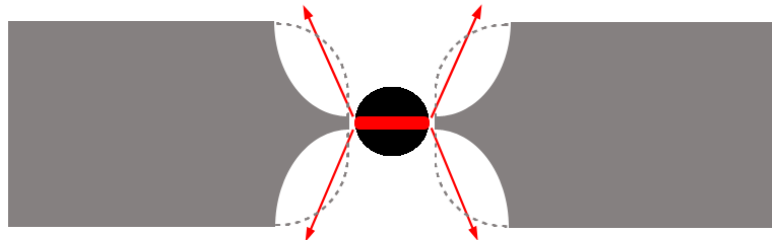


Figure 4.19: A schematic side view of the effects of the strong radiation pressure on the inner disk. The initially unperturbed inner disk (dashed region) is disrupted by the strong radiation pressure from the neutron star.

That the disk disruption indeed happens is supported by the observed systematic increase of the

column density on the Normal Branch, with the maximum measured at the hard apex as shown in Fig. 4.20. The changes of the column density are well correlated with the source position on the Z-track and so reflect changes intrinsic to the source. This suggests that as the source moves along the NB, more and more material is added to the line of sight leading to increased absorption. This provides evidence for the disruption of the inner disk and a progressive reduction of its height as the source moves towards the hard apex.

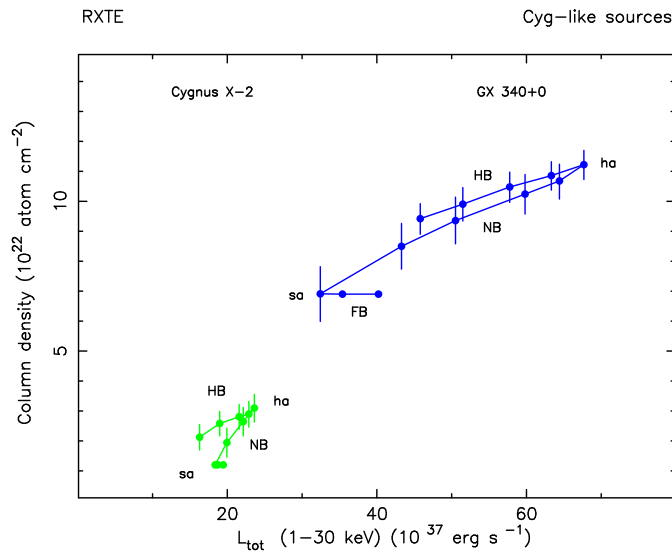


Figure 4.20: The changes of the column density observed in Cyg X-2 and GX 340+0.

The increase of the radiation pressure on the NB coincides also with the reduction of the size of the emission region on the neutron star. The blackbody radii decrease along the Normal Branch and stay small ($\lesssim 3$ km) on the HB in both Cyg X-2 (Sect. 4.1.3) and GX 340+0 (Sect. 4.2.3). This can be interpreted as a change of the emission region on the neutron star into an equatorial belt (Sect. 3.1.5). Church & Balucińska-Church (2001) studied a sample of LMXB in terms of the Extended ADC model (Sect. 2.2.2) and found that over a broad range of luminosities there is a relation between the half-height of the equatorial belt h on the neutron star and the half-height H of the inner, radiatively-supported disk, such that $h \approx H$. The half-height h can be derived from the values of R_{bb} , and in the present work, when the source is at the hard apex, the measured radii are 2.3 ± 0.4 km in Cyg X-2 and 2.9 ± 0.4 km in GX 340+0, giving $h = 0.53 \pm 0.18$ km and $h = 0.9 \pm 0.2$ km in the two sources, respectively, and these values are similar on the Horizontal Branch (Tables 4.3 and 4.7). Thus, on the Horizontal Branch, h is much smaller than the theoretical values of $H > 20$ km in these sources. This means that, if the relation $h \approx H$ is actually met, there must be a substantial disruption of the inner disk which, as was demonstrated above,

normally towers high above the disk plane. As discussed in Sect. 3.1.5, in one of possible scenarios to explain $h \approx H$ (Church & Balucińska-Church 2001), matter from the inner disk is radially accreted by the neutron star, this taking place at the full vertical extent of the inner disk edge and hence leading to $h \approx H$ directly. Thus, in the Cyg-like sources, the reduction of H by the strong radiation pressure on the upper NB and the HB will result in the observed reduced h (Church et al. 2006). The second scenario relates to the theory of Inogamov & Sunyaev (1999), in which accretion flow in the inner disk meets the neutron star at the equator and then spreads in latitude forming a belt of a half-height h which depends on the mass accretion rate. In this case, as the half-height H of the inner radiatively-supported disk is also determined by \dot{M} , the relation $h \approx H$ can be met (Sect. 3.1.5). Here, the strong radiation pressure may remove inner parts of the disk and locally reduce \dot{M} leading, again, to a reduced h as observed.

On the Horizontal Branch, the column density decreases despite f_{bb}/f_{Edd} still increasing, but this can be understood assuming that most of the plasma stored in the inner disk is blown away already at the hard apex, where radiation pressure becomes super-Eddington and the height of the inner disk is already substantially reduced. Beyond this point, along the Horizontal Branch, one can then see other effects of the strong radiation pressure acting on the disk and this is related to the behaviour of the kHz QPO as discussed later.

Finally, the changes of the radiation pressure shown in Fig. 4.18 are well correlated with the known dependence of radio emission on the Z-track position, i.e. radio is known to be strongest on the upper NB and the HB (Oosterbroek et al. 1994; Hjellming et al. 1990a) which coincides with the strongest radiation pressure in the two sources analysed here. Church et al. (2006) proposed that the radiation pressure plays a crucial role in the formation of jets, i.e. that the strong radiation pressure may be the necessary condition for the jet launching. The results obtained here agree well with this proposition, supported by the systematic changes of N_H and R_{bb} along the Normal Branch. In particular, the reduction of the blackbody radius into a narrow equatorial belt on the star favours the launching of jets. This is related to the fact that the inner radiatively-supported disk towers around the neutron star and any vector in the (r, z) plane, between the narrow emitting belt on the star and the inner disk, has a substantial vertical component as one moves away from the disk plane $z = 0$. This implies a significant vertical component of the radiation pressure acting on the disk (Fig. 4.19), again, in line with the model of Church et al. (2006). Collimation of a jet may be possible given that the inner walls of the accretion disk form a cone around the neutron star.

4.3.3 The ADC luminosity and changes of mass accretion rate

The luminosity L_{cpl} of the power law model component, representing emission from the accretion disk corona, increases between the soft apex and the hard apex by a factor of 1.3 - 2.7 (depending on the source, Sect. 4.1.3 and Sect. 4.2.3) and then decreases along the HB by about the same factor. This change is correlated with the observed X-ray count rate which increases along the NB and then decreases on the HB. The ADC luminosity comprises most of the total luminosity and thus, as argued by Church et al. (2006), such changes of L_{cpl} are unlikely not to be related to changes in mass accretion rate. Thus, following L_{cpl} , the mass accretion rate first increases in the direction soft apex \rightarrow hard apex, and then decreases in the direction hard apex \rightarrow left end of the HB. The increase on the NB is consistent with the increase of kT_{bb} on this branch suggesting heating of the neutron star. On the HB, kT_{bb} continues to increase in both sources and this is not obvious given the apparent decrease of L_{cpl} . The same behaviour was observed by Church et al. (2006) and Bałucińska-Church et al. (2010). Church et al. (2006) proposed that this could be related either to a delay between changes of \dot{M} in the disk and on the neutron star or to a reduction of \dot{M} locally at the neutron star by the strong radiation pressure, in the latter case not necessarily under condition of decreasing \dot{M} . Given the similarity of the results, the same scenarios could apply here. Nevertheless, given the fact that L_{cpl} decreases to almost the same low value as at the soft apex, and in fact in Cyg X-2 even slightly below that, it is more probable that this decrease reflects a real decrease of mass accretion rate in this direction, despite high kT_{bb} , and thus the first scenario appears more probable.

The inferred direction of changes of \dot{M} obtained in this work, favours the model of Church et al. (2006) in which mass accretion rate increases on the NB in the direction from the soft apex to the hard apex. This does not support the so-called standard view, based to a large extent on the results of Vrtilik et al. (1990) in which \dot{M} increases monotonically along the Z-track in the direction HB \rightarrow NB \rightarrow FB (Sect. 1.3.1), thus on the NB changing in the opposite way than that proposed here and also opposite to the changes of X-ray intensity on the NB.

During flaring, the luminosity of the Comptonized component appears constant (see Fig. 4.5 in Sect. 4.1 and Fig. 4.13 in Sect. 4.2). Its constancy, following the argument above, suggests that \dot{M} is also constant, and hence intensity flares cannot be explained by changes in accretion rate.

4.3.4 The Flaring Branch

Fitting results show that it is actually the blackbody component which changes on the Flaring Branch (Fig. 4.5 and Fig. 4.13). The luminosity of this component increases along the branch by 16% in Cyg X-2 and much more strongly, by 105%, in GX 340+0. In the model of Church et al. (2006), flaring was explained as unstable nuclear burning of accumulated matter on the neutron star. Their interpretation was based on the agreement at the soft apex of the mass accretion rate per unit area \dot{m} , calculated from spectral fitting results, with the theoretical value $\dot{m}_{ST} = 1.3 \times 10^5 \text{ g cm}^{-2} \text{ s}^{-1}$ of Bildsten (1998), below which nuclear burning is unstable (Sect. 1.4.1).

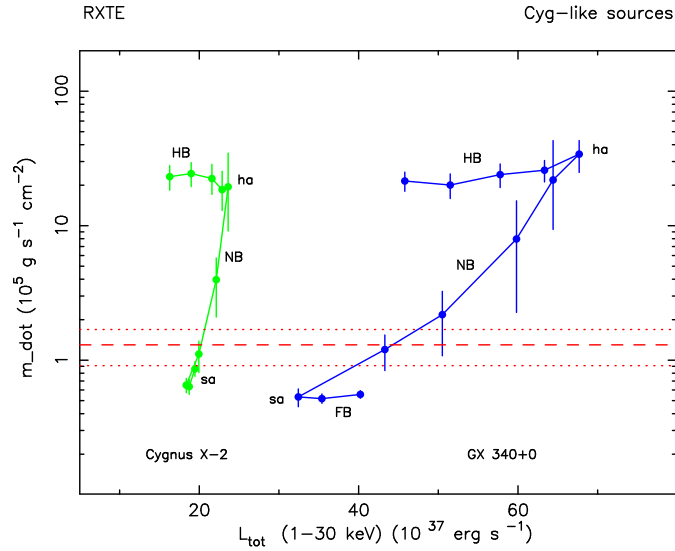


Figure 4.21: Mass accretion rate per unit emitting area (\dot{m}) in Cyg X-2 and GX 340+0.

To check whether spectral fitting results obtained in this work support the proposition of Church et al. (2006), the mass accretion rate per unit area was calculated from Eqn. 1.18. The mass accretion rate \dot{M} is obtained from the total X-ray luminosity (Eqn. 1.1) and the emission area is taken to be $4\pi R_{bb}^2 = L_{bb}/\sigma T_{bb}^4$. The result is shown as a function of the total 1 - 30 keV luminosity in Fig. 4.21, with \dot{m}_{ST} marked with a dashed line (and the 30% errors (Bildsten 1998) shown with dotted lines).

Let us follow the behaviour of \dot{m} along the Z-track of Cyg X-2 and GX 340+0. Values of \dot{m} are large ($\sim 5 - 30 \times 10^5 \text{ g cm}^{-2} \text{ s}^{-1}$) on the HB and the upper NB and in this range the nuclear burning is expected to be stable (Sect. 1.4.1, Table 1.2). However, as the source descends along the NB towards the soft apex, \dot{m} falls into the regime $\dot{m} < \dot{m}_{ST}$ for unstable nuclear burning of helium in a H/He-rich environment, and remains like that on the Flaring Branch. This is strongly

suggestive and agrees with the result of Church et al. (2006) and Bałucińska-Church et al. (2010). Also, the high values of \dot{m} on the other Z-track branches explain why flaring is not observed there, but starts from the soft apex only, as this is the point at which mass accretion rate is small and the emission area large (whole neutron star emitting), thus optimal for the onset of flaring as \dot{m}_{ST} is reached at this point.

In GX 340+0 there is evidence that the blackbody emitting region expands beyond the surface of the star in flaring and reaches $R_{bb} \sim 17.6$ km at the end of the Flaring Branch. The same effect was observed by Church et al. (2006) who measured R_{bb} to increase from 10.8 ± 1.1 km to 16.1 ± 0.8 km along the branch and interpreted this radius expansion as similar to the often observed photospheric radius expansion taking place in X-ray bursts when the Eddington limit is reached in the atmosphere of the star. From Fig. 4.18 one may see that the radiation pressure is not high on the FB with $f_{bb}/f_{Edd} \leq 0.3$ on the branch. However, the values of the flux ratio shown in Fig. 4.18 were calculated assuming a constant Eddington flux at the star of $R_* = 10$ km. This usually works well for all Z-track positions as the measured R_{bb} is almost always ≤ 10 km. Nevertheless, on the FB of GX 340+0 one could take into account that the emission radius becomes larger than 10 km and recalculate the flux ratio substituting R_* with R_{bb} obtained from spectral fitting. Having done this, for $R_{bb} \leq 18$ km, the effective Eddington flux is ~ 3 times smaller and f_{bb}/f_{Edd} reaches close to 1. This supports the interpretation of Church et al. (2006) that the radius expansion observed may take place as a consequence of the Eddington limit reached in flaring in GX 340+0.

It is also possible to address the issue of flare energetics. As pointed out in Sect. 1.4.1, nuclear burning is an order of magnitude less efficient than accretion power and so the fuel powering type I X-ray bursts is not burnt instantaneously, but has to be accumulated (by accretion) for some time before the burst. The energy released in a flash lasting time t at the luminosity L_f is $E_f = L_f t$ and on the energetic grounds is related to the accretion power L_{acc} by

$$E_f = \frac{1}{\alpha} L_{acc} \Delta T, \quad (4.1)$$

where α is the efficiency ratio between the two processes and ΔT is the time of matter accumulation prior to the flash. From this equation, the time ΔT needed to accumulate matter for nuclear burning is

$$\Delta T = \frac{\alpha E_f}{L_{acc}}. \quad (4.2)$$

Now, for a typical flare in the Cyg-like sources, lasting $t \sim 2 \times 10^3$ s with a luminosity of $L_f \sim 5 \times 10^{37}$ erg s $^{-1}$, the released energy is $E_f \sim 10^{41}$ erg. Thus, from Eqn. 4.2, given $\alpha = 30$ (H-rich fuel) and an accretion luminosity of $L_{acc} \sim 2.5 \times 10^{38}$ erg s $^{-1}$ (approximate average luminosity at the soft apex for the two sources studied here), such energy can be provided by matter accumulated over $\Delta T \sim 10^4$ seconds, thus on a timescale of hours.

4.3.5 The temperature of the neutron star and the ADC

The spectral fitting results revealed that in the case of both sources, there is in general a good correlation between the temperature of the blackbody and the cut-off energy of the power law. In the Extended ADC model, kT_{bb} is the temperature on the neutron star, whereas E_{co} reflects the electron temperature kT_e in the accretion disk corona. The observed correlation suggests that the two temperatures are not independent. The relation between the electron temperature in the ADC and the cut-off energy depends on whether the corona is optically thin or thick. In the optically thin case, $kT_e = E_{co}$, whereas in the optically thick case $kT_e = E_{co}/3$ (Sect. 3.1.6).

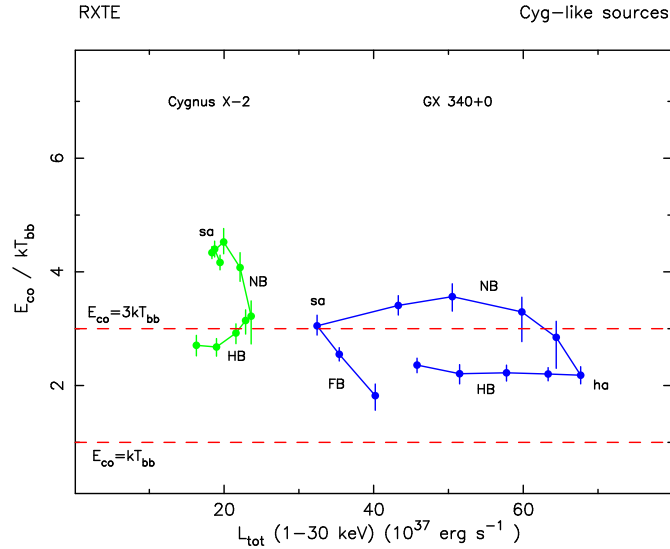


Figure 4.22: The ratio of the power law cut-off energy and the blackbody temperature.

Figure 4.22 shows the ratio E_{co}/kT_{bb} for all the Z-track positions in Cyg X-2 and GX 340+0. It can be seen that in the two sources, the ratio is close to that expected if there was thermal equilibrium $kT_{bb} \approx kT_e$ between the neutron star and the optically thick corona, where $kT_e = E_{co}/3$ and hence

$E_{co} \approx 3kT_{bb}$. The high optical depth is not unexpected given the higher plasma densities in these sources with high mass accretion rates.

A similar conclusion was drawn by Church et al. (2006) in the case of GX 340+0 and Jackson et al. (2009) in the case of GX 5-1, who obtained the average ratio E_{co}/kT_{bb} of 2.5 ± 0.5 and 2.7 ± 0.5 , respectively. Similarly, the average ratio and the 60% confidence standard deviation calculated based on the present results is 3.6 ± 0.8 (Cyg X-2) and 2.6 ± 0.6 (GX 340+0). It thus appears that the approximate thermal equilibrium between the neutron star and the corona is common to the Cyg-like Z-track sources.

4.3.6 The behaviour of the kHz QPO

The main goal of the analysis of the Cyg-like sources carried out in this work is to directly compare the spectral and timing results, as previously done by Jackson et al. (2009) for GX 5-1. The timing results for Cyg X-2 and GX 340+0 were presented in Sect. 4.1.4 and Sect. 4.2.4, respectively, where it was shown that the frequencies of the two QPO change monotonically along the Horizontal Branch of the Z-track and are positively correlated with the total luminosity (Fig. 4.8 and 4.16). The behaviour of the kHz QPO with spectral properties in the two sources is now compared. In particular, the presence of the QPO on the Horizontal Branch only suggests their relation to the high radiation pressure on that branch.

When discussing the nature of the kHz QPO, it is natural to associate their high frequencies with the frequencies of the orbital motion in the inner accretion disk at certain radii. This is often done, such as in the beat-frequency models or the relativistic precession model (Sect. 1.4.4), where at least one of the QPO frequencies (typically the upper one) is thought to correspond to the Keplerian motion at radial positions in the neighbourhood of the inner edge of the disk. The possible nature of the lower kHz QPO is less obvious and more model-dependent, but it is enough for the purpose of this discussion to take note of the fact that it is somehow linked to the upper kHz QPO as the changes of the two QPO appear linked. Thus, assuming Keplerian orbits in the disk, the radii can be calculated in the Newtonian approximation (following Eqn. 3.1) as

$$r = (G M_*)^{1/3} (2\pi\nu)^{-2/3}, \quad (4.3)$$

using the kHz QPO frequencies ν derived from the power spectra. The radii corresponding to the kHz QPO as a function of f_{bb}/f_{Edd} are shown in Fig. 4.23 which allows a direct comparison of all three sources.

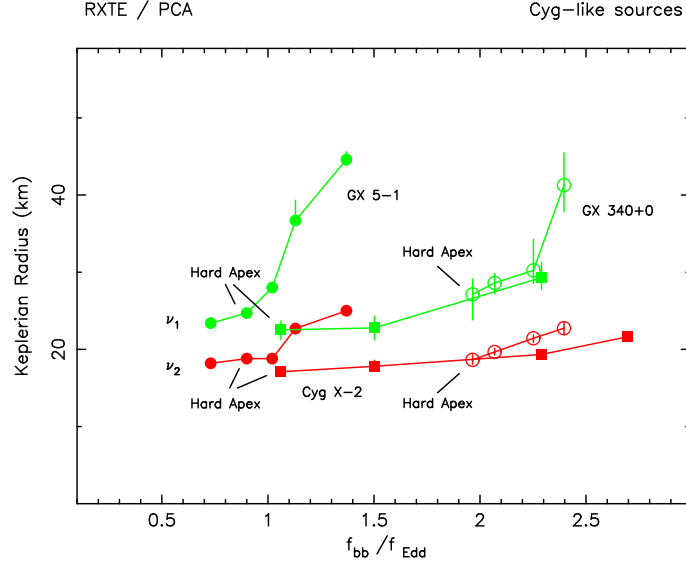


Figure 4.23: The Keplerian radii corresponding to the two kHz QPO as a function of the ratio of the blackbody to the Eddington emissive flux in all three Cyg-like sources. Data on GX 5-1 were adopted after Jackson et al. (2009). The upper kHz QPO (ν_2) is shown in red and the lower kHz QPO (ν_1) in green for each of the three sources: Cygnus X-2 (filled squares), GX 340+0 (open circles) and GX 5-1 (filled circles).

From Fig. 4.23 it can be seen that the radius corresponding to the upper kHz QPO (ν_2) in all sources is close to ~ 20 km when the radiation pressure is least and increases with the radiation pressure on the Horizontal Branch. Fig. 4.23 clearly suggests a picture in which the radiation pressure determines the radius at which the upper QPO occurs.

A proposition that the strong radiation pressure may affect the inner disk close to the neutron star was formulated by Church et al. (2006). Jackson et al. (2009) showed that in GX 5-1 the radius corresponding to the upper kHz QPO is constant when the source is on the upper Normal Branch and then shows a sudden change when the radiation pressure becomes super-Eddington (Fig. 4.23). This change took place on the HB close to the hard apex and was followed by a further increase of the Keplerian radius along the Horizontal Branch. The lower kHz QPO followed the same pattern responding to changes in the upper one, but at larger radii. A model was proposed in which the strong radiation pressure causes disk truncation and the disk edge serves as a natural place for the formation of the upper kHz QPO. Moving along the Horizontal Branch, the radiation pressure increases causing the inner disk edge to move outwards so that ν_2 decreases, the oscillation remaining at the inner disk edge. On this basis, the frequency ν_2 can be used to *measure* the inner disk radius r_{in} .

The changes observed in Cyg X-2 and GX 340+0 fit well into the above scenario. However, in the

case of the sources analysed here, unlike in GX 5-1, the radiation pressure is super-Eddington in all selections where the two kHz QPO were detected. Indeed, in Cyg X-2 f_{bb}/f_{Edd} is just above unity when the kHz QPO are detected close to the hard apex, whereas in GX 340+0, f_{bb} changes rapidly on the upper Normal Branch and is above $2.0 f_{Edd}$ when the QPO are detected. It is therefore not possible to examine the behaviour of the QPO frequencies in the range below and around $f_{bb} \approx f_{Edd}$, as studied by Jackson et al. (2009), which in both Cyg X-2 and GX 340+0 happens on the upper Normal Branch, where the kHz QPO were not detected. However, the behaviour of the kHz QPO on the Horizontal Branch is consistent with that observed by Jackson et al. (2009) and can be well explained by the strong radiation pressure pushing the inner disk edge away towards larger radii.

Jackson et al. (2009) suggested that the sudden change in the Keplerian radii that they observed at $f_{bb} \approx f_{Edd}$ was unlikely to be coincidental, but this could be questioned given the limited data obtained. However, the present results support their conclusion. The Keplerian radii in Cyg X-2 and GX 340+0, all detected in the regime $f_{bb} > f_{Edd}$, increase along the Horizontal Branch without any sudden changes. If the effect observed by Jackson et al. (2009) had been coincidental, then it would be expected to see similar abrupt changes in Cyg X-2 or GX 340+0 at random values of f_{bb}/f_{Edd} , which is not the case.

It is also possible to discuss the present results in terms of the theoretical models for the QPO. The major prediction of the beat-frequency models is that the QPO separation should be constant as related to the spin frequency of the neutron star. Fig. 4.24 shows the frequency separation obtained from the QPO frequencies measured in this work. The dashed lines correspond to the values of the average QPO frequency separation reported previously in these sources (Wijnands et al. 1997; Jonker et al. 2000) based on multiple observations of the twin kHz QPO on the Horizontal Branch. It can be seen that within errors the QPO separation in the two sources is consistent with being constant and is in good agreement with the previously published average values. Thus, it is not possible to discriminate against the beat-frequency model on this basis. However, the evidence against the model, based on observations of other sources, such as Sco X-1 (van der Klis 2000), is strong. Moreover, the beat-frequency model requires the disk to be truncated at a certain radius, such as the sonic-point, but this choice is not obvious and its relation to the Z-track branches unclear. The results obtained here favour the model of Jackson et al. (2009) in which the disk truncation is caused naturally by strong radiation pressure disrupting the inner disk.

The advantage of this model is that it explains why the kHz QPO occur in Cyg-like sources at basically one branch of the Z-track only, the Horizontal Branch ($f_{bb} \geq f_{Edd}$), and not at other Z-track positions where $f_{bb} < f_{Edd}$ and the disk may reach to the neutron star.

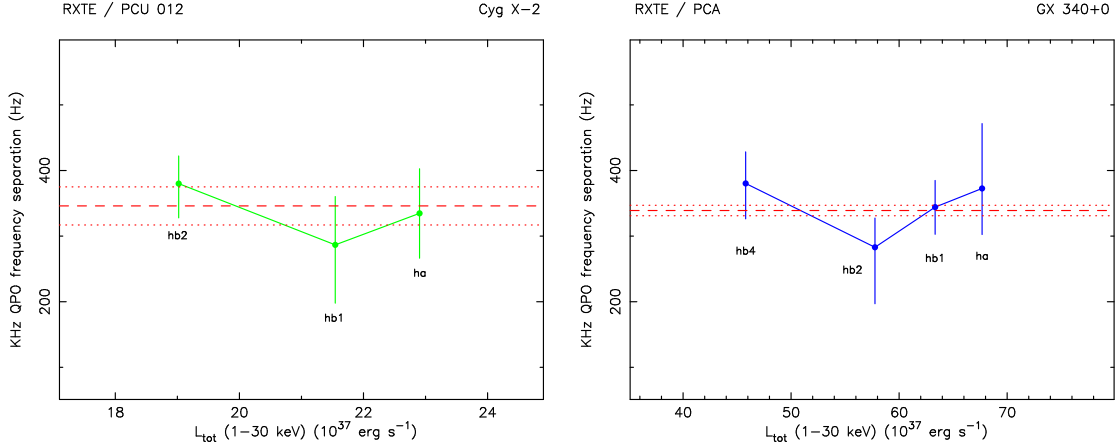


Figure 4.24: Frequency separation between the twin kHz QPO as calculated for the cases where both QPO were detected simultaneously in Cyg X-2 (left) and GX 340+0 (right). Errors are given at 90% (2σ) confidence level. The red dashed lines mark the average QPO frequency separation of 346 ± 29 Hz and 339 ± 8 Hz (with errors marked by the dotted lines) after Wijnands et al. (1997, in Cyg X-2) and Jonker et al. (2000, in GX 340+0), respectively.

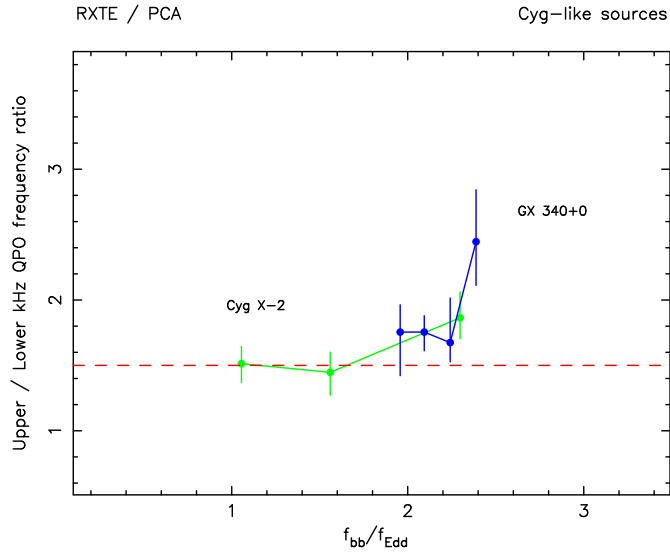


Figure 4.25: The ratio of the kHz QPO frequencies shown as a function of the f_{bb}/f_{Edd} ratio. The red dashed line shows the 3/2 frequency ratio around which the kHz QPO tend to cluster in neutron star LMXB.

A prediction of the relativistic disk resonance model is that the frequencies of two kHz QPO should preferably be in a 3/2 ratio as is known to be the case in some black hole systems. The most apparent difference between the high-frequency QPO in black hole systems and the kHz QPO

in the neutron star LMXB is that in the latter the frequencies of the QPO are not stable, but vary over a certain range showing a scatter of the frequency ratio around $3/2$, the reason for this, however, remains unclear. Figure 4.25 shows the frequency ratio of the two QPO as measured in this work. In both sources studied here, the kHz QPO frequency ratio is close to $3/2$, but the largest and significant deviation from this ratio occurs at the left end of the Horizontal Branch where the radiation pressure is strongest. One could thus hypothesize, that, assuming the above QPO frequency ratio is a consequence of a real physical mechanism, such as in the disk resonance model, and not of instrumental nature (Boutelier et al. 2010), the observed deviation from the theoretically expected $3/2$ value could be related to effects of strong radiation pressure. In fact, the stability of QPO frequencies in black hole binaries could be in line with this given the lack of the surface of the central star, as opposed to neutron star LMXB.

Chapter 5

Spectral investigations of the Sco-like Z-track sources

The causes of the difference between the Sco-like sources and the Cyg-like sources has not been understood. The aim of the work presented in this chapter is to investigate the Sco-like sources. Application of the Extended ADC model is expected to suggest an explanation for this sub-group of the Z-track sources. Analysis of GX 17+2 and Sco X-1 is carried out.

5.1 GX 17+2

5.1.1 Observations

The *RXTE* archival data of GX 17+2 were first remotely investigated using a local script which allows examination of the source in hardness-intensity and a choice of the best data. Based on this, the observation ID P20053 from April 1st - 4th, 1997, having a full Z-track was chosen. The observation (Table 5.1) spans over 274 ks with relatively large data gaps between sub-observations.

5.1.2 Analysis

The standard *RXTE* data analysis procedure was carried out using *HEASOFT* v.6.7 with the most recent version of the calibration database *CALDB*. The housekeeping data of the observation were examined and the screening conditions $\text{ELV} > 10^\circ$ and $\text{OFFSET} > 0.02^\circ$ were applied. It was found that all five PCU detectors were operational during the observation, Good Time Intervals

Table 5.1: Sub-observations of GX 17+2 within the *RXTE* observation P20053 made in April 1997.

Sub-observation	Start Date & Time (UT)	Duration (s)
20053-03-03-00	April 1, 1997, 19:13:46	23360
20053-03-03-01	April 2, 1997, 20:06:15	14752
20053-03-03-02	April 3, 1997, 21:46:09	8096
20053-03-03-03	April 4, 1997, 18:26:36	17968

(GTI) were produced giving almost 67 ks of useful, clean data.

The observation made in April 1997 corresponds to the *RXTE*/PCA calibration epoch 3 and the proper energy-to-channel conversion table relevant to this epoch was used to choose the energy bands: low (1.9 - 4.1 keV, channels 5 - 10), medium (4.1 - 7.3 keV, channels 11 - 19), high (7.3 - 18.5 keV, channels 20 - 50) and total (1.9 - 18.5 keV, channels 5 - 50). Standard2 lightcurves were extracted in SAEXTRACT from the top, left and right layers of all PCU units with a binning of 64 seconds. Background files were generated from the bright background model (count rate > 1300 count s^{-1} PCU $^{-1}$). Background lightcurves were extracted (in the total, low, medium and high energy bands) and used for background subtraction. A deadtime-correction was applied using the local script which increased count rate by $\sim 4\%$. The total (1.9 - 18.5 keV) background-subtracted and deadtime-corrected lightcurve is shown in Fig. 5.1.

Also, the medium and high lightcurves were used to obtain the hardness ratio (hard/medium) which is shown as a function of the total intensity in Fig. 5.2. The figure reveals the Z-track of GX 17+2. Small sections of the total lightcurve were separately analysed to identify their hardness-intensity positions on the Z-track which are labelled in Fig. 5.1. The observation begins with extensive flaring seen during the first ~ 25 ks which corresponds to a long Flaring Branch in hardness-intensity. Next, the source exhibited smaller intensity variations on the Horizontal Branch, and finally also along the Normal Branch at the end of the observation. The Z-track traced by GX 17+2 is well sampled which allows for a complete spectral analysis. The timescale of about 3 days on which the Z-track was traced in this observation is consistent with previous observations (e.g. Di Salvo et al. 2000).

In order to study the behaviour of the source along the Z-track, 17 data selections were made based on hardness and intensity. These are five selections (hb5 - hb1) on the HB, one (ha) at the hard apex, four (nb4 - nb1) on the NB, one (sa) at the soft apex, and six selections (fb1 - fb6)

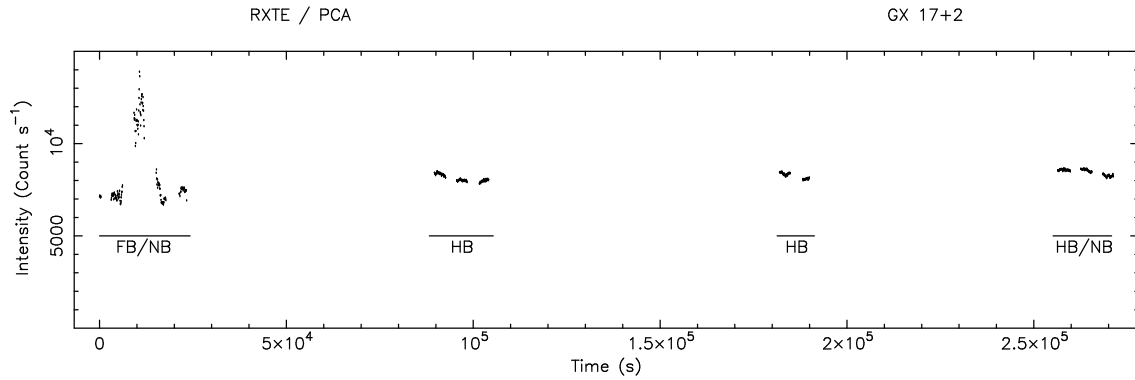


Figure 5.1: The total (1.9 - 18.5 keV) background-subtracted and deadtime-corrected lightcurve of GX 17+2. Each point corresponds to 64 seconds of data.

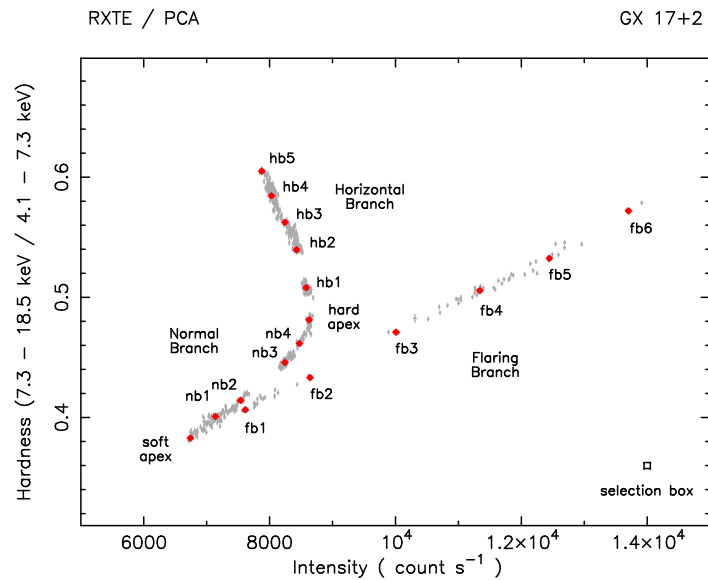


Figure 5.2: The corresponding background-subtracted and deadtime-corrected Z-track of GX 17+2. Red filled circles mark the positions of data selections chosen for spectral analysis; the actual size of a selection box is shown in the bottom right corner.

along the Flaring Branch. The selection size was in every case 100 count s^{-1} wide in intensity and 0.005 wide in hardness as shown in the bottom, right-hand corner of Fig. 5.2.

Selections were translated into Good Time Intervals for extraction of spectra along the Z-track. PCA and HEXTE (Cluster B, detectors 0, 1 and 3) on-source and background spectra were produced using SAEXTRACT and HXTLCURV, respectively. Appropriate response files were generated based on the latest available calibration data. All spectra were deadtime-corrected. Systematic errors of 1% were added to PCA spectral channels to take into account calibration uncertainties. PCA spectra had typically $10^3 - 10^4$ counts per channel and HEXTE spectra 100 counts per channel.

5.1.3 Results

Simultaneous fitting of PCA and HEXTE spectra was carried out using *Xspec*. The energy ranges were typically 3 to 20 - 25 keV for the PCA, and 18 to 25 - 50 keV for HEXTE. Channels were grouped together if necessary to improve their signal-to-noise ratio. An additional constant factor was introduced to the model to take into account the relative calibration of PCA and HEXTE, frozen at 1.0 for the PCA and left free for HEXTE. Values of the constant were in the acceptable range 0.6 - 0.9.

Initial fitting with the Extended ADC model revealed the presence of a clear excess at 6.5 keV consistent with an Fe line. An additional Gaussian line was added to the model leading to acceptable values of $\chi^2/\text{d.o.f.}$ in the range 25/52 - 59/45. The Gaussian line was broad with σ estimated from the residuals to be ~ 0.5 keV with little change around the Z-track. A similar width was reported in earlier studies by e.g. Ercan (1988) and Di Salvo et al. (2000). This value was used and frozen in fitting to prevent absorption of the neighbouring continuum.

As with all Z-track sources, the low value of the cut-off energy of the power law makes it difficult to constrain the photon index Γ so as previously done Γ was frozen at 1.7.

Several spectra with their best-fit models are shown in Fig. 5.3 as folded spectra with residuals (left panel) and unfolded versions (right versions). Spectral fitting results are given in Table 5.2 and Table 5.3.

Absorption At the soft apex, the column density is $5.1 \pm 0.9 \times 10^{22}$ atom cm^{-2} , but with errors of 5 - 10%, there is a trend of N_H first increasing on the Normal Branch and then decreasing again on the Horizontal Branch. This is as observed in the Cyg-like sources interpreted as evidence for

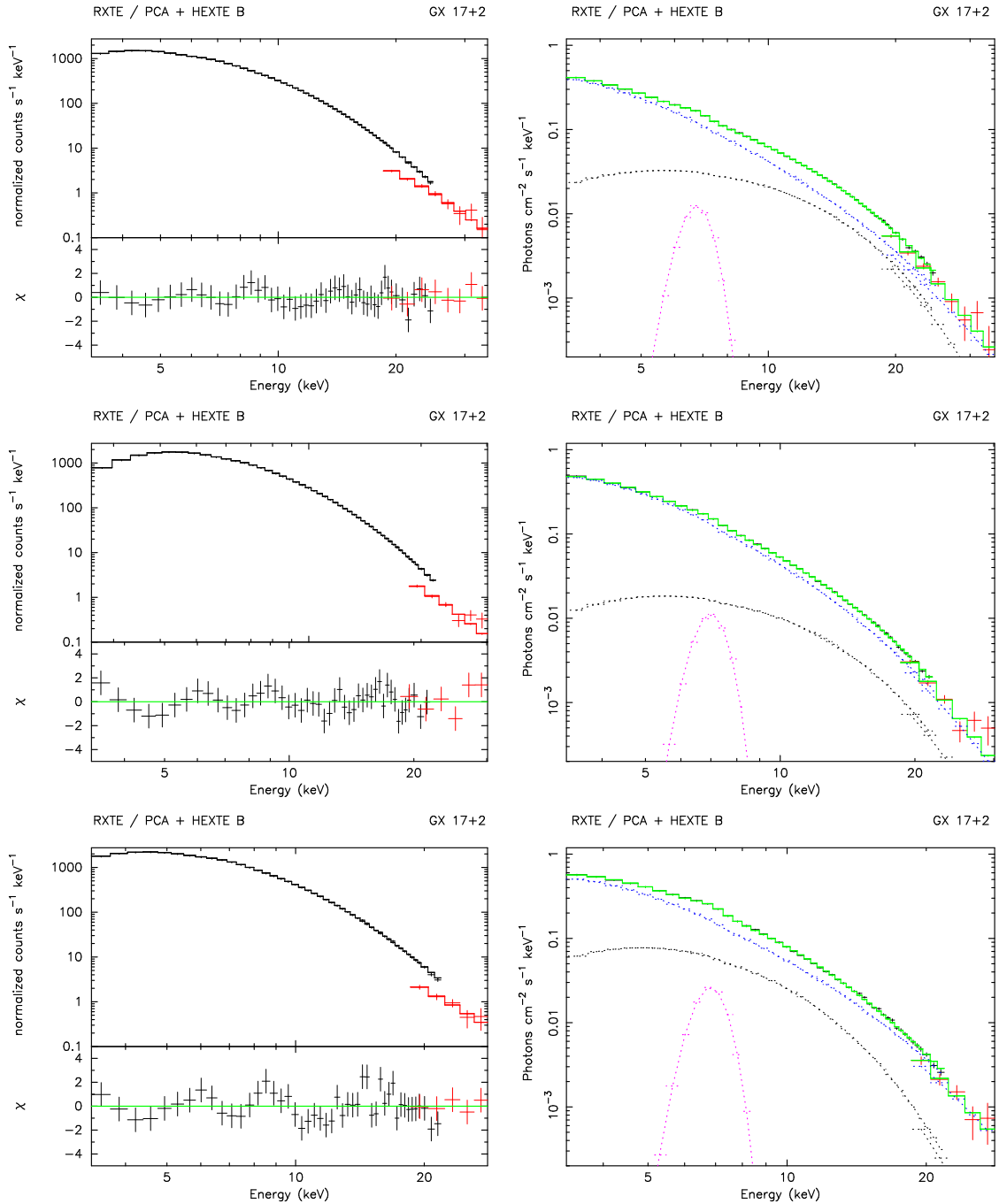


Figure 5.3: The folded spectra (left) and the unfolded spectra (right) of GX 17+2 from: Horizontal Branch (hb2, top), soft apex (sa, middle) and Flaring Branch (fb5, bottom). In the right panel: blackbody (black), cut-off power law (blue), emission line (magenta), and the total continuum model (green).

Table 5.2: The results of fitting the Extended ADC model to the spectra of GX 17+2. Errors are given at 90% confidence level.

Sel.	N_H	Blackbody		Emission line		Cut-off power law		$\chi^2/\text{d.o.f.}$
		kT_{bb}	norm	E_l	EW	E_{co}	norm	
hb5	4.2 ± 0.6	2.84 ± 0.14	6.5 ± 1.1	6.75 ± 0.25	94	7.81 ± 1.10	7.5 ± 0.9	48/58
hb4	4.6 ± 0.5	2.81 ± 0.11	5.7 ± 0.6	6.78 ± 0.25	102	7.59 ± 0.62	8.2 ± 0.7	25/52
hb3	5.0 ± 0.6	2.79 ± 0.12	5.4 ± 0.9	6.80 ± 0.27	104	6.94 ± 0.68	9.4 ± 0.9	33/47
hb2	5.2 ± 0.6	2.77 ± 0.13	5.3 ± 1.2	6.78 ± 0.28	106	6.50 ± 0.77	10.4 ± 1.1	43/51
hb1	6.1 ± 0.3	2.70 ± 0.10	4.2 ± 0.7	6.94 ± 0.25	118	5.98 ± 0.41	12.4 ± 0.8	36/50
ha	6.3 ± 0.5	2.59 ± 0.12	3.8 ± 0.7	6.98 ± 0.26	110	5.54 ± 0.39	13.7 ± 1.1	35/49
nb4	6.5 ± 0.3	2.48 ± 0.18	2.8 ± 0.8	7.01 ± 0.25	172	5.56 ± 0.40	13.9 ± 0.9	44/48
nb3	6.3 ± 0.6	2.33 ± 0.34	2.0 ± 0.9	6.97 ± 0.28	128	5.61 ± 0.50	13.6 ± 1.5	33/51
nb2	6.0 ± 0.7	1.74 ± 0.61	0.8 ± 0.9	6.83 ± 0.61	109	5.54 ± 0.35	12.7 ± 1.4	36/43
nb1	5.8 ± 0.7	1.52 ± 0.28	1.6 ± 1.2	6.78 ± 0.16	99	5.46 ± 0.23	11.8 ± 1.5	49/48
sa	5.1 ± 0.9	1.27 ± 0.08	3.2 ± 1.8	6.75 ± 0.17	169	5.61 ± 0.39	9.6 ± 2.0	45/42
fb1	5.2 ± 0.9	1.44 ± 0.09	4.1 ± 1.7	6.65 ± 0.14	180	5.79 ± 0.40	10.1 ± 1.9	27/38
fb2	5.9 ± 0.6	1.58 ± 0.13	4.6 ± 1.5	6.76 ± 0.16	178	5.88 ± 0.36	11.7 ± 1.7	40/44
fb3	6.1 ± 0.9	1.82 ± 0.15	6.5 ± 1.4	6.69 ± 0.19	160	6.01 ± 0.46	13.0 ± 2.1	36/43
fb4	6.4 ± 0.8	1.93 ± 0.11	8.2 ± 1.2	6.83 ± 0.22	150	6.40 ± 0.42	13.7 ± 1.9	59/45
fb5	6.6 ± 0.4	1.97 ± 0.09	10.9 ± 1.0	6.92 ± 0.22	115	6.43 ± 0.35	14.4 ± 1.4	37/54
fb6	6.5 ± 0.8	2.11 ± 0.11	13.3 ± 1.3	6.98 ± 0.29	117	6.91 ± 0.64	14.4 ± 2.2	40/43

The column density is expressed in 10^{22} atom cm^{-2} . The blackbody temperature, cut-off energy and line energy are given in keV. The blackbody normalization is given in 10^{37} erg s^{-1} assuming a distance of 10 kpc, the line equivalent width is in eV, and the cut-off power law normalization is in photons $\text{keV}^{-1} \text{cm}^{-2} \text{s}^{-1}$ at 1 keV.

Table 5.3: The auxiliary physical quantities: the blackbody radius, the half-height of the equatorial belt on the neutron star, the blackbody to the Eddington flux ratio, the mass accretion rate per unit area, the luminosities and the half-height H_{eq} of the inner disk.

Selection	R_{bb}	h	f_{bb}/f_{Edd}	\dot{m}	L_{bb}	L_{cpt}	L_{tot}	H_{eq}
hb5	2.1 ± 0.3	0.44 ± 0.11	4.5 ± 0.7	22 ± 6	3.6 ± 0.6	18 ± 2	22	19 ± 2
hb4	2.0 ± 0.2	0.40 ± 0.08	4.3 ± 0.5	25 ± 5	3.2 ± 0.4	20 ± 2	23	19.7 ± 1.6
hb3	2.0 ± 0.2	0.39 ± 0.09	4.2 ± 0.7	27 ± 6	3.0 ± 0.5	22 ± 2	25	21.0 ± 1.9
hb2	2.0 ± 0.3	0.39 ± 0.11	4.1 ± 0.9	28 ± 8	3.0 ± 0.7	23 ± 3	26	22 ± 2
hb1	1.9 ± 0.2	0.35 ± 0.08	3.7 ± 0.6	35 ± 8	2.4 ± 0.5	25 ± 2	28	23.8 ± 1.5
ha	1.9 ± 0.3	0.37 ± 0.10	3.1 ± 0.6	33 ± 9	2.1 ± 0.4	27 ± 2	29	25 ± 2
nb4	1.8 ± 0.4	0.32 ± 0.13	2.6 ± 0.8	38 ± 16	1.6 ± 0.5	27 ± 2	29	24.4 ± 1.8
nb3	1.7 ± 0.6	0.3 ± 0.2	2.0 ± 0.9	41 ± 30	1.1 ± 0.5	27 ± 3	28	24 ± 3
nb2	2.0 ± 1.8	$0.4_{-0.4}^{+0.7}$	0.6 ± 0.7	27 ± 27	0.5 ± 0.5	25 ± 3	25	22 ± 2
nb1	3.6 ± 1.9	1.3 ± 1.3	0.4 ± 0.3	8 ± 8	0.9 ± 0.7	23 ± 3	24	21 ± 2
sa	7.3 ± 2.2	5.4 ± 3.3	0.18 ± 0.10	1.7 ± 1.0	1.8 ± 1.0	19 ± 4	21	18 ± 4
fb1	6.4 ± 1.5	4.1 ± 1.9	0.30 ± 0.12	2.4 ± 1.1	2.3 ± 0.9	20 ± 4	23	19 ± 4
fb2	5.6 ± 1.3	3.2 ± 1.4	0.44 ± 0.14	3.6 ± 1.7	2.6 ± 0.9	24 ± 3	27	23 ± 3
fb3	5.1 ± 1.0	2.6 ± 1.0	0.76 ± 0.16	5.1 ± 1.9	3.7 ± 0.8	27 ± 4	31	26 ± 4
fb4	5.1 ± 0.7	2.6 ± 0.7	0.95 ± 0.14	5.7 ± 1.6	4.6 ± 0.7	30 ± 4	34	29 ± 4
fb5	5.6 ± 0.6	3.2 ± 0.6	1.03 ± 0.10	5.1 ± 1.0	6.1 ± 0.6	31 ± 3	38	32 ± 3
fb6	5.4 ± 0.7	2.9 ± 0.7	1.36 ± 0.13	5.9 ± 1.4	7.5 ± 0.7	33 ± 5	41	35 ± 5

R_{bb} , h and H_{eq} are in km, L_{bb} is bolometric in 10^{37} erg s^{-1} , \dot{m} is in 10^5 g $\text{cm}^{-2} \text{s}^{-1}$, L_{cpt} and L_{tot} are given in the 1 - 30 keV range in 10^{37} erg s^{-1} . A distance of 7.5 kpc was assumed for GX 17+2. The blackbody flux is given as a ratio to the Eddington flux of 1.4×10^{25} erg $\text{cm}^{-2} \text{s}^{-1}$ for a neutron star radius of 10 km radius.

the disk disruption and the present results will be viewed in terms of this. The behaviour of the column density on the Flaring Branch, unlike in the Cyg-like sources, also shows a clear trend increasing along the branch.

The blackbody component The changes of the blackbody parameters around the Z-track are shown in Fig. 5.4. The blackbody temperature (upper panel) is lowest ($kT_{bb} = 1.27 \pm 0.08$ keV) when the source is at the soft apex where the blackbody radius (lower panel) is 7.3 ± 2.2 km. The temperature increases continuously along the Normal Branch and then the Horizontal Branch where it reaches its maximum of ~ 2.8 keV. The substantial change of kT_{bb} implies that the radiation pressure will increase strongly by a factor of ~ 25 suggesting its importance on the upper NB/HB. The strong increase of the temperature is accompanied by a decrease of the blackbody radius which is only ~ 2 km at the hard apex and remains that small along the Horizontal Branch. Thus the reduction of the emission area on the neutron star is as observed in the Cyg-like sources.

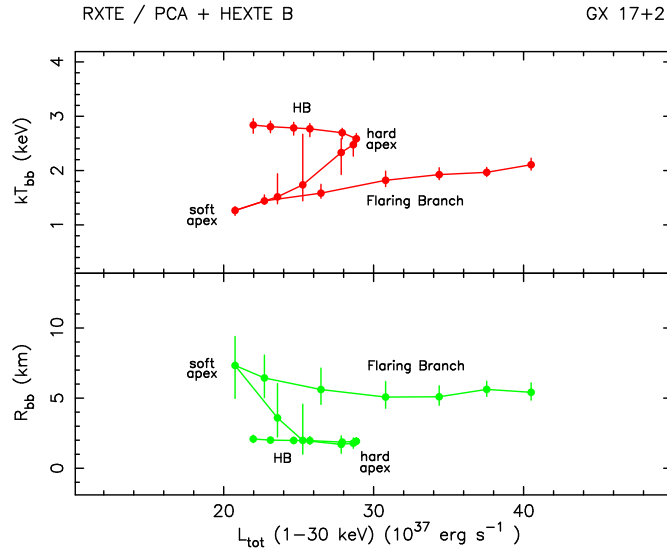


Figure 5.4: The temperature (top) and radius (bottom) of the blackbody shown as a function of the total 1 - 30 keV luminosity.

The changes on the Flaring Branch are not the same as on the NB, as the temperature also increases, but the radius does not show strong contraction remaining > 5 km on the branch.

The luminosities of the blackbody and the power law Figure 5.5 shows the luminosities of the two main model components as a function of the total (1 - 30 keV) luminosity of the source. The contributions of the components to the total are typically $L_{bb}/L_{tot} \leq 20\%$ and $L_{cpl}/L_{tot} \geq 80\%$.

L_{cpl} (lower panel) is low at the soft apex, increases on the NB by 40% and then decreases on the HB to its original low value at the soft apex, behaviour known from the Cyg-like sources. On the Flaring Branch, on the other hand, L_{cpl} increases monotonically all way up the branch by $\sim 70\%$. This is very different from what was observed in the Cyg-like sources in which the power law component showed little change on the FB and was consistent with being constant.

The changes of the blackbody luminosity are not substantial on the NB and the HB, where L_{bb} responds to the changes in kT_{bb} and R_{bb} which are roughly anti-correlated on these branches. However, a pronounced increase of L_{bb} can be seen on the Flaring Branch, at the end of which L_{bb} is over 4 times larger than that at the soft apex. The blackbody alone was seen responsible for flaring in the Cyg-like sources which was interpreted as of thermonuclear nature. It is not immediately clear if this increase in GX 17+2 is due to variation in \dot{M} , nuclear burning, or both.

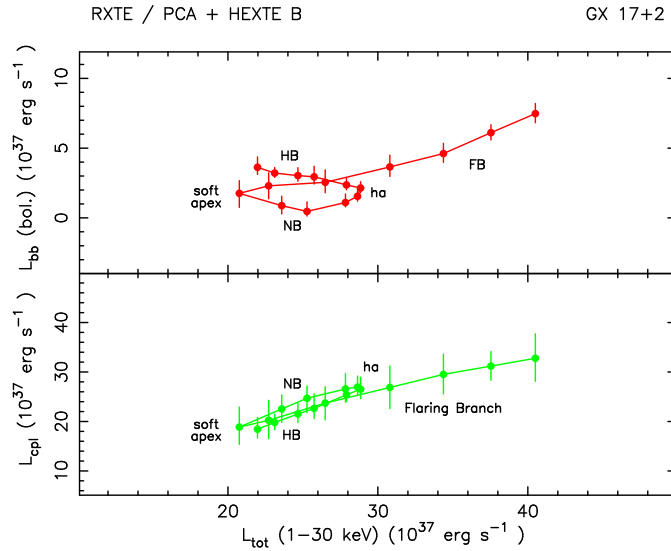


Figure 5.5: The luminosities of the model components: blackbody (upper panel) and cut-off power law (bottom).

The cut-off energy and normalization Variations of the power law parameters on the Z-track are shown in Fig. 5.6 (left). The cut-off energy (upper panel) is lowest on the Normal Branch and the soft apex being at 5.5 - 5.6 keV and constant within errors. Then it increases significantly as the source moves beyond the hard apex onto the HB reaching a maximum of 7.8 ± 1.1 keV. A significant increase of E_{co} is also observed on the FB. The changes in E_{co} appear to follow the variation of the blackbody temperature, as was observed in the Cyg-like sources suggesting that the electron temperature in the corona responds to the temperature of the neutron star. The ratio

of the two temperatures is shown on the right-hand side of Fig. 5.6, the average of E_{co}/kT_{bb} is 3.0 with a standard deviation of ± 0.7 , thus consistent with the corona being optically thick and in thermal equilibrium with the neutron star.

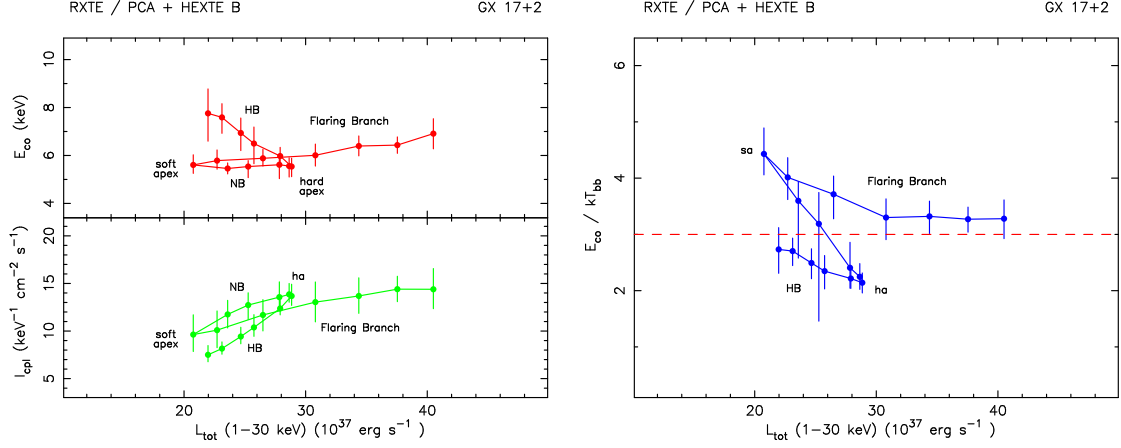


Figure 5.6: Left: The cut-off energy (top) and the normalization (bottom) of the cut-off power law. Right: The E_{co}/kT_{bb} ratio with the line marking $E_{co} = 3kT_{bb}$ expected for the optically thick ADC in thermal equilibrium with the neutron star.

The normalization of the cut-off power law component tightly represents changes in L_{cpl} which is a consequence of the frozen Γ and relatively limited changes in the cut-off energy on most parts of the Z-track.

The line emission The line energy shows limited changes on the Z-track, although there is a trend with E_l correlated with the changes in L_{cpl} as was also the case in the Cyg-like sources. The line energy $\sim 6.7 - 7.0$ keV suggests highly ionized species of iron, such as of Fe XXV and XXVI. With the frozen line $\sigma = 0.5$ keV, the equivalent width varied in the range 90 - 180 eV, without any clear trend on the Z-track.

5.1.4 Discussion

Fitting with the Extended ADC model reveals that GX 17+2 shares some characteristics with the Cyg-like sources. However, the differences in behaviour are clearly important.

Figure 5.7 compares the results for GX 17+2 (blue) with those obtained for the Cyg-like sources (black) from Sect. 4.1 and Sect. 4.2 for the blackbody kT_{bb} and R_{bb} (left) and the luminosities of the two main model components (right) as a function of the total 1 - 30 keV luminosity.

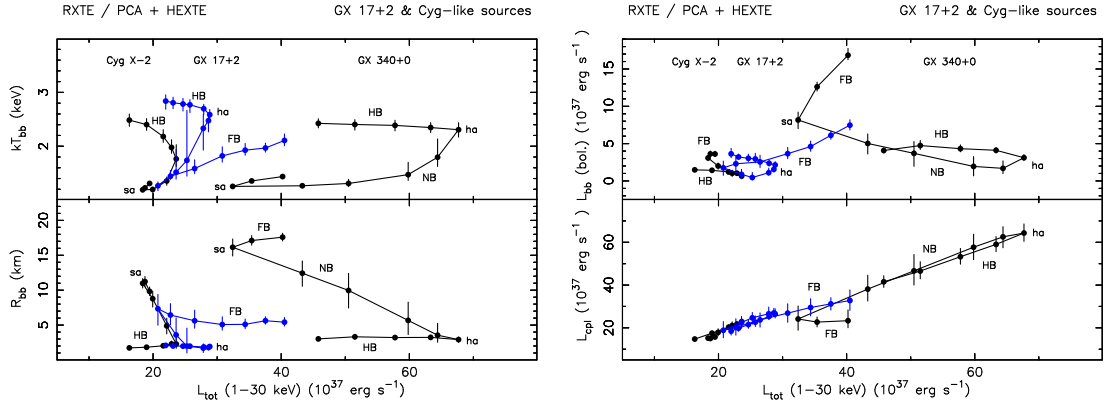


Figure 5.7: A comparison of the spectral fitting results for GX 17+2 (blue) and the Cyg-like sources (black). Left: The blackbody temperature (top) and the radius (bottom). Right: The luminosity of the blackbody (top) and the power law (bottom).

Characteristics common to GX 17+2 and the Cyg-like sources

At the soft apex From Fig. 5.7, one may see that, as in the case of the Cyg-like sources, the neutron star temperature in GX 17+2 is lowest when the source is at the soft apex and at ~ 1.27 keV is similar to the Cyg-like sources. This is in line with the low \dot{M} inferred from low L_{cpl} at the soft apex. Thus also in GX 17+2, the soft apex can be considered as a type of a quiescent state characterized by minimal mass accretion rate and at which the neutron star is cool.

On the Normal and the Horizontal Branch Moving on the Normal Branch there is an increase of the neutron star temperature in all sources. The increase of L_{cpl} strongly suggests that there is an increase of mass accretion rate in this direction. This is also consistent with an obvious observational property that the X-ray intensity increases between the soft apex and the hard apex. Thus, also in GX 17+2, the inferred direction in which \dot{M} changes on the Z-track does not support the standard view that this change is monotonic in the direction HB \rightarrow NB \rightarrow FB.

The increase of kT_{bb} on the NB and the HB in GX 17+2 will result in an increased radiation pressure from the neutron star, as was the case in Cyg X-2 and GX 340+0. Figure 5.8 shows the changes of the radiation pressure in GX 17+2. It is clear that in GX 17+2 the radiation pressure increases strongly as soon as the source leaves the soft apex on the NB, on the Horizontal Branch f_{bb} becomes several times super-Eddington.

In the Cyg-like sources, it was proposed that the strong radiation pressure disrupts the inner accretion disk and was the necessary condition for the launching of jets. This also appears to be the case in GX 17+2. A strong X-ray / radio correlation was reported by Penninx et al. (1988).

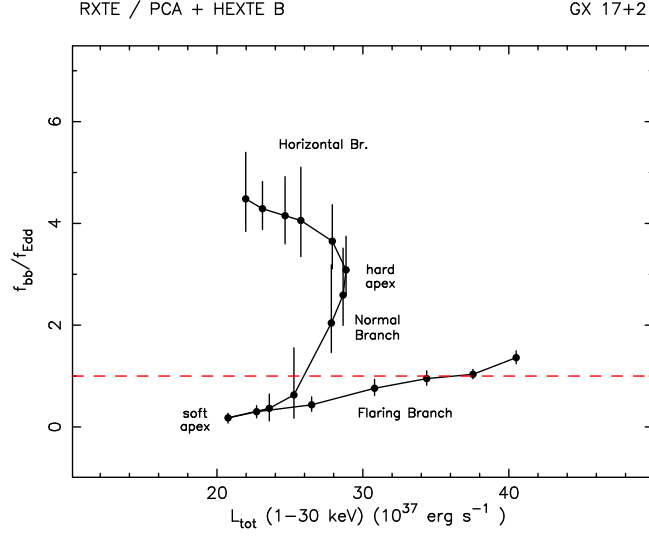


Figure 5.8: The ratio f_{bb}/f_{Edd} shown as a function of the total 1 - 30 keV luminosity. The Eddington limit is marked with a red dashed line.

They observed the radio flux to increase by an order of magnitude as the source was tracing the Z-track in the direction FB \rightarrow NB \rightarrow HB. This is therefore consistent with changes of the radiation pressure which is strongest on the HB. The changes of N_H on the Z-track of GX 17+2 are small and do not provide clear evidence for increases of intrinsic absorption related to the launching of jets. Nevertheless, the emission region on the neutron star in GX 17+2 on the upper Normal Branch and the Horizontal Branch, as in the Cyg-like sources, is clearly reduced (Fig. 5.7) to an equatorial belt of half-height $h \sim 0.4$ km. Such conditions favour the diversion of plasma into the vertical direction.

In GX 17+2, at the soft apex, R_{bb} of 7.3 ± 2.2 km suggests that no quite all of the neutron star surface is emitting. On the Normal Branch and the Horizontal Branch R_{bb} becomes small suggesting emission on the star originates from a narrow equatorial belt having a half-height of $h \lesssim 1$ km. This is consistent with the model for the Cyg-like sources (Sect. 3.1) in which the same behaviour was observed and interpreted in terms of the mechanisms for the accretion flow in the boundary layer. In the scenario of Inogamov & Sunyaev (1999) (Sect. 2.2.2), the vertical extent of the boundary layer on the neutron star $2h$ was related to the mass accretion rate. Thus, on the NB and the HB, if due to strong radiation pressure some of the accretion flow (a part of \dot{M}) was diverted away from the star, such as in the form of jets, the reduced \dot{M} would imply a reduced emission area on the neutron star. On the other hand, there could be radial inflow of matter from the inner disk onto the neutron star and in this case the strong radiation pressure, having reduced the half-height H of the inner disk, leads to the reduced h .

In what way is GX 17+2 different from the Cyg-like sources?

The nature of the Flaring Branch The results of spectral analysis reveal that the major difference between the Cyg-like sources and GX 17+2 is in the Flaring Branch. This branch looks very different in these sources, being always short in the Cyg-like sources, but very pronounced in GX 17+2 in which it corresponds to the largest changes in intensity, such as by a factor of 2 as in the observation analysed here.

From Fig. 5.7, it is clear that the luminosity of the power law increases on the Flaring Branch and it is the increase of L_{cpl} on the FB which makes the difference. The apparent constancy of L_{cpl} on the FB in the Cyg-like sources provided evidence that the mass accretion rate was also constant on this branch. In GX 17+2, L_{cpl} increases by a factor of almost 2 and this strongly suggests that mass accretion rate increases on the Flaring Branch, as it does on the Normal Branch in all sources.

In fact, the Normal and the Flaring branch in GX 17+2 share similar characteristics: the blackbody temperature, the power law cut-off energy and the luminosities of both the main model components increase along these branches. This explains why the NB and the FB are more closely aligned in hardness-intensity than the same branches in the Cyg-like sources, on which spectral properties are very different. Therefore, the first question is how are the branches physically different.

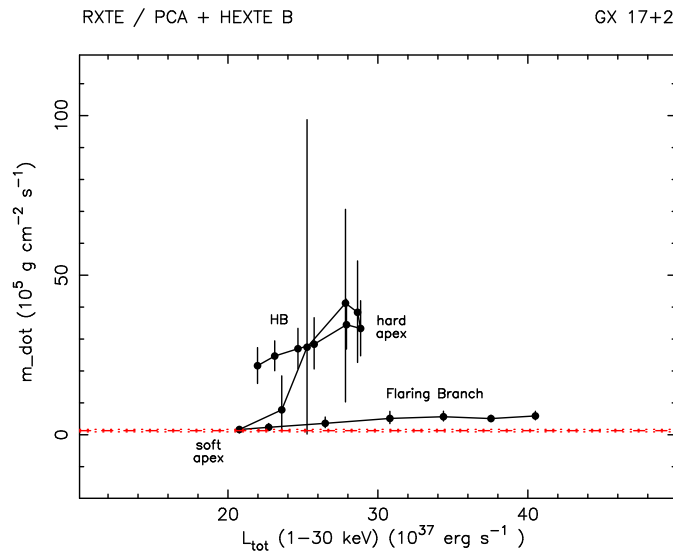


Figure 5.9: Mass accretion rate per unit emitting area \dot{m} in GX 17+2. The dashed red line marks the critical value \dot{m}_{ST} , its errors (shown with dotted lines) look very small in this figure.

In the Cyg-like sources it was proposed that mass accretion rate was constant on the FB and that flaring was due to unstable nuclear burning on the surface of the neutron star based on

the striking agreement of mass accretion rate per unit area \dot{m} with the theoretical limit \dot{m}_{ST} for unstable burning of helium. It is therefore interesting to examine the behaviour of \dot{m} on the Z-track of GX 17+2 as shown in Fig. 5.9. It can be seen that \dot{m} is far from the critical value on the Normal and the Horizontal Branch as was the case in the Cyg-like sources. However, within errors \dot{m} meets \dot{m}_{ST} when the source is at the soft apex and the lower Flaring Branch. This suggests that unstable burning can, in principle, start at the soft apex. On the upper Flaring Branch \dot{m} is generally higher than the critical value, but not by an order of magnitude, and this does not necessarily prevent unstable burning. Thus, if unstable nuclear burning starts at the soft apex, then it may continue on the FB under conditions of increasing mass accretion rate explaining the apparent strength of the branch in hardness-intensity.

Fig. 5.7 shows that L_{bb} increases on the whole Flaring Branch and the change is by a factor of ~ 4 . L_{cpl} increases on the FB by a factor of ~ 2 , so the larger change in L_{bb} may be understood as the combined effect of increasing mass accretion rate in the system and unstable nuclear burning on the neutron star.

The neutron star emission area on the Flaring Branch From Fig. 5.7 it is seen that R_{bb} is very different from that in the Cyg-like sources as it decreases in flaring. The presence of unstable burning may be the reason for which the blackbody radius does not contract to such small values as on the Normal Branch. As it was observed in the Cyg-like sources, unstable nuclear burning tends to maintain (as in Cyg X-2) or even expand (as in GX 340+0) the emission region on the neutron star. On the other hand, the radiation pressure in GX 17+2 is lower on the Flaring Branch than on the NB/HB leading to less disruption of the inner disk and less reduction of the neutron star emission region.

5.2 Scorpius X-1

The source was already analysed using the Extended ADC model by Barnard et al. (2003). In their observation, Sco X-1 exhibited extensive flaring forming a pronounced Flaring Branch in hardness-intensity which is the major characteristic of the Sco-like sources. In this section, another observation of Sco X-1 is analysed, in which the source exhibited unusually little flaring. First, the results will be compared with those for GX 17+2 and the Cyg-like sources, and second, the effects of strong flaring will be investigated.

5.2.1 Observations

The *RXTE* archive was remotely searched through in order to find observations during which the source showed relatively little flaring, such periods being very rare. A choice was made to select the observation P40706 from June 10th - 13th, 1999 which consists of a set of 20 sub-observations listed in Table 5.4.

Table 5.4: The *RXTE* sub-observations within the observation ID P40706 of Sco X-1.

Sub-observation	Start Date & Time (UT)	Duration (s)
40706-02-01-00	June 10, 1999, 09:13:02	2048
40706-02-03-00	June 10, 1999, 15:25:16	4128
40706-02-06-00	June 10, 1999, 23:26:31	3040
40706-01-01-000	June 11, 1999, 02:12:45	28160
40706-01-01-00	June 11, 1999, 10:02:08	4976
40706-02-09-00	June 11, 1999, 20:05:57	2592
40706-02-08-00	June 11, 1999, 21:48:24	2448
40706-02-10-00	June 11, 1999, 23:23:31	11744
40706-02-12-00	June 12, 1999, 03:44:26	1840
40706-02-13-00	June 12, 1999, 05:20:26	1840
40706-02-14-00	June 12, 1999, 06:55:26	1184
40706-01-02-00	June 12, 1999, 08:31:26	10608
40706-02-16-00	June 12, 1999, 13:50:38	3744
40706-02-17-00	June 12, 1999, 16:46:13	1856
40706-02-18-00	June 12, 1999, 21:42:44	2720
40706-02-19-00	June 12, 1999, 23:20:30	11856
40706-02-21-00	June 13, 1999, 03:43:36	1824
40706-02-22-00	June 13, 1999, 05:18:36	1824
40706-02-23-00	June 13, 1999, 06:54:36	1232
40706-01-03-00	June 13, 1999, 08:30:36	10592

5.2.2 Analysis

The most recent *HEASOFT* (version 6.10) was used in the standard analysis procedure. Examination of the housekeeping data showed that only two of five PCU units (PCU 0 & 2) were operational. In the case of Scorpius X-1, it is enough to use one PCU and one half of the detector as the source is very bright and its count rate is very high. Moreover, the effect of pulse pile-up is known to be important for such bright sources and an appropriate correction must be applied. The procedure of pile-up correction (Appendix A) works reliably only for a single PCU and so a decision was made to use PCU 2. Standard screening criteria were applied, i.e. $\text{ELV} > 10^\circ$ and $\text{OFFSET} < 0.02^\circ$ which gave ~ 86 ks of clean data.

Lightcurves with 64 s binning were extracted from Standard2 data in the energy bands: low (1.9 - 4.1 keV), medium (4.1 - 7.3 keV), high (7.3 - 18.5 keV) and total (1.9 - 18.5 keV). The channel-to-energy conversion was appropriate for the calibration epoch 4 of the mission. A background and deadtime corrections were carried out. The background-subtracted and deadtime-corrected lightcurve in the total 1.9 - 18.5 keV energy range is shown in Fig. 5.10.

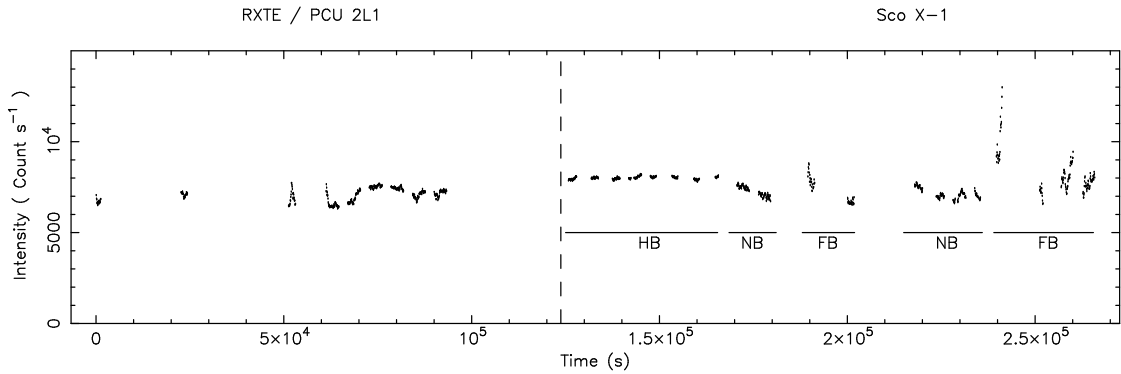


Figure 5.10: The background-subtracted and deadtime-corrected lightcurve of Sco X-1. In the analysis, only data after the vertical dashed line were used. The 64 s time binning was chosen.

Lightcurves obtained in the medium and the high energy bands were used to produce a hardness-intensity diagram revealing the Z-track of the source. However, it was apparent that there were two Normal Branches shifted a little with respect to each other. Having identified particular sub-observations in the diagram it became obvious that the first five of them (from 40706-02-01-00 to 40706-02-01-00) constituted part of a separate Z-track. Therefore, the first five sub-observations were not used in order to avoid mixing of data from different Z-tracks. The remaining sub-observations to the right from the vertical line in Fig. 5.10 were used for analysis. The identification of segments of data in the lightcurve with their Z-track positions showed that during

the first ~ 45 ks Sco X-1 was on the Horizontal Branch exhibiting little variation in intensity and then descended the Normal Branch after which it exhibited weak flaring. A stronger flaring event is visible at $t \sim 2.5 \times 10^5$ s near the end of the observation.

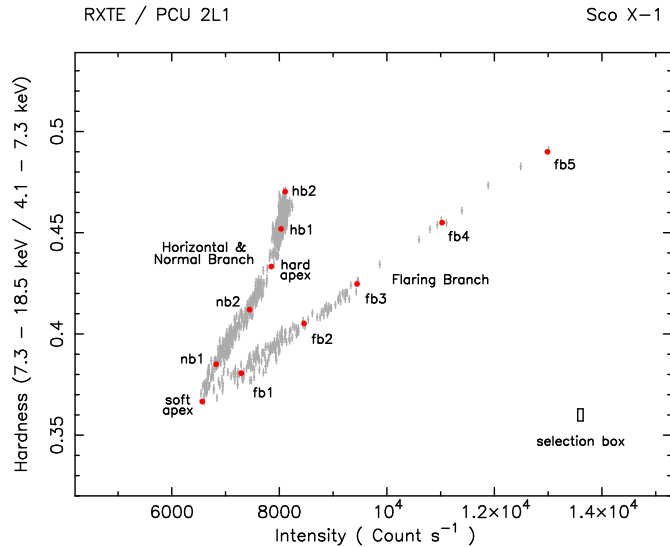


Figure 5.11: The background-subtracted and deadtime-corrected hardness-intensity of Sco X-1 with the positions of the data selections marked with red filled circles. A rectangular box in the bottom right corner shows the actual selection size. Data that have been excluded from the analysis (see text) are not shown.

Eleven data selections were made along the Z-track using boxes 100 count s^{-1} wide in intensity and 0.006 wide in hardness as shown in Fig. 5.11. For each selection, on-source and background spectra from Standard2 data were extracted and deadtime-corrected. The number of counts per PCU spectral channel was typically $10^3 - 10^4$. Pulse pile-up correction was made using a local script that follows the procedure of Tomsick & Kaaret (1998) described in Appendix A. In pulse pile-up, two photons may be seen in the detector as a single event which affects the measured energy and makes the observed spectrum distorted. The script produces a correction file for use in *Xspec*. In the PCA, the systematic errors of 1% are usually used, but in Sco X-1 Poisson errors are negligibly small and hence systematic errors of 1.5% were added. With Sco X-1, it is a common practice not to point the satellite directly at the source, but to use a small offset to avoid possible damage of the instruments. During the observation analysed here, the satellite was pointed at coordinates $\alpha = 16^{\text{h}}19^{\text{m}}50^{\text{s}}.4$ and $\delta = -16^{\circ}2'24''$, which is $24'$ off the real source position ($\alpha = 16^{\text{h}}19^{\text{m}}55^{\text{s}}.07$, $\delta = -15^{\circ}38'25''$). This is taken into account when spectral responses are generated. The information about the source real position was updated in headers of all spectral files using the FMODHEAD tool and then PCARSP was used to generate the appropriate response file.

HEXTE spectra were extracted for each selection using data from Cluster A obtaining typically 200 counts per channel. Deadtime corrections were applied. HEXTE spectra were additionally grouped in `grppha`, i.e. higher energy channels were re-binned into groups of two or four to get a better signal to noise ratio. HXTRSP was used to generate HEXTE response files appropriate to the offset pointing.

5.2.3 Spectral fitting results

The PCA and HEXTE spectra were fitted simultaneously. In the case of the PCA, the spectral range used was typically 3 - 20 keV and in HEXTE spectra it extended to 50 keV.

The PCA is not sensitive below 3 keV and so column densities below 10^{22} atom cm^{-2} are often difficult to constrain. In this work the column density was frozen at 0.3×10^{22} atom cm^{-2} as previously used by Barnard et al. (2003).

The impact of the choice of the photon index on spectral results was directly checked by comparing with those obtained for the observation P30036 by Barnard et al. (2003) (who used a free photon index) in a re-analysis of their observation with Γ frozen at 1.7. This showed that there was no major change in the variation of any parameter around the Z-track, and the parameter values changed by a few percent only. Thus, in the present analysis the photon index was frozen at 1.7 for consistency with all other studies carried out in this work.

Initial fitting revealed an excess at around 6.5 keV showing the presence of a broad emission line. The part of the spectrum between 5.0 and 8.0 keV was ignored and fitting repeated in order to get a better estimate of the continuum not affected by the line. Next, the continuum fit was frozen and a Gaussian line added to the model. Based on the relation $\text{FWHM} \approx 2.36 \sigma$ for a Gaussian line, σ was estimated to be 0.8 keV and frozen to avoid the line absorbing the neighbouring continuum. With the line added, acceptable values of $\chi^2/\text{d.o.f.}$ in the range 18/41 - 42/41 were obtained. Figure 5.12 shows typical folded spectra (left) and the corresponding unfolded spectra (right), whereas the results are given in Table 5.5 and Table 5.6.

The blackbody parameters Figure 5.13 shows the variation of the blackbody kT_{bb} and R_{bb} parameters on the Z-track. The temperature is minimal at 1.83 ± 0.14 keV when the source is at the soft apex. From this point, it increases along the Normal Branch reaching 2.28 ± 0.05 keV on the Horizontal Branch. Thus, unlike in the Cyg-like sources (and in GX 17+2), the change is not large, but significant. The blackbody radius at the soft apex is only 5.3 ± 0.9 km showing clearly

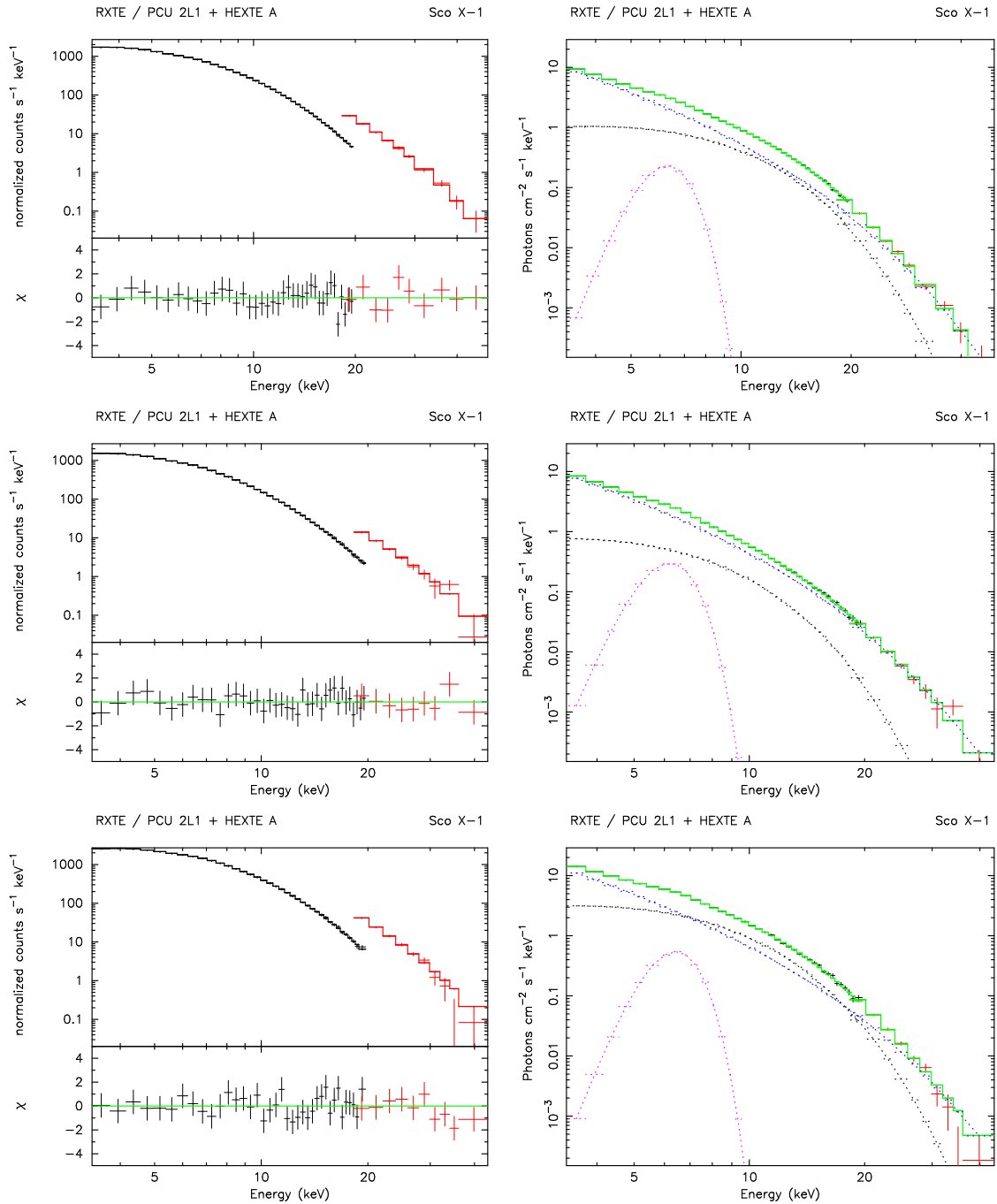


Figure 5.12: Representative folded and unfolded spectra of Sco X-1 are shown in the left and right panel, respectively. These are from: Horizontal Branch (hb2, top), soft apex (sa, middle) and Flaring Branch (fb5, bottom). In the left panel, PCA and HEXTE data, and best-fit model are shown with residuals in the inset underneath. In the right panel: blackbody (black), cut-off power law (blue), emission line (magenta), and the total spectrum (green) are shown unfolded.

Table 5.5: The spectral fitting results for Sco X-1 observation P40076 with reduced flaring.

Sel.	Blackbody		Emission line		Cut-off power law		$\chi^2/\text{d.o.f.}$
	kT_{bb}	norm	E_l	EW	E_{co}	norm	
hb2	2.28 ± 0.05	1.07 ± 0.05	6.29 ± 0.29	175	6.30 ± 0.29	130 ± 4	26/42
hb1	2.26 ± 0.03	1.01 ± 0.04	6.25 ± 0.24	203	5.98 ± 0.08	135 ± 4	36/50
ha	2.23 ± 0.08	0.89 ± 0.07	6.33 ± 0.20	235	5.85 ± 0.29	138 ± 6	36/50
nb2	2.14 ± 0.06	0.74 ± 0.05	6.30 ± 0.22	215	5.68 ± 0.13	138 ± 4	22/37
nb1	2.01 ± 0.07	0.54 ± 0.04	6.27 ± 0.19	241	5.66 ± 0.13	132 ± 4	28/44
sa	1.83 ± 0.14	0.52 ± 0.07	6.20 ± 0.19	254	5.62 ± 0.27	127 ± 8	19/41
fb1	1.85 ± 0.07	0.73 ± 0.07	6.30 ± 0.17	270	5.57 ± 0.18	135 ± 6	25/43
fb2	1.87 ± 0.06	1.17 ± 0.08	6.30 ± 0.19	256	5.63 ± 0.20	140 ± 7	42/41
fb3	1.90 ± 0.05	1.51 ± 0.09	6.29 ± 0.20	235	5.75 ± 0.13	145 ± 4	36/40
fb4	1.94 ± 0.04	2.03 ± 0.10	6.39 ± 0.22	210	5.93 ± 0.18	154 ± 8	38/44
fb5	2.05 ± 0.05	2.62 ± 0.14	6.42 ± 0.21	235	5.95 ± 0.33	175 ± 10	32/41

The units are: keV (the blackbody temperature, the cut-off energy and the line energy), 10^{39} erg s $^{-1}$ (the blackbody normalization, assuming a distance of 10 kpc), eV (the line equivalent width), and photons keV $^{-1}$ cm $^{-2}$ s $^{-1}$ at 1 keV (the cut-off power law normalization).

Table 5.6: The physical quantities derived from fitting results.

Selection	R_{bb}	h	f_{bb}/f_{Edd}	\dot{m}	L_{bb}	L_{cpl}	L_{tot}	H_{eq}
hb2	4.9 ± 0.2	2.4 ± 0.2	1.87 ± 0.09	8.5 ± 0.8	8.4 ± 0.4	38.5 ± 1.3	47.3	40.3 ± 1.3
hb1	4.84 ± 0.15	2.34 ± 0.14	1.81 ± 0.06	8.6 ± 0.5	7.9 ± 0.3	38.7 ± 1.0	47.2	40.1 ± 1.1
ha	4.7 ± 0.4	2.2 ± 0.3	1.71 ± 0.13	9.2 ± 1.4	7.0 ± 0.5	38.9 ± 1.7	46.4	39.5 ± 1.7
nb2	4.6 ± 0.3	2.2 ± 0.3	1.44 ± 0.09	8.8 ± 1.1	5.8 ± 0.4	38.0 ± 1.2	44.3	37.8 ± 1.2
nb1	4.5 ± 0.4	2.0 ± 0.3	1.13 ± 0.09	8.9 ± 1.4	4.2 ± 0.4	36.2 ± 1.2	41.0	34.9 ± 1.2
sa	5.3 ± 0.9	2.8 ± 0.9	0.78 ± 0.11	6.1 ± 2.0	4.1 ± 0.6	34.7 ± 2.0	39.3	34 ± 2
fb1	6.1 ± 0.6	3.7 ± 0.7	0.82 ± 0.07	4.9 ± 0.9	5.7 ± 0.5	36.6 ± 1.7	42.9	36.6 ± 1.7
fb2	7.6 ± 0.5	5.8 ± 0.8	0.85 ± 0.06	3.6 ± 0.5	9.1 ± 0.6	38.3 ± 1.9	48.2	41 ± 2
fb3	8.4 ± 0.5	7.0 ± 0.8	0.90 ± 0.05	3.2 ± 0.4	11.8 ± 0.7	40.3 ± 1.2	52.9	45.1 ± 1.3
fb4	9.3 ± 0.4	8.7 ± 0.8	0.97 ± 0.05	3.0 ± 0.3	15.9 ± 0.8	43.9 ± 2.1	60.6	52 ± 3
fb5	9.5 ± 0.5	8.9 ± 1.0	1.23 ± 0.07	3.4 ± 0.4	20.5 ± 1.1	50.0 ± 3.0	71.6	61 ± 4

The blackbody radius R_{bb} , the half-height of the equatorial belt on the neutron star h and the equilibrium half-height of the inner, radiatively-supported accretion disk H_{eq} are expressed in km, mass accretion rate is in units of 10^5 g cm $^{-2}$ s $^{-1}$, the blackbody luminosity (bolometric) is given in 10^{37} erg s $^{-1}$ while L_{cpl} and L_{tot} are in 1 - 30 keV range in 10^{37} erg s $^{-1}$. The distance to the source was taken to be 2.8 kpc.

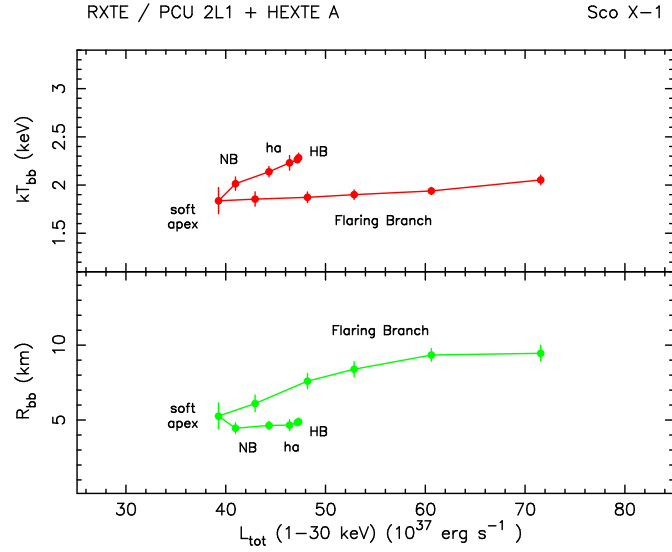


Figure 5.13: The parameters of the blackbody model component: temperature (top) and radius (bottom) as a function of the total (1 - 30 keV) luminosity.

that emission does not come from the whole surface of the neutron star. The blackbody radius shows little change on the NB and the HB remaining close to $\lesssim 5$ km which means that emission comes from an equatorial belt whose half-height is stable at $h \lesssim 2.5$ km.

On the Flaring Branch, the temperature shows a small continuous increase similar to the behaviour observed in GX 17+2. However, there is a large increase of R_{bb} along the branch to 9.5 ± 0.5 km suggesting that the emission region spreads over the star during flaring until the whole stellar surface is involved.

The luminosities The luminosities of the continuum emission components are shown in Fig. 5.14. The luminosity of the cut-off power law has a minimum at the soft apex and then increases to a maximum at the hard apex consistent with all the Z-track sources suggesting that the mass accretion rate increases in this direction. Beyond the hard apex the changes of L_{cpl} are not significant and hence the information about \dot{M} is limited.

However, the power law luminosity increases much more significantly (by $\sim 45\%$) on the Flaring Branch. This reveals an underlying change of mass accretion rate on this branch, unlike in the Cyg-like sources, but similar to what was observed in GX 17+2 suggesting that the nature of the FB in GX 17+2 and Sco X-1 may be similar.

The blackbody luminosity (top panel) increases on both the NB and the FB, but the magnitude of these changes is much larger on the Flaring Branch, where both kT_{bb} and R_{bb} increase leading to an increase of L_{bb} by a factor of ~ 5 . In consequence, the contribution of L_{bb} to the total increases

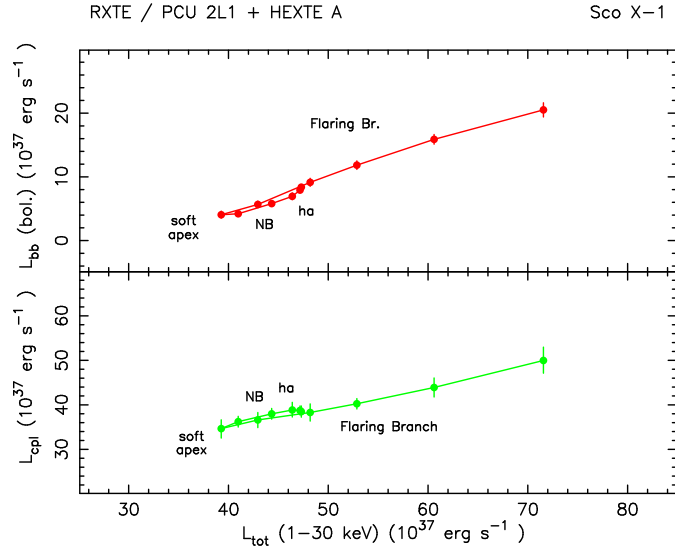


Figure 5.14: The luminosities of the two main model components: blackbody (bolometric, top panel) and cut-off power law (1 - 30 keV, lower panel).

from only 10% at the soft apex to almost 30% at the end of the Flaring Branch. Such changes of the blackbody are similar to those observed in the Cyg-like sources where they were attributed to thermonuclear burning on the neutron star. This was based on the agreement between mass accretion rate per unit area \dot{m} with the theoretical threshold for unstable burning \dot{m}_{ST} of Bildsten (1998). However, in the Cyg-like sources this happened at a constant mass accretion rate, whereas here mass accretion rate most probably increases, as it was seen in GX 17+2.

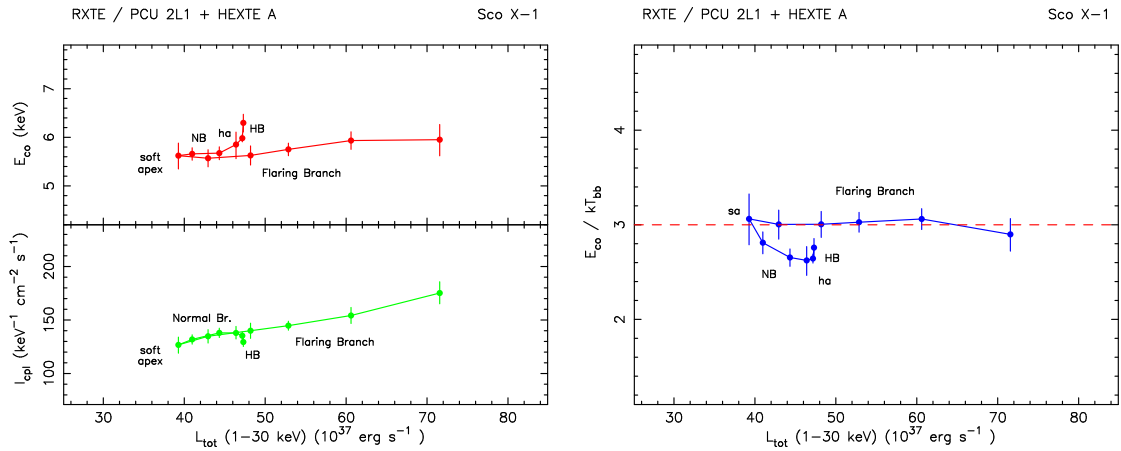


Figure 5.15: Left: The parameters of the cut-off power law: the cut-off energy (top) and the normalization (bottom). Right: The ratio of the cut-off energy and the blackbody temperature. The red dashed line marks the $E_{co}/kT_{bb} = 3$ ratio.

The ADC emission The cut-off energy and the normalization of the Comptonized emission are shown in Fig. 5.15, left panel. Given similar changes of the blackbody temperature, one can see that E_{co} correlates very well with kT_{bb} suggesting a link between the neutron star kT_{bb} and kT_e in the ADC. That this is the case is supported by the ratio E_{co}/kT_{bb} (right panel of Fig. 5.15) being very close to 3 (with an average of 2.88 ± 0.18) at all Z-track positions. This was also seen in other Z-track sources and suggests that thermal equilibrium between the neutron star and the optically thick corona is a common characteristic of these sources.

The emission line The emission line has a centroid energy in the narrow range 6.20 - 6.42 keV with little variation on the Z-track. Within 90% confidence errors (± 0.2) these values are consistent with the 6.4 keV $K\alpha$ line of neutral iron. The equivalent width of the line shows no major changes on the Z-track and is on average 230 eV.

5.2.4 Discussion and comparison with previous work

A comparison with the other Z-track sources

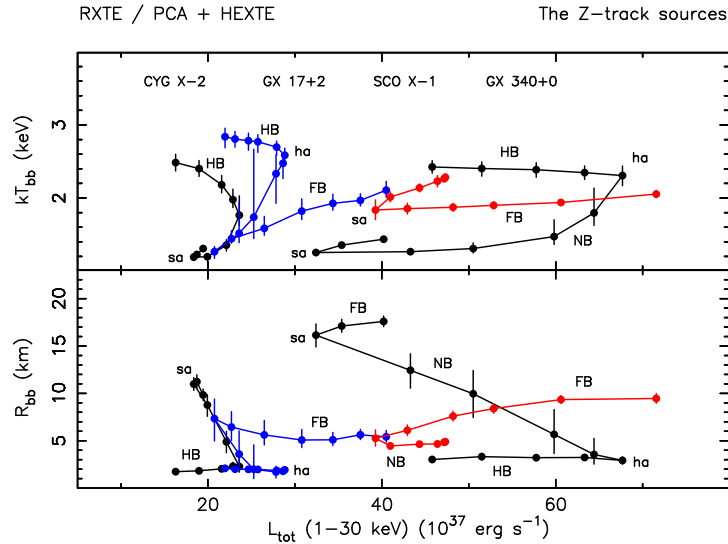


Figure 5.16: The blackbody temperature (top) and radius (bottom). The sources are shown with different colours: black - the Cyg-like sources, blue - GX 17+2, red - Sco X-1.

The neutron star blackbody From Fig. 5.16 it can be seen that the major difference is in kT_{bb} which in Sco X-1 is $\gtrsim 2$ keV at all Z-track positions, even at the soft apex, where it is low ~ 1.3 keV in the other sources. Similarly, R_{bb} at the soft apex in Sco X-1 is reduced below 10 km consistent with the high kT_{bb} (as in the Cyg-like sources close to the *hard* apex). During flaring,

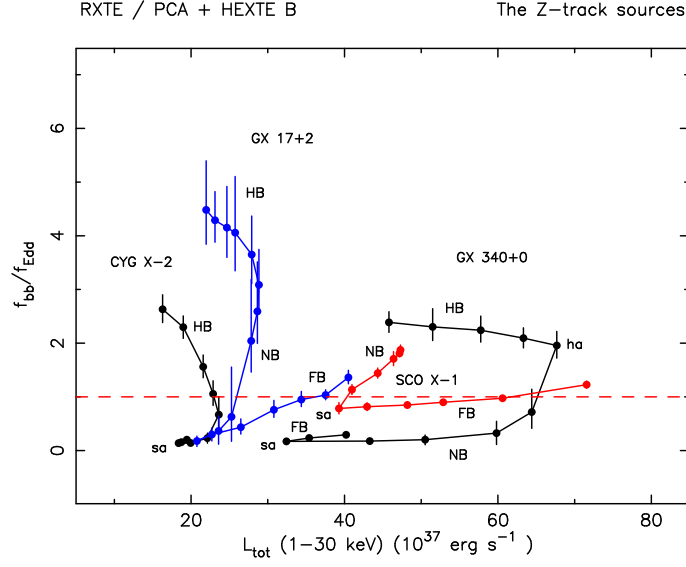


Figure 5.17: The strength of radiation pressure expressed as the ratio f_{bb}/f_{Edd} .

R_{bb} increases asymptotically to ~ 10 km suggesting that the whole neutron star then emits.

The launching of jets Figure 5.17 shows an important difference between Sco X-1 and the other sources, i.e. that because of the high kT_{bb} in Sco X-1 the radiation pressure is almost always super-Eddington, at all Z-track positions. Indeed, the minimal value of f_{bb}/f_{Edd} is ~ 0.8 , whereas in all other sources the radiation pressure is much smaller close to the soft apex.

In the Cyg-like sources, strong radiation pressure was thought to cause the launching of jets. These are often observed on the upper NB/HB, but not at the soft apex and on the Flaring Branch. In Sco X-1, the radiation pressure is strong at the whole Z-track and this leads to an important observational prediction that jets could, in principle, be observed on the whole Z-track in this source. In fact, it is already known that Sco X-1 is detected as radio-loud on the NB/HB, where its radio flux is strongest and most variable, but the source is also detected in a radio-quiet state when on the FB, the emission interpreted as synchrotron radiation such as of a jet (Hjellming et al. 1990b) and apparently not restricted to the NB and HB only. Future X-ray/radio observations should be aimed at improving our understanding of the relation between the strength of radiation pressure and the radio/jet emission in this source.

The increase of \dot{M} on the FB and the nature of flaring Fig. 5.18 shows that the luminosity of the Comptonized emission in Sco X-1, as in GX 17+2, increases strongly in flaring, while it is constant in the Cyg-like sources. Figure 5.19 shows that in the Cyg-like sources and in GX 17+2,

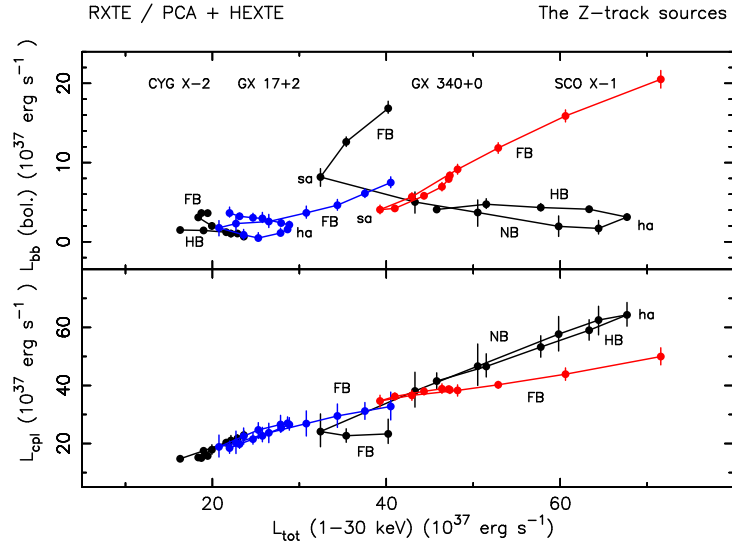


Figure 5.18: The luminosities of the blackbody (top) and the power law (bottom). The sources are shown with different colours: black - the Cyg-like sources, blue - GX 17+2, red - Sco X-1.

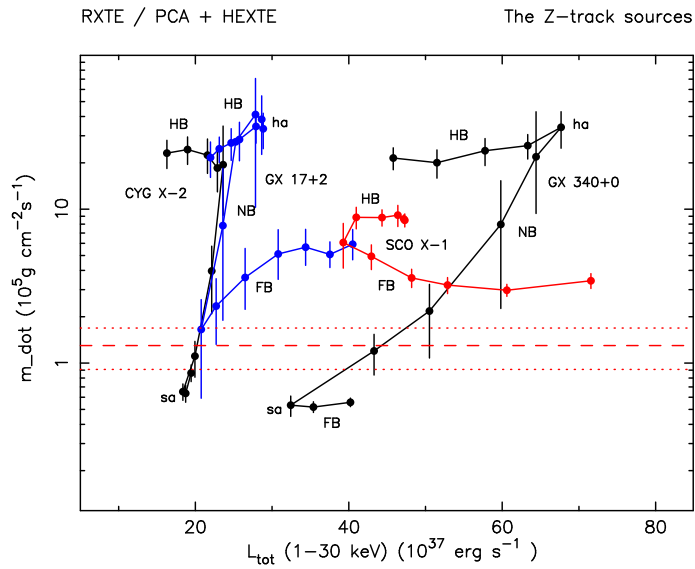


Figure 5.19: The mass accretion rate per unit emitting area, the logarithmic scale is used to improve clarity.

the condition for unstable nuclear burning is met ($\dot{m} \sim \dot{m}_{ST}$) at the soft apex. However, in Sco X-1 $\dot{m} > \dot{m}_{ST}$ at all Z-track positions which would suggest that unstable nuclear burning should not take place. However, the blackbody luminosity L_{bb} in Sco X-1 increases in flaring as in the Cyg-like sources and GX 17+2 suggesting that flaring does consist of unstable nuclear burning and increase of mass accretion rate.

Several possibilities exist of why unstable nuclear burning happens in Sco X-1 despite the measured $\dot{m} > \dot{m}_{ST}$. Firstly, the accreting area on the neutron star in Sco X-1 is reduced to an equatorial belt and so there are zones on the star beyond the belt in which \dot{m} is much lower. Thus, at the edges of the accreting belt of the neutron star, \dot{m} would be reduced and could fall into the unstable burning régime. Such a possibility was discussed by Galloway et al. (2008) when the accreted material is not evenly distributed on the neutron star. In consequence, if unstable burning starts there, it could spread over a larger fraction of the stellar surface (Bildsten 1993, 1995). This scenario was not considered here in the case of the Cyg-like sources in which accretion took place on the whole neutron star and so \dot{m} had to fall below \dot{m}_{ST} at every point on the star for the unstable burning to start. Secondly, the temperature on the neutron star in Sco X-1 is always close to 2 keV so that the radiation pressure is always strong. This should divert some plasma in the inner disk away from the neutron star and effectively reduce \dot{M} to the neutron star leading to reduced \dot{m} . However, for this to allow $\dot{m} \sim \dot{m}_{ST}$, the radiation pressure would need to reduce \dot{M} to the neutron star by a factor of ~ 5 which is not impossible. Also, as mentioned in Sect. 3.1.4, the definition of \dot{m} used here may somewhat overestimate the actual \dot{m} and this, if taken into account, would improve the agreement with \dot{m}_{ST} in Sco X-1 (and GX 17+2), though the actual magnitude of any modification is in fact uncertain. Nevertheless, comparing with the Cyg-like sources, a clear difference in flaring in Sco X-1 and GX 17+2 is apparent.

Comparison with the flaring-active observation

The results obtained in the present work for the observation P40706 with reduced flaring can now be compared with those obtained when the source exhibited strong flaring (observation P30036). This is aimed at testing if flaring has any effects on the source. The strong-flaring observation was analysed before using the Extended ADC model by Barnard et al. (2003) who allowed the photon index of the power law to vary in spectral fitting. The observation was reanalysed by Church et al. (2012) (submitted) with the photon index frozen at 1.7 and their fitting results are shown in Table 5.7 which can be directly compared with Table 5.5. Also, a visual comparison is made

here in Fig. 5.20 (blackbody parameters) and Fig. 5.21 (luminosities of the model components). It was found that, with all parameters showing the same general behaviour along the Z-track, an important physical difference is in the kT_{bb} of the neutron star blackbody (top panel of Fig. 5.20).

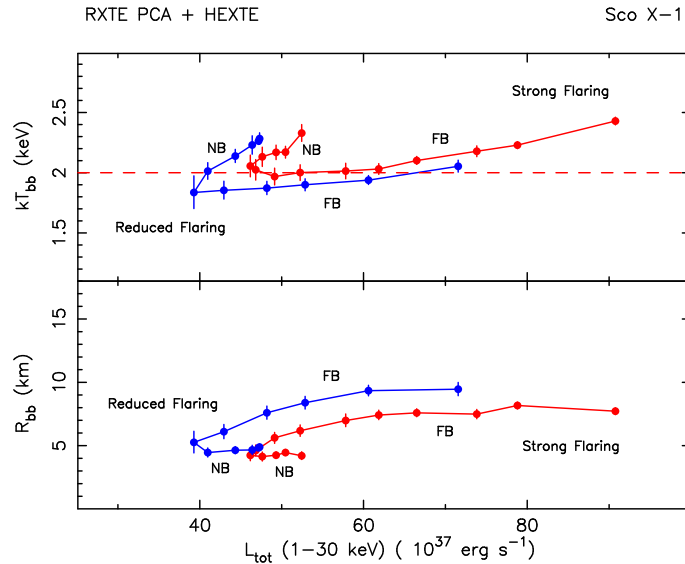


Figure 5.20: A comparison of the blackbody parameters in Sco X-1 showing strong flaring (observation P30036) and reduced flaring (observation P40706). The red dashed line marks the usual minimum temperature of the neutron star of 2 keV in the source.

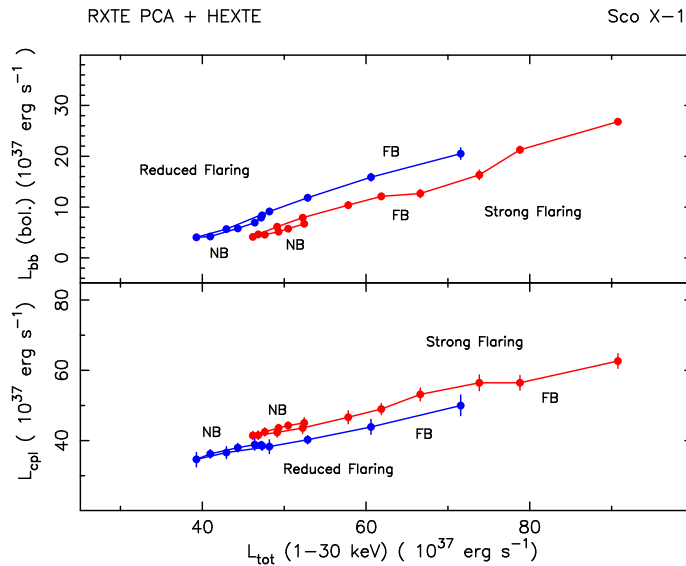


Figure 5.21: The luminosities of the Comptonized and blackbody emission in Sco X-1. The two observations: P30036 (with strong flaring) and P40706 (with reduced flaring) are compared.

In the observation with strong flaring the blackbody temperature is $\gtrsim 2$ keV at all Z-track positions. This is in agreement with other analyses of Sco X-1 carried out within the *X-ray Binaries*

Table 5.7: The spectral fitting results for Sco X-1 observation P30036 with strong flaring (Church et al. 2012a submitted).

Sel.	Blackbody		Emission line		Cut-off power law		$\chi^2/\text{d.o.f.}$
	kT_{bb}	norm	E_l	EW	E_{co}	norm	
nb4	2.33 ± 0.07	0.86 ± 0.07	6.39 ± 0.24	257	5.35 ± 0.37	171 ± 6	43/55
nb3	2.16 ± 0.05	0.73 ± 0.05	6.42 ± 0.22	175	5.71 ± 0.08	160 ± 4	36/55
nb2	2.17 ± 0.06	0.66 ± 0.04	6.40 ± 0.22	208	5.53 ± 0.08	162 ± 4	33/55
nb1	2.13 ± 0.08	0.58 ± 0.05	6.37 ± 0.23	239	5.50 ± 0.11	158 ± 4	32/55
sa	2.06 ± 0.09	0.53 ± 0.06	6.34 ± 0.16	236	5.44 ± 0.13	156 ± 5	42/55
fb1	2.02 ± 0.08	0.59 ± 0.05	6.33 ± 0.20	276	5.26 ± 0.14	160 ± 5	47/55
fb2	1.97 ± 0.07	0.78 ± 0.06	6.33 ± 0.19	259	5.22 ± 0.15	164 ± 5	49/55
fb3	2.00 ± 0.07	1.01 ± 0.07	6.34 ± 0.20	264	5.18 ± 0.18	170 ± 6	32/55
fb4	2.01 ± 0.06	1.32 ± 0.09	6.42 ± 0.20	254	5.23 ± 0.21	181 ± 8	45/55
fb5	2.03 ± 0.04	1.54 ± 0.08	6.43 ± 0.20	220	5.43 ± 0.13	184 ± 6	60/55
fb6	2.10 ± 0.03	1.62 ± 0.09	6.43 ± 0.20	263	5.40 ± 0.20	193 ± 5	61/45
fb7	2.18 ± 0.04	2.08 ± 0.12	6.52 ± 0.22	259	5.36 ± 0.25	214 ± 9	37/46
fb8	2.05 ± 0.03	2.71 ± 0.11	6.41 ± 0.22	235	5.50 ± 0.20	210 ± 7	28/40
fb9	1.99 ± 0.03	3.42 ± 0.08	6.41 ± 0.20	250	6.15 ± 0.15	215 ± 8	33/46

The blackbody temperature, the cut-off energy and the line energy are given in keV, the blackbody normalization, assuming a distance of 10 kpc, is expressed in $10^{39} \text{ erg s}^{-1}$, the line equivalent width is in eV, and the cut-off power law normalization is in photons $\text{keV}^{-1} \text{ cm}^{-2} \text{ s}^{-1}$ at 1 keV.

Group in which kT_{bb} has never been measured to be lower than ~ 2 keV. However, at the soft apex in the observation with reduced flaring (P40706), the temperature is $kT_{bb} = 1.83 \pm 0.14$ keV which is at 2σ confidence level significantly lower than 2.06 ± 0.09 keV measured in the P30036 observation. The difference is in fact even more significant, when measurements on the Flaring Branch in P40706 are included, all (except the last point at the end of the branch) having $kT_{bb} < 2$ keV seen as a significant depression of the blue curve below the red line in Fig. 5.20.

Thus, the result obtained here suggests that the lower neutron star temperature is associated with the period of reduced flaring in the source. On the other hand, this is also the first observational evidence that sheds light on the possible reason for which in general the neutron star in Sco X-1 is always hot, i.e. that this could be caused by large amounts of flaring.

5.3 Explaining the Sco-like sources

5.3.1 The high neutron star temperature

Figure 5.22 shows the temperature of the neutron star at the soft apex in all the six classical Z-track sources. In the case of GX 5-1, the values quoted are from Jackson et al. (2009), while the values for Sco X-1 and GX 349+2 are from Church et al. (2012), submitted. The value for Sco X-1 was taken from a reanalysis of the P30036 observation of Sco X-1 with strong flaring. However, the slightly lower value of the temperature in Sco X-1 obtained in the present work is also close to 2 keV.

It is striking that in the Cyg-like sources kT_{bb} is low (~ 1.3 keV), whereas Sco X-1 and GX 349+2 have much hotter neutron stars at the soft apex (~ 2 keV). In this respect, GX 17+2 is more similar to the Cyg-like sources.

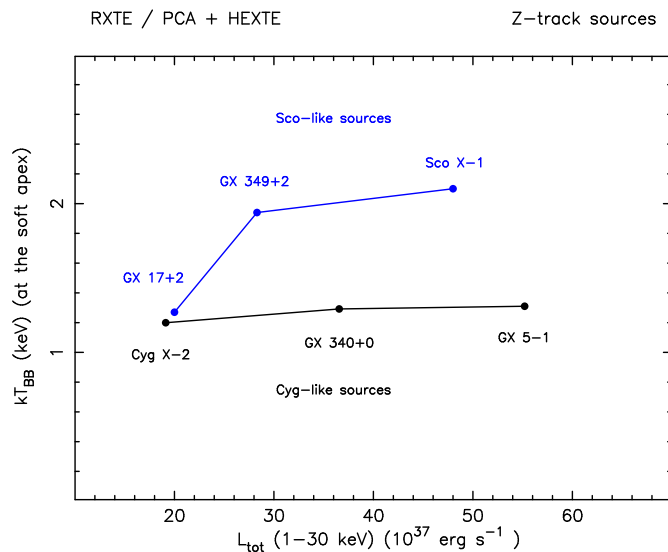


Figure 5.22: The blackbody temperature measured at the soft apex shown as a function of the total (1 - 30 keV) luminosity.

Results obtained in this work for Sco X-1 seem to reveal a possible explanation. In Sect. 5.2.4 it was shown that in typical observations of Sco X-1, when the source exhibits lots of strong flaring, the neutron star temperature is always above 2 keV. However, in the dataset P40076 analysed in this work, after a relatively long period of reduced flaring, the temperature at the soft apex and the lower FB was not as high suggesting a possible relation between the amount of flaring and the temperature of the neutron star. It is therefore of interest to look more closely at the Z-track sources in terms of their flaring activity.

5.3.2 The Z-track sources seen by the *RXTE*/All-Sky Monitor

The usage of *RXTE* pointed observations gives a rather limited insight into the long-term behaviour of X-ray sources. However, one may take advantage of the capabilities of the All-Sky Monitor (ASM) on-board *RXTE*. The ASM archived observations of the six Z-track sources were retrieved and the 14 year-long lightcurves produced in the whole 1 - 12 keV energy range available using all three Scanning Shadow Cameras (Fig. 5.23). Data points (typically a dozen per day) correspond to single observations (ASM dwells) lasting 90 seconds. Simultaneous entries from multiple cameras were averaged if these occurred. The lightcurves of the three Cyg-like sources are shown in the top three panels in green, and the Sco-like sources are in the bottom panels in blue.

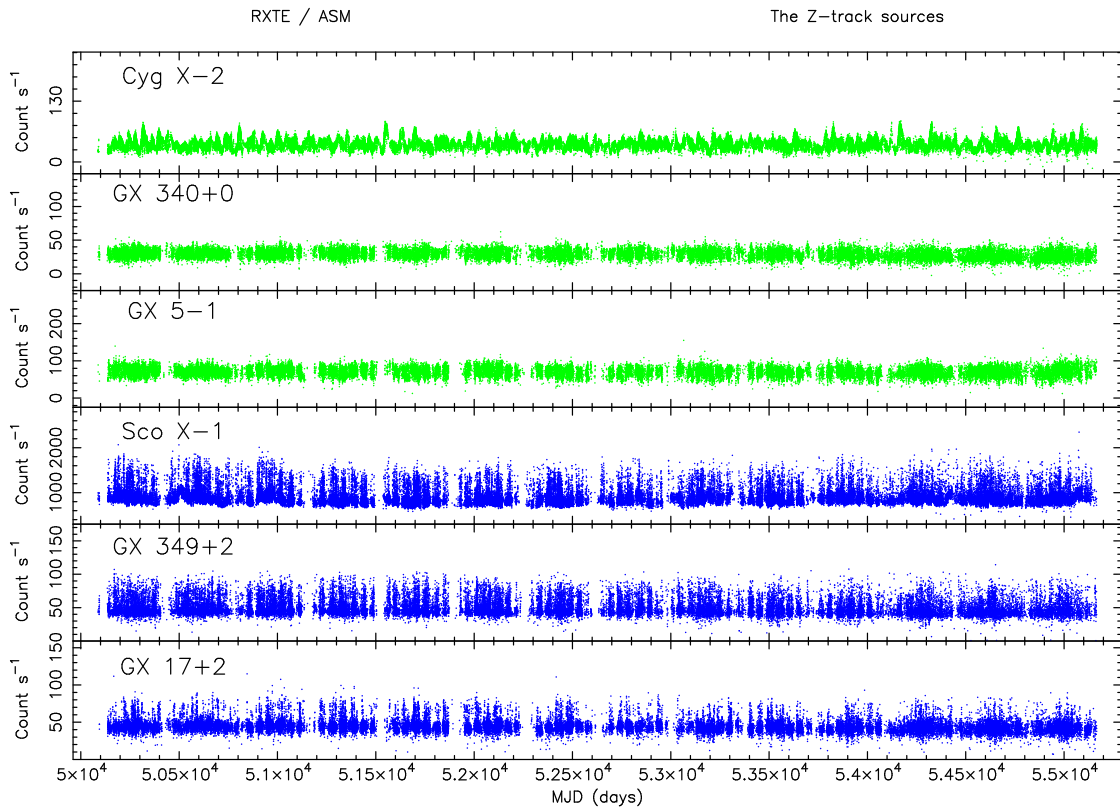


Figure 5.23: The long-term All-Sky Monitor lightcurves of all six classic Z-track sources: the Cyg-like sources (green) and the Sco-like sources (blue).

The figure shows that the most striking feature of the Sco-like sources is their extensive flaring clearly visible as strong intensity spikes in all three sources. This is never observed in the Cyg-like sources whose variability is related to the movement of a source along the NB and the HB, and flaring is in fact weak and not easily recognizable in the ASM lightcurves. This was directly

checked in the case of Cyg X-2 by combining *RXTE* data with pointed observations. The archival data were remotely accessed and all sub-observations identified in terms of their position on the Z-track showing only a few occasions on which flaring in Cyg X-2 could be observed. It must be noted here, that the ‘spikes’ visible in the lightcurve of Cyg X-2 in the top panel of Fig. 5.23 are not flaring events, but peaks of secular intensity changes very characteristic to this source (Sect. 3.2.2) as demonstrated in an expanded lightcurve in Fig. 5.24 (which can be compared with flaring in Fig. 5.25).

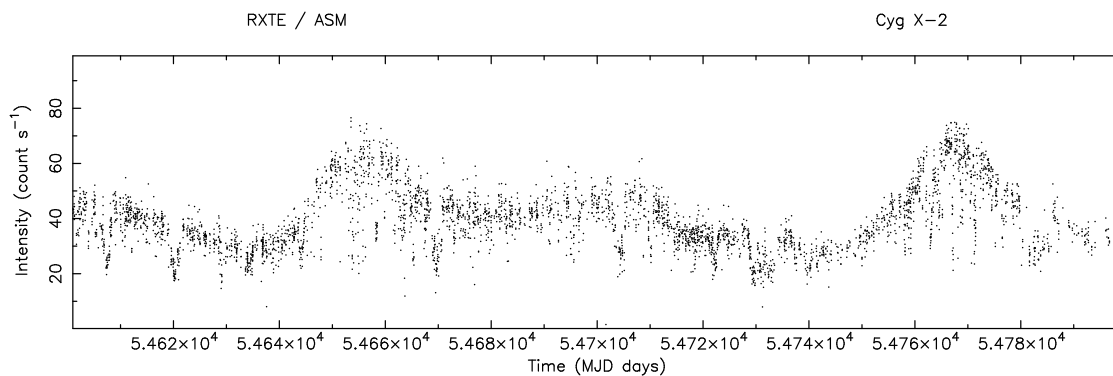


Figure 5.24: An example *RXTE*/*ASM* lightcurve of Cyg X-2 between MJD 54600 and MJD 54800 showing secular changes (long-term envelope) in the source not related to strong flaring. Short-term (~ 2 days) intensity variations have been identified as Z-track movement.

On the other hand, flaring in the Sco-like sources is not only strong, but also very frequent. Figure 5.25 (left) shows the lightcurve of Sco X-1 with an expanded view of part of it (right). Intensity spikes are visible and correspond to strong flares in the source. This was again checked by identifying these with corresponding Flaring Branches on the Z-track using pointed observations from the PCA.

Let us therefore concentrate on the Sco-like sources and their pronounced flaring. It is possible to obtain a rough estimation of flaring activity by simply counting flares and then dividing by the total observation time. For this, the whole lightcurve was divided into sections in which individual flares were easily visible and those that extended above the approximate hard apex intensity level (see Fig. 5.25, right), not to confuse strong flares with motion on the Normal/Horizontal Branch, were counted. The number of flares per section was then divided by the section timespan to obtain the rate of flaring. This was repeated manually for all sections of data and individual results were averaged to get an estimate of the rate at which flaring occurs. To verify and supplement this result, a dedicated computer program was created whose task was to identify flares, find the peak

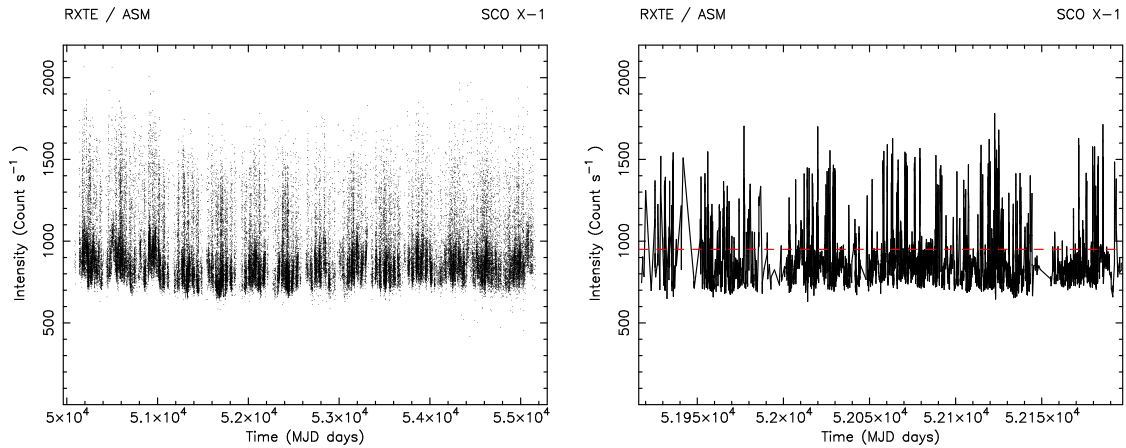


Figure 5.25: Left: The 14 year-long lightcurve of Sco X-1 from *RXTE*/*ASM*. Right: A zoom-in of an example part of the full lightcurve between MJD 51916 and 52197. The red dashed line gives the approximate position of the hard apex. Spikes extending above the red line are strong flaring events.

of each and record time intervals between flares throughout the 14-year-long lightcurves of the three Sco-like sources.

The two approaches gave similar results, the mean flare rates are listed in Table 5.8 while Fig. 5.26 compares the histograms of flare intervals in the three Sco-like sources. The results presented should be in fact treated as lower limits because the *ASM* lightcurves are not evenly sampled and have many data gaps (e.g. periodically, due to the Sun proximity avoidance of the satellite). The values obtained here were not corrected for these effects comparable for all sources.

Table 5.8: The average number of flare events per day estimated from long-term *RXTE*/*ASM* lightcurves for all Sco-like sources.

Source	Average flaring rate (day^{-1})
Sco X-1	$\gtrsim 0.6$
GX 349+2	$\gtrsim 0.6$
GX 17+2	$\gtrsim 0.2$

From Table 5.8 and Fig. 5.26, one may see that Sco X-1 and GX 349+2 are very similar in terms of their flaring rate which is comparable in the two sources. A lower limit is that in these two sources a flare occurs on average every 1.6 days with most flares between about 0.2 and 2.5 days apart, i.e. flares occur very often. In GX 17+2 the rate of flaring is about three times smaller with about 1 flare per 5 days, but the flare intervals have a similar distribution. The interval time bin between 0 and 0.15 days in Fig. 5.26 is empty because it was assumed that structures separated

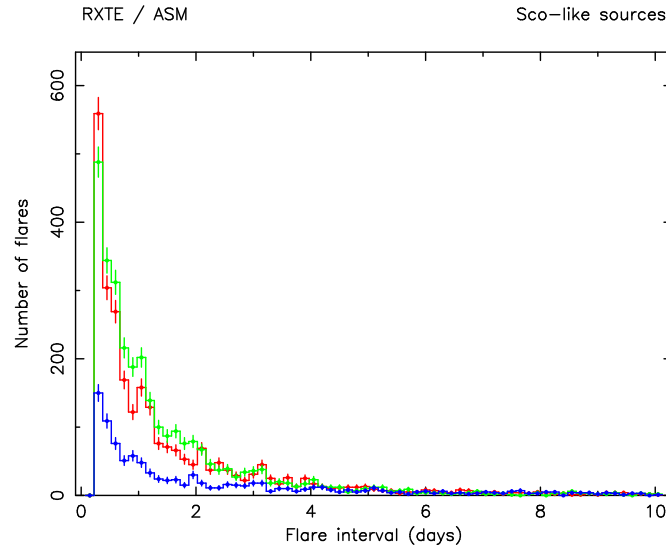


Figure 5.26: A histogram showing the distribution of time intervals between flares in the three Sco-like sources: Sco X-1 (red), GX 349+2 (green) and GX 17+2 (blue).

by less than 0.15 days correspond to changes within a flare and not separate flares. That this was usually the case was directly checked by carefully examining a sample of flares in the ASM lightcurves. The peak of the flare interval distribution at the lowest non-empty bin would suggest that the most typical interval between flares is comparable to the length of a flare itself. However, this result should be treated with caution as it may be affected by the modulation related to the the 90 minute orbital motion of the satellite and other effects, such as uneven sampling and in some cases problems of determining whether the observed feature in the lightcurve is a single flare with a complicated structure or two separate flares.

It is also interesting to notice that the flare intervals of typically between a few hours and days are in line with the energy consideration for flaring presented in Sect. 4.3.4. It was shown that in the Cyg-like sources only a few hour time is needed to accumulate enough matter in order to explain flaring as nuclear-powered on the energetic grounds. In the Sco-like sources, flaring is stronger, but $\gtrsim 50\%$ of the energy comes from changes in mass accretion rate, so that, again, matter accumulation over several hours is sufficient for flaring to be nuclear-powered.

5.3.3 On the possible heating of the neutron star by flaring

The following results obtained in this work suggest a relation between flaring and the neutron star temperature:

- Sco X-1 and GX 349+2 have a similar and high rate of flaring and their neutron star temper-

atures are also comparable, yet very different and higher than in the other Z-track sources.

- GX 17+2, whose neutron star temperature is lower than in the other two Sco-like sources, also exhibits frequent flaring, but its rate is a few times lower.
- The observation P40706 of Sco X-1 analysed in this work shows a relatively long period without strong flaring and the temperature measured at the soft apex is significantly lower than that typically found in other observations of this source when flaring was more pronounced.

Given the above, one may hypothesise that flaring, if frequent and strong enough, deposits energy effectively in the neutron star leading to its observed higher temperature. The thermal content of the neutron star due to heating by nuclear burning was considered by Lamb & Lamb (1978). They argued that for matter composed of normal neutrons the thermal energy of the star is $E_{th} = 5.0 \times 10^{45} \rho^{-2/3} T^2 M_*$ erg, where ρ is the average density of the neutron star (in units of $10^{15} \text{ g cm}^{-3}$), T is the internal temperature (in units of 10^8 K), and M_* is the mass of the star expressed in the solar masses. In the case of superfluid neutrons, the specific heat becomes reduced (Tsuruta et al. 1972) and is dominated by contribution from degenerate electrons in which case the thermal energy is given as $E_{th} = 3.2 \times 10^{44} (\frac{Y_e}{0.04})^{2/3} \rho^{-1/3} T^2 M_*$, where Y_e is the number of electrons per nucleon (Lamb & Lamb 1978). Let us then consider the cooling time for a neutron star which has been heated by flaring to $T \sim 3 \times 10^7 \text{ K}$. One can use the formulae above and assume that only an outer ~ 100 meter layer (3% of the star) is involved. This is clearly a very order of magnitude estimate as the depth of the layer is unknown. Then, approximate values of the extra thermal energy are $10^{42} - 10^{43}$ erg, for normal and superfluid neutron matter, respectively. The cooling time can be approximated as $\tau = E/\dot{E}$, where \dot{E} is the luminosity at which this energy is radiated away from the star. By substituting e.g. $L_{bb} \sim 10^{37} \text{ erg s}^{-1}$ for the rate of energy losses, the cooling time τ is found to be in the range of 1 - 10 days. However, in the case of type I X-ray bursts it is expected that most of deposited nuclear energy is quickly radiated away from the stellar surface, and only a few percent of it can be transferred into the star (e.g. Hanawa & Fujimoto 1984). Then, for a net energy inflow of only about $10^{35} \text{ erg s}^{-1}$, the equilibrium cooling rate would lead to a cooling timescale of an order of hundreds of years (Lamb & Lamb 1978). The problem is complicated as the effects of compressional heating, neutrino cooling and dependencies on e.g. chemical composition and the depth at which the energy deposition took place in the first place should be taken into account. In contrast to type I X-ray bursts, flaring lasts much longer, typically a few thousands of seconds, and has a higher duty time, and so heating and subsequent

cooling could proceed faster. Whether the actual cooling timescale can match that of a few days suggested by observations in the proposed model is unclear, this probably requiring cooling rate to be faster than in equilibrium.

In typical observations of Sco X-1 and GX 349+2, flaring is more frequent than the cooling time and the measured neutron star temperature remains always high. In the observation analysed in this work, with a few days without strong flaring in Sco X-1, some cooling would be expected and indeed observed as a significantly lower temperature of the neutron star. In GX 17+2, heating appears to be much less effective given a few times smaller flaring rate than in the other two Sco-like sources. If heating in this source leads to a smaller, say ~ 0.1 keV heating, then the cooling time is also respectively shorter ($\lesssim 1$ day) and we should not expect increased temperature of the neutron star, as observed.

5.3.4 How do the Sco-like sources differ from the Cyg-like sources ?

The results obtained here show that the (truly) Sco-like behaviour, i.e. the behaviour similar to Sco X-1, is characterized by strong and frequent flaring with changes of mass accretion rate, hardly any Horizontal Branch, and the high neutron star temperature at all times. Given this, GX 17+2, although commonly classified as a Sco-like source after Hasinger & van der Klis (1989) (Sect. 1.3.1), should be in fact considered as a hybrid, sharing some characteristics of the truly Sco-like sources (Sco X-1, GX 349+2) and the Cyg-like sources (Horizontal Branch evident, low neutron star temperature at the soft apex, less frequent flaring).

As mentioned in Sect. 1.3.1, the source XTE J1701-462 was reported to change from being Cyg-like into Sco-like as its luminosity was decreasing during the decay of its outburst (Remillard et al. 2006; Homan et al. 2007a; Lin et al. 2009; Homan et al. 2010). In that case, the identification of the Z-track stages was based on the shapes traced by the source in hardness-intensity and colour-colour, and on the observed changes in flaring. In particular, after the luminosity of the source has dropped from its initial value, the apparent strength of flaring in the hard energy band was used to justify the proposition that the source was Sco-like at that stage. It should be noted, however, that when plotting the lightcurve in the total energy band flaring is less strong and does not immediately suggest a Sco-like behaviour. Homan et al. (2007a) generalized their result and concluded that, contrary to scenarios involving inclination, strength of the magnetic field etc. (Sect. 1.3.1), the two sub-groups of the Z-track sources differ in mass accretion rate only, i.e. that all the Sco-like sources are systematically less luminous (by about 50 %) than the Cyg-like sources.

Let us consider the above possibility in terms of the six classic Z-track sources. From Fig. 5.22 it is apparent that there is no systematic difference in luminosity between the three Cyg-like and the other three Sco-like sources, their total luminosities covering roughly the same range $20 - 60 \times 10^{37} \text{ erg s}^{-1}$. However, one could argue that the best distance estimates for these sources, based on which the luminosities are calculated, are badly determined, and if this could be corrected, the luminosities would show a bimodal distribution as expected in the scenario of Homan et al. (2007a). To verify this possibility, the distances to the six Z-track sources with their maximum errors, as given in Table 3.1, were used to calculate corresponding ranges of luminosities, given that $L = f \times 4 \pi d^2$, where f is the measured flux (from spectral fitting, but model-independent) and d is the distance.

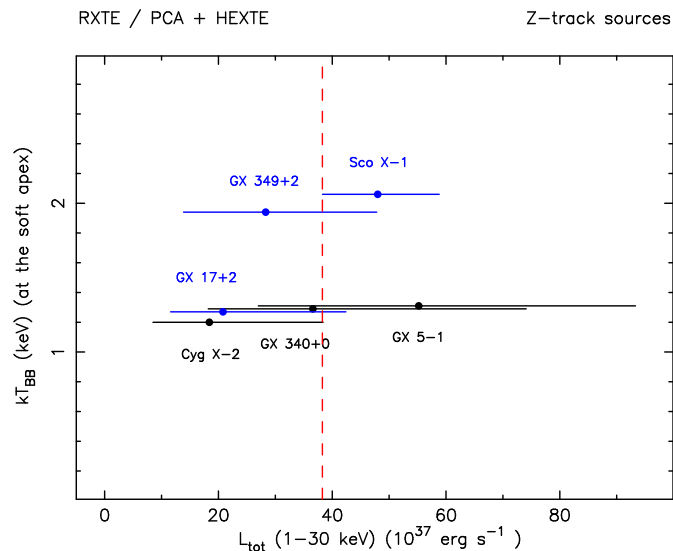


Figure 5.27: The same as in Fig. 5.22, but with the errors on the total (1 - 30 keV) luminosity shown. The red line emphasizes the lower limit for the luminosity of Sco X-1.

The results are shown in Fig. 5.27 which is the same as Fig. 5.22, but with the luminosity uncertainties explicitly shown. In the case of GX 340+0, GX 5-1, GX 17+2 and GX 349+2 the distances have large enough errors to shift the sources in the way required by the proposition of Homan et al. (2007a). However, the problem arises when comparing Cyg X-2 with Sco X-1. The distance to Sco X-1 was determined from the parallax measurement using long-term radio observations by Bradshaw et al. (1999). Its value, $2.8 \pm 0.3 \text{ kpc}$, is therefore very accurate. Even allowing for the lowest limit of 2.5 kpc, the luminosity of Sco X-1 is generally higher than that of Cyg X-2 for its upper distance estimate of $\sim 13 \text{ kpc}$ derived by Galloway et al. (2008) using a few type I X-ray bursts showing photospheric radius expansion for the assumed H-rich fuel content

thought to be the case in this source. A similar study of a single PRE burst in Cyg X-2 by Smale (1998) gave the distance of 11 ± 0.3 kpc. A larger distance (up to 17 kpc) would be possible if the burning fuel was pure helium, but this was thought to be unlikely based on theoretical grounds (Galloway et al. 2008). Also, the distance estimates based on type I X-ray bursts are already higher than ~ 7 kpc of Cowley et al. (1979); Orosz & Kuulkers (1999) obtained from the optical photometry of the source. This shows that it is rather unlikely that the luminosity of Cyg X-2 is actually larger than that of Sco X-1, especially that the luminosity difference of $\sim 50\%$ would be expected in the scenario of Homan et al. (2007a). Furthermore, it is even more unlikely that also the distances of the other sources could be different in just a right way to make all the Cyg-like sources more luminous than all the Sco-like sources. Thus, given the considerations above, the proposition of Homan et al. (2007a) is found improbable.

Present results suggest that the two sub-groups of the Z-track sources (with GX 17+2 being a hybrid) are distinguished by the presence of strong and frequent flaring which, if begins and continues, heats the neutron star and leads to strong radiation pressure at all times, as in Sco X-1 and GX 349+2. However, the reason for which flaring can become strong and frequent is unclear.

Chapter 6

A survey of Atoll sources

In this chapter, presented are the results of a survey of eight Atoll sources: 2S 0918-549, 4U 1636-053, 4U 1705-44, 4U 1728-34, 4U 1735-44, SLX 1735-269, 4U 1820-30, and 4U 1916-053. An overview of the previous work carried out on these sources was already presented in Sect. 3.4. Here, in all cases, archival *RXTE* observations were subject to spectral analysis in terms of the Extended ADC model to reveal the general behaviour of the Atoll sources as a group and to allow their comparison with the Z-track sources. Of special interest is the physical reason for which the spectral transition between the Banana state and the Island state (Sect. 1.3.2) takes place. The results will also be compared with those from the *ASCA* survey of Balucińska-Church et al. (2001) (Sect. 2.2.2).

6.1 Observations

A local script was remotely used in order to choose datasets from the *RXTE* archive for the spectral analysis of each of the Atoll sources in the sample. Observations in which clear spectral changes could be observed in hardness-intensity were selected and their detailed list is given in Table 6.1.

Table 6.1: Details of *RXTE* observations chosen for the analysis in the survey of Atoll sources.

Source	Sub-observation	Start Date & Time (UT)	Duration (s)
2S 0918-549	90416-01-01-00	June 18, 2004, 02:22:47	9984
	90416-01-01-01	June 18, 2004, 22:36:07	26160
	90416-01-01-04	June 19, 2004, 10:37:57	2656
	90416-01-01-020	June 19, 2004, 22:14:23	23616
	90416-01-01-06	June 20, 2004, 20:49:27	1904

	90416-01-01-03	June 20, 2004, 23:31:37	11312
	90416-01-01-07	June 22, 2004, 10:34:00	1920
	90416-01-01-05	June 23, 2004, 05:25:16	5216
	90416-01-02-00	June 25, 2004, 07:53:43	4592
	90416-01-02-01	June 29, 2004, 05:21:43	3920
4U 1636-536	91024-01-54-10	January 1, 2006, 02:54:45	2176
	91024-01-55-10	January 3, 2006, 19:08:29	2256
	91024-01-56-10	January 5, 2006, 18:17:30	2144
	91024-01-57-10	January 7, 2006, 17:27:30	1904
	91024-01-58-10	January 9, 2006, 20:09:15	2096
	91024-01-59-10	January 11, 2006, 15:45:48	2592
	91024-01-60-10	January 13, 2006, 22:44:29	2016
	91024-01-61-10	January 15, 2006, 22:05:25	1840
4U 1705-44	93060-01-12-10	September 3, 2007, 05:11:07	3424
	93060-01-13-10	September 7, 2007, 09:54:35	2608
	93060-01-14-10	September 11, 2007, 04:51:16	2096
	93060-01-15-10	September 15, 2007, 10:58:16	2880
	93060-01-16-10	September 19, 2007, 10:43:16	3120
	93060-01-17-10	September 23, 2007, 06:03:00	4752
	93060-01-18-10	September 27, 2007, 05:47:09	4016
	93060-01-19-10	October 1, 2007, 07:10:16	4560
	93060-01-20-10	October 5, 2007, 00:45:16	1008
	93060-01-21-10	October 9, 2007, 03:24:43	2960
	93060-01-22-10	October 13, 2007, 01:33:29	2864
	93060-01-23-10	October 17, 2007, 01:22:46	3616
	93060-01-24-10	October 21, 2007, 04:09:16	4016
	93060-01-25-10	October 25, 2007, 10:42:00	2112
	93060-01-26-10	October 29, 2007, 10:25:30	2144
	93060-01-27-10	November 2, 2007, 08:31:37	2608
	93060-01-28-10	November 6, 2007, 22:01:16	5280
	93060-01-39-10	November 10, 2007, 09:36:01	2944
	93060-01-40-10	November 14, 2007, 09:15:53	5600
	93060-01-41-10	November 19, 2007, 13:20:38	3696
4U 1728-34	20083-01-01-00	September 19, 1997, 05:52:14	17280
	20083-01-01-01	September 19, 1997, 12:29:45	9136
	20083-01-01-020	September 20, 1997, 07:32:46	23408
	20083-01-01-02	September 20, 1997, 14:03:07	8752
	20083-01-02-01	September 21, 1997, 15:43:23	19296
	20083-01-02-000	September 22, 1997, 05:59:49	28800
	20083-01-02-00	September 22, 1997, 21:59:49	16272
	20083-01-03-01	September 23, 1997, 23:50:09	3056
	20083-01-03-000	September 24, 1997, 09:14:50	28800
	20083-01-03-00	September 24, 1997, 17:14:50	3792
	20083-01-04-00	September 26, 1997, 12:29:32	26736
	20083-01-04-01	September 27, 1997, 09:18:44	26656
	20083-01-03-020	September 30, 1997, 04:33:06	21952

	20083-01-03-02	September 30, 1997, 10:39:07	12352
	20083-01-04-020	October 1, 1997, 06:09:03	28800
	20083-01-04-02	October 1, 1997, 14:09:03	4144
4U 1735-44	91025-01-03-00	October 28, 2006, 10:15:25	9040
	91025-01-03-01	October 29, 2006, 05:06:06	10736
	91025-01-03-02	October 21, 2006, 05:48:07	10560
	91025-01-03-03	November 1, 2006, 08:31:02	9072
4U 1820-30	20075-01-03-01	March 21, 1997, 15:19:19	4672
	20075-01-03-00	March 23, 1997, 16:54:56	21968
	20075-01-04-00	April 10, 1997, 16:52:13	24176
	20075-01-05-00	May 2, 1997, 14:02:54	16752
	20075-01-05-01	May 10, 1997, 13:05:43	14784
	20075-01-06-00	May 27, 1997, 07:50:21	15232
	20075-01-06-01	May 28, 1997, 10:20:59	7984
4U 1916-053	10109-02-01-00	May 14, 1996, 09:22:05	12784
	10109-02-02-00	May 15, 1996, 12:32:06	9536
	10109-02-03-00	May 16, 1996, 12:56:45	12864
	10109-02-04-00	May 17, 1996, 08:20:08	12544
	10109-02-05-00	May 18, 1996, 09:53:47	12384
	10109-02-06-00	May 19, 1996, 10:06:38	12624
	10109-02-07-00	May 20, 1996, 06:50:10	12352
	10109-02-08-00	May 21, 1996, 07:47:52	12848
	10109-02-09-00	May 22, 1996, 12:37:55	13696
	10109-02-10-00	May 23, 1996, 07:50:56	9136
	10109-02-10-02	May 23, 1996, 11:02:56	1024
SLX 1735-269	80138-03-05-00	September 18, 2003, 00:28:55	3680
	80138-03-06-00	September 18, 2003, 02:12:43	16592
	80138-03-07-00	September 27, 2003, 00:39:48	3440
	80138-03-07-01	September 27, 2003, 02:20:08	3712
	80138-03-07-02	September 28, 2003, 00:19:51	3312
	80138-03-07-03	September 28, 2003, 01:58:12	2512
	80138-03-08-00	October 6, 2003, 00:52:53	2528

6.2 Analysis

Data analysis was performed using *HEASOFT* v.6.11 and the latest version of the calibration database *CALDB*. The procedure was similar in the case of all sources and is presented below emphasising issues specific to particular sources. A detailed description of the analysis steps is also given in Appendix A.

The housekeeping data were examined in order to choose screening criteria. In all cases, standard conditions were applied, such as $\text{OFFSET} < 0.02^\circ$ and $\text{ELV} > 10^\circ$. In the case of faint sources it

is particularly recommended to filter out sections of data with increased noise. On its 90 minute orbit, the *RXTE* satellite regularly approaches the South Atlantic Anomaly (SAA), the region in which the inner radiation belt is closest to the Earth's surface. A passage through the SAA leads to increased noise caused by particles trapped in this region and such periods of time were filtered out by requiring that data collected during and up to 30 minutes after the passage were dismissed (parameter `TIME.SINCE.SAA`). Also, any other times of increased noise during the observations were rejected by requiring that the parameter `ELECTRON2`, measuring the background noise due to charged particles in the PCU 2 unit (which is almost always operational), was less than typically 0.1 - 0.2, as recommended by the mission specialists. The number of PCU detectors operational during every observation was found by examining the `NUM_PCU_ON` and `PCUn_ON` ($n = 0, \dots, 4$) parameters as a function of observation time. The list of detectors used for each of the sources is given in Table 6.2. All screening conditions were next translated into Good Time Intervals (GTI) using the `MAKETIME` tool giving, depending on the source, about 20 - 200 ks of good data.

Table 6.2: A list of PCU detectors used in the analysis.

Source	PCU used
2S 0918-549	2 3
4U 1636-536	2
4U 1705-44	2
4U 1728-34	0 1 2 3 4
4U 1735-44	2
SLX 1735-269	2 3
4U 1820-30	0 1 2 3 4
4U 1916-053	0 1 2

6.2.1 Lightcurves

Standard2 lightcurves were produced in the low, medium, high and total energy bands used throughout this work. Background data and lightcurves were extracted from the standard *RXTE* background models. For sources whose count rates were greater than ~ 40 counts s^{-1} PCU^{-1} , the bright background model `pca_bkgd_cmbrightv1e_eMv20051128.mdl` was used. In other cases (2S 0918-549, 4U 1916-053, SLX 1735-269) the faint model `pca_bkgd_cmfaint17_eMv20051128.mdl` was used. Lightcurves in all energy bands were then background subtracted and deadtime corrected following standard procedures.

An initial examination of the lightcurves revealed occasional type I X-ray bursts which are common

in the Atoll sources (Sect. 1.4.1). To better see the bursts, Standard1 lightcurves having a time resolution of 0.125 seconds were extracted. An example type I X-ray burst detected in 4U 1728-34, the source known to have frequent bursts (Sect. 3.4.4), is shown in Fig. 6.1. Given the better time resolution the times of burst maxima were accurately determined and as the presence of burst data could affect the analysis of persistent emission the bursts were filtered out in MGTIME by removing time sections of typically 20 s before and 300 s after the burst maximum from the observation-long GTI, as it is often done (e.g. Bloser et al. 2000).

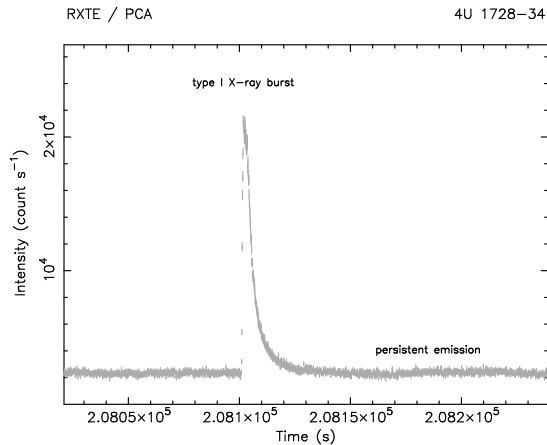


Figure 6.1: An example of a type I X-ray burst observed in 4U 1728-34.

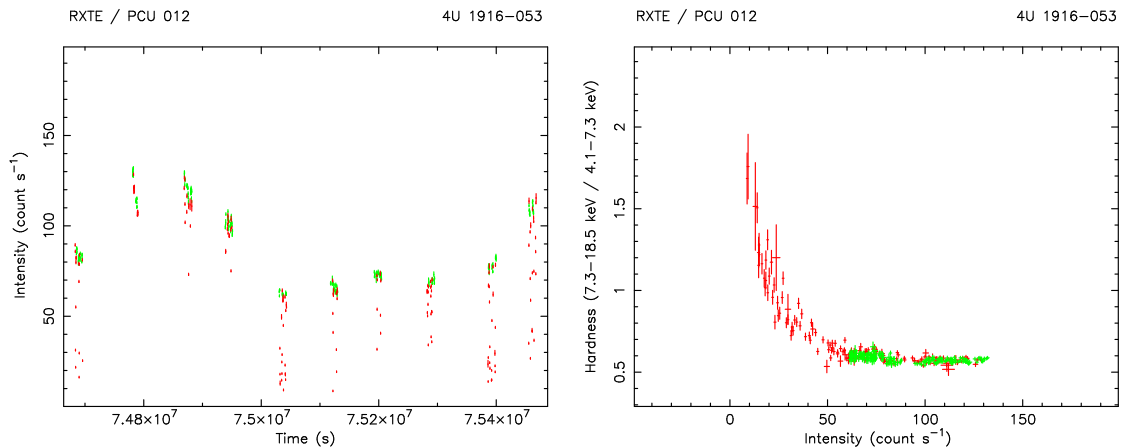


Figure 6.2: X-ray dipping (red) characteristic to 4U 1916-053 viewed in the lightcurve (left) and hardness-intensity (right). If not filtered out, dipping would have affected the analysis of persistent emission (green).

Additional filtering was necessary in the case of 4U 1916-053 in which X-ray dipping was visible every ~ 3000 seconds which corresponds to the orbital period of the system (Sect. 1.4.3, 3.4.8). Also, occasionally, inter-dipping between the main dips was visible at an orbital phase of about 0.5 - 0.6 which is a known feature of the source (e.g. Church et al. 1997). The presence of dipping

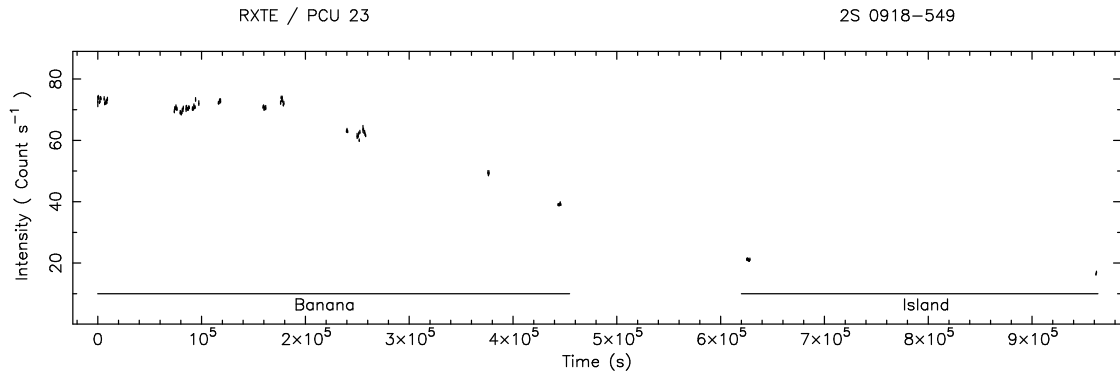


Figure 6.3: The lightcurve of 2S 0918-549 with 512 s binning showing a clear intensity change related to the spectral transition from the Banana to the Island branch.

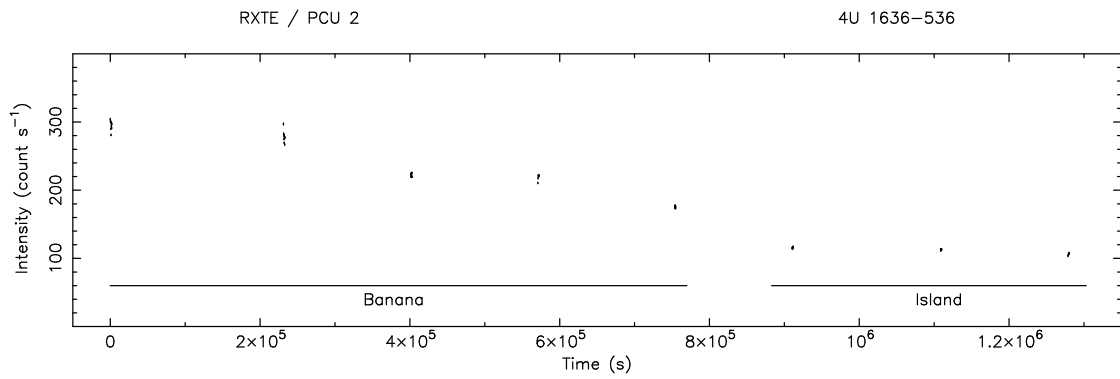


Figure 6.4: The lightcurve of 4U 1636-536. After a relatively bright period the source moves to the Island state at the lowest intensities. One point corresponds to 256 s of data.

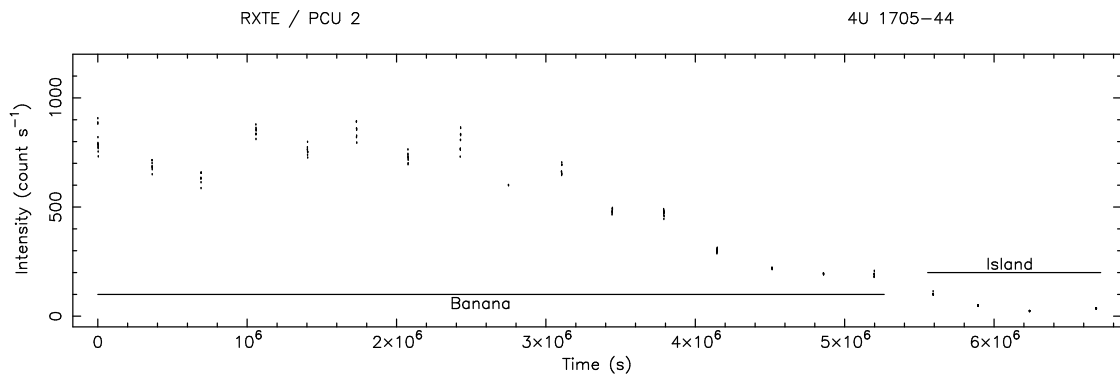


Figure 6.5: The 256 s-binned lightcurve of 4U 1705-44 showing the bright and most variable period followed by the spectral transition.

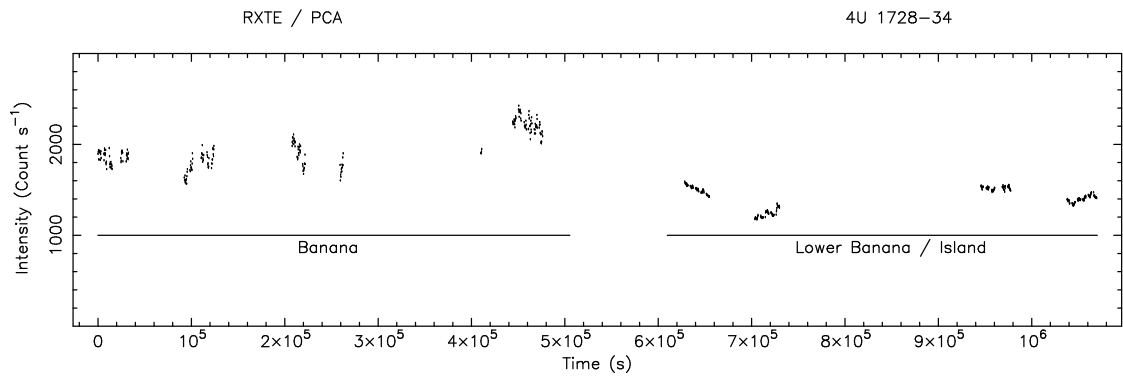


Figure 6.6: The lightcurve of 4U 1728-34 with each point corresponding to 256 s of data. The source moved from the Banana to the Lower Banana/Island state as its intensity decreased.

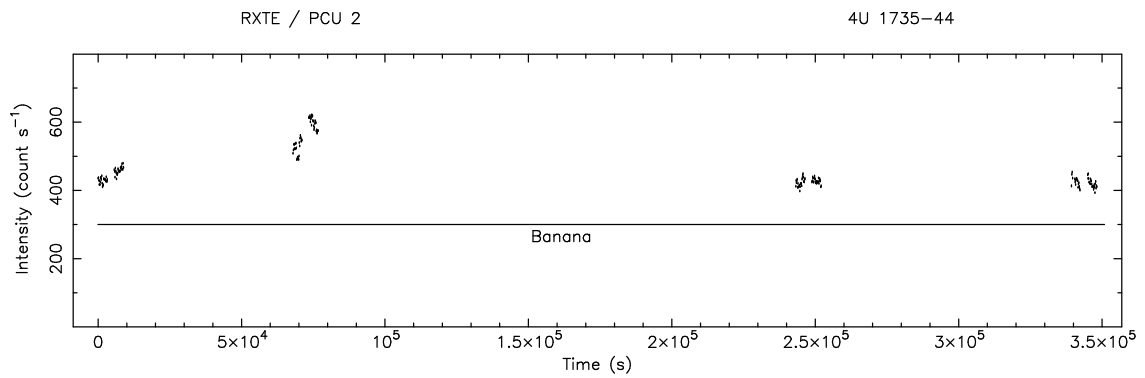


Figure 6.7: The 128 s-binned lightcurve of the bright Atoll source 4U 1735-44. Relatively small intensity changes are seen except for a single flare-like event at $\sim 7 \times 10^4$ s corresponding to the upper Banana branch.

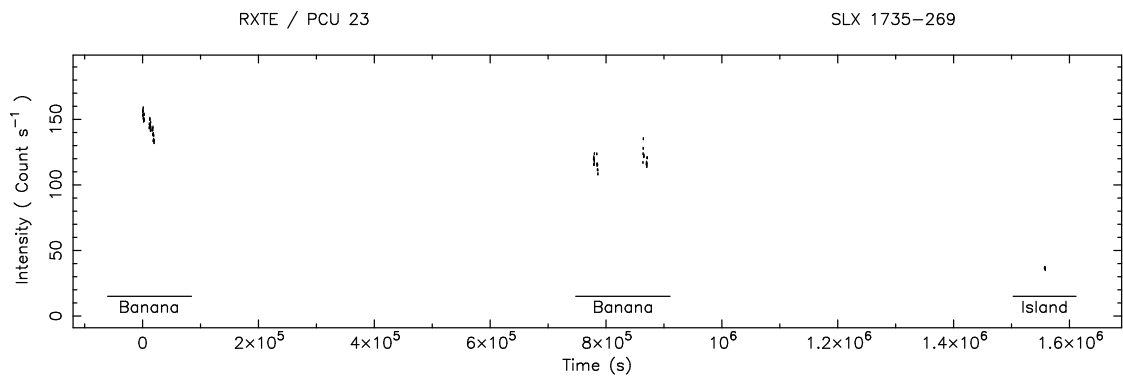


Figure 6.8: The lightcurve of SLX 1735-269 with 256 s time binning. The decreased intensity at the end of the observation corresponds to the Island branch.

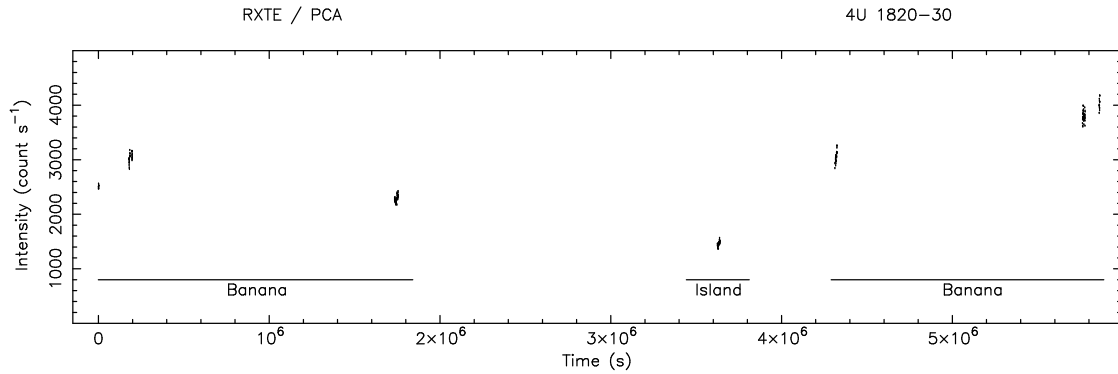


Figure 6.9: The lightcurve of 4U 1820-30 showing clear intensity changes, with most of the time spent by the source on the Banana branch. Each data point corresponds to 256 s of observation.

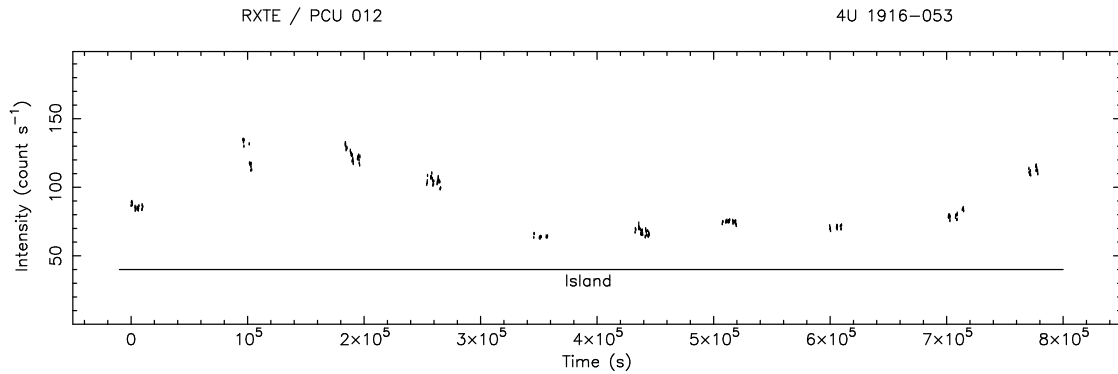


Figure 6.10: The 256 s-binned lightcurve of 4U 1916-053. Despite some intensity variation the source was most probably in the Island state during the observation.

alters substantially the hardness-intensity variation of the source, as shown in Fig. 6.2, mimicking the Banana to Island spectral transition. All sections of data with dipping were therefore carefully identified in the lightcurve and the corresponding time intervals were removed from the observation GTI.

The background-subtracted, deadtime-corrected lightcurves cleaned from X-ray bursts and dipping are shown in Figures 6.3 - 6.10, for the eight sources respectively. The original 16 s time binning was increased to 128 - 512 seconds (depending on the source) to reduce the unwanted fuzziness in hardness-intensity and colour-colour variations of the sources (below) which is often present given their low count rates in the PCA. Particular sections of the lightcurves were analysed separately to identify their corresponding positions in hardness-intensity and colour-colour tracks and these are labelled in the lightcurves.

6.2.2 Colour-colour & hardness-intensity variations

The low, medium and hard lightcurves were used in LCURVE to define the hard and the soft colours as hard/medium and medium/low count rate ratios, respectively. Given this, colour-colour variations of the sources were produced in which the hard colour is shown as a function of the soft colour, as well as hardness-intensity diagrams in which the hard colour is shown as a function of the total intensity. Figures 6.11 - 6.18 present the colour-colour (left) and hardness-intensity (right) variations (background and deadtime corrected) of the Atoll sources studied in this work (with overlaid data selections for the spectral analysis).

It is known that in the Atoll sources, overall intensity variations are typically large (by a factor of a few) and span over relatively long periods of time (weeks - months). Thus, given the sparse observational coverage with the PCA, it was found that the hardness-intensity variations are not always well sampled and suffer from numerous data gaps. On the other hand, colour-colour variations show usually more regular Atoll tracks. Also, in some cases using colour-colour improves statistics in data selections for spectral analysis, such as in 2S 0918-549, or makes the spectral transition better visible, as e.g. in 4U 1705-44. In two cases (4U 1636-536 and 4U 1916-053) a decision was made to study the sources based on their hardness-intensity changes and this was sensible given the limited or lack of change in colour-colour. In other cases there was no much difference between choosing colour-colour or hardness-intensity. Moreover, a quick-look spectral analyses carried out using data selections separately on colour-colour and hardness-intensity of a given source showed that the choice between these two options has basically no effect on the final results revealing the same behaviour of the source. In these cases a decision was made to use colour-colour diagrams for data selections.

Characteristic to the spectral transition is an increase in hardness at lowest intensity of a given source, whereas changes at higher intensity correspond to the Banana branch and may also involve changes in hardness, but of typically smaller amplitude, the best examples visible here in 2S 0918-549 (Fig. 6.11, left), 4U 1705-44 (Fig. 6.13, left) and 4U 1820-30 (Fig. 6.17, left). The colour-colour and hardness-intensity of the source 4U 1735-44 shown in Fig. 6.15 reveals that in this observation the source was not seen to trace the Island Branch, but only the Banana branch. In 4U 1916-053 the hardness-intensity variation (Fig. 6.18, right panel) shows an elongated pattern reminiscent of the Banana Branch. However, the colour-colour variation of the source does not confirm that. Instead, a cluster of points is visible suggesting that the source was rather in the Island/Lower Banana state. That this was most probably the case was found by comparing the

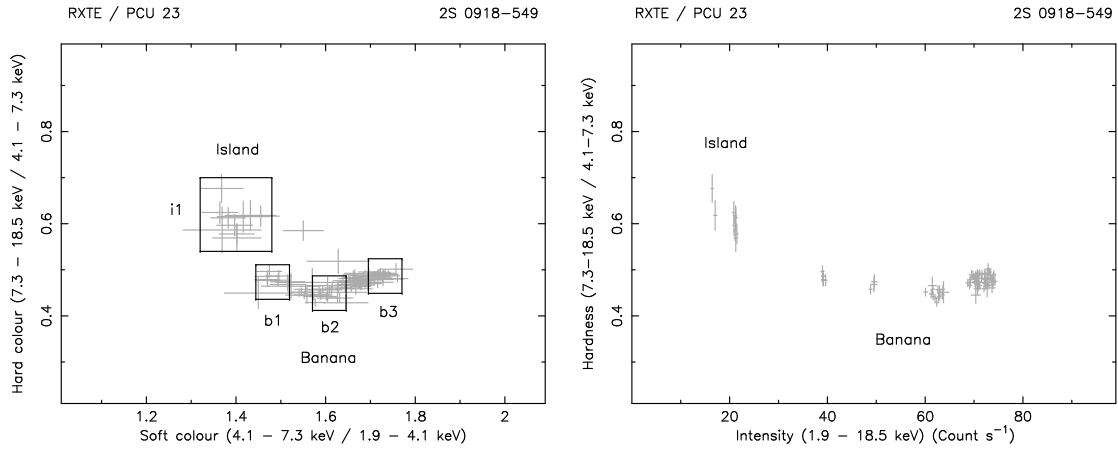


Figure 6.11: The 512 s-binned colour-colour (left) and hardness-intensity (right) variation of 2S 0918-549. Selection boxes for spectral analysis are shown.

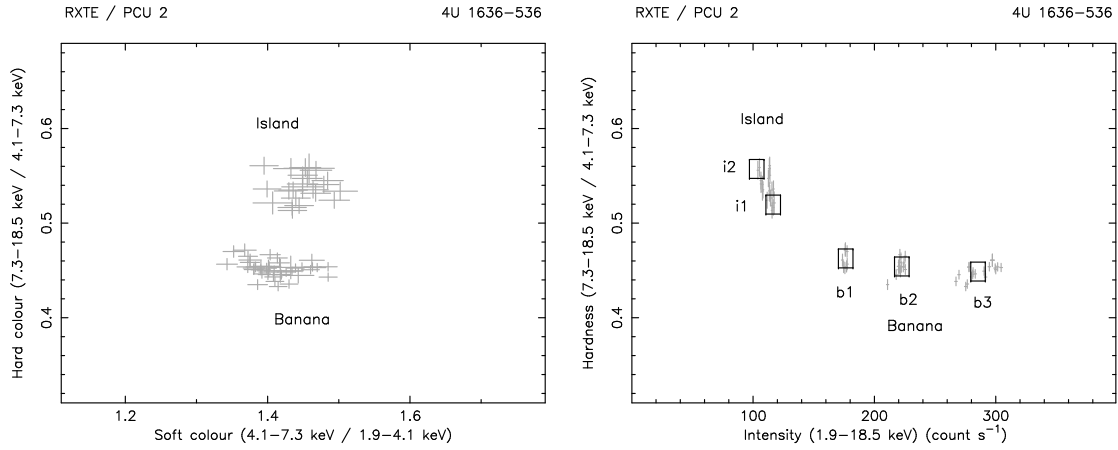


Figure 6.12: The colour-colour (left) and hardness-intensity (right) variation of 4U 1636-536 with each point corresponding to 256 s of data. Changes in colour-colour are limited in this case.

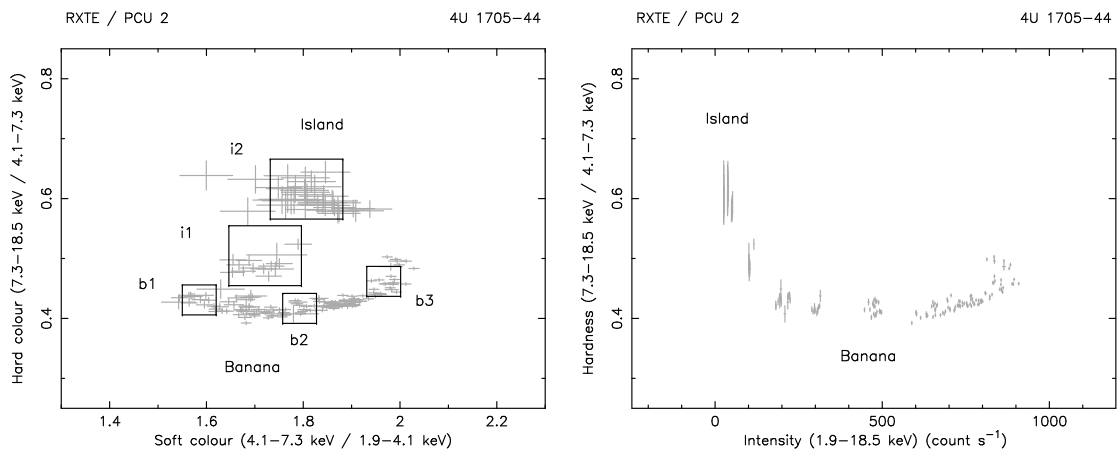


Figure 6.13: The colour-colour (left) and hardness-intensity (right) variation of 4U 1705-44 with a spectral transition clearly visible. A binning of 256 s was chosen.

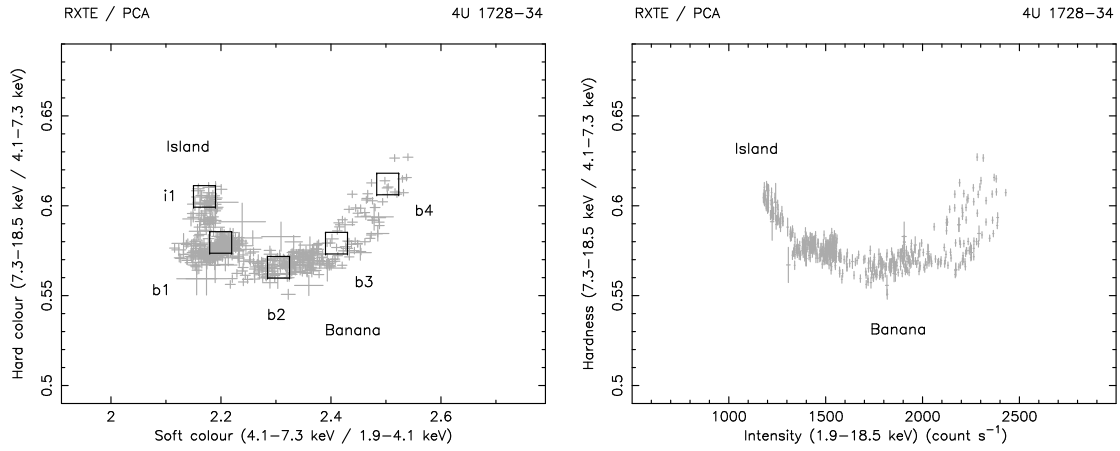


Figure 6.14: The variation in colour-colour (left) and hardness-intensity (right) of 4U 1728-34. A binning of 256 seconds was used.

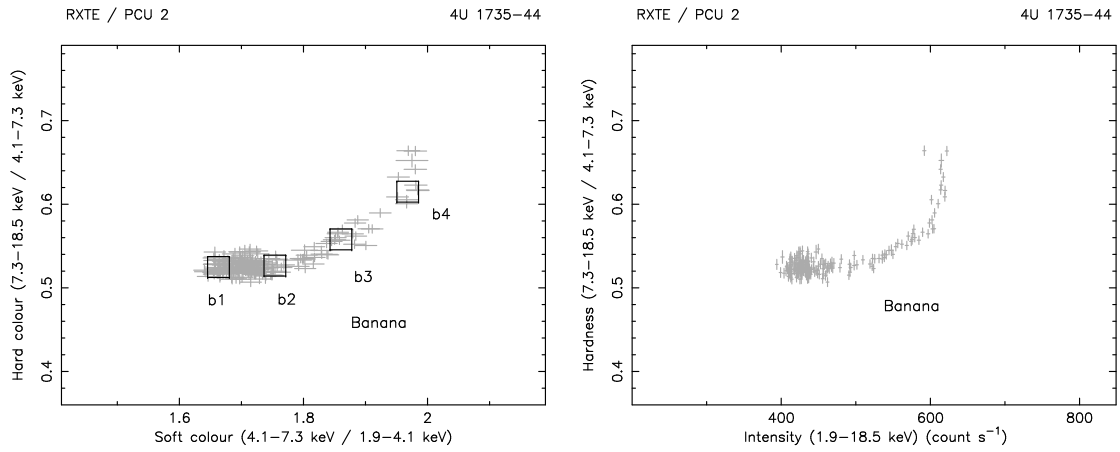


Figure 6.15: The 128 s-binned colour-colour (left) and hardness-intensity (right) diagrams of 4U 1735-44. The Upper Banana Branch corresponds to a flaring-like behaviour of the source.

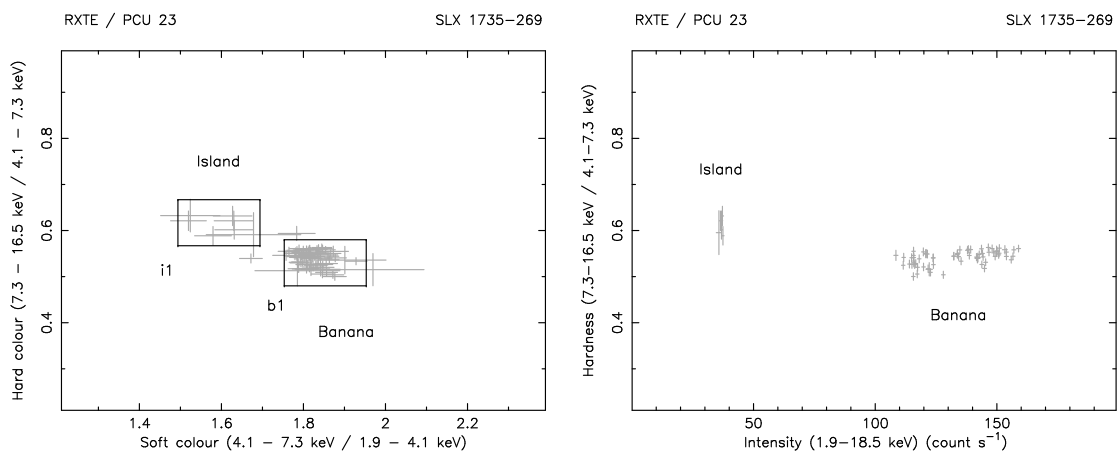


Figure 6.16: The colour-colour (left) and hardness-intensity (right) variation of SLX 1735-269. Each point corresponds to 256 s of data.

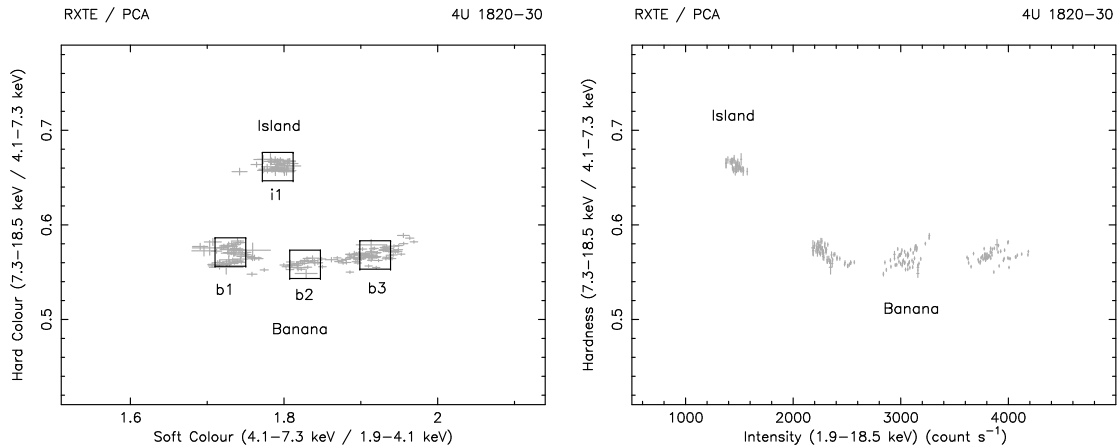


Figure 6.17: The variation in colour-colour (left) and hardness-intensity (right) of 4U 1820-30, 256 second binning was used. The Island and Banana spectral states are clearly visible.

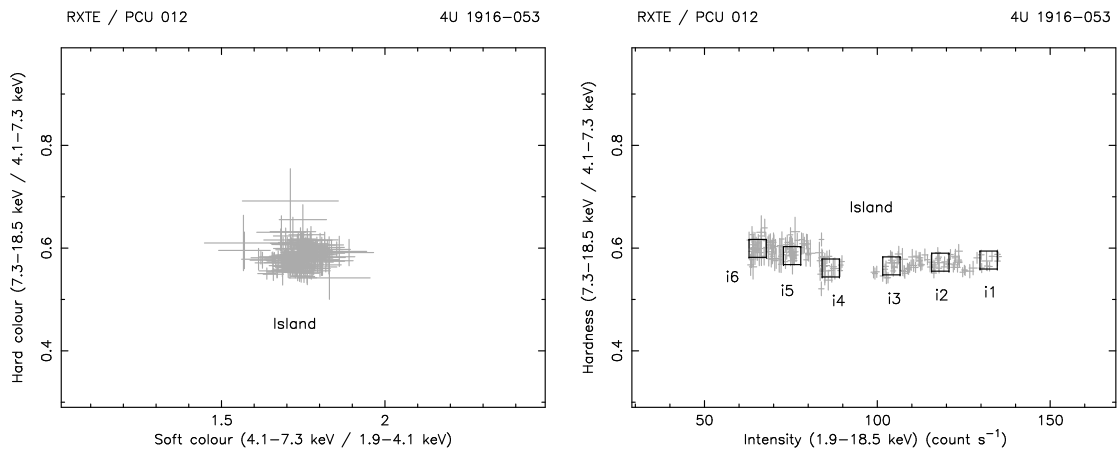


Figure 6.18: The colour-colour (left) and hardness-intensity (right) variation of 4U 1916-053. The binning was, again, 256 seconds. No apparent variation in colour-colour suggests that the source was in the Island state.

spectral fitting results obtained here (Sect. 6.2.3) with those obtained previously by Blosler et al. (2000) for another observation in which the two spectral states were better visible, the issue being also discussed further in Sect. 6.3.3.

Thus, as there was usually little doubt about the identification of the spectral states in the Atoll sources studied here, an additional timing analysis, that would otherwise help with identifications, was not necessary.

6.2.3 Results of spectral fitting

Spectral fitting was carried out on the PCA and the HEXTE spectra simultaneously using the Extended ADC model. The calibration differences between the two instruments were taken into

account by multiplying the model by a constant which was then frozen at 1.0 for the PCA and left free for the HEXTE. The value of this constant from fitting was in the range 0.55 - 1.02 and most typically ~ 0.8 , i.e. an acceptable value. In the case of PCA spectra, channels corresponding to energies below 3 keV, for which the instrument is not well calibrated, were excluded. The upper energy limit was restricted to typically 20 keV at which background noise becomes strong, and higher energies were well covered by the HEXTE data extending up to typically 50 keV with channels re-binned into groups of two or four to improve the signal to noise ratio. The number of counts per spectral channel was typically $10^3 - 10^5$ and $10^2 - 10^4$ in the PCA and HEXTE, respectively, allowing for good quality fitting.

The column density was initially allowed to vary in spectral fitting. In a few cases, when N_H was too low to constrain it with the PCA, its value was fixed at the average value from free fitting or at the value known from the radio survey of Kalberla et al. (2005). In other cases, this was not necessary as the column density could be constrained in free fitting, often revealing systematic changes along the Atoll pattern of a source.

In the majority of cases, an additional emission line at ~ 6.5 keV was evident in the fitting residuals and a Gaussian line was added to the model improving the goodness of fits to acceptable levels. When the line was present, its width was estimated based on the residuals without the line with typically $\sigma \sim 0.5$ keV, which was frozen so that it did not take over the continuum emission.

The line was not needed to improve the fitting in the case of the faintest sources: 2S 0918-549 and 4U 1916-053. Nevertheless, the absence of this line in these cases may be related to the low count rates and does not prove the absence of the line.

The cut-off energy in the Atoll sources is usually higher (Table 6.3) than in the Z-track sources. Thus, in principle, the photon index could be left free and constrained in free fitting. However, to allow a direct comparison between the Atoll sources with the Z-track sources, a decision was made to keep the photon index fixed at the value of 1.7 used before in this work. That this choice was reasonable is additionally motivated by the previous work of Church et al. (1998a) and Church & Balucińska-Church (2001) who analysed a sample of LMXB using the same spectral model and a free photon index and found that its value was typically close to that used here not having much influence on other model parameters. Also, it was directly checked in this work that when Γ was made free in fitting, its value did not change much so as to affect other parameters in any substantial way.

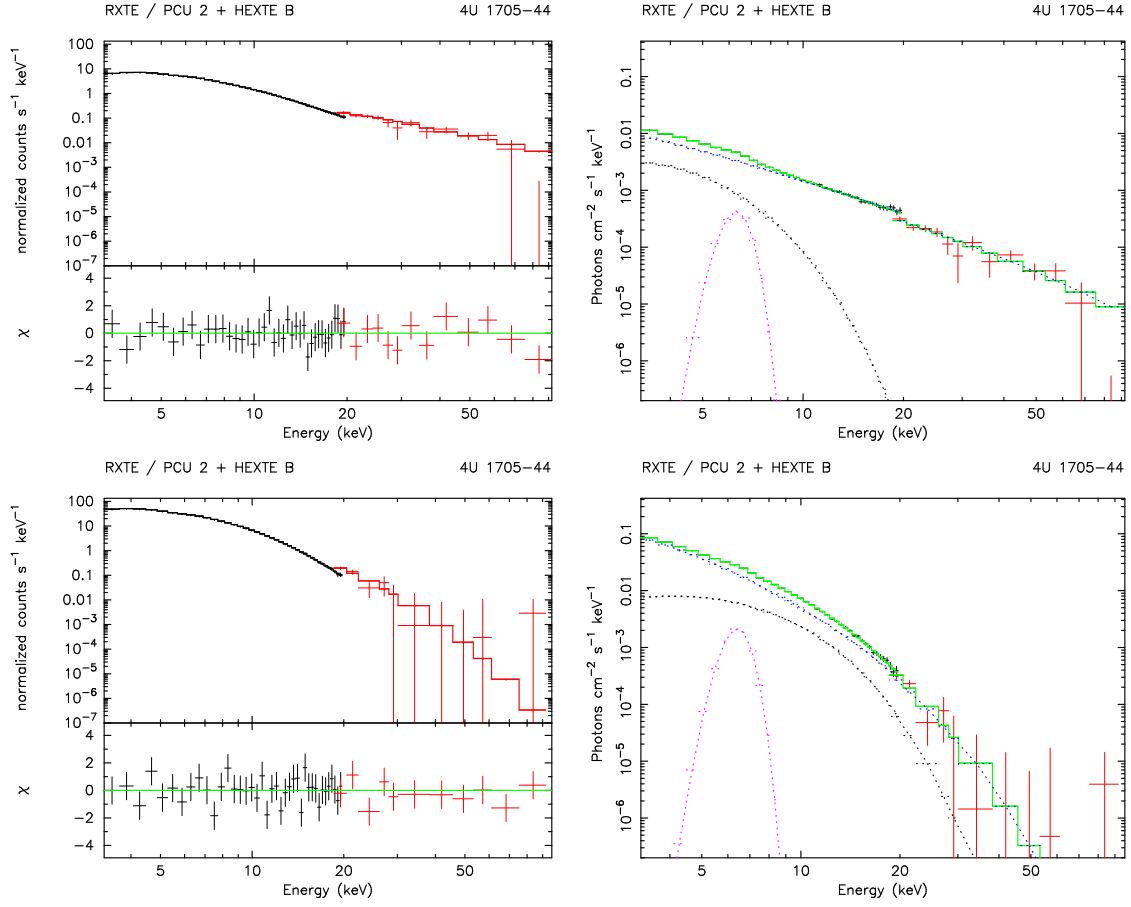


Figure 6.19: An example of the folded (left) and the unfolded (right) spectrum of one of the Atoll sources, 4U 1705-44, when the source was in the Island state (top) and the Banana state (bottom). In the folded spectrum the PCA and HEXTE data are shown in black and red, respectively. In the unfolded spectrum the particular model components are: the blackbody (black), the emission line (magenta) and the cut-off power law (blue), with the total spectrum shown in green.

The final form of the model, when the emission line was present, was $\text{const} \times \text{wabs} \times (\text{bbody} + \text{Gauss} + \text{cutoffpl})$. Spectral fitting with the model gave good results in all cases with the $\chi^2/\text{d.o.f.} \lesssim 1$. Figure 6.19 shows example spectra fitted with the Extended ADC model in the folded version (with fitting residuals to present the goodness of the fit) and the unfolded version to show the contribution of particular model components. The summary of spectral fitting results is presented in Table 6.3 and physical quantities obtained from these results are given in Table 6.4.

Table 6.3: The results of spectral fitting.

Source	Sel.	N_H	Blackbody kT_{bb}	norm	Emission line E_1	EW	Cut-off power law E_{co}	norm	$\chi^2/d.o.f.$
2S 0918-549	i1	0.3^f	0.64 ± 0.08	0.45 ± 0.08	-	-	37^{+21}_{-10}	0.25 ± 0.03	35/36
	b1	0.3^f	0.91 ± 0.06	0.55 ± 0.17	-	-	12.1 ± 1.8	0.71 ± 0.09	35/41
	b2	$0.5^{+1.0}_{-0.5}$	1.45 ± 0.11	0.9 ± 0.3	-	-	8.4 ± 0.9	1.4 ± 0.3	27/40
	b3	0.8 ± 0.8	1.71 ± 0.11	1.3 ± 0.2	-	-	8.0 ± 0.9	1.5 ± 0.2	42/42
4U 1636-536	i2	0.3^f	1.43 ± 0.19	$0.7^{+0.9}_{-0.7}$	7.05 ± 0.34	165	15.5 ± 1.5	3.6 ± 0.3	19/30
	i1	0.3^f	1.49 ± 0.65	0.9 ± 0.6	6.59 ± 0.29	108	13.0 ± 0.4	4.2 ± 0.2	28/35
	b1	0.3^f	2.15 ± 0.16	5.1 ± 1.1	7.25 ± 0.40	92	6.6 ± 0.7	8.6 ± 0.5	36/36
	b2	0.3^f	2.08 ± 0.10	6.5 ± 0.7	6.77 ± 0.27	62	6.6 ± 0.5	10.8 ± 0.5	32/35
	b3	0.3^f	1.88 ± 0.16	7.2 ± 0.9	6.78 ± 0.38	114	7.4 ± 0.5	13.1 ± 0.9	26/36
4U 1705-44	i2	1.8 ± 0.7	1.11 ± 0.10	1.25 ± 0.19	6.31 ± 0.18	130	62^{+46}_{-17}	0.87 ± 0.08	35/45
	i1	2.00^f	1.68 ± 0.13	2.9 ± 0.4	6.18 ± 0.15	115	9.4 ± 0.5	4.4 ± 0.3	35/43
	b1	2.1 ± 0.6	1.95 ± 0.15	7.0 ± 0.6	6.40 ± 0.13	111	5.8 ± 0.5	14.4 ± 1.8	35/43
	b2	4.7 ± 0.8	1.94 ± 0.16	14.2 ± 1.9	6.42 ± 0.16	183	5.3 ± 0.3	44 ± 4	52/42
	b3	5.8 ± 0.7	2.01 ± 0.08	31.3 ± 1.8	6.64 ± 0.17	184	5.3 ± 0.2	59 ± 4	43/43
4U 1728-34	i1	1.9 ± 0.4	1.92 ± 0.07	6.0 ± 0.8	6.54 ± 0.08	161	14.8 ± 0.9	7.7 ± 0.5	38/46
	b1	2.4 ± 0.3	2.21 ± 0.04	13.0 ± 0.3	6.61 ± 0.10	132	8.2 ± 0.3	11.5 ± 0.6	27/48
	b2	3.4 ± 0.3	2.18 ± 0.05	15.4 ± 0.4	6.63 ± 0.10	141	7.7 ± 0.3	16.1 ± 0.9	41/48
	b3	3.6 ± 0.4	2.10 ± 0.06	22.0 ± 0.7	6.63 ± 0.13	118	7.8 ± 0.5	18.1 ± 1.5	39/45
	b4	3.2 ± 0.4	2.12 ± 0.04	30.3 ± 0.6	6.50 ± 0.14	102	8.1 ± 0.5	16.4 ± 1.3	33/44
4U 1735-44	b1	2.6^f	2.37 ± 0.07	15.3 ± 1.3	6.98 ± 0.14	104	7.0 ± 0.4	21.6 ± 0.7	44/42
	b2	2.6^f	2.20 ± 0.09	17.3 ± 1.1	6.74 ± 0.14	105	7.7 ± 0.4	22.4 ± 0.8	48/41
	b3	2.6^f	2.27 ± 0.07	30 ± 2	6.85 ± 0.17	106	7.4 ± 0.6	25.3 ± 1.2	27/41
	b4	2.6^f	2.31 ± 0.07	38 ± 2	6.39 ± 0.30	63	8.7 ± 0.9	22.2 ± 1.1	30/41
SLX 1735-269	i1	1.5^f	0.81 ± 0.07	0.85 ± 0.13	6.82 ± 0.27	196	77 ± 20	0.40 ± 0.05	27/36
	b1	1.5^f	2.08 ± 0.06	3.9 ± 0.3	6.74 ± 0.15	79	6.1 ± 0.6	2.90 ± 0.19	34/42
4U 1820-30	i1	0.3^f	2.46 ± 0.06	10.9 ± 0.2	6.76 ± 0.16	65	15.3 ± 0.7	7.90 ± 0.15	48/48
	b1	0.3^f	2.45 ± 0.03	23.8 ± 1.0	6.65 ± 0.19	44	6.9 ± 0.3	18.0 ± 0.5	38/49
	b2	0.8 ± 0.3	2.31 ± 0.04	27.5 ± 0.8	6.58 ± 0.19	68	7.6 ± 0.3	23.5 ± 1.2	26/53
	b3	1.4 ± 0.3	2.27 ± 0.03	35.8 ± 0.8	6.73 ± 0.18	66	7.4 ± 0.3	27.9 ± 1.4	37/48
4U 1916-053	i6	0.3^f	1.34 ± 0.05	0.64 ± 0.11	-	-	76^{+67}_{-30}	0.41 ± 0.04	43/42
	i5	0.3^f	1.36 ± 0.04	0.74 ± 0.11	-	-	48 ± 11	0.50 ± 0.04	39/45
	i4	0.3^f	1.44 ± 0.11	0.70 ± 0.16	-	-	22 ± 4	0.70 ± 0.07	44/44
	i3	0.3^f	1.52 ± 0.08	0.93 ± 0.17	-	-	23 ± 5	0.82 ± 0.07	24/44
	i2	0.3^f	1.66 ± 0.11	1.00 ± 0.10	-	-	18.6 ± 1.8	1.01 ± 0.06	44/44
	i1	0.3^f	2.00 ± 0.14	1.39 ± 0.12	-	-	14.4 ± 1.9	1.22 ± 0.07	22/45

The column density N_H is given in 10^{22} atom cm^{-2} . The blackbody temperature, the cut-off energy and the line energy are in keV. The normalization of the blackbody is in 10^{36} erg s^{-1} for a distance of 10 kpc, and the normalization of the cut-off power law is in photons $\text{keV}^{-1} \text{cm}^{-2} \text{s}^{-1}$ at 1 keV and is multiplied by a factor of 10. The line EW width is given in eV.

^f - parameter was frozen in fitting.

Table 6.4: The physical quantities derived from the spectral fitting results.

Source	Selection	R_{bb}	h	f_{bb}/f_{Edd}	L_{bb}	L_{cpl}	L_{tot}	H_{eq}
2S 0918-549	i1	2.4 ± 0.7	0.6 ± 0.3	0.011 ± 0.002	0.011 ± 0.002	0.061 ± 0.006	0.07	0.062 ± 0.006
	b1	1.3 ± 0.3	0.17 ± 0.07	0.048 ± 0.016	0.015 ± 0.005	0.114 ± 0.015	0.13	0.109 ± 0.014
	b2	0.66 ± 0.16	0.04 ± 0.02	0.31 ± 0.11	0.025 ± 0.009	0.18 ± 0.04	0.20	0.17 ± 0.04
	b3	0.58 ± 0.09	0.034 ± 0.010	0.59 ± 0.09	0.037 ± 0.006	0.19 ± 0.03	0.22	0.19 ± 0.03
4U 1636-536	i2	0.7 ± 0.5	0.05 ± 0.05	0.3 ± 0.3	0.03 ± 0.03	0.83 ± 0.08	0.86	0.73 ± 0.07
	i1	0.7 ± 0.7	0.05 ± 0.05	0.4 ± 0.2	0.03 ± 0.02	0.89 ± 0.05	0.93	0.79 ± 0.04
	b1	0.82 ± 0.15	0.07 ± 0.03	1.6 ± 0.3	0.19 ± 0.04	1.21 ± 0.08	1.40	1.20 ± 0.07
	b2	0.99 ± 0.12	0.10 ± 0.02	1.37 ± 0.16	0.23 ± 0.03	1.52 ± 0.07	1.76	1.50 ± 0.07
	b3	1.3 ± 0.3	0.16 ± 0.06	0.91 ± 0.11	0.26 ± 0.03	2.00 ± 0.13	2.26	1.93 ± 0.13
4U 1705-44	i2	1.5 ± 0.3	0.21 ± 0.08	0.113 ± 0.017	0.041 ± 0.006	0.28 ± 0.03	0.32	0.28 ± 0.03
	i1	0.97 ± 0.16	0.09 ± 0.03	0.58 ± 0.08	0.095 ± 0.013	0.72 ± 0.04	0.83	0.70 ± 0.05
	b1	1.12 ± 0.18	0.13 ± 0.04	1.07 ± 0.08	0.236 ± 0.018	1.7 ± 0.2	1.96	1.7 ± 0.2
	b2	1.6 ± 0.3	0.26 ± 0.09	1.04 ± 0.10	0.47 ± 0.07	5.5 ± 0.6	5.97	5.1 ± 0.6
	b3	2.2 ± 0.2	0.49 ± 0.09	1.19 ± 0.10	1.03 ± 0.08	7.6 ± 0.7	8.70	7.4 ± 0.7
4U 1728-34	i1	0.96 ± 0.09	0.093 ± 0.017	1.00 ± 0.13	0.16 ± 0.02	1.31 ± 0.09	1.49	1.27 ± 0.08
	b1	1.07 ± 0.04	0.115 ± 0.009	1.74 ± 0.04	0.352 ± 0.009	1.41 ± 0.07	1.78	1.52 ± 0.08
	b2	1.19 ± 0.06	0.142 ± 0.013	1.67 ± 0.05	0.416 ± 0.010	1.90 ± 0.10	2.33	1.99 ± 0.11
	b3	1.54 ± 0.09	0.24 ± 0.03	1.42 ± 0.04	0.596 ± 0.018	2.15 ± 0.18	2.76	2.36 ± 0.19
	b4	1.78 ± 0.07	0.32 ± 0.02	1.47 ± 0.03	0.819 ± 0.017	1.98 ± 0.16	2.88	2.40 ± 0.19
4U 1735-44	b1	1.45 ± 0.11	0.21 ± 0.03	2.34 ± 0.21	0.86 ± 0.08	4.96 ± 0.17	5.85	4.98 ± 0.17
	b2	1.79 ± 0.16	0.32 ± 0.06	1.73 ± 0.11	0.97 ± 0.06	5.50 ± 0.19	6.51	5.55 ± 0.19
	b3	2.24 ± 0.17	0.50 ± 0.08	1.94 ± 0.15	1.72 ± 0.13	6.0 ± 0.3	7.81	6.7 ± 0.3
	b4	2.42 ± 0.17	0.58 ± 0.08	2.10 ± 0.12	2.16 ± 0.12	5.9 ± 0.3	8.09	6.9 ± 0.3
SLX 1735-269	i1	3.3 ± 0.7	1.1 ± 0.4	0.032 ± 0.005	0.058 ± 0.009	0.28 ± 0.04	0.35	0.29 ± 0.03
	b1	1.08 ± 0.07	0.116 ± 0.014	1.39 ± 0.09	0.281 ± 0.019	0.78 ± 0.05	1.06	0.91 ± 0.06
4U 1820-30	i1	0.97 ± 0.05	0.094 ± 0.009	2.70 ± 0.05	0.448 ± 0.009	2.08 ± 0.04	2.53	2.16 ± 0.04
	b1	1.45 ± 0.05	0.211 ± 0.013	2.63 ± 0.10	0.97 ± 0.04	2.97 ± 0.08	3.95	3.37 ± 0.09
	b2	1.74 ± 0.07	0.30 ± 0.02	2.11 ± 0.06	1.13 ± 0.03	4.2 ± 0.2	5.29	4.5 ± 0.2
	b3	2.06 ± 0.06	0.42 ± 0.03	1.96 ± 0.05	1.46 ± 0.03	4.8 ± 0.2	6.34	5.4 ± 0.3
4U 1916-053	i6	1.11 ± 0.13	0.12 ± 0.03	0.23 ± 0.04	0.052 ± 0.009	0.33 ± 0.03	0.38	0.33 ± 0.03
	i5	1.16 ± 0.11	0.14 ± 0.03	0.24 ± 0.04	0.059 ± 0.009	0.38 ± 0.03	0.44	0.37 ± 0.03
	i4	1.01 ± 0.19	0.10 ± 0.04	0.30 ± 0.07	0.056 ± 0.013	0.43 ± 0.05	0.48	0.41 ± 0.04
	i3	1.04 ± 0.15	0.11 ± 0.03	0.39 ± 0.07	0.074 ± 0.013	0.50 ± 0.05	0.57	0.49 ± 0.05
	i2	0.91 ± 0.12	0.08 ± 0.02	0.52 ± 0.05	0.080 ± 0.008	0.57 ± 0.03	0.65	0.55 ± 0.03
	i1	0.74 ± 0.11	0.055 ± 0.017	1.09 ± 0.09	0.112 ± 0.009	0.62 ± 0.03	0.73	0.62 ± 0.03

The blackbody radius, the half-height h of the accreting equatorial belt on the neutron star and the half-height of the inner radiatively-supported disk H_{eq} are expressed in km, L_{bb} is bolometric in 10^{37} erg s $^{-1}$, L_{cpl} and L_{tot} are in 10^{37} erg s $^{-1}$ in the 1 - 30 keV energy range. Conventionally, errors are not quoted for the total luminosity. The f_{bb}/f_{Edd} ratio is the blackbody flux $f_{bb} = L_{bb}/4\pi R_{bb}^2$ divided by the Eddington flux of 1.4×10^{25} erg cm $^{-2}$ s $^{-1}$ for a 10 km neutron star. The assumed distances to the sources are as in Table 3.1.

The behaviour of the Comptonization cut-off energy

The most striking result of this survey is shown in Fig. 6.20. The cut-off energy of the power law model component shows systematic behaviour as a function of the total 1 - 30 keV luminosity. For luminosities greater than $\sim 1 \times 10^{37}$ erg s $^{-1}$, the cut-off energy is small, typically in the range 5 - 8 keV depending on the source, and constant. Such low values of E_{co} are similar to those measured in the Z-track sources.

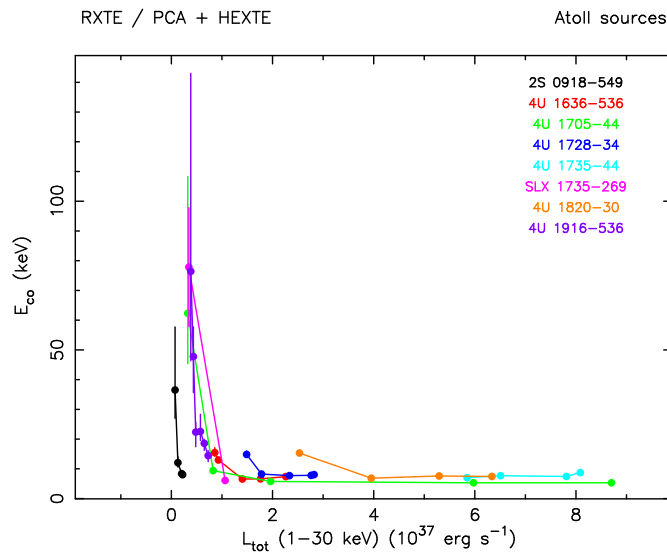


Figure 6.20: Changes in the cut-off energy of the power law model component.

However, the value of E_{co} changes markedly as the luminosity becomes less than $\sim 1 \times 10^{37}$ erg s $^{-1}$. In this low luminosity range, the cut-off energy increases with decreasing luminosity to ~ 15 - 80 keV. The change is very well visible in the spectra of the Atoll sources, such as in the example shown in Fig. 6.19. The effect is strong and secure given the large number of measurements in the sample of eight Atoll sources. Such a substantial change in E_{co} was not observed in the Z-track sources where $E_{co} \sim 5$ keV at all times, and this shows a major difference between the two groups of LMXB. The cut-off energy of the power law component is determined by the electron temperature in the accretion disk corona (e.g. Sect. 3.1.6). Thus, the behaviour observed here has an important consequence for the dependence of the coronal temperature on the total luminosity and its relation to the temperature of the neutron star which will be discussed later.

Changes of the neutron star blackbody

Figure 6.21 shows changes of the blackbody parameters, temperature (top) and radius (bottom), for the sample of the Atoll sources studied here. It can be seen, that the blackbody temperature

shows a systematic increase as the total (1 - 30 keV) luminosity increases. A more detailed inspection reveals that the major change of kT_{bb} (between about 1 and 2 keV) takes place for luminosities lower than $\sim 1 \times 10^{37}$ erg s $^{-1}$. Above this luminosity, kT_{bb} stabilizes and stays in the range 2.0 - 2.5 keV.

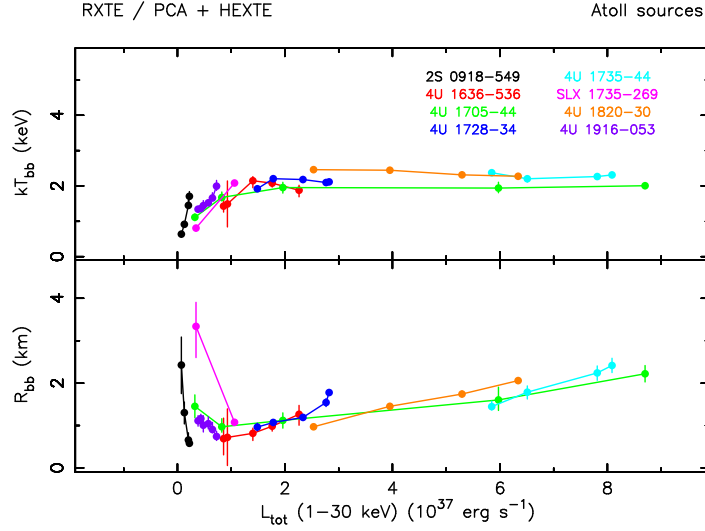


Figure 6.21: The behaviour of the blackbody parameters: temperature (upper panel) and radius (lower panel).

At this stage, it is only noted that changes of kT_{bb} of the magnitude observed here (by about 1 keV) are reminiscent of the changes of kT_{bb} along the Normal Branch in the Cyg-like Z-track sources in which this was interpreted as ongoing heating of the neutron star along this branch related to the increasing mass accretion rate (e.g. Sect. 4.3.3). A further discussion of this issue will be given later.

Also the blackbody radius varies systematically with the total luminosity as shown in Fig. 6.21. R_{bb} is at all times less than the ~ 10 km radius of the neutron star showing that the emission region is reduced to an equatorial belt on the star. Within the luminosity range covered by the data (up to $\sim 8 \times 10^{37}$ erg s $^{-1}$), R_{bb} stays below 3 km in all Atoll sources studied in this work. It is also apparent, that for luminosities greater than $\sim 1 \times 10^{37}$ erg s $^{-1}$, R_{bb} is positively correlated with the total luminosity. This will be addressed in relation to the earlier results of Church & Balucińska-Church (2001) who studied a dependence of the size of the emission region on the neutron star as a function of the total luminosity.

A feature unknown before is that R_{bb} is anti-correlated with the total luminosity for $L_{tot} < 1 \times 10^{37}$ erg s $^{-1}$. Indeed, R_{bb} has a clear minimum at about 1×10^{37} erg s $^{-1}$, and as L_{tot} drops below this luminosity, R_{bb} increases.

Luminosities of the emission components

The changes of the luminosity of the blackbody and the Comptonized emission are shown in Fig. 6.22. The luminosities of both emission components increase with L_{tot} .

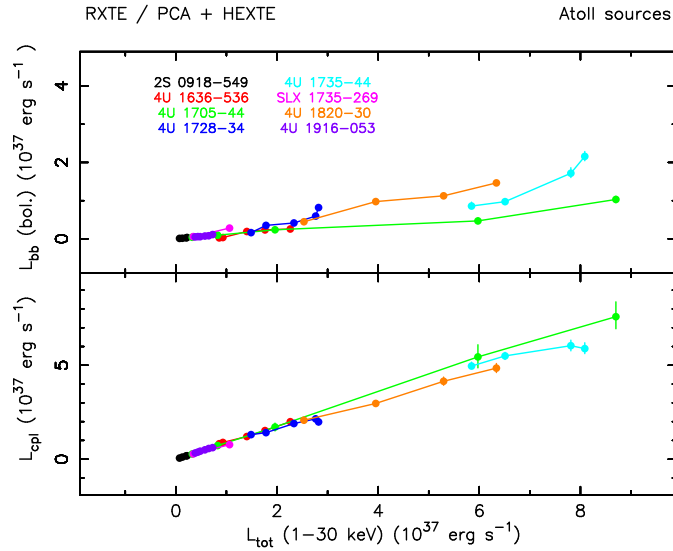


Figure 6.22: Changes in the luminosities of the two model components: blackbody (upper panel) and the Comptonized emission (lower panel).

In particular, the changes of the Comptonized luminosity, which contributes no less than 70% of L_{tot} , most likely reveal changes in \dot{M} through the accretion disk as argued in this work on many occasions before (e.g. Sect. 4.3.3). Thus, the monotonic increase of L_{cpl} in all sources with increasing L_{tot} suggests clearly the direction in which \dot{M} changes along the Atoll tracks.

The emission line

Figure 6.23 shows the centroid energy of the emission line as measured in the selections in which it was detected. It can be seen that the measured values lie well within the range 6.4 - 7.1 keV (between the two dashed lines) corresponding to the different ionization states of iron, from neutral FeI to H-like (Fe XXVI), respectively. No general relation between the line energy and the total luminosity can be seen which implies that the physical conditions in the region from which the line is emitted are roughly the same in all sources. The average centroid energy is 6.63 keV, with a relatively small (comparable to an error of a single measurement) standard deviation of 0.18 keV, which suggests the major contribution is of FeXXV localized most likely in the accretion disk corona. The line equivalent width was in the range 60 - 160 eV with no clear dependence on the total luminosity.

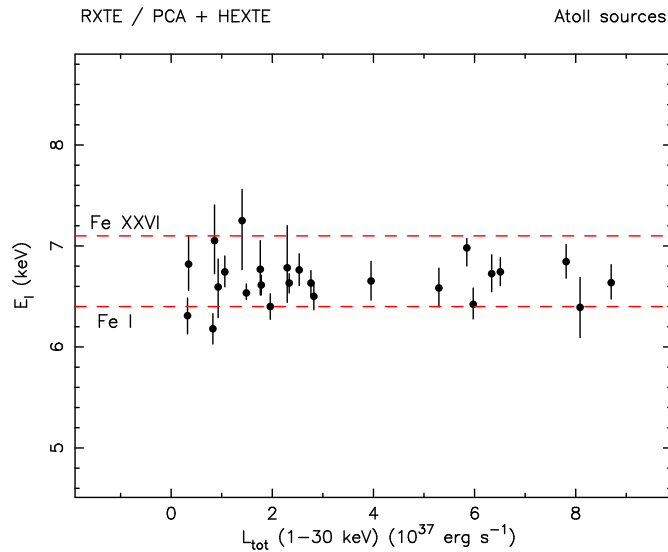


Figure 6.23: The centroid energy (with 90% errors) of the emission line in the Atoll sources.

6.3 Discussion

6.3.1 Changes of mass accretion rate

Spectral fitting results for the sample of Atoll sources analysed in this work show that the luminosities of both the blackbody and the cut-off power law component (Fig. 6.22) increase monotonically with increasing L_{tot} explaining the variations in X-ray intensity observed. In particular, the luminosity of the Comptonized emission is the best indicator of \dot{M} given its contribution to the total of more than 70% at all times. An apparent increase of L_{cpl} makes it clear that mass accretion rate increases in all Atoll sources with increasing X-ray intensity as one would expect. This increase corresponds to the movement of the source in colour-colour (hardness-intensity) in the direction Island \rightarrow Banana and this supports the standard view on that matter (Sect. 1.3.2) that \dot{M} increases from the Island to the Banana branch (Hasinger & van der Klis 1989). The same was recently suggested by Lin et al. (2009) based on the transitional source XTE J1701-462 observed during an outburst (Remillard et al. 2006). At the end of the outburst, the source was reported to exhibit Atoll behaviour (Homan et al. 2007b) and a transition from the Banana branch to the Island branch as its luminosity (mass accretion rate) decreased (Lin et al. 2009; Homan et al. 2010).

6.3.2 Emission from the neutron star

The blackbody component of the Extended ADC model is interpreted as emission from the surface of the neutron star. In all Atoll sources studied here, the measured blackbody radii are of typically 0.5 - 3 km meaning that emission comes from a narrow equatorial belt on the star, whose half-height h can be calculated from the blackbody radius (Eqn. 2.2). Given the present large number of measurements from the survey of eight Atoll sources and also those obtained earlier for the Z-track sources, the observed size of the neutron star emission region can now be better confronted with the two scenarios for the flow of matter between the disk and the neutron star: the theory of vertical spreading of Inogamov & Sunyaev (1999) and the scenario of radial inflow (Sect. 2.2.2). It is noted here, that the values of the blackbody radii are used here as they were obtained from spectral fitting to allow the most direct comparison with previous work of the *X-ray Binaries Group* and others. However, these may not be literally correct due to possible systematic effects considered in Sect. 2.2.2 and this will be taken into account in the discussion below.

In the radial inflow scenario, matter is expected to fall onto the neutron star from the whole vertical extent of the inner disk so that one would expect h to be directly determined by the half-height H of the radiatively-supported disk given by Eqn. 1.16. The radial dependence of H shows that the equilibrium half-height H_{eq} is reached ~ 20 km from the neutron star, the height rising rapidly to H_{eq} from zero at the surface of the neutron star. However, it should be noted that the disk only achieves $H \sim H_{eq}$ in bright Atoll sources and the Z-track sources, whereas somewhat smaller H are expected in the lower luminosity sources. A comparison between the observed h and the half-height of the inner disk H is made in Fig. 6.24 for the Atoll sources (blue points) together with the results for the Z-track sources (black).

The values of H_{eq} on the X-axis are proportional to the total luminosity via Eqn. 1.1 and Eqn. 1.16, such that $H_{eq} = \frac{3\sigma_T R_*}{8\pi m_p c G M_*} L$, and for example $H_{eq} \sim 1$ km and $H_{eq} \sim 10$ km correspond to $L \sim 1 \times 10^{37}$ erg s $^{-1}$ and $L \sim 1 \times 10^{38}$ erg s $^{-1}$, respectively. The horizontal dashed line shows the limit for h of 10 km as the emitting belt on the star cannot exceed the size of the star itself. In all cases the values of h are below the line except a few measurements in the Cyg-like Z-track sources where the measured blackbody radii were comparable or slightly larger than 10 km at the soft apex and on the Flaring Branch. In these cases it is thought that the emission region can expand outside the neutron star surface.

As the first step, one may compare the data with the relation $h = H_{eq}$, shown with the red, dashed-dotted diagonal line, expected to hold in the radial inflow scenario. From Fig. 6.24 it can

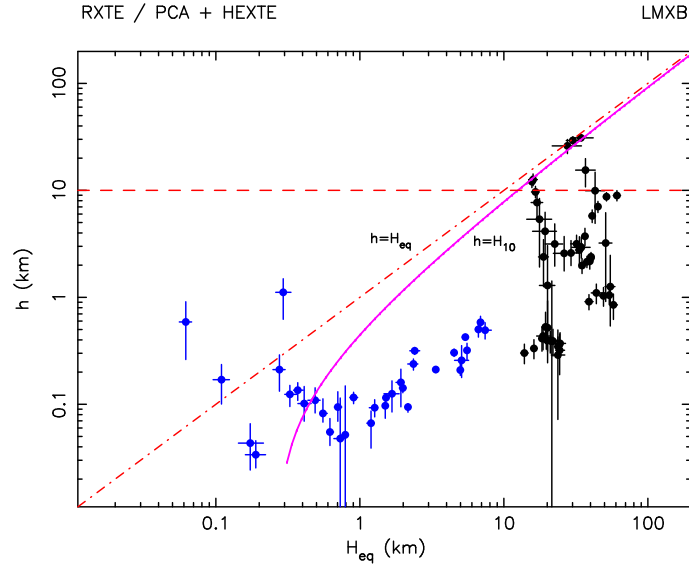


Figure 6.24: The half-height h of the emission region on the neutron star as a function of the equilibrium height H_{eq} of the inner radiatively-supported accretion disk. Data points are compared with the relations $h = H_{eq}$ (diagonal red line) and $h = H_{10}$ (magenta profile, see text).

be seen that in the Atoll sources (blue) only at the lowest luminosities, when $H_{eq} \lesssim 0.3$ km, do the data points scatter around the $h = H_{eq}$ line. However, as the luminosity increases, h follows the changes in R_{bb} (Fig. 6.21), first decreasing to a minimum at the luminosity $L \sim 1 \times 10^{37}$ erg s^{-1} (when $H_{eq} \sim 1$ km) and then increasing, but with h remaining systematically about ten times smaller than H_{eq} . In the Z-track sources (black), the data points close to $h = H_{eq}$ correspond to the soft apex and the lower Normal Branch/Flaring Branch of the Z-track, whereas the points that deviate from the diagonal line are those from the upper Normal Branch and the Horizontal Branch of the Z-track.

The deviation from $h = H_{eq}$ in low luminosity Atoll sources can be partially understood given that the equilibrium height H_{eq} is not reached if mass accretion rate (luminosity) is too low and the vertical structure of the inner disk is likely to be determined by radiation pressure only over a limited range of disk radii. This can be taken into account, and instead of H_{eq} one may take H_{10} being the disk half-height at the radius where the disk radiation pressure p_r becomes ten times greater than the gas pressure p_g , providing a better estimate of the real disk height at lower luminosities (Church & Balucińska-Church 2001). Following (Church & Balucińska-Church 2001), a dedicated script was used to find the disk radius r_{10} at which $p_{rad}/p_g = 10$ as a function of \dot{M} , and this was then used in Eqn. 1.16 to obtain H_{10} , this giving the height profile that can be overlaid in Fig. 6.24 (magenta line) to allow direct comparison with data. Some improvement is visible, with the H_{10} profile better approximating data points at low luminosities, the discrepancy,

however, remains large for most of the data points. It should be noted here, that the measured blackbody radii may be different than the actual ones due to possible systematics effects such as the combined effect of the electron scattering in the neutron star atmosphere and the gravitational redshift which, based on the example discussed in Sect. 2.2.2, could make the actual radius larger than the observed R_{bb} by a factor of ~ 1.7 . If so, then the values of $h \propto R_{bb}^2$ shown here would be underestimated by a factor of about 3 and this, if corrected for, would somewhat improve the agreement between h and H . However, it is in fact not certain what the actual modification might be and any correction factors should be treated with caution.

A comparison of the results obtained in the present work with those of Church & Balucińska-Church (2001) (Fig. 2.4) reveals that they are in a good agreement whenever the neutron star is relatively cool. Indeed, the blackbody temperatures measured in the survey of Church & Balucińska-Church (2001) were always lower than 1.6 keV and typically close to 1 keV. Such temperatures were measured in this work for the Atoll sources only at luminosities $\lesssim 1 \times 10^{37}$ erg s $^{-1}$ and for the Z-track sources when these were close to the soft apex. Otherwise, the measured kT_{bb} were higher, reaching 2.5 keV, and at these temperatures there is a clear discrepancy from either $h = H_{eq}$ or $h = H_{10}$ relation in all sources as seen in Fig. 6.24.

It is not clear why the blackbody temperature measured by Church & Balucińska-Church (2001) was not found higher than ~ 1.6 keV in any of the LMXB in their sample. One possibility is that this is a systematic effect of an underestimation of the blackbody related to the narrow 1 - 10 keV energy range of *ASCA* available in their spectral fitting. Alternatively, the present *RXTE* results, given the fact that the energies below 3 keV were not available in spectral fitting, may suffer from overestimation of the blackbody emission. Tests performed on the sources in the present work showed, that having restricted the spectra to a narrow energy range of e.g. 3 - 15 keV, there is no substantial change (5 - 10%) in the values of kT_{bb} . Church & Balucińska-Church (2001) allowed the photon index of the power law to vary in their spectral fitting, but this is unlikely to cause the difference, as the values obtained (typically 1.2 - 2.3) were generally close to 1.7 used in the present work, and showed no effect on the measured kT_{bb} . This was confirmed by additional tests performed in the present work which showed that with a free photon index the blackbody temperature indeed stays close (within a few percent) to its original value, with the photon index varying in a similar range to that reported by Church & Balucińska-Church (2001), but remaining close to $\Gamma = 1.7$. There is a possibility that during the observations studied by Church & Balucińska-Church (2001) the sources were often either close to the soft apex (the Z-

track sources) or in the Island/Lower Banana state (the Atoll sources), for which the blackbody temperature is lower. This would be consistent with the fact that Church & Balucińska-Church (2001) reported to have seen little variation in colour-colour in their observations, the situation typical to e.g. the Island state in the Atoll sources, but this could also be related to the time of *ASCA* observations being short and giving only snapshots of source variation in colour-colour. Also, the low temperatures reported by Church & Balucińska-Church (2001) in the case of the Z-track sources in their sample show clearly that the sources must have been observed close to the soft apex, and not elsewhere on the Z-track where the measured temperatures would have been higher.

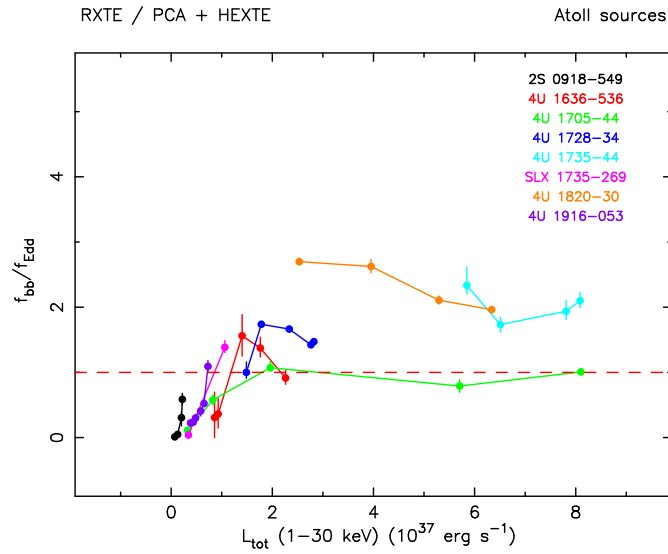


Figure 6.25: The ratio of the blackbody flux and the Eddington flux as a function of the total 1 - 30 keV luminosity in the Atoll sources.

The observed discrepancy from the relation $h = H$ when the neutron star is hot could be explained on the model for the Z-track sources (Sections 3.1.5, 4.3.2, 5.1.4, 5.16) in which the strong radiation pressure, scaling as T^4 , reduces the height of the inner disk and the effective H is smaller than H_{eq} or even H_{10} . Indeed, in the Z-track sources the points that deviate from the diagonal line in Fig. 6.24 are those corresponding to the Normal and the Horizontal branches on which the measured kT_{bb} is high and the radiation pressure strong. That the radiation pressure is also strong in the Atoll sources for luminosities higher than about $1 \times 10^{37} \text{ erg s}^{-1}$ is clearly visible in Fig. 6.25 showing the ratio of the blackbody emissive flux ($f_{bb} = L_{bb}/4\pi R_{bb}^2$) to the Eddington flux (at the surface of the 10 km neutron star). The flux ratio is small at lowest luminosities, but as the luminosity increases it becomes close to or higher than unity implying the increasing

strength of the radiation pressure from the surface of the neutron star. Thus, the relation $h = H$, expected in the radial inflow scenario for the boundary layer, can in principle be valid over all luminosities, but only if one takes into account that the disk height is reduced by the strong radiation pressure when the neutron star is hot. However, this explanation is only qualitative, as there is no theoretical relation between the strength of the radiation pressure and the fraction of the inner disk removed, so that the quantitative comparison with theory cannot be made.

Now, the present results are compared with the theory of Inogamov & Sunyaev (1999). In this scenario, accreted matter reaches the neutron star in the equatorial plane and then spreads vertically. According to Inogamov & Sunyaev (1999), most of emission comes from in-between two bright rings equidistant to the equator, the emission region being equivalent to an equatorial belt, and the meridional extent of the emission region is a function of the luminosity of the spreading layer L_{SL} . Church et al. (2002), working together with Inogamov, calculated the half-height h_{SL} of the emitting belt for L_{SL} being 1 %, 4 %, 20 % and 80 % of the Eddington luminosity to allow a comparison of the theory with observations. The half-height was calculated in two different ways. Firstly, the half-height h_{FWHM} was taken as the FWHM of the intensity profile of the emission region on the neutron star, the intensity being small at the equator and peaking at the bright rings on the neutron star positioned symmetrically with respect to the equator, then $h_{SL} \approx h_{FWHM}$. In the second approach, the intensity profile of the emission region was integrated and the half-height h_I was taken as the value for which the average intensity gave the same summed intensity as the integral of the real intensity profile (Church et al. 2002), and here $h_{SL} \approx h_I$. The two methods were found to give similar results as given in Table 6.5, whereas the difference between the two approaches provides some estimate of the error on h_{SL} . In the Extended ADC model, the

Table 6.5: Values of the half-height of the equatorial emitting belt on the neutron star calculated by Church et al. (2002) from the theory of Inogamov & Sunyaev (1999). Two options are given depending on the calculation method as described in the text. These are given for four values of the luminosity of the spreading layer L_{SL} corresponding to 1 %, 4 %, 20 % and 80 % of the Eddington luminosity.

L_{SL}	h_{FWHM}	h_I
0.18	0.12	0.09
0.70	0.44	0.32
3.52	2.45	1.50
14.1	11.62	8.52

The luminosity of the spreading layer L_{SL} is given in 10^{37} erg s $^{-1}$. The half-height h_{FWHM} and h_I are given in km.

luminosity of the spreading layer is the blackbody luminosity, i.e. $L_{SL} = L_{bb}$, and therefore one should expect an agreement between the observed h and the estimated h_{SL} with these shown as a function of L_{bb} , and this comparison is made in Fig. 6.26.

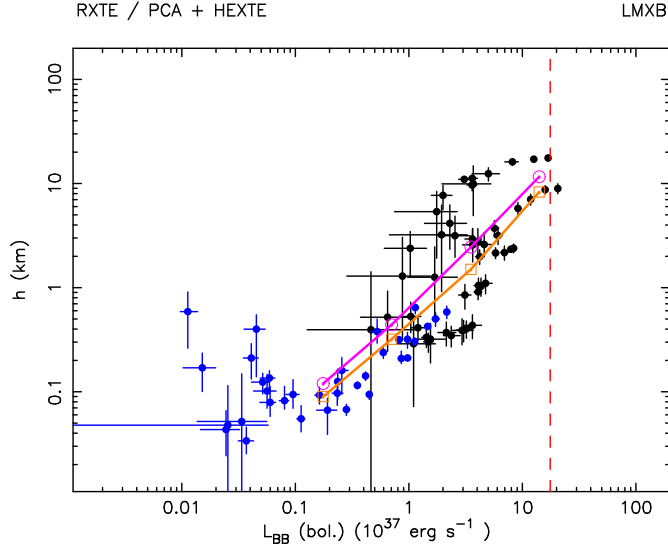


Figure 6.26: The half-height of the equatorial belt on the neutron star as a function of the bolometric blackbody luminosity. The Atoll sources and the Z-track sources are shown in blue and black, respectively. The vertical line marks the Eddington limit assumed to be $1.76 \times 10^{38} \text{ erg s}^{-1}$. The overlaid theoretical values of h_{SL} calculated in two different ways are shown with open circles (h_{FWHM} , magenta) and open squares (h_I , orange) for four values of L_{bb} between 1% and 80% of L_{Edd} (see text).

The theoretical values of h_{SL} obtained in two different ways mentioned above (h_{FWHM} and h_I) are shown next to each other, and these are given for the four values of L_{bb} as in Church et al. (2002). The result is very suggestive that there is a good quantitative agreement between the theoretical size of the equatorial belt expected from the theory and the observed values of h and this supports the theory of Inogamov & Sunyaev (1999) favouring the scenario in which the boundary layer is formed on the neutron star by the vertical spreading of matter. Also in this case, one might consider if some possible systematic effects affecting the blackbody emission from the neutron star (Sect. 2.2.2), and hence also R_{bb} and h , could alter the picture shown in Fig. 6.26 in any substantial way. However, within a factor of $\sim 2 - 3$ on h , the agreement with the theory remains good.

The strong radiation pressure and the launching of jets

The strong radiation pressure for total luminosities higher than $\sim 1 \times 10^{37} \text{ erg s}^{-1}$ in the Atoll sources could, by similarity to the Z-track sources, disrupt the inner accretion disk and divert

plasma into jets. In particular, the increase of the radiation pressure (Fig. 6.25) seems to coincide with the spectral transition from the Island to the Banana branch. Thus, the launching of jets could take place during the spectral transition and on the Banana branch where the radiation pressure is strong. However, it should be noted that the maximum half-height of the inner radiatively-supported disk, in the range of luminosities between about 1×10^{37} erg s⁻¹ and 8×10^{37} erg s⁻¹ concerned here, is in the range 1 - 7 km, thus rather limited when compared to $H \sim 50$ km in the Z-track sources. The emission geometry in the Z-track sources, a narrow equatorial belt exerting strong radiation pressure on the disk towering around it, was proposed to favour the launching of jets given a large vertical component of the disrupting force acting on the disk (e.g. Sect. 3.1.5, 5.1.4). Moreover, the conical opening of the disk in the Z-track sources provided rough collimation for the jet. In the Atoll sources, the amount of plasma above and below the disk plane available in the vicinity of the neutron star is clearly smaller and the inner disk does not tower around the neutron star implying that the jets, if launched, should be weaker than in the Z-track sources. This prediction seems to be in a good agreement with the hitherto observations of radio jets in the Atoll sources. As noted in Sect. 1.4.2, radio emission from the Atoll sources, when compared to the Z-track sources, is known to be weaker by about an order of magnitude and thought to be related to the spectral transitions (Migliari et al. 2003). Moreover, the Atoll sources analysed here from which the jets have been reported, 4U 1820-30 and 4U 1728-34, fulfill the strong radiation pressure condition (Fig. 6.25). It therefore appears that the model for the jet launching of Church et al. (2006), based on a disruption of the inner radiatively-supported disk by the strong radiation pressure, is capable of explaining the presence of jets not only in the Z-track sources, but also in the Atoll sources.

6.3.3 The transition from the Banana to the Island state

It was earlier shown in Fig. 6.20 that there is a clear dependence of E_{co} on the total luminosity common to all Atoll sources studied here. In particular, the survey results revealed a striking increase of E_{co} as the total luminosity falls below $\sim 1 \times 10^{37}$ erg s⁻¹, with $E_{co} \sim 6$ keV above this luminosity, and 15 - 80 keV below it (Fig. 6.20). The increase of E_{co} with decreasing luminosity can thus explain the characteristic spectral hardening observed in hardness-intensity and colour-colour during the transition between the (softer) Banana state and the (harder) Island state in the Atoll sources.

Let us therefore consider a possible physical cause of the state transition discussed above. In the

model of Church et al. (2006) for the sub-group of the Cyg-like Z-track sources, the cut-off energy corresponds to the electron temperature of plasma in the extended accretion disk corona. For the optically thin corona, $E_{co} = kT_e$, whereas in an optically thick corona $E_{co} = 3kT_e$ (Sect. 4.3.5). Figure 6.27 presents the ratio of the power law cut-off energy to the blackbody temperature, E_{co}/kT_{bb} , as a function of the total luminosity of the LMXB (Atoll and Z-track sources) studied in this work.

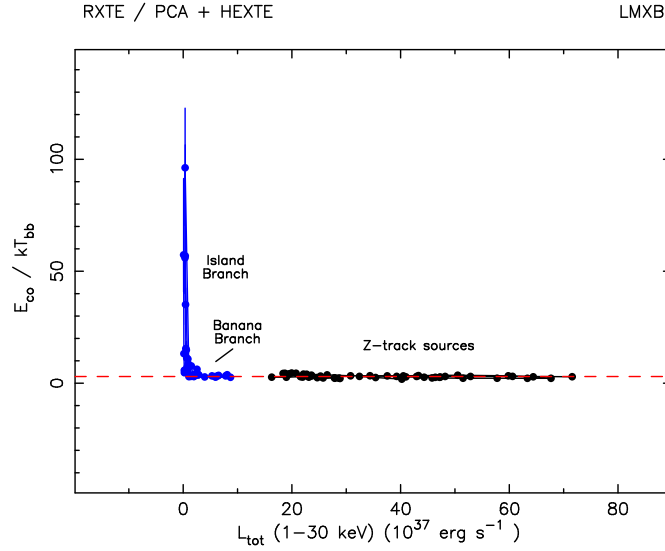


Figure 6.27: The ratio of the temperatures of the corona and the neutron star as a function of the total 1 - 30 keV luminosity. The Atoll sources (blue) and the Z-track sources (black) are shown together.

In the Z-track sources (black points), over a wide range of luminosities above $10 \times 10^{37} \text{ erg s}^{-1}$, the temperature ratio is close to 3 (red dashed line). A cut-off energy of a few keV was measured in these sources and interpreted as evidence for thermal equilibrium between the optically thick corona and the neutron star (e.g. Sect. 4.3.5).

Figure 6.27 shows that the equilibrium is sustained also in the Atoll sources over a limited luminosity range of about $1 - 10 \times 10^{37} \text{ erg s}^{-1}$ corresponding to locations of the sources on the Banana branch. However, the situation changes markedly when the luminosity falls below $\sim 1 \times 10^{37} \text{ erg s}^{-1}$ at which the corona becomes significantly hotter as revealed by very high values of the cut-off energy and in consequence the E_{co}/kT_{bb} ratio. This suggests that the spectral transition in the Atoll sources is related to a break down of the thermal equilibrium between the neutron star and the accretion disk corona. Thus, the Island branch appears to be a state in which the corona is very hot, far from thermal equilibrium with the neutron star and the spectrum of the source is strongly dominated by the Comptonization on very hot electrons in the corona.

The mechanism responsible for such a substantial coronal heating is, however, yet unknown, this situation resembling that of the solar corona. It should be also noted that if T_{ADC} varied strongly within the corona, E_{co} would also vary and the observed knee in the Comptonized emission would be very rounded. This is not observed given present quality of high-energy spectra, so it is taken as a working hypothesis that there are no gross temperature variations in the ADC itself.

The results obtained here suggest, in the first approximation, that there is a one-to-one relation between the electron temperature in the corona and the total luminosity (mass accretion rate) of a source, with the spectral transition related to the deviation of the corona from the equilibrium with the neutron star. An examination of Fig. 6.20 and its comparison with colour-colour (hardness-intensity) variations of particular sources, shows that the transition from the Banana to the Island state indeed takes place at about $L \sim 1 \times 10^{37}$ erg s⁻¹ in the case of 4U 1636-536, 4U 1705-44, 4U 1728-34 and SLX 1735-269. In line with this is the behaviour of 4U 1916-053 whose cut-off energy is above ~ 15 keV at all times with no clear transition to lower values which is consistent with its luminosity being below $\sim 1 \times 10^{37}$ erg s⁻¹. In another observation of this source, Bloser et al. (2000) observed the state transition to occur at $L \sim 1 \times 10^{37}$ erg s⁻¹ for the assumed distance of 9.3 kpc (similar to the 9.0 kpc used here) above which E_{co} dropped to 9 keV and the source was shown to trace the Banana branch. Thus, by comparison of the results obtained here with those of Bloser et al. (2000), it is found that during the observation analysed in the present work, the source was in the Island state and as its luminosity was increasing the source was moving towards the Banana branch. Furthermore, the colour-colour variation of 4U 1735-44 shown in Fig. 6.15 shows that during the observation studied here, the source was not in the Island state, but only in the Banana state. This is consistent with its luminosity being above $\sim 1 \times 10^{37}$ erg s⁻¹.

The transition between the Banana and the Island state in 4U 1820-30 observed here seems to have occurred at a somewhat higher luminosity than 1×10^{37} erg s⁻¹. However, given only a single measurement in the Island branch, this is at the moment uncertain and the Island branch may not have been fully traced in this observation. 2S 0918-549 shows a classic Atoll pattern with the Island and the Banana states well visible and yet for the distance assumed here (5.3 kpc) its luminosity is well below 1×10^{37} erg s⁻¹. However, it is possible to ask if such a situation can be related to uncertainties of distance estimates, given the fact that $L = f \times 4\pi d^2$ and hence the luminosity $L \propto d^2$ is sensitive to distance. The distance used for this source is quoted after Galloway et al. (2008) and is close to other estimates such as < 4.9 kpc (Jonker et al. 2001), 4.2 ± 1.3 kpc (Cornelisse et al. 2002) and ~ 4.75 kpc (in't Zand et al. 2005). In all these cases,

the measurement was based on type I X-ray bursts showing photospheric radius expansion, but it should be noted that in each case only a single burst was analysed. Moreover, Chevalier & Ilovaisky (1987), based on observations of the optical counterpart of the source, showed that its distance can be anywhere in the range 2 - 15 kpc and the upper limit (with an uncertainty of 2 kpc) was favoured by Christian & Swank (1997). It is therefore possible that the distance to this source obtained from observations of type I X-ray bursts is systematically underestimated and it was checked here that if the real distance was e.g. about 12 kpc, the spectral transition in the source would have occurred close to $\sim 1 \times 10^{37}$ erg s⁻¹.

The above discussion shows that, baring in mind distance uncertainties, there is evidence that the state transition from the Banana to the Island state in the Atoll sources is consistent with taking place at approximately the same luminosity of about 1×10^{37} erg s⁻¹. It is thus proposed that as mass accretion rate decreases and finally drops below a critical level, the spectral transition takes place caused predominantly by a break-down of thermal equilibrium between the accretion disk corona and the neutron star, revealing a substantial heating of the corona at lowest luminosities.

Chapter 7

Conclusions and future work

7.1 Conclusions of the present work

The Cyg-like sources

The aim of the work, following the similar work performed earlier by Jackson et al. (2009) in the case of GX 5-1, was to carry out a simultaneous spectral and timing analysis of the remaining two classic Cyg-like Z-track sources: Cyg X-2 and GX 340+0. The spectral fitting results were viewed in terms of the model for the Z-track in the Cyg-like sources of Church et al. (2006) and Bałucińska-Church et al. (2010), whereas the spectral/timing results were compared with those obtained by Jackson et al. (2009) and their model for the kHz QPO.

- The spectral fitting results are in a good agreement with those obtained independently before by Church et al. (2006) for GX 340+0 and Bałucińska-Church et al. (2010) for Cyg X-2, and support the model for the Z-track in the Cyg-like sources of Church et al. (2006).
- The soft apex in Cyg X-2 and GX 340+0 corresponds to a low accretion rate at which the neutron star is cool and accretes with its whole surface, whereas away from this point the physical conditions change strongly.
- The present results do not support the standard view in which the mass accretion rate increases monotonically along the Z-track from the Horizontal Branch, along the Normal Branch to the Flaring Branch. Here it was found that mass accretion rate increases on the Normal Branch between the soft apex and the hard apex, leading to heating of the neutron star, and then decreases to a low value between the hard apex and the left end of

the Horizontal Branch. On the Flaring Branch, the mass accretion rate is constant.

- The increasing neutron star temperature on the Normal Branch leads to strong radiation pressure which becomes super-Eddington close to the hard apex and increases further on the Horizontal Branch.
- The strong radiation pressure disrupts the inner disk, blowing plasma away from the disk plane and causing the observed increase of the column density on the Normal Branch. The diversion of plasma into the vertical direction can be the necessary condition for the launching of jets which are observed on the upper Normal Branch and the Horizontal Branch only, thus at the positions where the radiation pressure is strong.
- As the source moves from the soft apex towards the hard apex, the emission region on the neutron star changes from a full sphere into an equatorial belt. The height of the emitting equatorial belt responds to the changes of the height of the inner disk or the mass accretion rate to the neutron star, these being reduced by the strong radiation pressure.
- The onset of flaring corresponds to unstable nuclear burning on the neutron star under condition of constant mass accretion rate.
- The temperature ratio between the corona and the neutron star and the general positive correlation of these temperatures on the Z-track suggests that the neutron star and the corona are in thermal equilibrium.
- The simultaneous spectral and timing analyses suggest that the upper kHz QPO frequency is an oscillation always at the inner edge of the disk.
- The observed decrease of the kHz QPO frequencies between the hard apex and the left end of the Horizontal Branch can be explained in terms of the inner disk edge being pushed away from the neutron star by the increasing radiation pressure in agreement with the model proposed by Jackson et al. (2009).

GX 17+2

The present work revealed that the source is a hybrid between the classic Cyg-like sources and the Sco-like sources (Sco X-1 and GX 349+2) sharing some characteristics of each sub-group of the Z-track sources. This makes the standard classification of the source (as a Sco-like source) not fully appropriate in terms of its physical properties.

- GX 17+2 behaves in a similar way to the Cyg-like sources when it is on the Normal and the Horizontal Branch.
 - At the soft apex, the accretion rate is low which corresponds to a low temperature of the neutron star. The mass accretion rate then increases on the Normal Branch from the soft apex towards the hard apex.
 - There is a substantial increase of the blackbody temperature and radiation pressure along the Normal Branch and the Horizontal Branch. The strong radiation pressure can disrupt the inner accretion disk and be responsible for the launching of jets as in the Cyg-like sources.
- The main difference between GX 17+2 and the Cyg-like sources is on the Flaring Branch.
 - The mass accretion rate increases on the Flaring Branch leading to increased neutron star temperature and radiation pressure, with the emission region on the neutron star reduced, whereas in the Cyg-like sources the mass accretion rate was constant in flaring.
 - The Flaring Branch is oriented closely to the Normal Branch in hardness-intensity, and the source chooses to move along the Flaring Branch if conditions on the neutron star permit unstable nuclear burning. The observed strength of the Flaring Branch in GX 17+2 is a consequence of unstable nuclear burning under condition of increasing mass accretion rate.

The Sco-like sources

The results obtained for Sco X-1, supported by the results from *RXTE*/All-Sky Monitor for all six classic Z-track sources, suggests a model for the (truly) Sco-like sources (Sco X-1 and GX 349+2).

- As in GX 17+2, the nature of flaring is most probably unstable nuclear burning under condition of increasing mass accretion rate on the Flaring Branch.
- Observationally, the Sco-like sources are dominated by strong and frequent flaring as revealed by the long-term observations with the *RXTE*/ASM.
- The present results suggest a model in which strong and frequent flaring leads to heating of the neutron star as revealed by high neutron star temperature at all times, unlike in the other Z-track sources. This is supported by the analysed observation of Sco X-1 with reduced flaring showing evidence for some degree of cooling as expected.

- The radiation pressure from the neutron star in Sco X-1 is strong at all Z-track positions suggesting that the launching of jets may not be restricted to any particular branch of the Z-track.
- Within the known distance estimates to the Z-track sources, there is no evidence to support the suggestion of Homan et al. (2007a) that the Sco-like sources are systematically less luminous than the Cyg-like sources. The (truly) Sco-like sources are found to have similar luminosities to the Cyg-like sources, but differ by having hot neutron stars heated by prevalent flaring.

The Atoll sources

The aim of this work was to do conduct a survey of a sample of Atoll sources and test if spectral fitting with the Extended ADC model can shed more light on the physical nature of this group of Low Mass X-ray Binaries. The results can be summarized as follows:

- The mass accretion rate increases in the direction Island \rightarrow Banana and there is evidence that the spectral transition takes place at approximately the same luminosity in all sources. As the mass accretion rate increases, the neutron star becomes hotter leading to increased radiation pressure and increasing absorption intrinsic to the source, not previously known.
- The present results favour the scenario of Inogamov & Sunyaev (1999) in which the boundary layer is formed on the neutron star as an emitting equatorial strip whose height depends on the mass accretion rate to the neutron star.
- The strong radiation pressure disrupting the inner disk may explain observations of radio jets in Atoll sources. The limited amount of plasma in the inner radiatively-supported disk, when compared to the Z-track sources, could explain why the jets in the Atoll sources are an order of magnitude weaker than those in the Z-track sources.
- The state transition from the Banana Branch into the Island Branch takes place approximately at the luminosity $L = 1 \times 10^{37}$ erg s⁻¹ and is caused by a break-down of thermal equilibrium between the neutron star and the accretion disk corona, with the corona substantially heated up to 15 - 80 keV on the Island Branch. The equilibrium is maintained at higher luminosities: on the Banana Branch in the Atoll sources and in the Z-track sources.

7.2 The directions of future studies

One of the major unresolved problems is the secular (on a timescale of tens of days) intensity changes, such as those of Cyg X-2, the changes modulating the short-term (a few day) Z-track behaviour of the source. It is therefore desirable to study and compare the physical properties of the Z-track of Cyg X-2 traced at different overall intensity levels. This should help determine if the secular motion is related to changes of mass accretion rate in the system, or whether it is caused by obscuration effects related e.g. to the precession of the accretion disk.

The results of the present work show that in the Cyg-like sources, as mass accretion rate increases between the soft apex and the hard apex, the temperature of the neutron star increases. However, the star remains hot on the Horizontal Branch despite the fact that mass accretion rate most probably decreases on that branch back to a low value. This suggests time delays between the changes of mass accretion rate in the disk and those more local to the neutron star. It would be thus important to perform a detailed spectral study of the Z-track, paying attention to possible time delays between the changes in the Comptonized emission (reflecting changes in the disk) and the neutron star emission. Such a study should also treat the movement of the source in the direction HB \rightarrow NB and NB \rightarrow HB, separately, in order not to mix data from the cooling and heating phases of the Z-track movement.

Of great importance would be a simultaneous spectral and timing study of Sco X-1 in which the strong radiation pressure is not restricted to the upper Normal/Horizontal Branch, but is present at almost all Z-track positions. This could allow further testing of the model, studied in the present work on the Cyg-like sources, in which the strong radiation pressure is responsible for the observed behaviour of the kHz QPO on the Z-track. In fact, previous observations of Sco X-1 (e.g. van der Klis et al. 1996) show that the time variability of the source is exceptional, with the kHz QPO reported on all Z-track branches which provides initial support for the model involving the strong radiation pressure.

Also, the source should be a target of simultaneous X-ray/radio observations to test the possibility that the launching of jets in this source could take place at any Z-track position, as indicated by the present results, and the source is already known to have been detected in radio on all Z-track branches (Hjellming et al. 1990b).

Clearly needed are further studies of strong and frequent flaring in the Sco-like sources. The present results indicate that the phenomenon is related to unstable nuclear burning under condition of

changing mass accretion rate. However, the values of mass accretion rate per unit area measured in flaring in Sco X-1 do not agree with the critical value for unstable nuclear burning of Bildsten (1998). This suggests that, if the condition is actually met, either nuclear burning takes place at the edges of the emitting equatorial belt on the neutron star or some of accreted mass is diverted just before reaching the star, such as in the form of jets.

It is also necessary to study the possible effect of heating of the neutron star by flaring in the Sco-like sources. The research should involve spectral analyses of more observations with either strong or reduced flaring in Sco X-1 and GX 349+2 to verify the proposed hypothesis.

In line with the above proposals would be a study of the nature of flaring-like behaviour in bright Atoll sources, i.e. the GX Atoll sources, such as that observed in this work in 4U 1705-44, 4U 1728-34, 4U 1735-44 and 4U 1820-30 and classified as the Upper Banana Branch, and also that reported in the transient source XTE J 1701-462. A detailed spectral analysis of such sources should allow determining if the observed behaviour can be related to unstable nuclear burning, and if so, whether it is similar to the Cyg-like or the Sco-like flaring.

A study of GX Atoll sources would also supplement the results of the present survey of Atoll sources and fill the luminosity gap between the Atoll sources studied and the Z-track sources. The results could shed more light on the problem of the relation between the height of the emission region on the neutron star and the height of the inner disk in LMXB, which addresses the issue of the geometry of accretion flow in the boundary layer in disk-accreting systems in general. Furthermore, an extended survey should confirm that the spectral transition takes place at the same luminosity (mass accretion rate) in all Atoll sources or reveal if any secondary parameter may be involved.

There is strong evidence that the spectral transition from the Banana Branch to the Island Branch in the Atoll sources corresponds to the break-down of thermal equilibrium between the neutron star and the accretion disk corona. However, the cause of the substantial coronal heating at low luminosities is not known and requires further research, partially on theoretical grounds, to point towards a possible mechanism of energy transfer from the innermost regions of the system to the accretion disk corona. This would also address the issue of the dominant contribution of the Comptonized emission to the total luminosity in LMXB which is theoretically not understood given that most of energy release is expected from the boundary layer.

Of great interest is the transient source XTE J 1701-462 which showed the properties of Z-track and Atoll behaviour during the decay of an outburst. The present work suggests that the progress

in understanding e.g. the difference between the Cyg-like and the Sco-like sources may be partially hindered by insufficiently precise distance estimations to the six classic Z-track sources. A spectral study of the XTE J1701-462 in terms of the Extended ADC model would, in a distance-independent way, target the problem of the relation between the groups and sub-groups of LMXB and the proposition of Lin et al. (2009) that these are related to changes in mass accretion rate only.

Last but not least, the present work in the case of e.g. Cyg X-2 and Sco X-1 revealed a large potential of a combined usage of the PCA pointed observations and ASM long-term sky monitoring. The collective information about intensity, hardness-intensity and colour-colour changes in LMXB over the last 15 years of *RXTE* operations gives unprecedented insight into their behaviour in a broader context. The advantage of this could be used in the case of the other Z-track sources and also some Atoll sources with relatively high ASM count rates, to identify e.g. any datasets in which the source behaviour deviates from the standard, offering a unique possibility of better understanding Low Mass X-ray Binaries in general.

References

- Ables, J. G. 1969, *Proceedings of the Astronomical Society of Australia*, 1, 237
- Abramowicz, M., Kluzniak, W., Bursa, M., et al. 2007, in *Revista Mexicana de Astronomia y Astrofisica*, Vol. 27, 8–17
- Abramowicz, M. A., Bulik, T., Bursa, M., & Kluźniak, W. 2003, *A&A* , 404, L21
- Agrawal, V. K. & Sreekumar, P. 2003, *MNRAS*, 346, 933
- Alpar, M. A. & Shaham, J. 1985, *Natur*, 316, 239
- Anders, E. & Ebihara, M. 1982, *Geochimica et Cosmochimica Acta*, 46, 2363
- Anderson, S. F., Margon, B., Deutsch, E. W., Downes, R. A., & Allen, R. G. 1997, *ApJL*, 482, L69+
- Andrew, B. H. & Purton, C. R. 1968, *Natur*, 218, 855
- Armitage, P. J. 1998, in *Astronomical Society of the Pacific Conference Series*, Vol. 137, *Wild Stars in the Old West*, ed. S. Howell, E. Kuulkers, & C. Woodward, 294
- Armitage, P. J. & Livio, M. 1996, *ApJ*, 470, 1024
- Armitage, P. J. & Livio, M. 1998, *ApJ*, 493, 898
- Arp, H. C. 1965, in *Galactic Structure*, ed. A. Blaauw & M. Schmidt, 401
- Asai, K., Dotani, T., Mitsuda, K., et al. 1994, *PASJ*, 46, 479
- Asai, K., Dotani, T., Nagase, F., & Mitsuda, K. 2000, *ApJS*, 131, 571
- Augusteijn, T., Karatasos, K., Papadakis, M., et al. 1992, *A&A* , 265, 177
- Augusteijn, T., van der Hooft, F., de Jong, J. A., van Kerkwijk, M. H., & van Paradijs, J. 1998, *A&A* , 332, 561
- Baade, W. & Zwicky, F. 1934, *Proceedings of the National Academy of Science*, 20, 259
- Backer, D. C., Kulkarni, S. R., Heiles, C., Davis, M. M., & Goss, W. M. 1982, *Natur*, 300, 615
- Balbus, S. A. & Hawley, J. F. 1991, *ApJ*, 376, 214
- Balman, Ş. 2009, *AJ*, 138, 50
- Balucińska-Church, M., Barnard, R., Church, M. J., & Smale, A. P. 2001, *A&A* , 378, 847
- Balucińska-Church, M., Dotani, T., Hirotsu, T., & Church, M. J. 2009, *A&A* , 500, 873
- Balucińska-Church, M., Gibiec, A., Jackson, N. K., & Church, M. J. 2010, *A&A* , 512, A9+
- Balucińska-Church, M., Humphrey, P. J., Church, M. J., & Parmar, A. N. 2000, *A&A* , 360, 583
- Balucińska-Church, M., Reed, D., & Church, M. J. 2008, *Chinese Journal of Astronomy and Astrophysics Supplement*, 8, 319
- Balucińska-Church, M., Schulz, N. S., Wilms, J., et al. 2011, *A&A* , 530, A102+
- Barnard, R., Church, M. J., & Bałucińska-Church, M. 2003, *A&A* , 405, 237

- Barret, D., Kluźniak, W., Olive, J. F., Paltani, S., & Skinner, G. K. 2005a, *MNRAS*, 357, 1288
- Barret, D., McClintock, J. E., & Grindlay, J. E. 1996, *ApJ*, 473, 963
- Barret, D. & Olive, J.-F. 2002, *ApJ*, 576, 391
- Barret, D., Olive, J.-F., & Miller, M. C. 2005b, *Astronomische Nachrichten*, 326, 808
- Barret, D., Olive, J.-F., & Miller, M. C. 2006, *MNRAS*, 370, 1140
- Barret, D., Olive, J.-F., & Miller, M. C. 2007, *MNRAS*, 376, 1139
- Barziv, O., Kuulkers, E., Mendez, M., et al. 1997, *A&A* , 325, 1035
- Basinska, E. M., Lewin, W. H. G., Sztajno, M., Cominsky, L. R., & Marshall, F. J. 1984, *ApJ*, 281, 337
- Baumgartner, W. H., Tueller, J., Markwardt, C., & Skinner, G. 2010, in *Bulletin of the American Astronomical Society*, Vol. 42, AAS/High Energy Astrophysics Division #11, 675
- Bazzano, A., Cocchi, M., Ubertini, P., et al. 1997, *IAUC*, 6668, 2
- Becker, R. H., Smith, B. W., Swank, J. H., et al. 1977, *ApJL*, 216, L101
- Begelman, M. C. & McKee, C. F. 1983, *ApJ*, 271, 89
- Begelman, M. C., McKee, C. F., & Shields, G. A. 1983, *ApJ*, 271, 70
- Belian, R. D., Conner, J. P., & Evans, W. D. 1976, *ApJL*, 206, L135
- Belloni, T., Homan, J., Motta, S., Ratti, E., & Méndez, M. 2007, *MNRAS*, 379, 247
- Belloni, T., Méndez, M., & Homan, J. 2005, *A&A* , 437, 209
- Belloni, T. M. 2010, *ArXiv e-prints*
- Bildsten, L. 1993, *ApJL*, 418, L21
- Bildsten, L. 1995, *ApJ*, 438, 852
- Bildsten, L. 1998, in *NATO ASIC Proc. 515: The Many Faces of Neutron Stars.*, ed. R. Buccheri, J. van Paradijs, & A. Alpar, 419–+
- Bildsten, L. 2000, in *American Institute of Physics Conference Series*, Vol. 522, American Institute of Physics Conference Series, ed. S. S. Holt & W. W. Zhang, 359–369
- Bildsten, L., Chakrabarty, D., Chiu, J., et al. 1997, *ApJS*, 113, 367
- Bisikalo, D. V., Kaigorodov, P. V., Boyarchuk, A. A., & Kuznetsov, O. A. 2005, *Astronomy Reports*, 49, 701
- Blaauw, A. 1961, *BAIN*, 15, 265
- Blanco, V., Kunkel, W., Hiltner, W. A., et al. 1968, *ApJ*, 152, 1015
- Bloser, P. F., Grindlay, J. E., Kaaret, P., et al. 2000, *ApJ*, 542, 1000
- Boirin, L., Barret, D., Olive, J. F., Bloser, P. F., & Grindlay, J. E. 2000, *A&A* , 361, 121
- Boirin, L., Méndez, M., Díaz Trigo, M., Parmar, A. N., & Kaastra, J. S. 2005, *A&A* , 436, 195
- Boirin, L., Parmar, A. N., Barret, D., Paltani, S., & Grindlay, J. E. 2004, *A&A* , 418, 1061
- Bondi, H. 1952, *MNRAS*, 112, 195
- Bondi, H. & Hoyle, F. 1944, *MNRAS*, 104, 273
- Bonnet-Bidaud, J. M. & van der Klis, M. 1979, *A&A* , 73, 90
- Bornak, J., McNamara, B. J., Harrison, T. E., et al. 2009, *ApJL*, 701, L110
- Boutelier, M., Barret, D., Lin, Y., & Török, G. 2010, *MNRAS*, 401, 1290

- Bowyer, S., Byram, E. T., Chubb, T. A., & Friedman, H. 1965, *Science*, 147, 394
- Bradshaw, C. F., Fomalont, E. B., & Geldzahler, B. J. 1999, *ApJL*, 512, L121
- Bradt, H. V., Moore, G., Braes, L. L. E., et al. 1975, *ApJ*, 197, 443
- Bradt, H. V., Rothschild, R. E., & Swank, J. H. 1993, *A&AS*, 97, 355
- Bradt, H. V., Swank, J. H., & Rothschild, R. E. 1990, *Advances in Space Research*, 10, 297
- Bradt, H. V. D. & McClintock, J. E. 1983, *ARA&A*, 21, 13
- Braes, L. L. E., Miley, G. K., & Schoenmaker, A. A. 1972, *Natur*, 236, 392
- Breedon, L. M., Turner, M. J. L., King, A. R., & Courvoisier, T. J.-L. 1986, *MNRAS*, 218, 487
- Callanan, P. J., Curran, P., Filippenko, A. V., et al. 2002, *ApJL*, 574, L143
- Callanan, P. J., Filippenko, A. V., & Garcia, M. R. 1999, *IAUC*, 7219, 3
- Canizares, C. R. & Neighbours, J. E. 1975, *ApJL*, 199, L97
- Casares, J., Cornelisse, R., Steeghs, D., et al. 2006, *MNRAS*, 373, 1235
- Casares, J., González Hernández, J. I., Israelian, G., & Rebolo, R. 2010, *MNRAS*, 401, 2517
- Chevalier, C. & Ilovaisky, S. A. 1987, *A&A*, 172, 167
- Chou, Y. & Grindlay, J. E. 2001, *ApJ*, 563, 934
- Christian, D. J. & Swank, J. H. 1997, *ApJS*, 109, 177
- Church, M. J. 2001, *Advances in Space Research*, 28, 323
- Church, M. J. & Balucinska-Church, M. 1993, *MNRAS*, 260, 59
- Church, M. J. & Balucinska-Church, M. 1995, *A&A*, 300, 441
- Church, M. J. & Bałucińska-Church, M. 2001, *A&A*, 369, 915
- Church, M. J. & Bałucińska-Church, M. 2004, *MNRAS*, 348, 955
- Church, M. J., Balucinska-Church, M., Dotani, T., & Asai, K. 1998a, *ApJ*, 504, 516
- Church, M. J., Dotani, T., Balucinska-Church, M., et al. 1997, *ApJ*, 491, 388
- Church, M. J., Halai, G. S., & Bałucińska-Church, M. 2006, *A&A*, 460, 233
- Church, M. J., Inogamov, N. A., & Bałucińska-Church, M. 2002, *A&A*, 390, 139
- Church, M. J., Parmar, A. N., Balucinska-Church, M., et al. 1998b, *A&A*, 338, 556
- Church, M. J., Reed, D., Dotani, T., Bałucińska-Church, M., & Smale, A. P. 2005, *MNRAS*, 359, 1336
- Clark, G. W. 1975, *ApJL*, 199, L143
- Clark, G. W., Jernigan, J. G., Bradt, H., et al. 1976, *ApJL*, 207, L105
- Clark, G. W., Li, F. K., Canizares, C., et al. 1977, *MNRAS*, 179, 651
- Coe, M. J. 2000, in *Astronomical Society of the Pacific Conference Series*, Vol. 214, *IAU Colloq. 175: The Be Phenomenon in Early-Type Stars*, ed. M. A. Smith, H. F. Henrichs, & J. Fabregat, 656–+
- Cooke, B. A. & Ponman, T. J. 1991, *A&A*, 244, 358
- Corbet, S., Nowak, M. A., Fender, R. P., Tzioumis, A. K., & Markoff, S. 2003, *A&A*, 400, 1007
- Corbet, R. H. D. 1984, *A&A*, 141, 91
- Corbet, R. H. D. 1986, *MNRAS*, 220, 1047

- Cornelisse, R., Heise, J., Kuulkers, E., Verbunt, F., & in't Zand, J. J. M. 2000, *A&A* , 357, L21
- Cornelisse, R., Verbunt, F., in't Zand, J. J. M., et al. 2002, *A&A* , 392, 885
- Courvoisier, T. J.-L., Parmar, A. N., Peacock, A., & Pakull, M. 1986, *ApJ*, 309, 265
- Cowley, A. P. & Crampton, D. 1975, *ApJL*, 201, L65
- Cowley, A. P., Crampton, D., & Hutchings, J. B. 1979, *ApJ*, 231, 539
- Crampton, D., Cowley, A. P., Hutchings, J. B., & Kaat, C. 1976, *ApJ*, 207, 907
- Czerny, M. & Sztajno, M. 1983, *Acta Astronomica*, 33, 213
- D'Ai, A., di Salvo, T., Ballantyne, D., et al. 2010, *A&A* , 516, A36+
- D'Ai, A., Iaria, R., Di Salvo, T., Matt, G., & Robba, N. R. 2009, *ApJL*, 693, L1
- D'Ai, A., Życki, P., Di Salvo, T., et al. 2007, *ApJ*, 667, 411
- D'Amico, F., Heindl, W. A., Rothschild, R. E., & Gruber, D. E. 2001, *ApJL*, 547, L147
- David, P., Goldwurm, A., Murakami, T., et al. 1997, *A&A* , 322, 229
- Davidson, A., Malina, R., & Bowyer, S. 1976, *ApJ*, 203, 448
- Davidson, K. & Ostriker, J. P. 1973, *ApJ*, 179, 585
- Deutsch, E. W., Margon, B., Anderson, S. F., Wachter, S., & Goss, W. M. 1999, *ApJ*, 524, 406
- di Salvo, T., Burderi, L., Riggio, A., Papitto, A., & Menna, M. T. 2008, in *American Institute of Physics Conference Series*, ed. M. Axelsson, Vol. 1054, 173–182
- di Salvo, T., D'Ai, A., Iaria, R., et al. 2009, *MNRAS*, 398, 2022
- Di Salvo, T., Farinelli, R., Burderi, L., et al. 2002, *A&A* , 386, 535
- Di Salvo, T., Goldoni, P., Stella, L., et al. 2006, *ApJL*, 649, L91
- di Salvo, T., Iaria, R., Méndez, M., et al. 2005, *ApJL*, 623, L121
- di Salvo, T., Iaria, R., Méndez, M., et al. 2004, in *Revista Mexicana de Astronomía y Astrofísica Conference Series*, ed. G. Tovmassian & E. Sion, Vol. 20, 218–218
- Di Salvo, T., Méndez, M., & van der Klis, M. 2003, *A&A* , 406, 177
- Di Salvo, T., Méndez, M., van der Klis, M., Ford, E., & Robba, N. R. 2001, *ApJ*, 546, 1107
- Di Salvo, T., Stella, L., Robba, N. R., et al. 2000, *ApJL*, 544, L119
- Díaz Trigo, M., Parmar, A. N., Boirin, L., Méndez, M., & Kaastra, J. S. 2006, *A&A* , 445, 179
- Dicke, R. H. 1968, *ApJL*, 153, L101
- Dieters, S. W. & van der Klis, M. 2000, *MNRAS*, 311, 201
- Done, C., Gierliński, M., & Kubota, A. 2007, *The Astronomy and Astrophysics Review*, 15, 1
- Done, C., Życki, P. T., & Smith, D. A. 2002, *MNRAS*, 331, 453
- Dotani, T., Mitsuda, K., Makishima, K., & Jones, M. H. 1989, *PASJ*, 41, 577
- Ebisawa, K., Bourban, G., Bodaghee, A., Mowlavi, N., & Courvoisier, T. J.-L. 2003, *VizieR Online Data Catalog*, 3411, 19059
- Ebisuzaki, T. 1987, *PASJ*, 39, 287
- Edgar, R. 2004, *NewAR*, 48, 843
- Elvis, M., Page, C. G., Pounds, K. A., Ricketts, M. J., & Turner, M. J. L. 1975, *Natur*, 257, 656
- Ercan, E. N. 1988, *AP&SS*, 147, 145

- Ercan, E. N. & Cruise, A. M. 1984, MNRAS, 209, 271
- Fabbiano, G. 1989, ARA&A, 27, 87
- Fabian, A. C., Guilbert, P. W., & Ross, R. R. 1982, MNRAS, 199, 1045
- Falanga, M., Götz, D., Goldoni, P., et al. 2006, A&A , 458, 21
- Farinelli, R., Frontera, F., Zdziarski, A. A., et al. 2005, A&A , 434, 25
- Farinelli, R., Titarchuk, L., & Frontera, F. 2007, ApJ, 662, 1167
- Farrell, S. A., Webb, N. A., Barret, D., Godet, O., & Rodrigues, J. M. 2009, Natur, 460, 73
- Fender, R. P. 1999, ArXiv Astrophysics e-prints
- Fender, R. P., Belloni, T. M., & Gallo, E. 2004, MNRAS, 355, 1105
- Fender, R. P. & Hendry, M. A. 2000, MNRAS, 317, 1
- Fender, R. P., Roche, P., Pooley, G. G., et al. 1997, in ESA Special Publication, Vol. 382, The Transparent Universe, ed. C. Winkler, T. J.-L. Courvoisier, & P. Durouchoux, 303
- Fiocchi, M., Bazzano, A., Ubertini, P., & Jean, P. 2006, ApJ, 651, 416
- Fomalont, E. B., Geldzahler, B. J., & Bradshaw, C. F. 2001a, ApJL, 553, L27
- Fomalont, E. B., Geldzahler, B. J., & Bradshaw, C. F. 2001b, ApJ, 558, 283
- Ford, E. C., van der Klis, M., & Kaaret, P. 1998a, ApJL, 498, L41+
- Ford, E. C., van der Klis, M., van Paradijs, J., et al. 1998b, ApJL, 508, L155
- Forman, W., Jones, C., Cominsky, L., et al. 1978, ApJS, 38, 357
- Frank, J., King, A., & Raine, D. 1992, Accretion power in astrophysics., ed. Frank, J., King, A., & Raine, D.
- Frank, J., King, A., & Raine, D. J. 2002, Accretion Power in Astrophysics: Third Edition, ed. Frank, J., King, A., & Raine, D. J.
- Frank, J., King, A. R., & Lasota, J.-P. 1987, A&A , 178, 137
- Friedman, H., Byram, E. T., & Chubb, T. A. 1967, Science, 156, 374
- Galloway, D. K., Chakrabarty, D., Munro, M. P., & Savov, P. 2001, ApJL, 549, L85
- Galloway, D. K., Munro, M. P., Hartman, J. M., Psaltis, D., & Chakrabarty, D. 2008, ApJS, 179, 360
- Galloway, D. K., Psaltis, D., Chakrabarty, D., & Munro, M. P. 2003, ApJ, 590, 999
- Galloway, D. K., Psaltis, D., Munro, M. P., & Chakrabarty, D. 2006, ApJ, 639, 1033
- Galloway, D. K., Yao, Y., Marshall, H., Misanovic, Z., & Weinberg, N. 2010, ApJ, 724, 417
- Geldzahler, B. J. 1983, ApJL, 264, L49
- Giacconi, R., Gorenstein, P., Gursky, H., et al. 1967, ApJL, 148, L129+
- Giacconi, R., Gursky, H., Paolini, F. R., & Rossi, B. B. 1962, Physical Review Letters, 9, 439
- Giacconi, R., Murray, S., Gursky, H., et al. 1974, ApJS, 27, 37
- Gibiec, A., Balucinska-Church, M., & Church, M. 2011, in The X-ray Universe 2011, Presentations of the Conference held in Berlin, Germany, 27-30 June 2011, ed. J.-U. Ness & M. Ehle, 402–+
- Gierliński, M. & Done, C. 2002, MNRAS, 331, L47
- Gies, D. R. & Bolton, C. T. 1986, ApJ, 304, 371
- Goldwurm, A., Vargas, M., Paul, J., et al. 1996, A&A , 310, 857

- Gottlieb, E. W., Wright, E. L., & Liller, W. 1975, *ApJL*, 195, L33
- Grimm, H.-J., Gilfanov, M., & Sunyaev, R. 2003, *MNRAS*, 339, 793
- Grindlay, J., Gursky, H., Schnopper, H., et al. 1976, *ApJL*, 205, L127
- Grindlay, J. E., Bailyn, C. D., Cohn, H., et al. 1988, *ApJL*, 334, L25
- Grindlay, J. E., Cohn, H., & Schmidtke, P. 1987, *IAUC*, 4393, 1
- Grindlay, J. E., Hertz, P., Steiner, J. E., Murray, S. S., & Lightman, A. P. 1984, *ApJL*, 282, L13
- Grindlay, J. E., McClintock, J. E., Canizares, C. R., et al. 1978, *Natur*, 274, 567
- Grindlay, J. E. & Seaquist, E. R. 1986, *ApJ*, 310, 172
- Haardt, F., Done, C., Matt, G., & Fabian, A. C. 1993, *ApJL*, 411, L95
- Haberl, F., Stella, L., White, N. E., Gottwald, M., & Priedhorsky, W. C. 1987, *ApJ*, 314, 266
- Haberl, F. & Titarchuk, L. 1995, *A&A*, 299, 414
- Hanawa, T. & Fujimoto, M. Y. 1984, *PASJ*, 36, 199
- Hansen, C. J. & van Horn, H. M. 1975, *ApJ*, 195, 735
- Hasinger, G. 1987, in *IAU Symposium*, Vol. 125, *The Origin and Evolution of Neutron Stars*, ed. D. J. Helfand & J.-H. Huang, 333–+
- Hasinger, G., Langmeier, A., Pietsch, W., & Sztajno, M. 1985, *SSRv*, 40, 233
- Hasinger, G., Langmeier, A., Sztajno, M., Truemper, J., & Lewin, W. H. G. 1986, *Natur*, 319, 469
- Hasinger, G. & van der Klis, M. 1989, *A&A*, 225, 79
- Hasinger, G., van der Klis, M., Ebisawa, K., Dotani, T., & Mitsuda, K. 1990, *A&A*, 235, 131
- Heasley, J. N., Janes, K. A., Zinn, R., et al. 2000, *AJ*, 120, 879
- Hellier, C. & Mason, K. O. 1989, *MNRAS*, 239, 715
- Hertz, P., Vaughan, B., Wood, K. S., et al. 1992, *ApJ*, 396, 201
- Hewish, A., Bell, S. J., Pilkington, J. D. H., Scott, P. F., & Collins, R. A. 1968, *Natur*, 217, 709
- Hirano, T., Hayakawa, S., Nagase, F., & Tawara, Y. 1986, *AP&SS*, 119, 77
- Hjellming, R. & Blankenship, L. C. 1973, *Natur*, 243, 81
- Hjellming, R. M. & Han, X. 1995, in *X-ray Binaries*, ed. W. H. G. Lewin, J. van Paradijs, & E. P. J. van den Heuvel, 308–330
- Hjellming, R. M., Han, X. H., Cordova, F. A., & Hasinger, G. 1990a, *A&A*, 235, 147
- Hjellming, R. M., Stewart, R. T., White, G. L., et al. 1990b, *ApJ*, 365, 681
- Hjellming, R. M. & Wade, C. M. 1971, *ApJL*, 168, L21+
- Hoag, A. A. & Weisberg, J. M. 1976, *ApJ*, 209, 908
- Hoffman, J. A., Lewin, W. H. G., & Doty, J. 1977, *ApJL*, 217, L23
- Hoffman, J. A., Lewin, W. H. G., Doty, J., et al. 1976, *ApJL*, 210, L13
- Hoffman, J. A., Marshall, H. L., & Lewin, W. H. G. 1978, *Natur*, 271, 630
- Homan, J., Kaplan, D. L., van den Berg, M., & Young, A. J. 2009, *ApJ*, 692, 73
- Homan, J., van der Klis, M., Fridriksson, J. K., et al. 2010, *ApJ*, 719, 201
- Homan, J., van der Klis, M., Jonker, P. G., et al. 2002, *ApJ*, 568, 878
- Homan, J., van der Klis, M., Wijnands, R., et al. 2007a, *ApJ*, 656, 420

- Homan, J., Wijnands, R., Altamirano, D., & Belloni, T. 2007b, *The Astronomer's Telegram*, 1165, 1
- Homan, J., Wijnands, R., Rupen, M. P., et al. 2004, *A&A* , 418, 255
- Homer, L., Charles, P. A., Hakala, P., et al. 2001, *MNRAS*, 322, 827
- Hoyle, F. & Lyttleton, R. A. 1939, *Proceedings of the Cambridge Philosophical Society*, 35, 405
- Hynes, R. I. 2010, *ArXiv e-prints*
- Iaria, R., Lavagetto, G., Di Salvo, T., et al. 2006, *Chinese Journal of Astronomy and Astrophysics Supplement*, 6, 010000
- Inogamov, N. A. & Sunyaev, R. A. 1999, *Astronomy Letters*, 25, 269
- Inoue, H., Waki, I., Koyama, K., et al. 1984, *PASJ*, 36, 831
- in't Zand, J. J. M. 1992, PhD thesis, Space Research Organization Netherlands, Sorbonnelaan 2, 3584 CA Utrecht, The Netherlands
- in't Zand, J. J. M., Cumming, A., van der Sluys, M. V., Verbunt, F., & Pols, O. R. 2005, *A&A* , 441, 675
- Jackson, N. K., Church, M. J., & Bałucińska-Church, M. 2009, *A&A* , 494, 1059
- Jahoda, K., Swank, J. H., Giles, A. B., et al. 1996, in *Society of Photo-Optical Instrumentation Engineers (SPIE) Conference Series*, ed. O. H. Siegmund & M. A. Gummin, Vol. 2808, 59–70
- Janiuk, A. & Misra, R. 2012, *A&A* , 540, A114
- Jimenez-Garate, M. A., Raymond, J. C., & Liedahl, D. A. 2002, *ApJ*, 581, 1297
- Jones, M. H. & Watson, M. G. 1989, in *ESA Special Publication*, Vol. 296, *Two Topics in X-Ray Astronomy*, Volume 1: X Ray Binaries. Volume 2: AGN and the X Ray Background, ed. J. Hunt & B. Battrick, 439–444
- Jongert, H. C. & van der Klis, M. 1996, *A&A* , 310, 474
- Jonker, P. G., Méndez, M., & van der Klis, M. 2002, *MNRAS*, 336, L1
- Jonker, P. G., van der Klis, M., Homan, J., et al. 2001, *ApJ*, 553, 335
- Jonker, P. G., van der Klis, M., Wijnands, R., et al. 2000, *ApJ*, 537, 374
- Jonker, P. G., Wijnands, R., van der Klis, M., et al. 1998, *ApJL*, 499, L191+
- Joss, P. C. 1977, *Natur*, 270, 310
- Joss, P. C. & Rappaport, S. A. 1984, *ARA&A*, 22, 537
- Juett, A. M. & Chakrabarty, D. 2003, *ApJ*, 599, 498
- Juett, A. M., Psaltis, D., & Chakrabarty, D. 2001, *ApJL*, 560, L59
- Kaaret, P., Piraino, S., Bloser, P. F., et al. 1999, *ApJL*, 520, L37
- Kahn, S. M. & Grindlay, J. E. 1984, *ApJ*, 281, 826
- Kalberla, P. M. W., Burton, W. B., Hartmann, D., et al. 2005, *A&A* , 440, 775
- Kaminker, A. D., Pavlov, G. G., Shibanov, Y. A., et al. 1989, *A&A* , 220, 117
- Katz, J. I. 1975, *Natur*, 253, 698
- Kellogg, E., Gursky, H., Murray, S., Tananbaum, H., & Giacconi, R. 1971, *ApJL*, 169, L99
- King, A. 1995, in *X-ray Binaries*, ed. W. A. G. Lewin, J. van Paradijs, E. P. J. van den Heuvel
- King, I. R., Stanford, S. A., Albrecht, R., et al. 1993, *ApJL*, 413, L117
- Kluźniak, W. 2008, *NewAR*, 51, 841

- Kluzniak, W. & Abramowicz, M. A. 2001, ArXiv Astrophysics e-prints
- Kluzniak, W. & Abramowicz, M. A. 2002, ArXiv Astrophysics e-prints
- Kluźniak, W., Lasota, J.-P., Abramowicz, M. A., & Warner, B. 2005, *A&A* , 440, L25
- Kong, A. K. H., Charles, P. A., & Kuulkers, E. 1998, *NewA*, 3, 301
- Kulkarni, S. R. & Narayan, R. 1988, *ApJ*, 335, 755
- Kunkel, W., Osmer, P., Smith, M., et al. 1970, *ApJL*, 161, L169+
- Kuulkers, E., den Hartog, P. R., in't Zand, J. J. M., et al. 2003, *A&A* , 399, 663
- Kuulkers, E., Homan, J., van der Klis, M., Lewin, W. H. G., & Méndez, M. 2002, *A&A* , 382, 947
- Kuulkers, E. & van der Klis, M. 1996, in *Roentgenstrahlung from the Universe*, ed. H. U. Zimmermann, J. Trümper, & H. Yorke, 155–156
- Kuulkers, E., van der Klis, M., Oosterbroek, T., et al. 1994, *A&A* , 289, 795
- Kuulkers, E., van der Klis, M., & van Paradijs, J. 1995, *ApJ*, 450, 748
- Lamb, D. Q. & Lamb, F. K. 1978, *ApJ*, 220, 291
- Lamb, F. K., Shibasaki, N., Alpar, M. A., & Shaham, J. 1985, *Natur*, 317, 681
- Langmeier, A., Hasinger, G., & Truemper, J. 1989, *ApJL*, 340, L21
- Langmeier, A., Hasinger, G., & Truemper, J. 1990, *A&A* , 228, 89
- Langmeier, A., Sztajno, M., Hasinger, G., Truemper, J., & Gottwald, M. 1987, *ApJ*, 323, 288
- Lapidus, I. I., Syunyaev, R. A., & Titarchuk, L. G. 1986, *Soviet Astronomy Letters*, 12, 383
- LaSala, J. & Thorstensen, J. R. 1985, *AJ*, 90, 2077
- Lavagetto, G., di Salvo, T., Falanga, M., et al. 2006, *A&A* , 445, 1089
- Lavagetto, G., Iaria, R., di Salvo, T., et al. 2004, *Nuclear Physics B Proceedings Supplements*, 132, 616
- Lawrence, A., Cominsky, L., Engelke, C., et al. 1983, *ApJ*, 271, 793
- Leahy, D. A., Darbro, W., Elsner, R. F., et al. 1983, *ApJ*, 266, 160
- Lewin, W. H. G., Doty, J., Clark, G. W., et al. 1976, *ApJL*, 207, L95
- Lewin, W. H. G., Hoffman, J. A., Doty, J., Li, F. K., & McClintock, J. E. 1977, *IAUC*, 3075, 1
- Lewin, W. H. G., Lubin, L. M., Tan, J., et al. 1992, *MNRAS*, 256, 545
- Lewin, W. H. G. & van Paradijs, J. 1986, *Comments on Astrophysics*, 11, 127
- Lewin, W. H. G., van Paradijs, J., Cominsky, L., & Holzner, S. 1980, *MNRAS*, 193, 15
- Lewin, W. H. G., van Paradijs, J., & Taam, R. E. 1993, *SSRv*, 62, 223
- Lewin, W. H. G., van Paradijs, J., & van den Heuvel, E. P. J. 1995, *Cambridge Astrophysics Series*, 26
- Lightman, A. P. & Eardley, D. M. 1974, *ApJL*, 187, L1
- Lin, D., Remillard, R. A., & Homan, J. 2009, *ApJ*, 696, 1257
- Lin, D., Remillard, R. A., & Homan, J. 2010, *ApJ*, 719, 1350
- Liu, Q. Z., van Paradijs, J., & van den Heuvel, E. P. J. 2005, *A&A* , 442, 1135
- Liu, Q. Z., van Paradijs, J., & van den Heuvel, E. P. J. 2006, *VizieR Online Data Catalog*, 3455, 51165

- Liu, Q. Z., van Paradijs, J., & van den Heuvel, E. P. J. 2007, *VizieR Online Data Catalog*, 3469, 90807
- London, R. A., Howard, W. M., & Taam, R. E. 1984, *ApJL*, 287, L27
- Lynden-Bell, D. & Pringle, J. E. 1974, *MNRAS*, 168, 603
- Lyne, A. G., Manchester, R. N., & Taylor, J. H. 1985, *MNRAS*, 213, 613
- Madej, J. 1991, *ApJ*, 376, 161
- Mahasena, P., Inoue, H., Asai, K., & Dotani, T. 2003, *PASJ*, 55, 827
- Majczyna, A., Madej, J., Joss, P. C., & Różańska, A. 2005, *A&A*, 430, 643
- Maraschi, L. & Cavaliere, A. 1977, in *X-ray Binaries and Compact Objects*, ed. K. A. van der Hucht, 127–128
- Maraschi, L., Treves, A., & van den Heuvel, E. P. J. 1976, *Natur*, 259, 292
- Margon, B., Bowyer, S., Lampton, M., & Cruddace, R. 1971, *ApJL*, 169, L45+
- Markert, T. H., Laird, F. N., Clark, G. W., et al. 1979, *ApJS*, 39, 573
- Marshall, H. L. 1982, *ApJ*, 260, 815
- Marti, J., Mirabel, I. F., Rodriguez, L. F., & Chaty, S. 1998, *A&A*, 332, L45
- Matsuoka, M., Mitsuda, K., Ohashi, T., et al. 1984, *ApJ*, 283, 774
- McClintock, J. E., Bradt, H. V., Doxsey, R. E., et al. 1977, *Natur*, 270, 320
- McClintock, J. E. & Remillard, R. A. 1986, *ApJ*, 308, 110
- McClintock, J. E., R. R. A. 2006, in *Compact stellar X-ray Sources*, ed. W. A. G. Lewin, M. van der Klis
- Meekins, J. F., Wood, K. S., Hedler, R. L., et al. 1984, *ApJ*, 278, 288
- Méndez, M. & van der Klis, M. 1999, *ApJL*, 517, L51
- Mendez, M., van der Klis, M., Wijnands, R., et al. 1998, *ApJL*, 505, L23+
- Mereghetti, S. & Stella, L. 1995, *ApJL*, 442, L17
- Meyer, F. & Meyer-Hofmeister, E. 1982, *A&A*, 106, 34
- Middleditch, J. & Priedhorsky, W. 1985, *IAUC*, 4060, 1
- Migliari, S. & Fender, R. P. 2006, *MNRAS*, 366, 79
- Migliari, S., Fender, R. P., Rupen, M., et al. 2003, *MNRAS*, 342, L67
- Migliari, S., Fender, R. P., Rupen, M., et al. 2004, *MNRAS*, 351, 186
- Migliari, S., Miller-Jones, J. C. A., Fender, R. P., et al. 2007, *ApJ*, 671, 706
- Miller, B. W., Margon, B., & Burton, M. G. 1993, *AJ*, 106, 28
- Miller, J. M., Wijnands, R., Homan, J., et al. 2001, *ApJ*, 563, 928
- Miller, M. C., Lamb, F. K., & Psaltis, D. 1998, *ApJ*, 508, 791
- Miller-Jones, J. C. A., Sivakoff, G. R., Altamirano, D., et al. 2010, *ApJL*, 716, L109
- Mirabel, I. F. & Rodrigues, I. 2003, *A&A*, 398, L25
- Mirabel, I. F. & Rodríguez, L. F. 1994, *Natur*, 371, 46
- Mitsuda, K. & Dotani, T. 1989, *PASJ*, 41, 557
- Mitsuda, K., Inoue, H., Koyama, K., et al. 1984, *PASJ*, 36, 741

- Molkov, S., Revnivtsev, M., Lutovinov, A., & Sunyaev, R. 2005, *A&A* , 434, 1069
- Mook, D. E., Messina, R. J., Hiltner, W. A., et al. 1975, *ApJ*, 197, 425
- Morley, R., Church, M. J., Smale, A. P., & Balucinska-Church, M. 1999, *MNRAS*, 302, 593
- Morrison, R. & McCammon, D. 1983, *ApJ*, 270, 119
- Morton, D. C. 1967a, *ApJ*, 150, 535
- Morton, D. C. 1967b, *ApJ*, 147, 1017
- Mukherjee, A. & Bhattacharyya, S. 2011, *MNRAS*, 411, 2717
- Muno, M. P., Remillard, R. A., & Chakrabarty, D. 2002, *ApJL*, 568, L35
- Narita, T., Grindlay, J. E., & Barret, D. 2001, *ApJ*, 547, 420
- Narita, T., Grindlay, J. E., Bloser, P. F., & Chou, Y. 2003, *ApJ*, 593, 1007
- Nelemans, G., Jonker, P. G., Marsh, T. R., & van der Klis, M. 2004, *MNRAS*, 348, L7
- Ng, C., Díaz Trigo, M., Cadolle Bel, M., & Migliari, S. 2010, *A&A* , 522, A96+
- Norris, J. P. & Wood, K. S. 1987, *ApJ*, 312, 732
- Nyquist, H. 1928, *Trans. AIEE*, 47, 617
- Oda, M., Kahn, S., Grindlay, J., Halpern, J., & Ladd, E. 1981, *IAUC*, 3624, 1
- Ohashi, T., Inoue, H., Koyama, K., et al. 1982, *ApJ*, 258, 254
- Oosterbroek, T., Lewin, W. H. G., van Paradijs, J., et al. 1994, *A&A* , 281, 803
- Orosz, J. A. & Kuulkers, E. 1999, *MNRAS*, 305, 132
- Paczynski, B. 1974, *A&A* , 34, 161
- Paczynski, B. 1976, in *IAU Symposium, Vol. 73, Structure and Evolution of Close Binary Systems*, ed. P. Eggleton, S. Mitton, & J. Whelan, 75
- Pandel, D., Kaaret, P., & Corbel, S. 2008, *ApJ*, 688, 1288
- Parmar, A. N., White, N. E., Giommi, P., & Gottwald, M. 1986, *ApJ*, 308, 199
- Parsignault, D. R. & Grindlay, J. E. 1978, *ApJ*, 225, 970
- Pavlinisky, M. N., Grebenev, S. A., & Sunyaev, R. A. 1994, *ApJ*, 425, 110
- Pavlov, G. G., Shibanov, I. A., & Zavlin, V. E. 1991, *MNRAS*, 253, 193
- Pedersen, H., Lub, J., Inoue, H., et al. 1982, *ApJ*, 263, 325
- Pedersen, H., van Paradijs, J., & Lewin, W. H. G. 1981, *Natur*, 294, 725
- Penninx, W. 1989, in *ESA Special Publication, Vol. 296, Two Topics in X-Ray Astronomy, Volume 1: X Ray Binaries. Volume 2: AGN and the X Ray Background*, ed. J. Hunt & B. Battrick, 185–196
- Penninx, W., Lewin, W. H. G., Tan, J., et al. 1991, *MNRAS*, 249, 113
- Penninx, W., Lewin, W. H. G., Zijlstra, A. A., Mitsuda, K., & van Paradijs, J. 1988, *Natur*, 336, 146
- Penninx, W., Zwarthoed, G. A. A., van Paradijs, J., et al. 1993, *A&A* , 267, 92
- Petro, L. D., Bradt, H. V., Kelley, R. L., Horne, K., & Gomer, R. 1981, *ApJL*, 251, L7
- Petrucci, P. O., Haardt, F., Maraschi, L., et al. 2001, *ApJ*, 556, 716
- Piraino, S., Santangelo, A., di Salvo, T., et al. 2007, *A&A* , 471, L17

- Piraino, S., Santangelo, A., Ferrigno, C., et al. 2004, in ESA Special Publication, Vol. 552, 5th INTEGRAL Workshop on the INTEGRAL Universe, ed. V. Schoenfelder, G. Lichti, & C. Winkler, 369–+
- Piraino, S., Santangelo, A., & Kaaret, P. 2000, *A&A* , 360, L35
- Piraino, S., Santangelo, A., & Kaaret, P. 2003, in Astronomical Society of the Pacific Conference Series, ed. E. P. van den Heuvel, L. Kaper, E. Rol, & R. A. M. J. Wijers , Vol. 308, 291–+
- Pravdo, S. H. 1983, *ApJ*, 270, 239
- Press, W. H., Flannery, B. P., & Teukolsky, S. A. 1986, Numerical recipes. The art of scientific computing, ed. Press, W. H., Flannery, B. P., & Teukolsky, S. A.
- Priedhorsky, W., Hasinger, G., Lewin, W. H. G., et al. 1986, *ApJL*, 306, L91
- Priedhorsky, W. & Terrell, J. 1984, *ApJL*, 284, L17
- Pringle, J. E. 1981, *ARA&A*, 19, 137
- Prins, S. & van der Klis, M. 1997, *A&A* , 319, 498
- Psaltis, D., Belloni, T., & van der Klis, M. 1999, *ApJ*, 520, 262
- Psaltis, D., Lamb, F. K., & Miller, G. S. 1995, *ApJL*, 454, L137
- Radhakrishnan, V. & Srinivasan, G. 1982, *Current Science*, 51, 1096
- Rappaport, S. & van den Heuvel, E. P. J. 1982, in *IAU Symposium*, Vol. 98, *Be Stars*, ed. M. Jasek & H.-G. Groth, 327–344
- Rebusco, P. 2008, *NewAR*, 51, 855
- Reis, R. C., Fabian, A. C., & Young, A. J. 2009, *MNRAS*, 399, L1
- Remillard, R. A., Lin, D., the ASM Team at MIT, & NASA/GSFC. 2006, *The Astronomer's Telegram*, 696, 1
- Remillard, R. A., Munro, M. P., McClintock, J. E., & Orosz, J. A. 2002, *ApJ*, 580, 1030
- Retter, A., Chou, Y., Bedding, T. R., & Naylor, T. 2002, *MNRAS*, 330, L37
- Revnivtsev, M., Gilfanov, M., & Churazov, E. 2000, *A&A* , 363, 1013
- Rhoades, C. E. & Ruffini, R. 1974, *Physical Review Letters*, 32, 324
- Rozanska, A. & Czerny, B. 1996, *Acta Astronomica*, 46, 233
- Sandage, A., Osmer, P., Giacconi, R., et al. 1966, *ApJ*, 146, 316
- Savonije, G. J. 1979, *A&A* , 71, 352
- Schachter, J., Filippenko, A. V., & Kahn, S. M. 1989, *ApJ*, 340, 1049
- Schmidtke, P. C. 1988, *AJ*, 95, 1528
- Schulz, N. S., Hasinger, G., & Truemper, J. 1989, *A&A* , 225, 48
- Schulz, N. S., Huenemoerder, D. P., Ji, L., et al. 2009, *ApJL*, 692, L80
- Schwarzschild, M. & Härm, R. 1965, *ApJ*, 142, 855
- Shakura, N. I. & Sunyaev, R. A. 1973, *A&A* , 24, 337
- Shakura, N. I. & Sunyaev, R. A. 1976, *MNRAS*, 175, 613
- Shannon, C. E. 1949, *Proc. Inst. Radio Eng.*, 37, 10
- Shapiro, S. L., Lightman, A. P., & Eardley, D. M. 1976, *ApJ*, 204, 187
- Shapiro, S. L. & Teukolsky, S. A. 1983, *Black holes, white dwarfs, and neutron stars: The physics of compact objects*, ed. Shapiro, S. L. & Teukolsky, S. A.

- Shih, I. C., Bird, A. J., Charles, P. A., Cornelisse, R., & Tiramani, D. 2005, *MNRAS*, 361, 602
- Shih, I. C., Charles, P. A., & Cornelisse, R. 2011, *MNRAS*, 412, 120
- Shklovsky, I. S. 1967, *ApJL*, 148, L1+
- Skinner, G. K., Willmore, A. P., Eyles, C. J., Bertram, D., & Church, M. J. 1987, *Natur*, 330, 544
- Smak, J. 1982, *Acta Astronomica*, 32, 199
- Smak, J. 1984, *Acta Astronomica*, 34, 161
- Smale, A. P. 1998, *ApJL*, 498, L141
- Smale, A. P. & Corbet, R. H. D. 1991, *ApJ*, 383, 853
- Smale, A. P., Corbet, R. H. D., Charles, P. A., Menzies, J. W., & Mack, P. 1986, *MNRAS*, 223, 207
- Smale, A. P., Mason, K. O., White, N. E., & Gottwald, M. 1988, *MNRAS*, 232, 647
- Smale, A. P. & Mukai, K. 1988, *MNRAS*, 231, 663
- Smale, A. P., Mukai, K., Williams, O. R., Jones, M. H., & Corbet, R. H. D. 1992, *ApJ*, 400, 330
- Smale, A. P., Zhang, W., & White, N. E. 1997, *ApJL*, 483, L119+
- Soong, Y. & Rothschild, R. E. 1983, *ApJ*, 274, 327
- Steehgs, D. & Casares, J. 2002, *ApJ*, 568, 273
- Stella, L., Friedhorsky, W., & White, N. E. 1987a, *ApJL*, 312, L17
- Stella, L. & Rosner, R. 1984, *ApJ*, 277, 312
- Stella, L. & Vietri, M. 1998, *ApJL*, 492, L59
- Stella, L. & Vietri, M. 1999, *Physical Review Letters*, 82, 17
- Stella, L., White, N. E., & Friedhorsky, W. 1987b, *ApJL*, 315, L49
- Stirling, A. M., Spencer, R. E., de la Force, C. J., et al. 2001, *MNRAS*, 327, 1273
- Strickman, M. & Barret, D. 2000, in *American Institute of Physics Conference Series*, Vol. 510, American Institute of Physics Conference Series, ed. M. L. McConnell & J. M. Ryan, 222–226
- Strohmayer, T. Bildsten, L. 2006, in *Compact stellar X-ray Sources*, ed. W. A. G. Lewin, M. van der Klis
- Strohmayer, T. E. 2001a, *ApJL*, 552, L49
- Strohmayer, T. E. 2001b, *ApJL*, 554, L169
- Strohmayer, T. E. & Brown, E. F. 2002, *ApJ*, 566, 1045
- Strohmayer, T. E., Zhang, W., Swank, J. H., & Lapidus, I. 1998a, *ApJL*, 503, L147
- Strohmayer, T. E., Zhang, W., Swank, J. H., et al. 1996, *ApJL*, 469, L9+
- Strohmayer, T. E., Zhang, W., Swank, J. H., White, N. E., & Lapidus, I. 1998b, *ApJL*, 498, L135
- Suleimanov, V., Poutanen, J., & Werner, K. 2011, *A&A*, 527, A139
- Sunyaev, R. A. & Titarchuk, L. G. 1980, *A&A*, 86, 121
- Suzuki, K., Matsuoka, M., Inoue, H., et al. 1984, *PASJ*, 36, 761
- Swank, J. H. 2006, *Advances in Space Research*, 38, 2959
- Swank, J. H., Becker, R. H., Boldt, E. A., et al. 1977, *ApJL*, 212, L73
- Swank, J. H., Becker, R. H., Pravdo, S. H., Saba, J. R., & Serlemitsos, P. J. 1976, *IAUC*, 3000, 5

- Sztajno, M., van Paradijs, J., Lewin, W. H. G., et al. 1986, MNRAS, 222, 499
- Sztajno, M., van Paradijs, J., Lewin, W. H. G., et al. 1985, ApJ, 299, 487
- Tananbaum, H., Gursky, H., Kellogg, E., & Giacconi, R. 1971, ApJL, 168, L25+
- Tarengi, M. & Reina, C. 1972, Natur, 240, 53
- Tarter, C. B., Tucker, W. H., & Salpeter, E. E. 1969, ApJ, 156, 943
- Tauris, T. M., v. P. J. 2006, in Compact stellar X-ray Sources, ed. W. A. G. Lewin, M. van der Klis
- Tawara, Y., Hirano, T., Kii, T., Matsuoka, M., & Murakami, T. 1984, PASJ, 36, 861
- Titarchuk, L. 1994, ApJ, 434, 570
- Tjemkes, S. A., van Paradijs, J., & Zuiderwijk, E. J. 1986, A&A , 154, 77
- Truemper, J., Sztajno, M., Pietsch, W., van Paradijs, J., & Lewin, W. H. G. 1985, SSRv, 40, 255
- Trümper, J., Pietsch, W., Reppin, C., et al. 1978, ApJL, 219, L105
- Tsuruta, S., Canuto, V., Lodenquai, J., & Ruderman, M. 1972, ApJ, 176, 739
- Tudose, V., Fender, R. P., Linares, M., Maitra, D., & van der Klis, M. 2009, MNRAS, 400, 2111
- Turner, M. J. L. & Breedon, L. M. 1984, MNRAS, 208, 29P
- Turner, M. J. L., Breedon, L. M., Ohashi, T., Courvoisier, T., & Inoue, H. 1985, SSRv, 40, 249
- Šimon, V. 2003, A&A , 405, 199
- Vacca, W. D., Sztajno, M., Lewin, W. H. G., et al. 1987, A&A , 172, 143
- van Amerongen, S., van Paradijs, J., & Pedersen, H. 1987, A&A , 185, 147
- van der Klis, M. 1989, ARA&A, 27, 517
- van der Klis, M. 1995, in X-ray Binaries, ed. W. A. G. Lewin, J. van Paradijs, E. P. J. van den Heuvel
- van der Klis, M. 2000, ARA&A, 38, 717
- van der Klis, M. 2004, ArXiv Astrophysics e-prints
- van der Klis, M. 2005, Astronomische Nachrichten, 326, 798
- van der Klis, M., Hasinger, G., Damen, E., et al. 1990, ApJL, 360, L19
- van der Klis, M., Jansen, F., van Paradijs, J., et al. 1987, ApJL, 313, L19
- van der Klis, M., Jansen, F., van Paradijs, J., et al. 1985, Natur, 316, 225
- van der Klis, M., Swank, J. H., Zhang, W., et al. 1996, ApJL, 469, L1
- van der Klis, M., Wijnands, R. A. D., Horne, K., & Chen, W. 1997, ApJL, 481, L97+
- van Paradijs, J. 1978, Natur, 274, 650
- van Paradijs, J., Allington-Smith, J., Callanan, P., et al. 1990a, A&A , 235, 156
- van Paradijs, J., Hasinger, G., Lewin, W. H. G., et al. 1988a, MNRAS, 231, 379
- van Paradijs, J. & McClintock, J. E. 1994, A&A , 290, 133
- van Paradijs, J., Penninx, W., Lewin, W. H. G., Sztajno, M., & Truemper, J. 1988b, A&A , 192, 147
- van Paradijs, J., Sztajno, M., Lewin, W. H. G., et al. 1986, MNRAS, 221, 617
- van Paradijs, J., van der Klis, M., van Amerongen, S., et al. 1990b, A&A , 234, 181

- van Straaten, S., van der Klis, M., di Salvo, T., & Belloni, T. 2002, *ApJ*, 568, 912
- van Straaten, S., van der Klis, M., & Méndez, M. 2003, *ApJ*, 596, 1155
- van Straaten, S., van der Klis, M., & Wijnands, R. 2005, *ApJ*, 619, 455
- Verbunt, F. & Hut, P. 1987, in *IAU Symposium*, Vol. 125, *The Origin and Evolution of Neutron Stars*, ed. D. J. Helfand & J.-H. Huang, 187–+
- Verbunt, F., v. E. P. J. 1995, in *X-ray Binaries*, ed. W. A. G. Lewin, J. van Paradijs, E. P. J. van den Heuvel
- Vrtilek, S. D., Kahn, S. M., Grindlay, J. E., Seward, F. D., & Helfand, D. J. 1986, *ApJ*, 307, 698
- Vrtilek, S. D., Penninx, W., Raymond, J. C., et al. 1991, *ApJ*, 376, 278
- Vrtilek, S. D., Raymond, J. C., Garcia, M. R., et al. 1990, *A&A* , 235, 162
- Wachter, S. & Margon, B. 1996, *AJ*, 112, 2684
- Walter, F. M., Mason, K. O., Clarke, J. T., et al. 1982, *ApJL*, 253, L67
- Walter, R., Zurita Heras, J., Bassani, L., et al. 2006, *A&A* , 453, 133
- Waters, L. B. F. M., van den Heuvel, E. P. J., Taylor, A. R., Habets, G. M. H. J., & Persi, P. 1988, *A&A* , 198, 200
- Waters, L. B. F. M. & van Kerkwijk, M. H. 1989, *A&A* , 223, 196
- Webbink, R. F., Rappaport, S., & Savonije, G. J. 1983, *ApJ*, 270, 678
- White, N. E., Becker, R. H., Boldt, E. A., et al. 1981, *ApJ*, 247, 994
- White, N. E., Parmar, A. N., Sztajno, M., et al. 1984, *ApJL*, 283, L9
- White, N. E., Peacock, A., Hasinger, G., et al. 1986, *MNRAS*, 218, 129
- White, N. E., Peacock, A., & Taylor, B. G. 1985, *ApJ*, 296, 475
- White, N. E., Stella, L., & Parmar, A. N. 1988, *ApJ*, 324, 363
- White, N. E. & Swank, J. H. 1982, *ApJL*, 253, L61
- White, N. E., N. F. P. A. N. 1995, in *X-ray Binaries*, ed. W. A. G. Lewin, J. van Paradijs, E. P. J. van den Heuvel
- Whitehurst, R. 1988, *MNRAS*, 232, 35
- Wijnands, R. 2001, *Advances in Space Research*, 28, 469
- Wijnands, R., Homan, J., van der Klis, M., et al. 1998, *ApJL*, 493, L87+
- Wijnands, R. & van der Klis, M. 1998a, *Natur*, 394, 344
- Wijnands, R. & van der Klis, M. 1998b, in *American Institute of Physics Conference Series*, ed. S. S. Holt & T. R. Kallman, Vol. 431, 381–384
- Wijnands, R. & van der Klis, M. 1999, *ApJ*, 514, 939
- Wijnands, R., van der Klis, M., Homan, J., et al. 2003, *Natur*, 424, 44
- Wijnands, R. A. D. & van der Klis, M. 1997, *ApJL*, 482, L65
- Wijnands, R. A. D., van der Klis, M., Kuulkers, E., Asai, K., & Hasinger, G. 1997, *A&A* , 323, 399
- Wijnands, R. A. D., van der Klis, M., van Paradijs, J., et al. 1996, *IAUC*, 6447, 1
- Willis, A. J., Wilson, R., vanden Bout, P., et al. 1980, *ApJ*, 237, 596
- Willmore, A. P., Mason, K. O., Sanford, P. W., et al. 1974, *MNRAS*, 169, 7
- Wilms, J., Allen, A., & McCray, R. 2000, *ApJ*, 542, 914

Wilson, C. A., Patel, S. K., Kouveliotou, C., et al. 2003, *ApJ*, 596, 1220

Woosley, S. E. & Taam, R. E. 1976, *Natur*, 263, 101

Xiang, J., Lee, J. C., Nowak, M. A., Wilms, J., & Schulz, N. S. 2009, *ApJ*, 701, 984

Yokogawa, J., Imanishi, K., Tsujimoto, M., Koyama, K., & Nishiuchi, M. 2003, *PASJ*, 55, 161

Yoshida, K., Inoue, H., Mitsuda, K., Dotani, T., & Makino, F. 1995, *PASJ*, 47, 141

Zdziarski, A. A., Gierliński, M., Wen, L., & Kostrzewa, Z. 2007, *MNRAS*, 377, 1017

Zhang, G., Méndez, M., Altamirano, D., Belloni, T. M., & Homan, J. 2009, *MNRAS*, 398, 368

Zhang, W., Jahoda, K., Swank, J. H., Morgan, E. H., & Giles, A. B. 1995, *ApJ*, 449, 930

Zhang, W., Lapidus, I., Swank, J. H., White, N. E., & Titarchuk, L. 1997, *IAUC*, 6541, 1

Zhang, W., Smale, A. P., Strohmayer, T. E., & Swank, J. H. 1998, *ApJL*, 500, L171+

Zhong, J. & Wang, Z. 2011, *ApJ*, 729, 8

Appendix A

A guide to *RXTE* data analysis

A detailed overview of the *RXTE* data analysis procedure is given below with an emphasis on topics most relevant to the present work. The original and most up-to-date information on data analysis issues is available on-line at the mission-dedicated site (<http://heasarc.gsfc.nasa.gov>).

A.1 Data retrieving and organization

RXTE observational data are archived by the NASA's Goddard Space Flight Center. A single *RXTE* pointed observation consists of a number of sub-observations with time gaps between them resulting from e.g. restrictions related to the orbital motion of the satellite. Raw data consist of housekeeping data and scientific data.

Housekeeping data provide information about conditions under which an observation took place. Based on them, screening criteria can be applied to raw data to select only Good Time Intervals (GTI) of the observation (below) useful for scientific purposes.

PCA scientific data are organized in several different ways (modes) depending on a purpose of usage and are described in Table A.1. Most often used are Standard2 data which have a time binning of 16 seconds and are collected in 129 spectral channels in the energy range from 1 keV to 100 keV (nominally). Standard1 data are useful for a deadtime correction of PCA spectra or for the extraction of lightcurves when a better (than 16 s) time resolution of 0.125 second is needed (e.g. for an analysis of X-ray bursts). Single Bit data, Event mode data and Good Xenon data are typically used for timing analyses given their very fine time resolution of 125 μ s or better.

Table A.1: PCA most commonly used data modes and their properties.

Data mode	Time resolution	Energy resolution	Usability
Standard1	0.125 s	no	deadtime correction, lightcurves
Standard2	16 s	129 channels	lightcurves and spectra
Event	$\leq 125 \mu\text{s}$	yes, depends on configuration	timing and spectral analysis
Single Bit	$\leq 125 \mu\text{s}$	no	timing analysis
Good Xenon	$1 \mu\text{s}$	256 channels	timing and spectral analysis

A.2 The analysis procedure

RXTE X-ray data analysis is performed using a dedicated, multi-mission software *HEASOFT*. Information about the calibration issues of the X-ray detectors (PCA and HEXTE) is incorporated within the calibration database *CALDB* which is accessed by the software during the analysis. A set of standard analysis tools is available within *FTOOLS*, their names are highlighted with SMALL CAPITALS throughout the text in this work. All these facilities were maintained and improved during the mission.

In the first step of the analysis procedure, housekeeping data from every particular sub-observation are filtered with *XTEFILT* to retrieve entries for the most important parameters of an observation, a list of which may be reviewed using *FLCOL*. Filtered housekeeping data from individual sub-observations are next merged into a single 'filter file' of the observation using *FMERGE*.

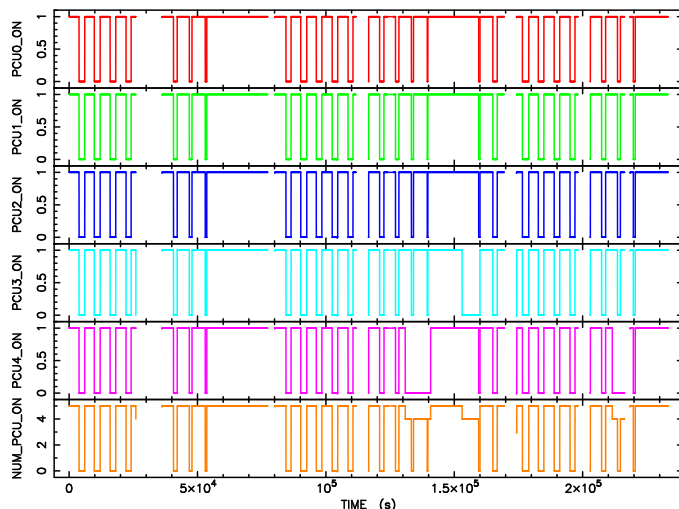


Figure A.1: An example of operations of the five PCU detectors on-board *RXTE* (five top panels) and the total number of PCU on (bottom panel).

The filter file can then be examined by plotting a given housekeeping parameter versus time. Fig. A.1 shows an example of the performance of the PCU detectors during an *RXTE* observation based on parameters `PCUn_ON`, where $n=0,\dots,4$ is the detector number. `PCUn_ON` is 0 if the n -th PCU is not operational at a given time and 1 otherwise. The bottom panel of Fig. A.1 shows the total number of the PCU that are operational (parameter `NUM_PCU_ON`). For the analysis, one wishes to choose the largest number of PCU possible that offer relatively full coverage of the observation. Other most commonly considered parameters are shown in the example in Fig. A.2. The angular distance from the Earth's limb (top panel) is given by the `ELV` parameter. For the purpose of spectral analysis, it is recommended to avoid satellite pointing close to the Earth's atmosphere as it absorbs mostly low energy X-rays leading to unwanted spectral distortions. The pointing of the satellite with respect to the target is provided by the `OFFSET` parameter (second panel from top). Its value is usually close to 0 with negligible deviations due to the HEXTE rocking mechanism.

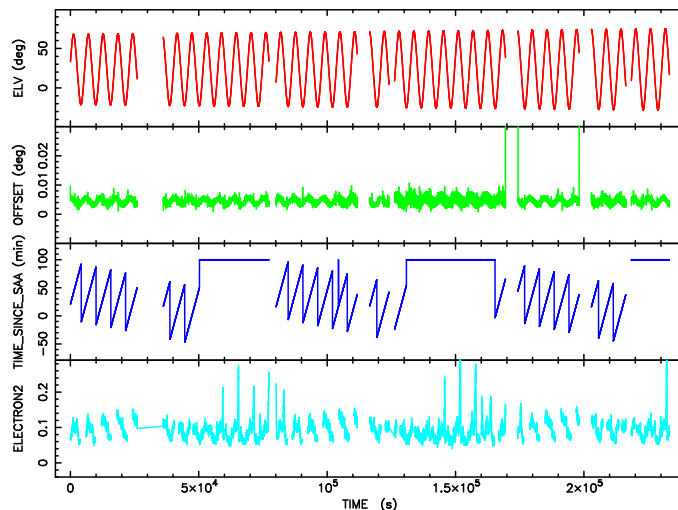


Figure A.2: Example variations of standard housekeeping parameters which are examined in order to choose screening conditions.

However, occasional periods of satellite's slew motions must be filtered out. The time from the last passage close to the South Atlantic Anomaly (SAA) is given by the `TIME_SINCE_SAA` parameter (second panel from bottom). The SAA corresponds to an area in which the inner van Allen belt reaches closest to the Earth. Up to about 30 minutes after the last SAA passage of the satellite the background noise due to trapped particles is increased which is unwanted when studying faint sources. Electron noise (parameters `ELECTRONn`, with $n=0,\dots,4$) can be reviewed for any periods of unusually high background levels resulting from electrons coming from a solar flare or the Earth's magnetosphere (bottom panel shows an example for PCU 2). The most common screening criteria

involving the parameters mentioned above are listed in Table A.2. Applying these criteria in MAKETIME leaves only Good Time Intervals (GTI) of the observation free of unwanted effects that would otherwise contaminate scientific products.

Table A.2: The *RXTE* standard screening criteria used to obtain Good Time Intervals.

Parameter	Meaning	Condition
PCUn_ON	operationality of a PCU detector	usually a maximum number of PCU that are available is used to get best signal to noise ratio
ELECTRONn	instrumental noise level	ELECTRON2 < 0.1 (for faint sources)
TIME_SINCE_SAA	distance to the South Atlantic Anomaly	TIME_SINCE_SAA > 30.0 or TIME_SINCE_SAA < 0.0 (for faint sources)
ELV	elevation above the Earth's limb	ELV > 10
OFFSET	deviation from the nominal target	OFFSET < 0.02

In the case of the PCA, background information is not obtained during an observation. Instead, the PCA team provides mission-long background models that are often improved and updated. Currently, two background models are available: the bright model - `pca_bkgd_cmbrightvle_eMv20051128.mdl` and the faint model - `pca_bkgd_cmfaint17_eMv20051128.mdl`. Thus, for a given set of Standard2 data, a relevant set of background Standard2 modelled data can be generated using PCABACKEST and one of the background models.

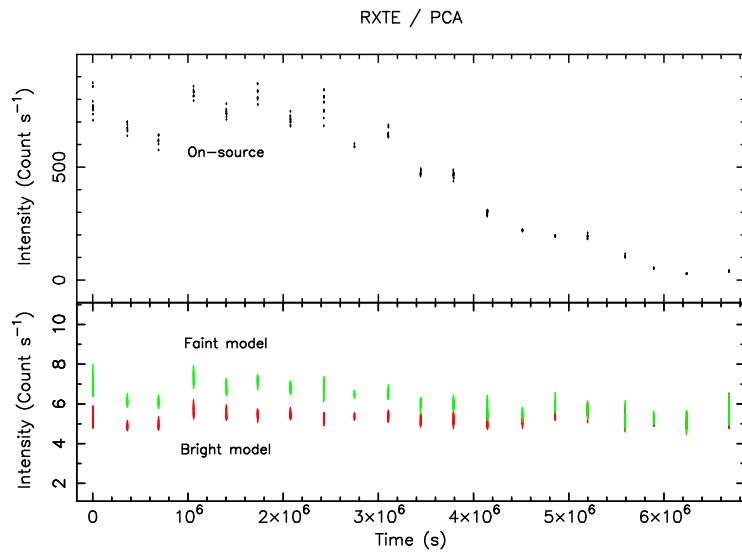


Figure A.3: An example comparison of the bright and the faint PCA background models in terms of the total count rate per PCU.

Fig. A.3 shows an example comparison of the two background solutions depending on a count rate of a source. In the Figure shown is an on-source (source plus background) lightcurve (upper panel) whose count rate decreases in time from about 900 to 30 count s^{-1} PCU $^{-1}$. In the lower panel, the corresponding background lightcurves are compared revealing a difference between the background solutions and it can be seen that the higher the count rate the larger the difference. As recommended by mission specialists, the bright background model should be used for sources whose count rate is above 40 count s^{-1} PCU $^{-1}$.

PCA lightcurves are extracted in SAEXTRACT which works on on-source data and background data, separately. A number of parameters can be chosen in the process as described below. Each PCU detector consists of several layers that are further divided into two halves, left and right. The most common choice for the extraction of scientific products is the top, left and right layer only (LR1), given its best signal to noise quality, as it detects about 90% of photons and 50% of noise events. The tool SAEXTRACT allows also for a choice of a time bin for the lightcurve. The default and minimal option with Standard2 data is 16 seconds, but this can be increased to any multiple of 16, such as 64 seconds which is commonly done to improve quality. Finally, it is possible to choose an energy range of interest by selecting a minimal and maximal energy channel to be used in extraction. Standard2 data have 129 energy channels and a choice is made based on the channel-to-energy conversion table given by mission specialists at http://heasarc.nasa.gov/docs/xte/e-c_table.html. The conversion used should be appropriate to the *RXTE* calibration epoch of an observation. Lightcurves are then typically produced in several energy bands. Table A.3 summarizes the information regarding the *RXTE* calibration epochs and the channel-to-energy conversion scheme used conventionally in this work.

Table A.3: The *RXTE* calibration epochs and corresponding channel-to-energy conversion schemes.

Epoch	Period	Energy bands / Standard2 channels		
		Low (1.9 - 4.1 keV)	Medium (4.1 - 7.3 keV)	High (7.3 - 18.5 keV)
1	up to March 21, 1996	6 - 14	15 - 27	28 - 69
2	March 21, 1996 - April 15, 1996	6 - 12	13 - 23	24 - 59
3	April 15, 1996 - March 22, 1999	5 - 10	11 - 19	20 - 50
4	March 22, 1999 - May 13, 2000	5 - 9	10 - 17	18 - 43
5	May 13, 2000 - now	5 - 9	10 - 17	18 - 44

The loss of the propane layer by PCU 0 defined the beginning of epoch 5, and hence for this epoch the information given relates to PCU 1 - 4 only.

Having extracted on-source and background lightcurves, background subtraction is performed in

LCMATH. The tool subtracts the background count rate from the on-source count rate taking into account any differences in the exposure time between the two lightcurves. Low, medium and high background-subtracted lightcurves can be then used together in LCURVE which can produce the summed intensity (the total lightcurve) and hardness ratios (high/medium, medium/low and high/low). These products are next used to obtain hardness-intensity or colour-colour variations of a source.

A.3 Data selections and spectra

Data selections can be made by specifying criteria on e.g. hardness and intensity. For instance, a rectangular selection having a size of $100 \text{ count s}^{-1} \times 0.02$ in intensity and hardness, respectively, could be defined by example conditions: $200 < \text{Intensity} < 300$ and $0.20 < \text{Hardness} < 0.22$. Such conditions, typically for a number of data selections, are then used in MAKETIME to produce the corresponding GTI. Spectra can then be extracted for each data selection individually using SAEXTRACT in a similar way as was described earlier in the case of lightcurves. In this case, however, no energy filtering is done and all 129 Standard2 spectral channels are used, while the energy band selection is made later at the stage of spectral fitting.

The on-source spectrum is deadtime-corrected following a mission-specific procedure described in Sect. A.4.1. An appropriate response file for the PCA is produced using PCARSP in which a choice of particular PCU detectors and their layers is possible to match the combination used for the extraction of spectra. The response file incorporates the redistribution matrix file (RMF) and the auxiliary response file (ARF) of the instrument. The redistribution matrix file is a map between energy and pulse amplitudes of recorded events, whereas the auxiliary response file gives the effective area and the quantum efficiency as functions of event energy. Any remaining calibration uncertainties are taken into account in GRPPHA by adding systematic errors of typically 0.5 - 1% to spectral channels as recommended by mission specialists. The same tool can be used to group energy channels if needed which is common at higher energies to improve signal to noise ratio.

In the case of HEXTE, two separate detector clusters are available: A and B (or 0 and 1), each carrying 4 detectors (although detector 3 in Cluster B failed early in the mission), see Sect. 1.5.2 for a detailed description of the instrument. The extraction of spectra is handled by the instrument-specific script HXTLCURV. The script uses selection GTI (the same ones as used for the PCA spectra) together with a housekeeping data file (present in every sub-observation) and

the standard deadtime coefficients file provided by mission specialists (hxtdead_200002_pwa.fits and hxtdead_200002_pwb.fits for Cluster A and B, respectively). HXTLCURV produces a set of on-source and off-source (background) spectra for each sub-observation separately. If the selection GTI span over more than one sub-observation, then spectra from all sub-observations are combined in SUMPHA to obtain a single on-source and background spectrum per data selection. In the case of HEXTE, background information is gathered during an observation thanks to the special rocking mechanism of the satellite (described in 1.5.2). No systematic errors are applied in this case, and an additional channel grouping can be applied in GRPPHA.

The performance of HEXTE is considered to be quite stable over the mission time and hence the standard response files (RMF and ARF files) provided by mission specialists are commonly used. These are hexte_97mar20c_pwa.rmf and hexte_00may26_pwa.arf (for Cluster A), and (for Cluster B) hexte_97mar20c_pwb013.rmf and hexte_00may26_pwb013.arf. They have 256 spectral channels and must be re-binned in order to match the 64 channel pattern of a HEXTE spectrum. The tool RDDESCR is used to find the channel pattern of the spectrum and then RBNRMF applies this pattern to the response file. Alternatively, the tool HXRSP can be used to produce a single response file incorporating both the RMF and the ARF files with a proper channel pattern.

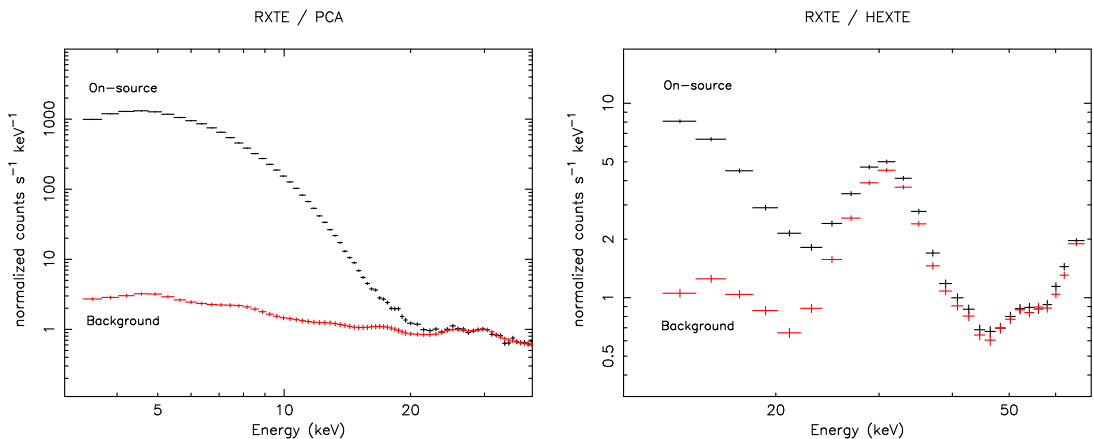


Figure A.4: A comparison of on-source and background spectra in the case of PCA (left) and HEXTE (right).

A comparison of example on-source and background spectra in the case of the PCA and the HEXTE is shown in Fig. A.4. In this example background becomes important at energies of about 20 - 30 keV and 40 - 60 keV in the case of the PCA and the HEXTE, respectively. This is taken into account when defining the useful upper energy limits of the two instruments for spectral fitting. The typical lower energy limits are 3.0 keV (PCA) and 18.0 keV (HEXTE) below which the instruments are poorly calibrated and the effective area small.

A.4 Corrections

A.4.1 Deadtime

Any detector, having recorded an event (e.g. an incoming photon), needs a small instant of time to 'recover' its detecting capabilities before it is able to detect another event. This recovery time is called deadtime and must be corrected for as it causes that the observed count rate is smaller than the real one. The correct count rate is then related to the observed one in the following way

$$I_r = \frac{I_o}{1 - DTF}, \quad (\text{A.1})$$

where I_r and I_o are the real and observed intensities, respectively, and DTF is a deadtime factor. In the case of the PCA, two types of events that can cause deadtime are technically distinguished: very large events (VLE) and other (nonVLE) which include: good xenon events (good data), coincident events (detected in more than one anode simultaneously, most likely due to particles but can also be caused by two real photons) and propane events (detected in a propane layer in front of the main xenon detection layer). The correction procedure involves extraction of lightcurves (per each PCU) from these types of events using Standard1 data as these have a better time resolution (1/125 s) than Standard2 data (16 s). As both nonVLE and VLE events contribute to the deadtime effect, DTF is calculated as follows

$$DTF = \frac{1.0 \times 10^{-5} I_{\text{nonVLE}}}{N} + \frac{1.5 \times 10^{-4} I_{\text{VLE}}}{N}, \quad (\text{A.2})$$

where I_{nonVLE} and I_{VLE} are the intensities obtained from nonVLE and VLE events, respectively, and N is the number of PCU detectors that were operational during an observation. The values 1.0×10^{-5} and 1.5×10^{-4} correspond to estimated deadtimes in the case of nonVLE (10 μs) and VLE (150 μs) events, respectively. The whole procedure is incorporated into scripts that can perform the correction on lightcurves and spectra.

A.4.2 Pulse pile-up

At extreme count rates, more than a single photon can be detected simultaneously by an instrument leading to erroneous information regarding e.g. energy of an event. The effect is known as pulse pile-up and must be taken into account when analysing bright sources (such as Sco X-1 in this work). The pile-up correction is performed on a deadtime-corrected spectrum. A

mission-specific script follows the procedure described by Tomsick & Kaaret (1998) (unpublished, see http://www.universe.nasa.gov/xrays/programs/rxte/pca/tomsick_98.pdf). The procedure assumes that PCA deadtime-corrected count rate in a given energy bin i (one of N bins) is A_i , the time window for an occurrence of pulse pile-up is τ (known to be $1.84 \mu\text{s}$) and the count rate after the pile-up correction is B_i . Then B_i is

$$B_i = A_i - \tau \sum_{k=1}^{i-1} A_k A_{i-k} + 2\tau A_i \sum_{k=0}^N A_k. \quad (\text{A.3})$$

The first term is simply the originally recorded count rate (deadtime-corrected), the second term corrects for counts which were added to given channels due to pile-up and the third term deals with those removed from spectral channels due to this effect.

A.4.3 Pointing offset

In the case of some sources (e.g. Sco X-1) a non-zero pointing offset is often applied during an *RXTE* observation. This means that the satellite is not looking directly at a source, but slightly next to it, and the position difference is called the pointing offset. This is done to avoid any potential damage to the instruments due to high count rate of the source. This affects mostly flux and hence also spectral results, e.g. normalizations of model components. To counteract, it is first necessary to find the real sky position of a source and use FMODHEAD to imprint the real source coordinates in the header of a spectral file. Having done these, a response file can be generated as usually. In the process, new coordinates are compared with the actual satellite's pointing (stored in housekeeping data) and the difference is taken into account in the response file.

A.5 Power spectra and timing analysis

A.5.1 Signal decomposition

A search for any periodicities in a lightcurve of a source is usually done by means of the Fourier Transform and its numerical implementations (e.g. Press et al. 1986). Any time-binned lightcurve may be a subject to such an analysis in which Fourier coefficients are derived based on the formula

$$a_j = \sum_{k=0}^{N-1} x_k \exp(2\pi k j/N), \quad (\text{A.4})$$

where x_k are values of intensity in a k -th bin of the lightcurve. Squared Fourier coefficients a_j^2

are proportional to the power of emission at a j -th frequency bin giving a power spectrum (Leahy et al. 1983). The Fourier power spectra are limited to the Nyquist frequency which is $\nu_N = \nu_{max}/2$ and $\nu_{max} = 1/T$, where T is the length of the lightcurve. This corresponds to the Nyquist theorem (Nyquist 1928; Shannon 1949) which stands that a study of a signal with the period P requires original data with at least twice as good time resolution as P itself.

A.5.2 Preparation of PCA data

A typical analysis involves producing a power spectrum from GTI applied to raw data. First, each good time interval of a selection must be expressed in relation to the beginning of a given raw data file and ‘relative GTI’ are calculated. Next, the relative GTI can be applied in GROSSTIMEFILT tool which extracts only these good data from original raw data.

High time resolution PCA data are recorded in several data modes listed in Table A.1. During a particular observation, only several of such modes are being used (depending on the principal investigator’s choice and observation objectives).

In the case of Single Bit data (with no energy resolution) the procedure is concluded by selecting raw data based on relative GTI as described above. Selected Single Bit data can then be used directly for the production of power spectra. In the case of Event Mode data the procedure involves further screening on energy. This is particularly useful when one needs to examine QPO dependence on energy, also rejection of very low and very high energies is usually beneficial for a signal to noise ratio. An energy range of interest must be translated into spectral channels relevant to the Event mode. To do this, it is first required to extract a spectrum from Event mode data using SEEXTRCT which works in a very similar way as SAEXTRCT on Standard2 data. Also a response file can be produced in PCARSP as described earlier using the spectrum file and the observation filter file. Next, the spectrum and its response are used in *Xspec* to determine the energy-to-channel relation. Having chosen the energy channels, an energy filter is prepared in SEBITMASK, which translates the channel (energy) range of interest into a binary code (a bitmask). The application of the bitmask to the raw data files is next done in FSELECT which gives final, energy-filtered Event mode data files.

A.5.3 Producing power spectra

Prepared Single Bit and/or Event Mode data files for a given data selection can be read into POWSPEC to produce a power spectrum. The original time resolution may be changed into any

of its multiples, depending on the frequency range of interest (following the Nyquist theorem, as above). Before doing calculations, POWSPEC divides the original lightcurve into shorter intervals and performs a Discrete Fourier Transform for each interval separately. An interval length T allows determination of the frequency resolution $\Delta\nu = 1/T$ which is also equal to the value of the lowest frequency bin in the output power spectrum. The longer the intervals the finer the resolution in the final power spectrum but also the larger the errors on power in individual frequency bins, so the best choice (to be found by trial and error) should be a compromise between the two subtleties. Then, POWSPEC averages individual power spectra into a single final product (a frame), although the user may choose to obtain more than one frame, averaging parts of data into particular frames, separately, but each having a lower signal to noise. An additional re-binning option (into geometrical series or arithmetical series) is available. A final power spectrum is normalized and the default option is the normalization after Leahy et al. (1983)

$$P_j = \frac{2|a_j|^2}{N_{\text{ph}}}, \quad (\text{A.5})$$

where N_{ph} is the total number of photons. With this normalization the Poisson white noise level has a power of 2. However, a few other normalization options are available, including those in which the white noise level can be automatically subtracted if needed.

A.5.4 Conversion into an *Xspec*-usable format

A very useful approach is to convert a POWSPEC product (a power spectrum with the `.fps` extension) into a file with the `.pha` extension which allows fitting the power spectrum in *Xspec* in the same way as in a typical spectral analysis. The conversion involves creating two new columns (minimal and maximal frequency of a frequency bin) to be added to the FITS file of the original power spectrum which is handled with FCALC. The header information must be deleted which is performed with FDUMP, and preserved are only the columns wanted: power, error, frequency_min ($\nu - \frac{1}{2}\Delta\nu$) and frequency_max ($\nu + \frac{1}{2}\Delta\nu$). This gives an ascii table of numbers which can be then converted into a '.pha' file in FLX2XSP which also generates a corresponding response file necessary in *Xspec*, determining the channel-to-frequency relation, which is in this case a unit matrix and does not modify the power spectrum in any way. The procedure described here allows then to perform fitting of a power spectrum using a rich model database of *Xspec*.

Appendix B

Attached papers

B.1 *A model for the Z-track phenomenon, jet formation and the kilohertz QPO based on Rossi-XTE observations of the Z-track sources*

Church, M. J., Bałucińska-Church, M., Jackson, N. K., **Gibiec, A.** 2008

Proceeding of the 'Microquasars and Beyond 2008' workshop, Turkey, held in Foca, Izmir, Turkey, September 1-5, 2008

available on-line at <http://pos.sissa.it/cgi-bin/reader/conf.cgi?confid=62>

B.2 *On the nature of the Cygnus X-2 like Z-track sources*

Bałucińska-Church, M., **Gibiec, A.**, Jackson, N. K., Church, M. J. 2010

Astronomy & Astrophysics, vol. 512, p. A9

B.3 *The nature of the Cygnus X-2 like Low Mass X-ray Binaries*

Gibiec, A., Bałucińska-Church, M., Church, M. J. 2010

Poster presentation at the '38th COSPAR Scientific Assembly'

held in Bremen, Germany, July 18-25, 2010

paper number E13-0060-10

B.4 *On the nature of the Z-track in GX 17+2*

Gibiec, A., Church, M. J., Bałucińska-Church, M., Burke, M. 2010

Poster presentation at the '38th COSPAR Scientific Assembly'

held in Bremen, Germany, July 18-25, 2010

paper number E13-0053-10

B.5 *Dipping in Cygnus X-2 in a multi-wavelength campaign due to absorption of extended ADC emission*

Bałucińska-Church, M., Schulz, N. S., Wilms, J., **Gibiec, A.**, Hanke, M., Spencer, R. E.,

Rushton, A., Church, M. J. 2011

Astronomy & Astrophysics, vol. 530, p. A102

B.6 *Resolving the nature of the dipping/flaring branch in Cygnus X-2*

Gibiec, A., Bałucińska-Church, M., Church, M. J. 2011

Poster presentation at the 'The X-ray Universe 2011' conference

held in Berlin, Germany, June 27-30, 2011

article ID: 212, http://xmm.esac.esa.int/external/xmm_science/workshops/2011symposium/

B.7 *On the nature of the Sco X-1 like super-Eddington sources*

Gibiec, A., Bałucińska-Church, M., Church, M. J. 2011

Oral presentation at JENAM-2011 conference

session: "Close Binaries with Compact Components"

held in Saint Petersburg, Russia, July 4-8, 2011

B.8 *Dipping versus Flaring in Z-track sources: resolving the controversy*

Bałucińska-Church, M., Church, M. J., **Gibiec, A.** 2012

Proceeding of the Frascati Workshop 2011

"Multifrequency behaviour of high energy cosmic sources"

Memorie della Societa Astronomica Italiana, v.83, p.178

B.9 *Spectral investigations of the nature of the Sco X-1 like sources*

Church, M. J., **Gibiec, A.**, Bałucińska-Church, M., Jackson, N. K.

Astronomy & Astrophysics, submitted 2012